RHEOLOGY OF MODEL NANOPARTICLE SUSPENSIONS IN EPOXY

A Dissertation

by

KEVIN LEE WHITE

Submitted to the Office of Graduate and Professional Studies of
Texas A&M University
in partial fulfillment of the requirements for the degree of

DOCTOR OF PHILOSOPHY

Chair of Committee,	Hung-Jue Sue
Committee Members,	Terry S. Creasy
	Anastasia Muliana
	Tahir Çağin
Head of Department,	Andreas A. Polycarpou

December 2013

Major Subject: Mechanical Engineering

ABSTRACT

The rheology and linear viscoelasticity of several model nanoparticle suspensions in epoxy have been systematically investigated. Three detailed studies were carried using α-zirconium phosphate (ZrP) nanoplatelets as model 2-dimensional nanoparticles. The effect of inter-particle interactions was investigated using three different surface modifiers to exfoliate the nanoplatelets. The role of nanoparticle size was separately investigated by synthesizing the ZrP nanoplatelets with average lateral diameters ranging from 100 – 1000 nm. The rheology of highly concentrated suspensions of ZrP nanoplatelets was also probed, and found to show unique properties due to the self-assembly of the nanoplatelets in discrete layers with regular inter-layer spacing. The rheological properties of each model system are discussed based on the motion of the individual particles, and the nature of interaction on local and higher order length scales.

Multi-walled carbon nanotubes (MWCNTs) were used as model 1-dimensional nanoparticles. We present a method to disentangle the MWCNTs to individual particles based on a novel functionalization technique. The rheology of suspensions containing the disentangled MWCNTs reveals that flocculation does not occur over long time scales, and suggests that the treatment does not significantly modify nanoparticle size.

The role of interaction between particles with different geometries was investigated using suspensions containing electrostatically tethered ZrP nanoplatelets and MWCNTs. The flow properties of this system are proposed to originate from direct interaction

between the particles, and the contributions of the individual phases are found to be preserved on distinct length scales. A mechanism is proposed to account for the unique strengthening behavior observed in solid epoxies containing the hybrid nanoparticles.

The findings presented here consider a broad range of nanoparticle shapes and sizes, and provide detailed insights into how particle-level effects contribute to bulk response in the liquid state. A framework to understand the fundamental behavior and interaction of isolated nanoparticles is presented based on the rheological signatures. Approaches to relate liquid-state behavior to solid systems are discussed. Future work on the local relaxation processes is anticipated to greatly improve understanding of the interfacial properties and driving forces for phase transitions for more complex systems.

DEDICATION

This dissertation is dedicated to my family. To my grandparents, Jack and Jean Sills, and, in memory of Leonard and Gladys White, for their love and dedication. To my parents, Leonard and Karen White, for their constant support and motivation. To my sister, Amy, for challenging and encouraging me. And to my sister, Samantha, for giving me someone to strive to be an example for.

ACKNOWLEDGEMENTS

I would like to thank my committee chair, Professor Hung-Jue Sue, for providing opportunities and encouragement that extend well beyond this dissertation research. I would also like to thank my committee members, Prof. Terry Creasy, Prof. Anastasia Muliana, and Prof. Tahir Cagin, for their guidance and support throughout the course of the dissertation research, and Prof. Partha Mukherjee for serving as a substitute committee member during my final exam.

I deeply appreciate the support and discussions from my colleagues and close friends in Prof. Sue's research group. Without significant contributions from my co-workers the scope of this dissertation would not have been possible. Significant contributions were made by Dr. Xi Zhang, Dr. Minhao Wong, Spencer Hawkins, Haiqing Yao, Peng Li, and Peng Liu. Prior work of Prof. Luyi Sun, Dr. W.-J. Boo, Dr. Dazhi Sun, Dr. Chien-Chia Chu, Dr. Tao-Hua Lee, Dr. Jia Liu, Dr. Shin-ji Iio, and Graham Warren, was also critical to this work. I would like to thank my colleagues at Texas A&M University (TAMU), and the faculty and staff of the Mechanical Engineering department and Polymer Technology Center, particularly Isabel Cantu, for support.

The initial funding that got me involved in research was through the Air Force Research Lab (AFRL) Minority Leaders Program (MLP). My experience as an undergraduate during the summer of 2008 convinced me to pursue a doctorate in Mechanical Engineering. I am very appreciative of guidance from Dr. Ryan Justice and

Dr. Dave Phillips, who served as my mentors during the internship, the MLP program coordinators, Dr. Merlin Theodore and Dr. Jennifer Fielding, and the technical director, Dr. Jeff Baur. Prof. Dimitri Lagoudas and Prof. Dan Davis of TAMU were also critical in making the opportunity possible. I would like to acknowledge L.L. Clarkson for his role in establishing the MLP, which I found to be extremely successful in its objective of increasing involvement of under-represented groups in engineering and scientific research. My experience with the program was greatly enhanced by interactions with Tobey Cordell of Universal Technology Corp., Dr. Baburaj Eranezhuth of Clarkson Aerospace, and Dr. Angela Campbell of the AFRL. Throughout the course of the research, and through various side projects, I have been very fortunate to have the opportunity to interact and exchange ideas with a number of professional scientists, and would like to personally thank Dr. Jack Douglas of NIST, Dr. Ha Pham of Dow Chemical Company, Dr. Nikhil Verghese of Sabic Technology Center, Dr. Thomas Tsotsis of Boeing, and Dr. Ivan Liang of Dow Chemical Company for valuable discussions.

We are very grateful to KANEKA Corporation for financial support throughout the duration of this research. Acknowledgement is also extended to Dr. Tony Golato of Hexcel for donating release paper for early research on partially cured thin films, and to Hexion Specialty Chemicals, DOW Chemical and Toray Industries for donating materials.

I was very fortunate to have the opportunity to carry out research at Kyushu University (Fukuoka, Japan) under the guidance of Professor Atsushi Takahara during

the summer of 2012. I am indebted to the support provided by Professor Takahara, and would like to acknowledge several other colleagues that assisted in our studies, which provided new and important insights into phase behavior and microstructure of polymer nanocomposites. At Kyushi University, I was greatly aided by Prof. Hiroshi Jinnai, Prof. Otsuka, Prof. Ryohei Ishige, Dr. Higaki, Dr. Ma Wei, Dr. Higuchi, Dr. Xi, Tao Di, and Hiroshi Arita. I am also very grateful to the hospitality of Prof. Masaya Kotaki of the Kyoto Institute of Technology, and Prof. Takuzo Aida and Dr. Yoshimitsu Itoh of the University of Tokyo.

TABLE OF CONTENTS

Page

LIST OF FIGURES

FIGURE Page

LIST OF TABLES

TABLE Page

CHAPTER I

INTRODUCTION

1.1 Background

Nanoparticles are of significant interest to academic and commercial fields, particularly those related to mechanical, electronic, photonic, and biological applications. The unique properties associated with nanoparticles originate from the substantial increase in surface area to volume ratio as particle dimension decreases, and the existence of quantum size effects not present in bulk materials. For example, in semi-conducting metal oxide nano-crystals, also known as quantum dots (QDs), the electronic band gap depends on the fraction of non-coordinated atoms at the particle surface [1, 2]. Their optoelectronic properties are therefore size-dependent and can be tailored. The distance between neighboring QDs also influences the optical characteristics due to short-range quantum coupling. Significant electronic energy transfer occurs at interparticle distances of up to 10 nm [3, 4]. As the distance decreases, the quantum size effects diminish, and their properties approach those of the bulk material [5]. Nanoparticles also possess large surface area to volume ratios that are crucial for applications as catalysts, gas storage devices, efficient energy conversion, and barrier property enhancement. The benefits related to surface area can be substantially diminished due to particle aggregation, as illustrated in Figure 1-1. Preservation of particle dispersion during handling at all length scales is critical, particularly for sensor

and multi-functional composite applications. The resulting higher-order microstructure must also be well controlled to realize the desired change in properties in the bulk.

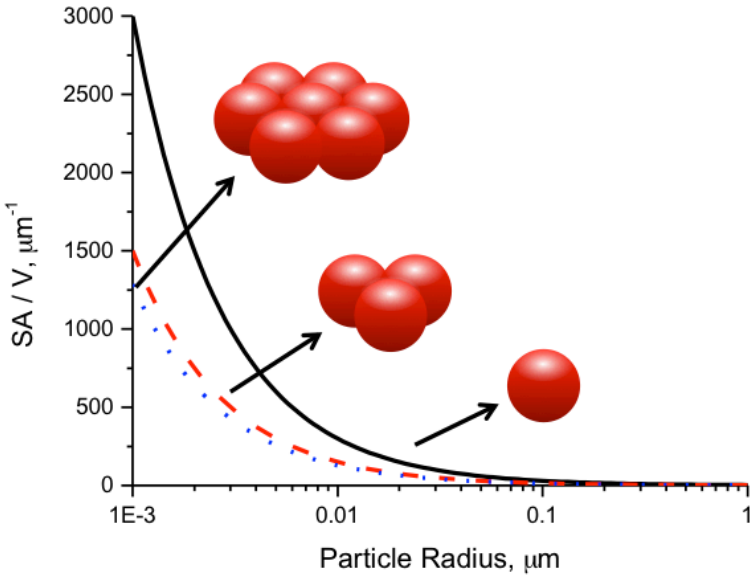

Figure 1-1. Estimated surface area to volume ratio, *SA/V*, as function of particle radius, for individual spherical particles (solid line), clusters of 3 particles (dashed line), and clusters of 7 particles (dotted line).

The ability to predict mesoscale structure based on the various attributes of nanoparticles, particularly particle size, size distribution, aspect ratio, and chemical functionality, is necessary to understand and potentially tailor the physical response of multi-functional materials. Recently, molecular-scale modeling approaches have indicated that simple estimates of particle shape and local order in a fluid are sufficient to predict various categories of structural order for a large number of convex polyhedra [6]. However, these discontinuous nano-scale modeling approaches implicitly assume

local constitutive relationships that may introduce considerable error if interfacial interactions or non-local coupling between mechanical fields are present [7]. Extensive experimental investigations have been attempted, but very little detail on the fundamental physics of the nanoparticles is possible because of challenges in achieving reproducible properties of an ensemble of individual nanoparticles. A schematic highlighting the important of interfacial interaction and size scales for nanoparticles is shown in Figure 1-2.

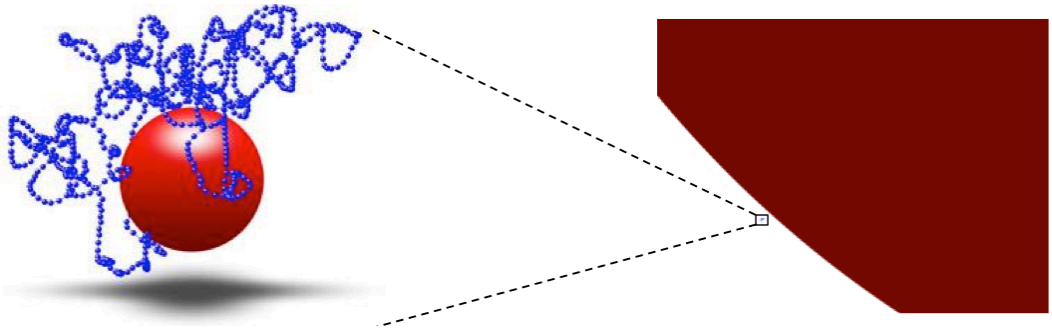

Figure 1-2. Schematic showing importance of length scale with nanoparticles. (Left) Nanoparticle with diameter of 10 nm is able to directly interact with polymer chains (shown with radius of gyration, $R_g \approx 20$ nm). (Right) Relative to particle with diameter of 10 μm, the dimensions of the same polymer chain and nanoparticle are negligible.

The current gap in knowledge bridging between continuum and molecular scale behaviors may be partially attributed to the lack of characterization methods available to visualize meso-scale interactions. Rheological measurements are the primary meso-structural characterization tool in the dissertation research because of the intimate relationship between the molecular-scale characteristics of a fluid and its resistance to

deformation and flow (c.f. [8-11]). The availability of rigorous mathematical tools to analyze the kinematics of deformation enables the measured response to be directly related to the material physics across an exceptionally broad range of length and time scales [12]. This framework has been used with tremendous success to understand the molecular-scale structure/morphology and dynamics of polymers [13], and significant progress has been made regarding the dynamics of glass-forming liquids [12, 14, 15].

The majority of work on the rheology of nanoparticle suspensions has been inherently phenomenological because of the lack of effective methods to disperse nanoparticles into various media with adequate reproducibility. As a consequence, reported properties are often conflicting and inconsistent, which pose significant barriers to applications. The poorly defined microstructure also prevents clear understanding of the role of the nanoparticles on bulk response [7]. Investigations into the melt-state rheology of polymer nanocomposites have similarly been limited to empirical observations that depend on various experimental conditions, particularly processing method, nanoparticle type, material supplier, and pre-treatment. These challenges have resulted in a significant gap between the atomic and molecular-scale properties of individual nanoparticles, and the poorly understood, and often conflicting, macroscopic performance of nanoparticle suspensions and nanocomposites.

Most prior research has focused solely on developing methods to achieve random dispersions on local length scales, which should be favorable for optical and some mechanical properties [16]. For simultaneous improvement of multiple properties, more complex morphologies of the dispersed phase may be desirable [17, 18]. If the shape

and interaction of nanoparticles are well controlled, the mesoscale organization of nanoparticles may be potentially guided to favor formation of higher-order structures [19-26]. These approaches have potential advantages because properties may modified across multiple length scales. This provides unique opportunities for simultaneous improvements in properties that are typically in opposition, such as stiffness and ductility. Higher order structures may be able to interact with their environment on multiple length scales, which is desirable for photonic crystals and other optical systems [27]. The parameters governing dispersion and organization, and the resulting macroscale properties of the composite material, remain poorly understood from theoretical and empirical viewpoints

1.2 Research objectives and significance

This dissertation focuses on establishing unambiguous relationships between molecular-scale organization of nanoparticles and macroscale property changes in nanocomposite materials using physics-based principles. The approach has been to measure the rheological and viscoelastic properties of fluids containing model nanoparticles with well-defined local and mesoscale order. Changes in the elastic and viscous response of suspensions provide direct insight into colloidal interactions between nanoparticles, fluid-mediated interactions, and changes in mobility due to packing, local dispersion, and longer range order. A schematic of the concentration dependence of shear viscosity, η, for polymer solutions is shown in Figure 1-3. We also investigated the rheology of fluids containing interacting rod-like and plate-like

nanoparticles to show how differences in shape can potentially be exploited to improve dispersion and promote synergistic property enhancement at low concentration.

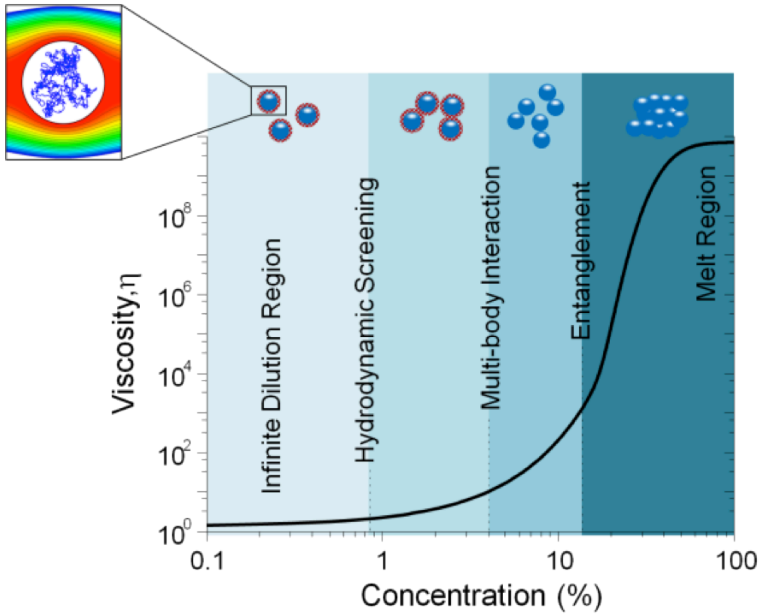

Figure 1-3. Schematic showing the different regimes of behavior of shear viscosity as function of concentration in polymer solutions. Adapted from [28].

The reported studies in this dissertation take advantage of novel methods developed in Professor H.-J. Sue's research group at Texas A&M University to tune the structure and dispersion of various nanoparticles, which are summarized in Table 1-1. This allows clear identification of behavior associated with the individual particles at low concentration, and factors influencing transitions due to the geometric packing constraints of non-spherical particles at higher concentrations. The results are used to approach several challenging questions in the field. For example, what is the rheological signature associated with an individual dispersion, and how is this affected by shape and

interactions? Is an individual dispersion necessary for property improvement, and are there situations where some degree of controlled aggregation is preferred? What are effective methods to control and quantify structure? Many of these questions have been approached previously, but not with the same degree of structural control and range of particle shape, size, and interactions considered here. This work probes a unique range of behaviors and offers a consistent framework to interpret rheological behavior.

Table 1-1. Summary of results from research group regarding synthesis and dispersion of model nanoparticles in various solutions and polymers.

Nanoparticle System	**Comments**	**Ref.**
ZnO-QD	ZnO-QDs synthesized with diameter of 2-5 nm	[29, 30]
Bulk ZnO-QD	Surfactant-free ZnO-QDs self-assembled into 3D colloidal crystal	[31]
PMMA / ZnO-QD	Diameter 5 nm; small aggregates	[32]
PMMA / ZrP-NP / ZnO-QD	Diameter 5.0 ± 0.3 nm; ZrP nanoplatelets used as colloidal dispersant; uniform dispersion of individual QDs without ligand	[33]
Epoxy / ZrP-NP / ZnO-QD	Nearly monodisperse (5.0 ± 0.3 nm); ZrP nanoplatelets used as colloidal dispersant	[34, 35]
ZrP	ZrP-NPs synthesized with controlled diameter	[36-39]
Epoxy / ZrP	Exfoliation state and aspect ratio of ZrP nanoplatelets in epoxy tailorable; highly dispersed	[40-49]
PP / ZrP-NP	Nanoplatelets dispersed by in-situ polymerization	[50]
CNTs	CNTs debundled to individual level by nanoplatelet-assisted dispersion method	[51-54]
Epoxy / ZrP-NP / MWCNT	MWCNTs disentangled with nanoplatelet-assisted dispersion method; hybrid ZrP/MWCNT particles uniformly dispersed in epoxy matrix; hybrid shows unique mechanical properties	[55]
PP / MWCNT	MWCNT disentangled with nanoplatelet-assisted dispersion method; ZrP nanoplatelets subsequently removed; MWCNTs compatibilized to achieve stable dispersion in PP	[56, 57]

Abbrev.: Zinc oxide quantum dot (ZnO-QD); poly(methyl methacrylate) (PMMA); zirconium phosphate nanoplatelet (ZrP-NP); polypropylene (PP); carbon nanotubes (CNTs); multi-walled carbon nanotubes (MWCNTS).

1.3 Dissertation layout

In Chapter II, a literature review is presented regarding structure-property relationships for suspensions containing solid particles. In Chapters III-VII, investigations on the rheology of suspensions containing model nanoparticles are described. A summary of the different systems investigated in this work is provided in Figure 1-4. In Chapters III-V, ZrP nanoparticles are used as model 2-dimensional plate-like particles, and have tunable shape and size. In Chapter III, the nanoplatelets are exfoliated into individual sheets with monodisperse thickness using 3 different surfactants. The role of surface modifier on the length scale and nature of inter-particle interactions is considered in detail. In Chapter IV, the ZrP nanoplatelets are synthesized with a range of lateral diameters to investigate the effect of aspect ratio on rheology and linear viscoelasticity. The behavior shows a unique separation of elastic and viscous responses that are proposed to originate from the extremely broad range of relevant length and time scales in the system. In Chapter V, the rheology of highly concentrated suspensions of ZrP nanoplatelets with smectic liquid crystalline organization is investigated.

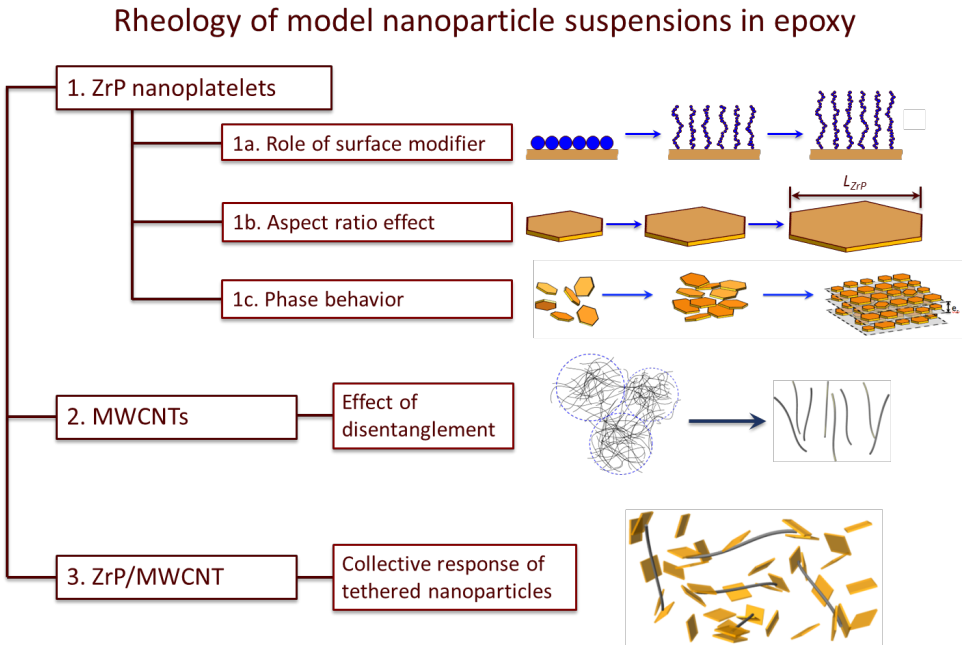

Figure 1-4. Schematic showing structure of dissertation.

In Chapter VI, the rheology of suspensions containing disentangled multi-walled carbon nanotubes (MWCNTs) is investigated and compared with the behavior of clustered MWCNTs. In Chapter VII, the rheology of suspensions containing electrostatically interacting ZrP and MWCNT nanoparticles is reported, and related to the mechanical properties and fracture behavior of solid nanocomposite systems.

In Chapter VIII, a detailed summary and conclusions section is provided. The insights gained from work are discussed to better understand behavior of solid-state systems. Future work is suggested that may provide more detailed insight into changes in response originating on different length scales.

CHAPTER II

LITERATURE REVIEW

2.1 Introduction

Predicting macroscale response from an assumed configuration of characteristic inclusions is one of the fundamental problems in statistical mechanics, and is relevant to disciplines spanning structural scales from the atomic and molecular level (such as kinetic theories of gases and liquids, polymer physics, electron transport), to the continuum-level (multi-phase flow, fracture mechanics, and transport in heterogeneous media). Alternatively, the same tools may be used to interrogate the molecular-structure of materials based on the associated change in volume-averaged and time-averaged properties.

This dissertation is concerned with the relationship between macroscale properties of fluids and polymers, and the dispersion and organization of particles with dimensions on the nanometer scale, which are referred to here as nanoparticles. The introduction of a small concentration of nanoparticles can substantially improve the thermomechanical, optical, and electrical properties of polymers, but the specific particle-level mechanism responsible for the improvement is generally unclear. In several cases, there has been significant investment in systems based on flawed assumptions regarding the scalability and generality of a specific observation. The resulting performance of the "nano"-composites is generally inconsistent and well below expectations, which pose significant barriers to commercial applications. These early problems reflect inherent problems in

the field related to the lack of available techniques to process and characterize materials on the nanoscale. Most processing techniques used today are top-down, mechanical methods developed for micron-scale fiber composites and particulate filled systems. Common characterization techniques are similarly limited by compromises between time, resolution, and sampling size, and may not be sensitive to the relevant processes for a desired property of interest.

For non-spherical nanoparticles, the vast majority of research to date has focused solely on achieving random dispersions on local length scales. Any resulting properties that do not meet expectation are generally explained based on experiences with micron-scale fillers, in particular, inadequate dispersion and adhesion. This level of discussion ignores the most exciting features of nanoparticles, which is that they interact with their environment on a much smaller length scale than their micron-scale counterparts. This distinction offers tremendous opportunities to design functional materials with properties tailored to specific applications by controlling material structure from the bottom-up. Controlling the mesoscale organization of nanoparticles into higher-order structures also offers potential for targeting properties across length scales. An important example relevant to this work is colloidal liquid crystals. High aspect ratio plate-like particles are widely used as rheological modifiers and for polymer composite applications, and increasing the degree of order is expected to provide greater improvements in certain properties, particularly modulus, strength, and barrier properties. Achieving long-range organization offers new properties associated with the higher-order structure, such as specific wavelength filtering of light.

The approach of this dissertation is to investigate the rheological and viscoelastic properties of fluids containing model nanoparticles with well-defined local and mesoscale order. From a practical perspective, the behavior of nanoparticle-filled fluids is of interest for heat transfer fluids, flow modifiers for commercial products, and microfluidic devices and sensors. From a fundamental perspective, these studies provide clear microstructural mechanisms associated with specific macroscale properties, which will be useful to distinguish relevant properties in more complex systems.

In this chapter, the origins of rheological and viscoelastic response of suspensions is briefly reviewed. The focus will be on topics relevant to issues considered in the dissertation. Relevant equations and descriptions used in later sections are presented. Theoretical and experimental description of model systems with well-defined microstructure and interactions are provided, along with some concluding remarks on the usefulness of rheology to probe nanoscale phenomena.

2.2 Motion of isolated spheres

The focus of this brief review will be limited to landmark theoretical, experimental, and computational findings that provide unambiguous connections between the individual particle motions, and resulting bulk properties. The simplest case to consider is a large, rigid spherical particle added to a liquid medium. The spherical inclusion introduces a hydrodynamic perturbation that modifies the velocity distribution of the fluid medium (c.f. inset in Figure 1-3). The Navier-Stokes equations describe the motion of a fluid and may be expressed in general form with the equation

(2.1) $$\rho\left(\frac{\partial \boldsymbol{v}}{\partial t} + \boldsymbol{v}\cdot\nabla\boldsymbol{v}\right) = -\nabla p + \nabla\mathbb{T} + \boldsymbol{f}$$

where ρ is the fluid density, $\boldsymbol{v}$ is the velocity vector, p is the pressure, $\boldsymbol{T}$ is the deviatoric stress tensor, and $\boldsymbol{f}$ is the sum of body forces acting on a unit volume of the fluid. The symbol ∇ is the vector differential operator, given by $\nabla = \hat{x}\frac{\partial}{\partial x} + \hat{y}\frac{\partial}{\partial y} + \hat{z}\frac{\partial}{\partial z}$ in the 3-dimensional Cartesian coordinate system. This expression is applicable to describe fluid motion where the fluid can be regarded as a continuum, but cannot be solved in many cases and therefore requires simplifying assumptions in the case of suspensions. If the discrete nature of the fluid is important (often defined based on the Knudsen number), statistical mechanics or molecular dynamics approaches may be necessary [58].

The first major contribution toward the modern understanding of the rheology of suspensions was by George Gabriel Stokes. Stokes modified the Navier-Stokes equations based on the assumption that the rigid spheres do not interact, have homogeneous composition and smooth surfaces, and are falling in a viscous fluid under the influence of gravity. In the limit of small Reynolds numbers (ratio of inertial forces to viscous forces), where the fluid exhibits laminar flow (sufficiently low velocity to neglect inertia), the non-linear convective acceleration term in Eqn. (2.1), $(\boldsymbol{v}\cdot\nabla\boldsymbol{v})$, vanishes. In the case of incompressible flow and constant viscosity, η, the deviatoric stress term is $\nabla\mathbb{T} = \eta\nabla^2\boldsymbol{v}$, which simplifies to

(2.2) $$\rho\left(\frac{\partial \boldsymbol{v}}{\partial t}\right) = -\nabla p + \eta\nabla^2\boldsymbol{v} + \boldsymbol{f}$$

For steady flow conditions (time-independent), $\frac{\partial \boldsymbol{v}}{\partial t} = 0$, and in the absence of any body forces, Eqn. (2.2) can be expressed

(2.3) $$\nabla p = \eta \nabla^2 \boldsymbol{v}$$

which provides a linear solution that can be easily solved. Stokes proposed that the change in velocity distribution is a consequence of the drag force, F_d, acting on the interface between the particle and fluid, and showed that

(2.4) $$F_d = 6\pi\eta R v_s$$

where a is the radius of the rigid sphere and v_s is the settling velocity of the rigid sphere.

Stokes' discovery was a major breakthrough in hydrodynamics and describes the velocity of a sphere in a material with known viscosity. However, it does not provide any details regarding the change in viscosity or mean stress field due to the presence of the sphere. The solution to the former problem was provided by Albert Einstein as part of his Ph.D dissertation [59, 60]. Einstein considered how the behavior of molecules and particles manifest in observable phenomena. His conjecture was that viscosity should be dependent on the size of any dissolved particles, and from this assumption, he derived two equations relating viscosity to the size and number of the molecules in terms of Avogadro's number [61]. The most general form of his equation is

(2.5) $$\frac{\eta_s}{\eta} = \eta_r = 1 + 2.5\phi$$

where η_s is the viscosity of the suspension, η is the viscosity of the unfilled fluid, η_r is the relative viscosity, and ϕ is the volume fraction of filler particles. This expression is still used today and the linear relationship between viscosity and concentration has been widely confirmed for dilute suspensions of particles with arbitrary shape.

This was the first work to determine molecular size using liquids, and after a few math errors and experimental values were corrected, Einstein's relations impressively

found Avogadro's number to be $N_A = 6.56\ x\ 10^{23}$ (the modern estimate is $6.022\ x\ 10^{23}$), which was quite remarkable at the time [62]. Even more astounding was that only 11 days after finishing his dissertation, he submitted a second paper based on this framework that mathematically demonstrated that the random, jittery motion of small particles in water (Brownian motion), is a consequence of a tremendous number of collisions with the water molecules . This mechanism had previously been suggested based on the kinetic theory of gases, but it was concluded that, "…a molecule would not have the power to budge the particle [10,000 times larger than the water molecule] any more than a baseball could budge an object that was a half-mile in diameter [60]". Einstein showed that the motion was actually *required* by the thermal energy in the system, which causes random oscillations on the atomic scale and results in millions of collisions between the fluid molecules and the suspended particles. This rather straightforward statistical approach was an extension of Einstein's original question regarding how the actions of molecules and atoms could be observed in the visible world, and indirectly provided the first direct evidence that atoms and molecules exist as real, physical objects.

2.3 Viscosity of suspension of spheres

The shear viscosity of a suspension of isolated spheres is a function of only two dimensionless groups: the particle volume fraction, ϕ, and the Peclet number,

(2.6) $$Pe = \frac{\dot{\gamma} a^2}{D_o}$$

where $\dot{\gamma}$ is the shear rate, a is the diameter of the sphere. The Einstein diffusion coefficient, derived from Eqn. (2.4), is given by

$$D_o = \frac{k_B T}{6\pi\eta_m a} \tag{2.7}$$

Here, $k_B T$ is the thermal energy of the system.

The Peclet number is an important dimensionless number for rheology because it a measure of the magnitude of departure from equilibrium. Physically, it is the ratio of the characteristic time scale of deformation, $1/\dot{\gamma}$, and the time scale for the system to recover equilibrium arrangement due to Brownian motion, a^2/D_o.

Except for a few limiting cases, the function $\eta = f(\phi, Pe)$ is not known theoretically. The most basic system is a dilute suspension of hard spheres. In the dilute limit, all direct interparticle interactions are neglected, and it is assumed that there is no overlap in hydrodynamic disturbances caused by the flow, which will introduce 2-body hydrodynamic interactions. Einstein solved this problem by considering the disturbance of flow around the isolated particles . He proposed that the isolated disturbances result in additive contributions to the rate of energy dissipation in the fluid, which is equivalent an increase in fluid viscosity. Under conditions of creeping flow around a sphere, he derived Eqn. (2.5). Although there is some debate about the appropriate for the pre-factor for ϕ, the prediction that at low concentration, viscosity is linearly proportional to volume fraction, independent of particle size, polydispersity, temperature, shear rate, etc., has been confirmed, and provided the first experimental approaches to study molecules [63, 64].

The main limitation of Eqn. (2.5) is that higher-order interactions become significant, even at low concentrations (c.f. Figure 1-3). At non-dilute concentration, inter-particle interactions become significant and present significant theoretical challenges. Near the dilute limit, the interactions may be treated with a power-law expansion of the form

$$\eta_r(\dot{\gamma}) = 1 + k_1\phi + k_2\phi^2 + k_3\phi^3 + \cdots \tag{2.8}$$

The power-law series approach is rationalizing by assuming that the coefficients, k_i, corresponding to different powers of volume fraction, ϕ^i, correspond to i-body interactions. Although this framework is somewhat compelling from a theoretical perspectives, it is very limited because (1) multi-body effects on are challenging to predict from hydrodynamics, and (2) the relevant range of volume fractions for each higher order term becomes progressively smaller.

For the idealized case of hard spheres, there has been some success using an equation of the form in Eqn. (2.8). To account for pair-wise interactions, the pair distribution function at equilibrium may be expanded with respect to a parameter of interest, such as Peclet number. The relevant physics depend on assumptions in the expansion. This theoretical approach is described in detail by Batchelor, and represents a major theoretical contribution because it provides an extensive theory to directly evaluate bulk stress due to the particles [65]. The majority of prior approaches had been based on Einstein's concept of hydrodynamic disturbance and energy dissipation.

For a non-dilute suspension of hard spheres with random particle distribution, neglecting Brownian motion, Batchelor and Green [66] obtained

(2.9) $$\eta_{r,\infty} = 1 + \frac{5}{2}\phi + 5.2\phi^2$$

In the absence of Brownian motion, the change in viscosity due to the hard spheres is purely hydrodynamic. The prediction in Eqn. (2.9) therefore refers to the increment in viscosity due to pair-wise interactions at high shear rate. The predicted behavior is Newtonian.

Batchelor also determined the effect of Brownian motion [67]. Using the same approach to expand the pair distribution, he assumed that dominant Brownian motion results in additional stress due to the random movements of the particles. He calculated the extra stress term and showed that dominant Brownian motion for semi-dilute hard spheres generates a $0.97\phi^2$ contribution to viscosity. In the limit of $Pe \to 0$, this may be expressed as a zero shear viscosity

(2.10) $$\eta_{r,o} = 1 + \frac{5}{2}\phi + 6.2\phi^2$$

The difference between Eqn. (2.9) and Eqn. (2.10) indicates that for systems of non-interacting spheres subjected to dimensionless shear rate over the range $Pe \to 0$ to $Pe \to \infty$, the response will be Newtonian at high and low shear rates, with a region of shear thinning near $Pe \sim O(1)$. The concentration dependence of shear viscosity for the hard sphere suspensions is shown in Figure 2-1.

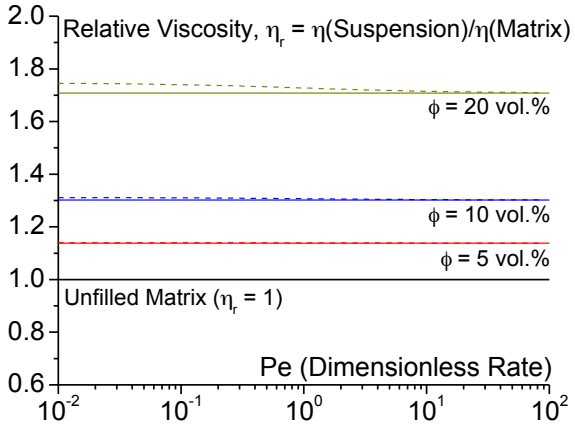

Figure 2-1. Viscosity of suspension of hard spheres as function of Peclet number for suspensions with φ = 5, 10, and 20 vol.%. Solid lines calculated with Batchelor's equation for pair-wise interaction, neglecting Brownian motion [Eqn. (2.9)]. Dotted lines include Brownian motion component [Eqn. (2.10)].

The shear thinning behavior is associated with the extra energy dissipation due to Brownian motion. The total contribution of Brownian motion is only $\sim O(\phi^2)$, and from Figure 2-1, it is clear that the magnitude is not large. For non-spherical particles, the differences becomes substantial and the transition to hydrodynamically dominated response provides a useful comparison between shear viscosity and linear viscoelastic measurements. There are a number of empirical equations proposed to describe the shear thinning transition. Depending on the degree of shear thinning, the width of the transition, and which features of the flow curve are visible, there are advantages to each. The Cross equation is robust and found to be useful for the systems reported here, and is given by

$$\eta = \eta_\infty + \frac{\eta_o - \eta_\infty}{1+(\lambda\dot{\gamma})^n} \tag{2.11}$$

where η_∞ is the infinite shear rate viscosity, η_o is the zero-shear viscosity, λ is the characteristic time, and n is the power-law exponent [68-71]. For n = 0, the equation

reduces to $\eta = \eta_o$, and the flow is Newtonian. As n increases, the transition between high and low shear plateau plateaus becomes more sharply defined, and n = 1, is equivalent to friction between solid surfaces moving relative to each other. The characteristic time, λ, is defined as the inverse of $\dot{\gamma}$ where $\eta = (\eta_o - \eta_\infty)/2$. The shear-thinning behavior of the hard sphere suspensions is shown in Figure 2-1b, and is obviously very minor.

From Figure 2-1, it appears that based on the theoretical calculations, model hard sphere suspensions do not show very pronounced rheological behavior. This has been experimentally demonstrated in many studies on non-colloidal spheres, which do not generally show non-Newtonian response until volume fractions ~ 45% and higher [63, 72]. For real suspensions, there may be significant deviations from the ideal, hard-sphere behavior at low concentrations due to colloidal interactions [73]. One feature of interest is for dense suspensions, which show very high viscosity at low shear rate, a transition to shear thinning due to the formation of a well-ordered layers, and a disorder transition with pronounced shear thickening behavior at high shear rates [74-79]. These systems are very complex, but it has been suggested that this range of behaviors is characteristic of all systems over a broad enough experimental range [76].

There are no well accepted theoretical descriptions of concentrated suspensions, which reflects the significant range of complex behaviors observed [80-84]. At high concentrations, flow behavior becomes strongly dependent on the specific properties of the particles, and the nature of interaction with the suspending medium. For highly

concentrated systems, confinement of the matrix may result in further non-Newtonian characteristics [85, 86].

There are a number of empirical forms that have been proposed to account for rheology of concentrated systems. Among the most common is the Krieger-Dougherty relation, which was originally proposed as an empirical equation [87], but later shown to have theoretical basis [88]:

$$\eta_r = \left(1 - \frac{\phi}{\phi_m}\right)^{-[\eta]\phi_m} \tag{2.12}$$

Here, ϕ_m is the maximum packing fraction of the suspended phase and $[\eta]$ is the intrinsic viscosity of the particles, equal to k_1 in Eqn. (2.8). For hard spheres, Eqn. (2.5) shows that $[\eta] = 5/2$. This form describes the divergence of viscosity approaching a concentration where the particle motion is effectively frozen.

Bicerano et al. [89] noted that a divergent equation of the form in Eqn. (2.12) may expanded to include shear-rate and temperature dependent effects through ϕ_m. For hard spheres, the maximum packing fraction is shear rate dependent. For example, De Kruif et al. investigated the rheology of colloidal silica with surface-treatment to minimize inter-particle interaction, and found that increasing shear rate shifted the maximum packing fraction from $\phi_m = 0.63$ for $\dot{\gamma} \to 0$, to $\phi_m = 0.71$ for $\dot{\gamma} \to \infty$ [90]. For non-spherical particles, the functional dependence is more pronounced because shearing deformations effectively increase the orientational order of the system.

Quemada provided an expression for hard spheres with similar form, where $\eta_r = (1 - \phi/\phi_m)^{-2}$ [91]. Here, ϕ_m is a packing volume fraction that varies between 0.58 and 0.72, depending on system. Philipse and co-workers recently adapted this

expression to describe the rheology of moderate aspect ratio, plate-like particles [92-97]. Their approach is to set $\phi^* = 1$ and replace volume fraction with an effective volume fraction, ϕ_{eff}, that accounts for fluid volume trapped by particles through average motion. The trapped volume is expressed by $\alpha\phi_{exl}$, where $\alpha = f(Pe)$, and $\phi_{exl} \approx 2\phi_p/3r_p$ is the volume fraction of spheres with excluded volume encompassing the particle. The value of $\alpha = \left(1 - \sqrt{\eta_m/\eta}\right)/\phi_{exc}$. This approach is an example of interpreting the rheology of a complex system by mapping the results to the well-established behavior of hard sphere systems [63].

2.4 Suspensions of non-spherical particles

2.4.1 Overview

From the discussion above, it is apparent that even for the simplest model of monodisperse hard spheres, there are significant, intractable theoretical challenges. For non-spherical particles, there is significantly greater complexity because (1) the magnitude of hydrodynamic disturbance (particle stress contribution) depends on orientation with respect to the flowing direction, and (2) the particles rotate under most flow fields of interest. For flow fields that lack a rotational component, such as elongational flow and equi-biaxial extension, there may be closed form solutions available for $[\eta]$ in limiting cases of high aspect ratio [98]. In most cases, there will be a shearing component to deformation (although this does not necessarily mean simple shearing flow is relevant [99]), and the velocity gradient perpendicular to the flow direction establishes both translational and rotational motion of the suspended particles.

The resulting particle contribution must therefore be time-averaged, and in order to extend the result to predict suspension viscosity, the distribution of orientations for all fibers must be known. A number of different factors influence the nature of the orientation distribution, particularly aspect ratio, concentration, Peclet number, particle flexibility, and permanent deformation.

The general theory of dilute suspension rheology for non-spherical particles is reviewed in considerable detail by Brenner [100]. Several reviews on the rheology of fiber suspensions are also available and provide excellent surveys of the field [63, 64, 101-103]. Here, the focus is on general concepts related to the motion of the particles, the magnitude of hydrodynamic disturbance predicted by theory, relevant time scales for motion, and brief consideration of some non-ideal effects related to interactions and flexibility.

2.4.2 Motion of isolated non-spherical particle

The equations of motion for an isolated ellipsoidal particle were derived by Jeffery [104], using the same hydrodynamic approach developed by Einstein for isolated spheres. Here, we will limit discussion to simple shearing flow, where the suspending fluid is assumed to be confined between two infinite, parallel plates, and shearing deformation is applied along the x-direction, parallel to the plate, as shown in Figure 2-2. The velocity field for steady shear is 1-dimensional, and given by $V_x = \dot{\gamma} y$ in the x (flow) direction, and $V_y = V_z = 0$ in the y-direction (velocity gradient) and z-direction (vorticity), respectively.

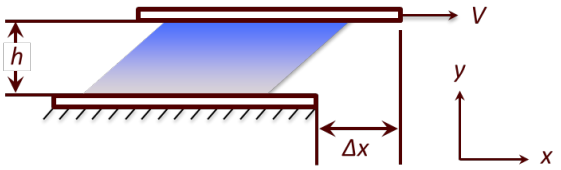

Figure 2-2. Schematic showing geometry of simple shearing flow.

Jeffery showed that for slow, steady shear deformation of an incompressible fluid, the stresses acting over the surface of an isolated ellipsoid vanish, and as a result, there is no resultant force [104]. Hence, the center of mass of the particle displaces affinely with the fluid. The only remaining contribution due to the motion of the fluid across the surface of the ellipsoid is a resultant couple that can be separated into two components. The first vanishes when the ellipsoid has the same resultant spin as the fluid. The second vanishes when the ellipsoid is aligned in the shearing direction (defined by the x-axis here). In the absence of external body forces acting on the particle, or inertia, the two components are balanced at all times and result in a fixed, periodic rotation of the ellipsoid in a characteristic orbit, commonly referred to as a Jeffery orbit (Figure 2-3). The orientation of the particle is defined by a unit vector, $\hat{\boldsymbol{e}}$, parallel to the axis of rotation for the particle, with Euler angles defined in spherical coordinates. The influence of the particle on the bulk flow behavior is determined by the magnitude of particle cross-section across the flowing direction. For prolate ellipsoids (rod-shaped, with axial ratio, $r > 1$), this is given by $u_y = \sin\theta \cos\phi_1$. For oblate ellipsoids (disk-shaped, $r < 1$), the axis of symmetry is perpendicular to the thin dimension, and the

maximum hydrodynamic distortion is for $\phi_1 = \pi/2$. The relevant projection of $\boldsymbol{u}$ in this case is $u_x = \sin\theta \sin\phi_1$.

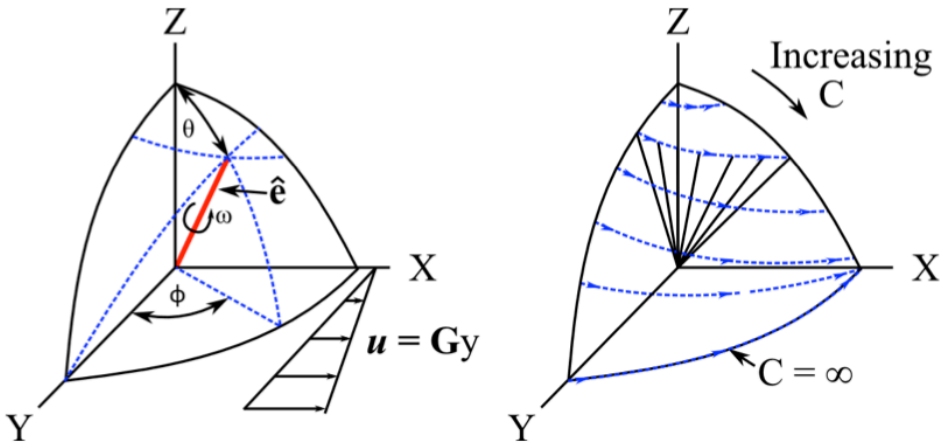

Figure 2-3. Schematic showing motion of isolated ellipsoid under simple shear. (Left) spherical coordinate system for ellipsoid with axis of symmetry $\hat{\boldsymbol{e}}$. (Right) Jeffery orbit for isolated ellipsoid for different Jeffery orbits, C.

The predicted motion has important consequences on flow properties that depend on the axial ratio of the ellipsoid (and the aspect ratio of the related real particles). In the absence of Brownian motion and other effects, such as body forces or particle-particle interaction, the equations of motion under steady shearing are given by the coupled differential equations

(2.13) $$\frac{d\boldsymbol{\phi_1}}{dt} = \dot{\phi} = \frac{\dot{\gamma}}{r^2+1}\left(r^2\cos^2\phi + \sin^2\phi\right)$$

(2.14) $$\frac{d\theta}{dt} = \frac{\dot{\gamma}}{4}\left(\frac{r^2-1}{r^2+1}\right)\sin 2\theta \sin 2\phi$$

The solutions to these equations show that the particle rotates in a fixed orbit described by the Jeffery orbit constant, C, and phase angle, k. Later experimental work directly

confirmed the predictions for real particles (fibers and disks) [105-113], and showed that the dependence on initial conditions may be relaxed in real systems [114-116].

The magnitude of particle influence depends on its projection across the flow direction. One important consequence of Eqn. (2.13) is that the angular velocity of the particle is largest in this configuration, and the effect is amplified with increasing aspect ratio (Figure 2-4). In other words, *larger particles tend to spend the majority of each orbit aligned in the direction that minimizes their hydrodynamic distortion*. Although the maximum hydrodynamic disturbance increases strongly with aspect ratio, $\sim O(L^3)$, the increase in aspect ratio decreases the probability of finding a particle aligned across the flow direction, which suppresses the scaling of viscosity at dilute concentrations.

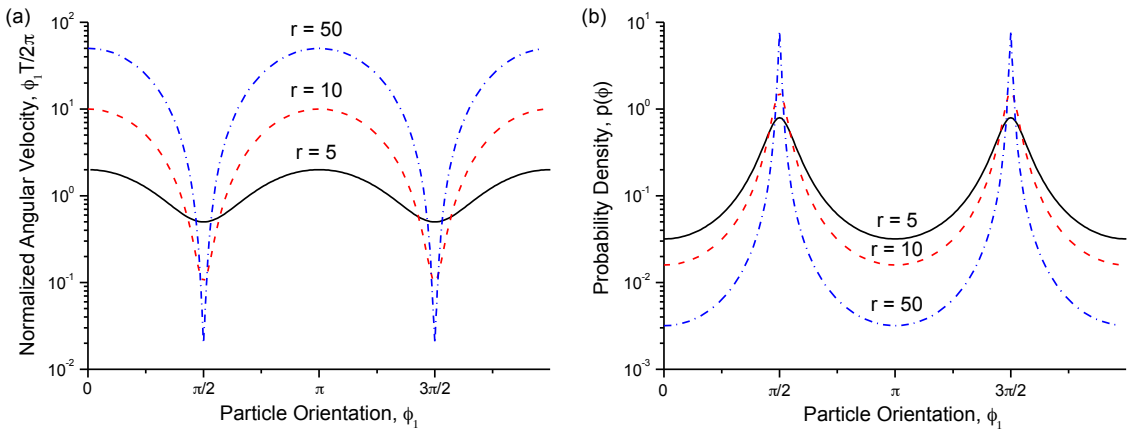

Figure 2-4. (a) Angular velocity, normalized by period of rotation, and (b) probability density function of orientation, as functions of particle orientation with respect to flow direction, ϕ_1.

The observed balance between maximum hydrodynamic disturbance and probability of flow-alignment with aspect ratio is particularly critical to understand the behavior of non-dilute concentrations. One consequence of pair-wise hydrodynamic interactions is to shift the distribution of orbit constants, $p(C)$, to larger C, which increases the time-averaged u_y [117]. The shift in $p(\phi)$ is negligible, and nearly constant up to high concentrations [118]. Detailed description of the various types of periodic motion exhibited by individual ellipsoids are discussed in detail by Hinch and Leal [119], and more recently, are compared to analogous behaviors exhibited by liquid crystalline polymers by Petrie [101]. The effect of concentration on hydrodynamic and non-hydrodynamic interactions, and the resulting changes in periodic rotation, have been investigated in several papers by Koch and collaborators [117, 118, 120-128].

2.4.3 Period of rotation

The period of rotation predicted by Jeffery's equations of motion for an isolated ellipsoid in steady shear depends only on aspect ratio and shear rate, and is given by

$$T_r = \frac{2\pi}{\dot{\gamma}}(r + r^{-1}) \tag{2.15}$$

This definition of orbital period is important from an experimental perspective because it establishes a measurable link between the flow behavior of ideal ellipsoids and real particles. Bretherton showed that any arbitrarily shaped particle with axial symmetry will follow a Jeffrey orbit with period given by Eqn. (2.15) [99]. However, the calculated r associated with the measured period will be smaller than the aspect ratio of the real particle, r_p, due to hydrodynamic consequences of particle shape and sharp

edges [129, 130]. The relationship between the real aspect ratio, r_p, and the axial ratio of an effective ellipsoid, r, was extensively investigated in a series of papers by Mason and collaborators using meticulous visual observation of isolated rods and disks rotating in a concentric cylinder [105-107, 111-113, 115, 116, 131, 132]. These papers established that the behavior predicted by Jeffery is observed in a broad range of real systems, and provided several empirical relations for $r = f(r_p)$ using model systems with low polydispersity. One widely used correlation that accurately describes the "equivalent spheroid" for both disks and rods is given by:

$$\log(r) = 0.78\log(r_p) + 0.051 \tag{2.16}$$

where r is an effective axial ratio of an equivalent spheroid with the same motion as the observed real particles.

Correlations such as Eqn. (2.16) are necessary to predict the flow behavior of systems containing particles that cannot be directly observed, such as nanoparticles. However, this must be approached with caution because it requires that the relevant assumptions on the micron-scale are still satisfied. In particular, the magnitude and scaling of inter-particle interactions may significantly affect flow behavior and cause deviations in time scale of motion. Furthermore, correlations are generally valid only for a limited set of model systems.

As aspect ratio increases, the flexibility of a particle increases significantly, and the particle becomes more susceptible to shear-induced compressive stresses. This has been considered in detail by Forgacs and Mason for fibers and is mentioned below [110, 133]. No equivalent theoretical description has been successfully applied to plate-like

particles, to our knowledge. A number of simulation approaches have been reported that capture the predicted rotation and periodicity for plate-like particles, but are generally limited to aspect ratios ~ 5-10 [134-138]. These approaches may potentially be used to extend the correlation between ellipsoids and real particles for higher aspect ratios and include the effects of flexibility, provided that the appropriate physics relevant to the particle length scale are represented.

One consequence of increasing concentration is that hydrodynamic interactions with neighboring particle affect the period of rotation by increasing the rate of tumbling out of the flow direction. This should result in substantial changes in the particle contribution to viscosity, and has been experimentally observed for intermediate concentration [117, 120-122, 124-126]. However, the relationship between inter-particle interaction and period of rotation is complex. In the semi-dilute region, Petrich et al. [118] observed that the period was decreased due to pair-wise hydrodynamic interactions, as expected, but found an increase in T_r in the concentrated regime. One remarkable aspect of this finding is that even for concentrations where the average distance between particles is on the order the fiber diameter, there is still observable periodic agreement that follows the simple motion described by the hydrodynamics of isolated fiber [118]. The non-monotonic nature of T_r was shown to be consistent with a transition from random interactions that enhance rotation at semi-dilute concentrations, to local nematic alignment and restriction in rotational freedom in the concentrated systems.

2.4.4 Equilibrium orientation distribution

Jeffery's equations provide an excellent description of the motion of an individual fiber, but neglect the problem of orientation distribution. In his concluding remarks, Jeffery speculated that the particles will tend to adopt an average orientation that minimizes their effect of viscosity [104]. In this case, the particles will align in the flow direction and $[\eta] = 2$, which is less than the theoretical predictions for spheres and is a lower bound. In real systems, this is not observed because the equilibrium orientation distribution depends on a number of parameters. In the simplest case, the distribution may be described using an appropriate form of Pe for rotational diffusion. In the limit of $Pe \to 0$, the equilibrium distribution of Jeffery orbits, $p(C)$ (more commonly, $p(C_b)$ is used, where $C_b = C/C + 1$, because C may take any value between 0 and ∞) will be isotropic due to Brownian motion, which apply rotary torques across the particle surface and randomizes position and orientation. This distribution will be skewed due to various factors, and generally will favor alignment in the shearing plane, which decreases $[\eta]$. The limiting intrinsic viscosity for dominant Brownian motion is Newtonian over a range of shear rates, and defined as $[\eta]_o = \lim_{Pe\to 0}[\eta]$.

In the limit of dominant shearing forces, $Pe \gg 1$, and the equilibrium distribution of orientations becomes strongly skewed in the flow direction. In this case, the intrinsic viscosity reaches a steady state that depends on aspect ratio, $[\eta]_\infty$, and the suspension behavior is Newtonian. A number of theoretical approaches have been developed to predict $[\eta]$ in different limiting cases. These have been reviewed by several authors and

will not be considered in detail here [100, 101]. One interesting prediction from Leal and Hinch [139], is that the scaling between limiting regions follows $Pe^{-2/3}$.

To account for Brownian motion in real systems, the rotational Peclet number, $Pe = \dot{\gamma}/D_r$, where D_r is the rotary diffusion coefficient, D_r. The framework established by Brenner is useful because it can be applied to any axially symmetric particle by defining the equivalent ellipsoid with $r = f(r_p)$ [100]. As outlined by Brenner, the rotary diffusion is given by

$$D_r = \frac{k_B T}{6 V_p \eta_s \ {}^{r}K_{\perp}} \tag{2.17}$$

where $\zeta = 6 V_p \eta_s \ {}^{r}K_{\perp}$ is the rotational friction constant [13]. The dimensionless material scalar, ${}^{r}K_{\perp}$, is a function of aspect ratio is a dimensionless scalar that depends only on geometry. For ellipsoids with axial ratio $r = a/b$ where a and b are the polar and equatorial radii of the ellipsoid, respectively:

$${}^{r}K_{\perp} = \frac{2(\mathrm{r}^2+1)}{3(\mathrm{r}^2\alpha_{\parallel}+\alpha_{\perp})} \tag{2.18}$$

The α terms are shape integrals related to the spheroid geometry, and are expressed

$$\alpha_{\parallel} = \frac{2(\mathrm{r}^2\beta-1)}{\mathrm{r}^2-1} \tag{2.19}$$

$$\alpha_{\perp} = \frac{\mathrm{r}^2(1-\beta)}{\mathrm{r}^2-1} \tag{2.20}$$

where the shape factor, β, depends on the shape of the ellipsoid

$$\beta = \begin{cases} \dfrac{\cosh^{-1}\mathrm{r}}{\mathrm{r}\sqrt{\mathrm{r}^2-1}}, & \mathrm{r}>1 \\ \dfrac{\cos^{-1}\mathrm{r}}{\mathrm{r}\sqrt{1-\mathrm{r}}}, & \mathrm{r}<1 \end{cases} \tag{2.21}$$

2.4.5 Viscosity of rod suspensions

Simha [140] and Kuhn and Kuhn [141] derived expressions for $[\eta]$ in the limit of dominant Brownian motion based on the energy dissipation of non-interacting rods, which are given by

(2.22) $$[\eta] = \frac{r^2}{15\left[\ln(2r) - \frac{3}{2}\right]} + \frac{r^2}{5\left[\ln(2r) - \frac{1}{2}\right]} + c$$

where $r = L/d$ is the aspect ratio of a rod, and $c = 14/15$ for Simha, and $c = 1.6$, for Kuhn and Kuhn. The first term is the contribution of Brownian motion to energy dissipation. The second term is the contribution due to the hydrodynamic disturbance of the solid particles. In the limit of large aspect ratio, the Brownian contribution approaches 3 times the magnitude of the hydrodynamic contribution, and the shape of the particle is irrelevant, which is an important basis for slender body theory [142].

The influence of concentration is challenging to approach from a robust theoretical perspectives for suspensions containing rods, because the presence of inter-particle interactions will influence the instantaneous and average orientation distributions. Berry and Russel [143] considered pair interactions in the dilute region for weak shearing flow, and found that the combination of hydrodynamic and Brownian forces results in greater degree of shear thinning than predicted from dilute theory, given by

(2.23) $$\eta_r = 1 + [\eta]\phi + \frac{2}{5}[\eta]^2\phi^2$$

This form is useful in the dilute region, but fails to capture the more substantial thinning behavior observed in real suspensions at semi-dilute concentrations. For rods, the Brownian torques due to pair-wise interactions are substantial at low shear rates, but are

orientation-dependent and decrease with shear rate, thereby enhancing shear thinning behavior.

At higher concentrations, near-field hydrodynamic interactions between multiple rods become significant. The framework developed by Doi and Edwards for rigid rod polymers is a mean field approach that is based on the change in rotary and translation diffusion of a given rod due to interactions with neighboring rods [13, 144-146]. They proposed that at concentrations of $n \gg a^{-3}$, where n is the number density ($n = \phi/V_p$, where V_p is the volume of an individual particle) and a is the interaction length-scale ($\sim L$ here), rods begin to hinder the diffusion of neighbors and the particle motion becomes coupled. The relaxation behavior of the system is determined by the speed that a rod can escape the cage formed by the surrounding neighbors. The cage concept was introduced by Edwards [147], and the motion exhibited by the rods to exit the cage was modeling based on the reptation concept of de Gennes [148]. This mean-field approach predicts the viscosity of entangled, cylindrical rods to be

$$\eta_r = \frac{32}{15\pi^2}\frac{r^6}{\ln(r)}\frac{1}{\beta(1-\alpha r\phi)^2}\,\phi^3 \tag{2.24}$$

in the limit of $n \gg a^{-3}$, where $r \gg 1$ and $Pe \to 0$. The parameter α represents the extent to which the motion of the rods is constrained. The reduction in available volume reduces translational diffusion parallel to the rod axis, and results in an additional hindrance to chain motion. Near the isotropic-nematic transition, the parameter α is less significant because of the mutual orientation of neighboring rods. In this case, the scaling of Eqn. (2.24) reduces to $\eta_r \propto \phi^3$ [149].

2.5 Suspensions of disks and cylinders

2.5.1 Overview

The rheological behavior of clay platelets has been extensively investigated because of their importance in natural processes, and as filler to modify the rheology and mechanical properties of various fluids and polymers [150, 151]. However, most clays are obtained naturally and have a wide distribution of compositions and properties that depend on mining location. The individual clay particles are poorly defined, heterogeneous crystals with highly polydisperse size, shape, and aspect ratio. The particles also have a heterogeneous and asymmetric charge distribution, and show significant long-range electrostatic interactions that favor swelling rather than exfoliation, resulting in highly complex flow behavior even at low concentration [152]. A limited number of theoretical and simulation studies have been carried out to directly relate macroscale properties of systems containing plate-like solid particles to the physical characteristics of the particles [137, 138, 149, 153, 154].

The general framework of dilute suspension rheology for ellipsoidal particles, described in the previous section, is relevant to the behavior of disk-shaped particles. In this case, we define an equivalent oblate ellipsoid with axial ratio, $r < 1$. Throughout this paper, we will continue to define aspect ratio, r_p, as the ratio between largest and smallest dimensions for convenience (i.e. $r_p > 1$ for rods and disks), and reserve the symbol r for axial ratio of an ellipsoid.

2.5.2 Predictions of viscosity

Since both rod-like and plate-like particles are considered in this dissertation, it is useful to compare between the predicted magnitudes of hydrodynamic distortion. Kuhn and Kuhn calculated the intrinsic viscosity of a dilute suspension of disks to be

$$[\eta] = \frac{4}{9} + \frac{32}{15\pi r} \tag{2.25}$$

Comparing the two derivations by Kuhn and Kuhn (Eqn. (2.22) and Eqn. (2.25)), the difference in η_r is small for small aspect ratios, but linearly diverges with slope of $0.05r$ (for $r > 5$). For particles with $r = r^{-1} = 10$, the intrinsic viscosity of the rod is ~ 2x larger than the disk. At an equivalent volume fraction, the rods should therefore have 2x larger contribution to viscosity at zero shear rate. At $r = r^{-1} = 100$ and 1000, the ratio increases to ~10x and 60x, respectively.

There are a number of additional factors that complicate analysis of the behavior of plate-like particles. For rods, a significant amount of theoretical work has used slender body approximations, which neglect the thickness of the particles and provide generalized expressions for the particle stress [142]. For plates, there is no robust support for an equivalent approximation, and excluded volume may be regarded as having an effect in all cases. This may lead to complex stacking phenomenon, which has been only recently explored in simulations [137, 138].

An additional complication barring useful comparison between rods and disks is that the transitions between concentration regimes are different. This is a consequence of the fact that the length-scale influenced by a rod is given by length L for all orientations about the particle center of mass, while at any given time, the rods only physically

occupies this length scale in 1 dimension. For transport properties, we are generally interested in volume and time averaged quantities, and the influence is statistically distributed over a unit sphere (in most general case), such that the length scale is amplified by a factor of L^2. Using the same argument for disks or plates, we see that they physically occupy a length scale of $L/2$ from their center of mass, and hydrodynamically influence an additional distance that can be neglected on scales longer than $L/2$. The plates thereby influence their environment over length scales $\sim O(L)$, but instantaneously only occupy the space in 2 dimensions. The length scale amplification due to time and volume averaging is a factor of L. For spheres, all directions are influenced equally (undistorted), and there is no amplification effect due to the spatial and temporal averaging.

Based on this geometric argument, it is obvious that if the volume and time averaging approach is appropriate for the system of interest, the concentration at the onset of interactions, defined by the overlapping of influenced volumes, will be $\phi \sim O\left(\frac{1}{r^2}\right)$, $\sim O\left(\frac{1}{r}\right)$, and $\sim O(1)$ for rods, plates, and spheres, respectively. Since $n = \phi/V_p$, and $V_p = \frac{\pi d^2 L}{4} \approx d^2 L = L^3/r_p$ for rods, and $V_p \approx L^2 t = L^3/r_p$ for plates (where $r_p > 1$ in both cases), the number density should follow the same scaling. In other words, the rods begin to show hydrodynamic interactions at much lower concentration than plates of equivalent anisometry, resulting in a further distinctions between expected scaling.

2.6 Suspension viscoelasticity

2.6.1 Background

The relaxation behavior of complex fluids is a consequence of the finite time required for structures on different length scales, and subject to varying internal constraints, to adjust to small perturbations in equilibrium structure [28]. The length scales responsible for the resistance of a suspension to deformation may be investigated by altering the time scale (frequency and shear rate), temperature, and magnitude of applied deformation.

During dynamic mechanical measurements, a sinusoidally-driven strain displacement, $\gamma(t) = \gamma_o \sin(\omega t)$, is applied to a sample, where γ_o is the peak strain amplitude, ω is the angular frequency, in radians, and t is time (Figure 2-5). The relative elastic or viscous response of the fluid is given by the finite phase lag between applied field, $\gamma(t)$, and measured response, $\sigma(t) = \sigma_o \sin(\omega t + \delta)$. For an ideal Hookean spring, the resultant stress is in-phase with the applied strain, and the response is perfectly elastic, with $\sigma(t) = \sigma_o \sin(\omega t)$ and $\delta = 0$. For an ideal Newtonian fluid, the stress is in-phase with the strain rate, $d\gamma/dt = \dot{\gamma} = \omega\gamma_o \cos(\omega t)$, and the linear viscoelastic response is purely dissipative, with $\sigma(t) = \sigma_o \cos(\omega t)$ and $\delta = 2\pi$. For small γ_o, two viscoelastic parameters, the storage modulus, $G'(\omega)$, and loss modulus, $G''(\omega)$, may be defined to describe the magnitude of elastic (solid-like) and viscous (fluid-like) components of response, respectively. The storage modulus, $G'(\omega) = |G^*| \cos(\delta)$ is a measure of the ability of a material to store and recovery energy during a cycle of deformation. The loss modulus, $G''(\omega) = |G^*| \sin(\delta)$, is a measure of energy

dissipated as heat. The total resistance of the material to shearing deformation is given by the magnitude of complex shear modulus, $|G^*| = \sqrt{G'^2 + G''^2} = \sigma(\omega)/\gamma_o$.

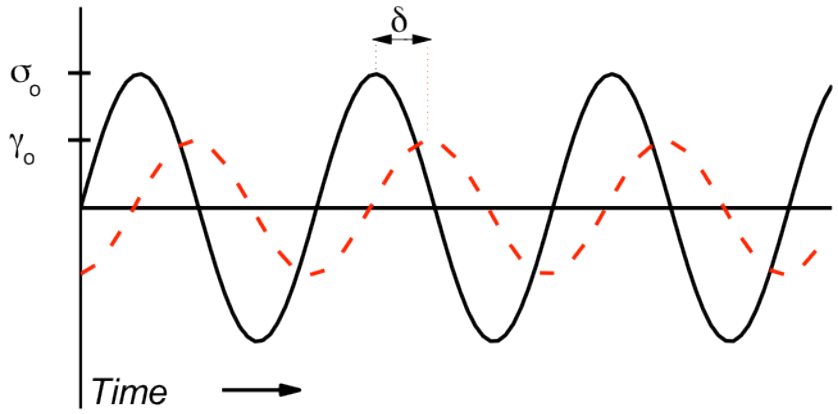

Figure 2-5. Schematic of stress and strain as function of time during small amplitude oscillatory deformation.

The complex viscosity from linear viscoelastic measurements is defined as

(2.26) $$\eta^*(\omega) = \eta' - i\eta'' = G''/\omega - iG'/\omega$$

The real part, $\eta' = G''/\omega$, is in-phase with the applied rate of shear, and is a dissipative term, referred to as the dynamic viscosity. The imaginary part, $\eta'' = G'/\omega$, is generally referred to as the out-of-phase viscosity, and is related to free energy storage. The dynamic viscosity can be related back to predictions of linear viscoelastic behavior for different systems. For suspensions of hard spheres at low frequencies, the behavior is Newtonian ($\delta \rightarrow 90°$) because the perturbed microstructure fully recovers equilibrium over long time. At high frequency, the time scales are too rapid with respect to D_o for appreciable relaxation. These limits are analogous to the earlier derivations for pair-wise

viscosity in the limits of infinite and low Peclet number, given by Eqn. (2.9 and Eqn. (2.10), respectively.

2.6.2 Suspensions of spherical particles

For suspensions of spherical particles, elasticity may be present due to various mechanisms. For example, dispersions of particles with strong electrostatic repulsion [1,2] will exhibit strong viscoelasticity due to the nature of inter-particle forces. At equilibrium, the microstructure is arranged such that the free energy related to particle interactions is minimized. When the system is perturbed, there is an increase in electrostatic energy. When the strain is removed, the microstructure is at a higher energy state, and there is a drive to recover the initial minimum free energy. The bulk manifestation of this is relaxation behavior and phase lag. Suspensions of attractive spheres that form flocculated aggregates may also show viscoelasticity [3,4]. Here, the particles are aggregated and show mesoscale disorder, but within the clustered structure, the particles still occupy equilibrium positions. When shearing deformation is applied, the flocs deform and the free energy in the system increases. The direct interactions between locally crowded particles provides the thermodynamic driving force to recover equilibrium.

In the case of microemulsions, the particles themselves are deformed, which increases the surface area, and thereby increases surface free energy [5,6]. Even for hard spheres, there may be viscoelastic effects at high particle concentrations. The “hard” nature is due to infinite repulsion at the contact point between surfaces. As

concentration increases, the number of available positions that the particles can be freely occupy decreases. In the equilibrium state, the arrangement of particles reflects liquid-like organization. Any perturbation from the equilibrium arrangement increases the configurational free energy, which is the driving force for structural recovery and viscoelastic character.

For the hard sphere suspensions, the particle motion and equilibrium are governed by random motion from Brownian forces. When the system is subject to shearing stresses, it is diffusive motion associated with Brownian forces that randomizes the microstructure. On long time scales, the original state of the system is recovered and there is no measurable viscoelastic response. In other words, there is an increase in free energy due to the distortion of the microstructure, but this increased energy is dissipated as heat. Only for measurements on intermediate time scales will the increase in free energy result in observable viscoelasticity [155]. At high frequencies, the time scale of the measurement may be sufficiently short that the system does not appreciably relax. In this case, there is a recovery in limiting Newtonian behavior, and $\eta^*(\omega)$ at high frequency will be given by purely hydrodynamic contributions.

2.6.3 Suspensions of rod-like particles

For non-spherical particles, there are additional modes of elasticity that may be present even in the limit of infinite dilution. These are associated with the rotation of the particles, and internal modes of flexibility, which may be significant even for relatively rigid particles. Dynamic viscoelastic measurements provide an important tool to

characterize the fundamental nature of motion in polymer systems. Detailed studies on these systems have been carried out and may provide a foundation for understanding viscoelastic origins for nanoparticle systems.

Zimm proposed a theory for linear molecules based on a bead-spring structure [156]. The macromolecule is divided into a *N* sub-units, which consist of an array of springs inter-connected by beads at junction points. When the material is distorted, each spring stores elastic energy due to an associated decrease in configurational entropy. The contribution to viscous dissipation is due to frictional resistance concentrated at the beads. The longest relaxation time for this system is associated with the configurational change as the molecular ends move in opposite directions. Other relaxation modes are also present and reflect internal dynamics. This model has been successfully applied for a number of systems, included branched polymers, and has been extended to include hydrodynamic intra-molecular (self-intersecting) interactions, which are important for non-theta solvent conditions [157-160]. The reduced shear moduli for the Zimm model are given by

(2.27) $$[G']_R = \sum_p^N \frac{\omega^2\tau_p^2}{1+\omega^2\tau_p^2}$$

and

(2.28) $$[G'']_R = \sum_p^N \frac{\omega\tau_p}{1+\omega^2\tau_p^2}$$

where τ_p is the relaxation time of the p-th sub-unit. The brackets refer to shear moduli at infinite dilution, which are given by $[G'] = \lim_{c\to 0} G'$ and $[G''] = \lim_{c\to 0}(G'' - \omega\eta_m)/c$, where c is the weight concentration. The dimensionless reduced moduli are

typically reported, where $[G']_R = [G']M/RT$ and $[G'']_R = [G'']M/RT$. The longest relaxation time, which is related to the motion of the ends of the molecule in opposite directions, is

(2.29) $$\tau_1 = [\eta]\eta_s M/RTS_1$$

where $[\eta] = \lim_{\omega\to 0}[G'']/\omega\eta_s$ is the intrinsic viscosity, M is the molecular weight, and R is the gas constant. The final term, S_1, is a ratio of the sum of the rapid relaxation modes with respect to the longest relaxation time, and is given by $S_1 = \frac{\Sigma\tau_p}{\tau_1} = 2.37$.

For rigid molecules, there are several theories that have the form

(2.30) $$[G']_R = m_1 \frac{\omega^2\tau_o^2}{1+\omega^2\tau_o^2}$$

(2.31) $$[G'']_R = \omega\tau_o\left[\frac{m_1}{1+\omega^2\tau_o^2} + m_2\right]$$

where $m = \frac{1}{m_1+m_2}$; numerical coefficients that depend on details of model. Kirkwood and Auer [161] extended the previous theory of Kirkwood and Riseman [162] to consider the influence of Brownian motion on a linear array of beads. In the limit of large aspect ratio, they obtained $m_1 = 3/5, m_2 = 1/5$. Yamakawa [163] obtained the same constants for cylinders of high aspect ratio, and for intermediate aspect ratios, showed $m_2 > 1/5$.

For an infinitely rigid molecule, there is a single relaxation time governing viscoelastic response, which is related to end-over-end rotation. The relaxation time depends on the dimensions of the molecule, and for high aspect ratio systems, is given by

(2.32) $$\tau_o = \left(\frac{\pi}{18k_BT}\right)\frac{L^3}{\ln r}$$

One useful feature of this type of molecular model is that the structure and internal flexibility of complex particles, such as bio-polymer aggregates of helices, may be inferred based on the observed relaxation time. For example, the first experimental work that observed true rigid-rod viscoelastic behavior was for the tobacco mosaic virus (TMV) [164]. In both isolated form and as dried aggregates, the TMV shows rigid behavior. In contrast, viscoelastic measurements showed that poly(γ-benzyl-L-glutamate), a protein with helical arrangement, is semi-flexible [165, 166].

The semi-flexible nature is captured well with a hybrid model approach, where τ_1/τ_o is used as an empirical fitting factor [166]. In these systems, the longest relaxation time, τ_o, retains the same definition of end-over-end rotation, but the molecular-scale nature of the more rapid mode, τ_1, depends on the particular system of interest. In the case of random coils, the elastic energy reflects changes in configurational entropy, which is consistent with the Zimm approach. For other types of macromolecules, there may also be various other modes, such as accordion-like extension and twisting.

2.7 Concluding remarks

Viscoelasticity may also be used to investigate nanoscale features of the surface . For example, the foundations of suspension rheology are based on an assumption of a no-slip interface. In real systems, this condition may be violated and result in a boundary layer at the particle surface. For hard spheres, this has been reported to result in scaling of

$G' \sim \omega^{1/2}$ in the limit of high frequency, rather than the expected plateau region. Mackay et al. related this type of interfacial slip to surface roughness [167].

Short-range interactions, both inter-particle and hydrodynamic, between solid particles also govern transitions in viscosity, such as shear thickening. Wagner has reviewed the ways that lubrication forces and inter-particle interaction may be influenced by heterogeneities such as roughness, solvation layers, non-uniform distribution of surface charges, and adsorbed species [168]. Additional forces that may influence rheology and need to be considered in detailed treatments are friction and time-dependent components of response. Improvements in direct force measurements and other micro-rheology approaches have led to advances in understanding of inter-particle interactions, which are needed to bridge between phenomenological models for specific systems, and predictive models that can be more broadly used.

CHAPTER III

EFFECT OF SURFACE MODIFIER ON FLOW PROPERTIES OF EPOXY CONTAINING INDIVIDUALLY DISPERSED PLATE-LIKE NANOPARTICLES

3.1 Introduction

The viscoelasticity and flow behavior of colloidal suspensions originate from a complex interplay of inter-particle interactions, particle-fluid interactions, and fluid-mediated interactions. Model systems with well-defined shape, size, polydispersity, and inter-particle interactions are necessary to study the origin of macroscale properties in colloidal suspensions, and are relevant to understanding mechanical properties and transport phenomena in composites and other heterogeneous media [169]. There has been significant progress in theory, experiment, and simulation of hard spheres, which are non-deformable, spherical particles that interact only through infinite repulsive interactions at the interface between contacting particles [80, 90, 155, 170-173]. Little work has been done on fundamental flow properties of suspensions of plate-like particles, despite the commercial significance of layered silicates and the emerging importance of graphene and other 2-D nanoparticles [149, 174, 175]. This is largely due to a lack of suitable model systems for unambiguous investigation.

Here, we investigate the rheological behavior of α-zirconium phosphate (ZrP) nanoplatelets that are exfoliated to individual sheets using 3 different surfactants. ZrP crystallizes into a layered structure that is similar to the commercially important class of layered silicates, but has a higher concentration of active sites along the surface of each

layer, and homogeneous charge distribution between layers. As a result, ZrP can be more easily intercalated and exfoliated using a variety of surface modifiers, and may be used as a model system for fundamental structure-property relationships study of systems containing layered materials with various degrees of dispersion and exfoliation [40-42, 44, 45, 47-49, 176]. Here, the ZrP nanoplatelets are synthesized with average lateral diameter of ~ 100 nm, and crystallize into a layered structure of individual hexagonal crystals with monodisperse thickness of ~ 0.7 nm. The effect of surface modifier is investigated using 3 surfactants that have been previously reported to spontaneously delaminate ZrP stacks into individual sheets in epoxy [36, 39, 45, 46, 177-181]. A schematic showing the geometry of the individual platelets exfoliated with the surface modifiers is shown in Figure 3-1. The first is tetra-*n*-butyl ammonium hydroxide (TBA^+OH^-), which is a strong base with diameter similar to the thickness of the individual plates [182]. The TBA^+ ions attach to the surface of the ZrP plates and provide electrostatic stability [53]. In epoxy, the length scale of electrostatic repulsion will be suppressed, and significant electroviscous effects are not anticipated. The other two surfactants are Jeffamines, designated M600 and M1000, which are block copolymers that consist of a terminal primary amine group, and flexible polyether backbone with propylene oxide (PO) and ethylene oxide (EO) blocks. The number designation refers to the approximate molecular weight of the oligomers. The M1000 has a block copolymer structure with propylene oxide (PO)/ethylene oxide (EO) ratio of 3/19, which gives it hydrophilic characteristics. The M600 has a similar block copolymer structure, but is hydrophobic due to an increased ratio of PO/EO, which is

9/1. The effect of different polyetheramine surface modifiers on the intercalation and exfoliation of ZrP nanoplatelets, and on mechanical properties of epoxy/ZrP nanocomposites, has been previously reported [183, 184]. The influence of the polyetheramine composition on flow behavior of dispersions containing the exfoliated ZrP nanoplatelets has not been previously reported.

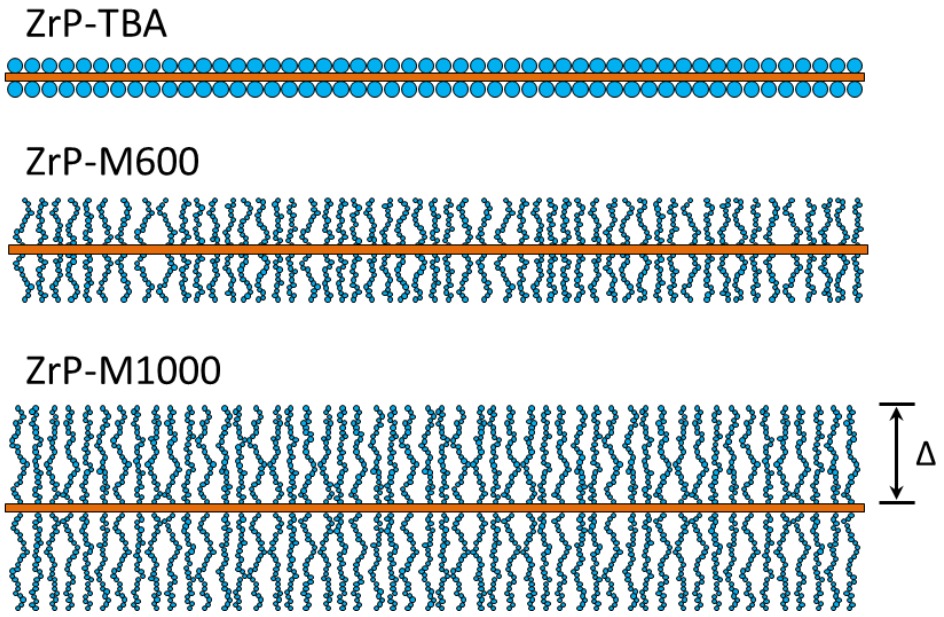

Figure 3-1. Schematic showing relationship between thickness of ZrP nanoplatelets and size of different surface modifiers used in this work. Relative thickness of the platelets and surface layers are drawn approximately to scale, assuming that M600 and M1000 form extended brush layer. Aspect ratio of platelet is drawn to scale ($r_p \approx 100$). Details of the grafting density and structure of the M600 and M1000 are not representative.

ZrP nanoplatelets intercalated with M600, designated ZrP-M600, show significantly increased inter-layer spacing in aqueous solution and organic solvent. When dispersed in an epoxy suspending material, the nanoplatelets have been reported to exfoliate into

individual nanoplatelets under appropriate conditions [45, 183]. At concentration of 1 vol.% ZrP-M600, the exfoliated nanoplatelets are randomly oriented and moderately improve mechanical properties of epoxy [42]. At higher concentration, ~ 2 vol.%, the improvement in mechanical properties is much larger, and the dispersed nanoplatelets show local orientation in aligned domains, but do not show long-range liquid crystalline order [42, 45].

Recently, Wong et al. [185] reported that ZrP exfoliated with M1000, designated ZrP-M1000, self-assemble into smectic liquid crystals (lamellar organization) with concentration-dependent iridescence in organic solvent. Smectic liquid crystalline organization was also observed for dispersions of the ZrP-M1000 in epoxy monomer at concentrations of 1.7 vol.% and higher. The smectic liquid crystals show unique rheological properties that are distinct from smectic crystals formed from small molecules and liquid crystalline polymers, and behave as viscoelastic fluids up to ~ 2.8 vol.%. At concentrations up to 8.2 vol.%, the colloidal liquid crystals show solid-like response under small shear due to the interpenetration of the surface-attached brush layers, but exhibit extreme shear thinning and at moderate shear rates, have viscosity similar to the unfilled epoxy monomer [186]. In the cured state, the epoxy nanocomposites retain smectic mesophase, and show excellent mechanical and barrier properties [187, 188]. Here, we investigate the effect of the different surface modifiers on the rheology of ZrP suspensions at concentrations in the dilute and semi-dilute range. We find that the behavior of the ZrP-TBA and ZrP-M1000 systems is consistent with a stable dispersion of isolated, rigid nanoplatelets that interact through purely repulsive,

short-range interactions. For the ZrP-M600 system, there is significant deviation in linear viscoelastic and steady shear response, which is attributed to the formation of local microstructure. The potential origins of the change in inter-particle potential and the influence on colloidal phase behavior are discussed.

3.2 Experimental

3.2.1 Materials

Zirconyl chloride ($ZrOCl_2 \cdot 8H_2O$, 98%, Aldrich), phosphoric acid (H_3PO_4, 85%, EM Science), and tetra-*n*-butylammonium hydroxide (TBA^+OH^-, Aldrich) were used as received. Jeffamine M600 and M1000, commercial polyoxyalkyleneamines with reported average molecular weight of ~ 600 and 1000 g/mol, respectively, was donated by Huntsman Chemical. EPON 862, a diglycidyl ether of bisphenol F (DGEBF) liquid epoxy monomer, was obtained from Hexion Specialty Chemicals (Columbus, OH). DER 332, a diglycidyl ether of bisphenol A (DGEBA) liquid epoxy monomer, was obtained from Dow Chemical Company. Both epoxy monomers have narrow monomer molecular weight and show similar viscosity over a range of temperatures. The epoxy precursor was dried in a vacuum overnight prior to sample preparation to remove entrapped air and moisture.

3.2.2 Preparation of exfoliated ZrP nanoplatelets and dispersion in epoxy

The ZrP nanoplatelets were prepared using a hydrothermal method, which has been described in detail previously [39]. The recovered ZrP was dried at 65°C for 24 hr, and

subsequently ground with a mortar and pestle into a fine powder prior to exfoliation. The ZrP nanoplatelets were exfoliated to individual layers with identical thickness using TBA^+OH^-, M600, and M1000 as surface modifiers. The detailed exfoliation procedures have been described in detail previously [42, 45, 181, 185, 187]. After removing excess surface modifier and evaporating the water, the exfoliated ZrP nanoplatelets were dispersed in acetone. The epoxy precursor was dissolved in acetone and added dropwise to the acetone/ZrP suspension until the desired concentration was achieved. No curing agent was used in this work. The dispersion was allowed to stir for 4 hr. The solvent was removed with a rotary evaporator to obtain the colloidal suspensions of exfoliated ZrP nanoplatelets in epoxy.

3.2.3 Characterization

Thermogravimetric analysis (TGA) was carried out using a Q500 TGA (TA Instruments; New Castle, DE, USA) to determine the mass fraction of ZrP nanoplatelets in the suspension, and to confirm that all solvent and excess surfactant was removed. The volume fraction, φ, of ZrP was calculated from the mass fraction using reported densities of the epoxy monomer, TBA^+OH^-, M600, M1000, and ZrP nanoplatelets, which are 1.16, 0.995, 0.979, 1.066, and 2.76 g/cm^3 [189], respectively.

Rheological measurements were carried out using an ARES-G2 rotational rheometer (TA Instruments). A forced convection oven with dried air flow at constant rate was used to control temperature and environmental conditions. The temperature was monitored with a piezoelectric thermocouple mounted beneath the bottom fixture. For

all measurements, the temperature variation was within ± 0.01 °C of the reported temperature.

Measurements were carried out primarily with parallel plate geometries (25 mm and 40 mm diameter; gap of 1.5 – 3 mm). Cone and plate geometry (50 mm diameter plate; 0.02 rad cone; 0.051 mm truncation spacing) was also used for several samples and provided consistent results. To determine the role of loading history, measurements were carried out before and after the application of steady shear. Unless otherwise noted, linear and non-linear viscoelastic measurements were reproducible following steady shear, and the reported measurements are from representative pre-sheared suspensions. Sample recovery was verified by measuring the shear modulus with small strain amplitude, $\gamma = 1\%$, at angular frequency of $\omega = 1$ rad/s, immediately following steady shear or large amplitude deformation. No significant equilibration or recovery time was necessary at the concentrations investigated in this work.

Small-amplitude oscillatory shear (SAOS) measurements were carried out within the linear viscoelastic region (LVR) over a frequency range of $\omega = 0.1 – 100$ rad/s. Large-amplitude oscillatory shear (LAOS) measurements were carried out to verify the range of linear response. Shear viscosity was measured with two separate sweeps to verify consistency of measurements. The first sweep was carried out by increasing shear rate from $\dot{\gamma} = 10^{-3}$ s^{-1} to 100 s^{-1}. A second sweep was subsequently performed by decreasing $\dot{\gamma}$ over the same range. Up to 5 minutes was allowed to reach steady state viscosity during each measurement. Unless otherwise noted, the results of the two sweeps were nearly identical and the second sweep (decreasing $\dot{\gamma}$) is reported. As an additional

check, the shear viscosity was measured at several fixed shear rates as a function of time to verify steady state was reached. The maximum shear rate was limited to $\dot{\gamma} = 100\ s^{-1}$ to prevent ejection of material from the gap and prevent shear-induced heating of the samples. To confirm that wall slip was absent, the gap between parallel plates was varied between multiple measurements, and no change in linear viscoelastic or steady shear response was observed.

To prevent the inclusion of experimental artifacts, a cut-off threshold for minimum stress was defined for each geometry. The minimum transducer torque of the ARES G2, specified by TA Instruments, is ~ 0.1 μN.m. For the 25 and 40 mm parallel plate geometries, the calculated minimum shear stress is on the order of 0.1 Pa, which coincides with the observed onset of significant scatter in phase angle. For the cone and plate geometry, the minimum shear stress is on the order of 0.01 Pa. For measurements with stress near or smaller than these thresholds, the storage modulus, G', and phase angle, δ, are discarded. The transducer resolution limited the measurement of the low-frequency elastic response of the epoxy monomer and suspensions at low concentration. Machine inertia at high angular frequency was confirmed to be negligible below $\omega = 100$ rad/s.

3.3 Results

3.3.1 Non-linear viscoelasticity

For each system, strain amplitude sweeps were carried out to determine the range of linear viscoelastic response. In the suspensions containing ZrP-TBA nanoplatelets, the

storage modulus, G', is not significantly above the resolution of the transducer until $\phi \approx$ 0.8 vol.% ZrP. Linear response is observed in the ZrP-TBA suspensions at large strains, $\gamma \sim 100\%$, for concentrations up to 2.1 vol.%. For the ZrP-M600 and ZrP-M1000 systems, the magnitude of elastic response is well-defined at low concentration, $\phi \sim 0.04$ vol.%, and the suspensions show greater strain sensitivity during LAOS (Figure 3-2).

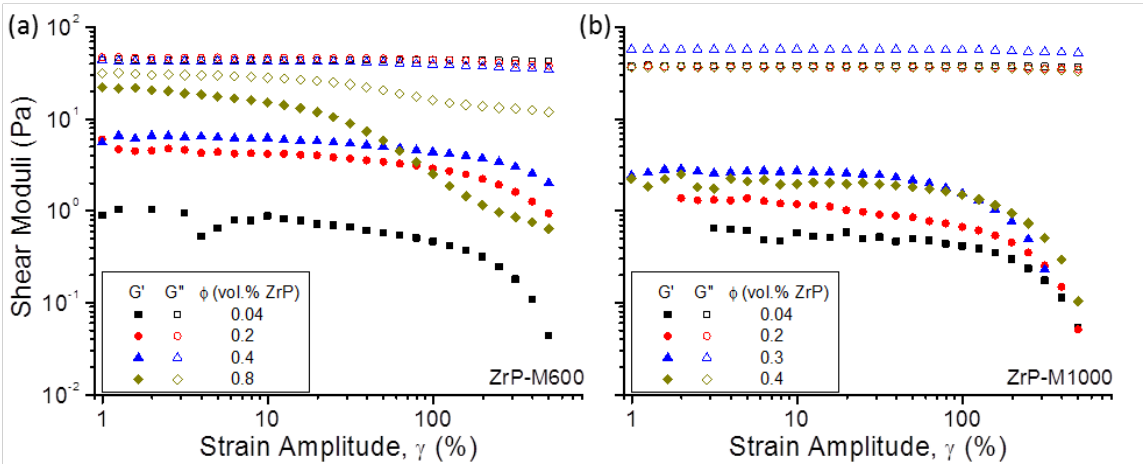

Figure 3-2. Large amplitude oscillatory shear response of the suspensions. Storage modulus, G', and loss modulus, G'', shown as functions of strain amplitude, γ, for suspensions containing ZrP nanoplatelets exfoliated with (a) M600 and (b) M1000 polyetheramine oligomers.

The strain amplitudes associated with the onset of steep decline in G' and G'' are designated $\gamma_c(G')$ and $\gamma_c(G'')$, respectively, and are listed in Table 3-1 for the ZrP-M600 and ZrP-M1000 systems. At 0.04 vol.% ZrP, both systems show linear response in G' and G'' up to strain amplitudes of $\gamma \sim 150\%$. The critical strain for strain softening in G' decreases roughly linearly with concentration for both systems. In the ZrP-M600

system, $\gamma_c(G'')$, also decreases linearly with concentration. For the ZrP-M1000 system, $\gamma_c(G'')$ appears to be independent of concentration.

Table 3-1. Summary of non-linear viscoelastic properties for ZrP-M600 and ZrP-M1000 systems.

System	$\boldsymbol{\phi}$ vol.% ZrP	$\boldsymbol{\gamma_c(G')}$ %	$\boldsymbol{\gamma_c(G'')}$ %
ZrP-M600	0.04	133	190
	0.21	90	180
	0.42	49	115
	0.84	27	22
ZrP-M1000	0.04	200	166
	0.21	180	150
	0.34	120	142
	0.42	80	150

Measurements at $T = 25$°C, $\omega = 10$ rad/s.

3.3.2 Linear viscoelasticity of ZrP-TBA system

Representative examples of the linear viscoelastic response of the ZrP-TBA systems measured at 25°C are shown in Figure 3-3. For suspensions containing 0.04 – 0.3 vol.% ZrP-TBA, G' is increased relative to the unfilled matrix at high frequencies, but there is no change in magnitude or scaling behavior to suggest the presence of microstructure or non-local interaction. The magnitude and scaling of G'' is not significantly affected by the ZrP-TBA nanoplatelets in this concentration range. At 0.8 vol.% ZrP-TBA, there is a significant increase in viscoelastic response, and at angular frequencies of $\omega \sim 1$ rad/s and greater, the suspension shows weak solid-like response. At lower frequency, there is a transition to viscous flow behavior. The transition is in excellent agreement with the

calculated rotary diffusion (Eqns. (2.17) - (2.21)), with average lateral diameter of 100 nm, which is $D_r \approx 1.4$ 1/s at 25°C.

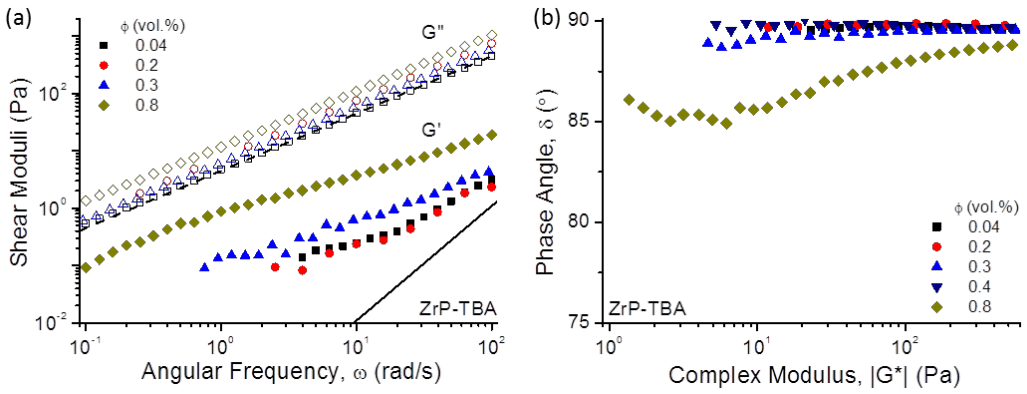

Figure 3-3. Linear viscoelasticity of ZrP-TBA suspensions at various concentrations. (a) Storage modulus, G' (filled), and loss modulus, G'' (unfilled), as functions of angular frequency, ω. (b) Phase angle, δ, as a function of complex modulus, $|G^*|$ (vGP plot). Measurements carried out at T = 25°C. The storage and loss moduli of the unfilled epoxy monomer are shown as solid and dashed lines, respectively, in (a).

The viscoelastic parameters G' and G'' are inter-related functions defined by the magnitude of complex modulus, $|G^*|$, and phase angle, δ. To identify subtle differences in relaxation behavior, it is more useful to directly consider δ as a function of complex modulus, $|G^*|$, which is referred to as the van Gurp-Palmen (vGP) plot [190]. The phase angle is determined by the time delay between applied deformation and measured response, and is an independent, direct measurement of the relative fluid-like or solid-like character of a material. The classical limits of viscoelasticity are defined by a Hookean spring, which is an ideal solid with $\delta = 0°$, and a Newtonian dashpot, which is an ideal fluid with $\delta = 90°$. The complex modulus is the ratio of the maximum stress

and strain amplitude, and is a measure of the total resistance of the material to deformation. Evaluating viscoelastic response from δ as a function of $|G^*|$ was first introduced as a method to validate application of time-temperature superposition (TTS) [190]. Measurements of linear viscoelasticity taken at different temperatures and time scales may only be superimposed if they represent the same relaxation process, in which case $|G^*|$ will be a single-valued function of δ [191]. This method is particularly useful to identify subtle variations in relaxation behavior that may arise from phase separation above a critical temperature, long-chain branching, crosslinking, or thermal degradation [192-195].

For the work here, the vGP representation is useful to determine if there is any progressive change in relaxation behavior with increasing concentration. The vGP representation of several suspensions containing ZrP-TBA nanoplatelets is shown in Figure 3-3b. The response of the suspensions with 0.04 – 0.4 vol.% ZrP-TBA is essentially Newtonian over all measurable frequencies, with $\delta \sim 90°$. At ~ 0.3 vol.%, there is a weak decrease in δ at high $|G^*|$, which suggests some interaction on long time scales. The limited elastic response shows that the individual nanoplatelets behave as independent, rigid plates, with no permanent contacts or microstructure suitable to store elastic energy. For the unfilled epoxy monomer, the phase angle is ~ 90^o for all measurements at room temperature and higher (Appendix I). Lower temperature measurements were carried out to determine G', and show a small decrease in δ at high frequency. The inflection at high frequency and low temperature is characteristic of a Maxwell fluid on time scales approaching its characteristic relaxation time. Any

reversible, and consistent, decrease in δ below this transition must be associated with the nanoparticle phase.

For the suspension containing 0.8 vol.% ZrP-TBA, δ approaches a plateau near 90° at high $|G^*|$, which corresponds to localized measurements at $\omega \gg D_r$. In this measurement range, the contribution of the dispersed phase is purely hydrodynamic and there is vanishing elastic contribution. On longer time scales, there is a decrease in δ with decreasing $|G^*|$, which corresponds to the region of solid-like response at intermediate frequency in Figure 3-3a. At lower frequency, δ shows a well-defined minima, and subsequently increases toward $\delta = 90^o$ in the limit of small $|G^*|$. The minima in δ is designated δ_n^o, and provides a characteristic value describing the magnitude of solid-like response at the transition to viscous flow behavior (Table 3-2). At much higher concentration, δ_n^o is a well-defined feature of each system (Chapter V). The trend of decreasing δ_n^o with increasing ϕ is found for the other systems in this chapter.

Table 3-2. Summary of linear viscoelastic properties of nanoplatelet suspensions describing relaxation transition between solid-like and fluid-like response.

System	ϕ vol.%	ω_c rad/s	τ_c s	G_n^o Pa	δ_n^o °
ZrP-TBA	0.81	0.7	9.0	3.2	84.9
ZrP-M600	0.04	4.0	1.6	2.6	86.9
	0.21	1.1	5.7	2.9	83.0
	0.42	1.0	6.3	2.0	78.2
ZrP-M1000	0.04	2.8	2.2	4.0	88.4
	0.21	1.5	4.2	4.5	85.4
	0.34	1.0	6.3	8.0	84.2
	0.41	0.71	8.9	3.1	83.1

Minimum phase angle is δ_n^o; G_n^o and ω_c are the magnitude of complex modulus and angular frequency at δ_n^o; relaxation time, τ_c, calculated from $\tau_c = 2\pi/\omega_c$. Values for G_n^o and ω_c are from measurements carried out at T = 25°C.

The well-defined minima in relaxation behavior for the ZrP-TBA system at 0.8 vol.% provides a convenient reference point to probe the temperature dependent relaxation of this system. Additional measurements were carried at temperatures between 10° and 50°C. Shift factors were used to account for the change in time and stress scales with temperature. Over a narrow temperature range, all measurements in the LVR will superimpose onto a temperature-independent curve for thermorheologically simple materials [190]. For a broad range of temperatures, a small stress shift factor, b_T, may be needed to compensate for small changes in the density of the fluid [191]. Any change in the dominant relaxation modes in the system, such as phase separation, crosslinking, degradation, etc. [194, 195], will change the shape of the curve, which provides an indirect approach to determine the origin of temperature-dependent relaxation due to the nanoparticle phase.

The relaxation behavior of the suspension containing 0.8 vol.% ZrP-TBA is consistent over the measurement range, which validates the use of TTS. The results show that there is no significant change in dispersion state or mechanism of interaction of the nanoparticles with temperature, and indicates that no curing reaction or degradation takes place. A linear viscoelastic master curve was constructed from isothermal measurements taken over a temperature range of 10 – 50°C (Figure 3-4). The magnitude of both shift factors is nearly the same as the unfilled epoxy monomer. Several previous reports on the rheology of well-dispersed, plate-like nanoparticles found similar behavior for particles that are not physically or chemically bound to the dispersing phase [196, 197]. The minima in δ is well-defined at several temperatures, and the magnitude is nearly constant, $\delta_n^o = 84.9 \pm 0.4^o$, which further validates its use as a characteristic descriptor of the relaxation behavior.

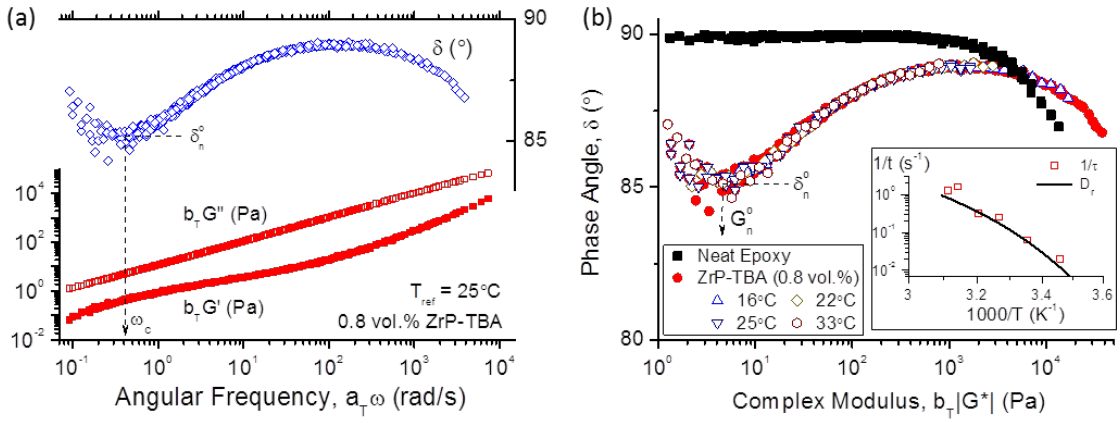

Figure 3-4. (a) Linear viscoelastic master curve for suspension containing 0.8 vol.% ZrP-TBA, obtained from isothermal measurements over temperature range of 10 – 50°C. (b) vGP representation of linear viscoelastic master curve. Several temperatures are highlighted to show individual measurements. The relaxation of the unfilled epoxy matrix is included for reference. The inset is the characteristic relaxation time calculated from the frequency at the minima in δ. The solid line in the inset is the calculation of rotary diffusion coefficient.

The time scale of the relaxation process at 0.8 vol.% ZrP-TBA was calculated from the characteristic frequency corresponding to δ_n^o, as $\tau_c = 2\pi/\omega_c$ (Table 3-2). The relaxation time varies inversely with temperature (Figure 3-4b), which indicates that the elastic response is related to the mobility of the nanoparticles in the matrix. Based on the assumptions for this system, the relaxation mechanism for semi-dilute suspensions should be determined by the time scale available for Brownian motion to relax perturbations in the positional and orientational distribution due to small amplitude deformation. The temperature dependence of D_r is given by T/η_m, where η_m is the viscosity of the unfilled epoxy. Calculations of D_r show excellent agreement with the experimentally observed relaxation times (Figure 3-4). The results strongly indicate that the viscoelastic response observed here is due to localized motion and interaction of

individual, stable particles organized in an equilibrium microstructure, and that relaxation occurs on a time scale governed by rotary diffusion.

3.3.3 Linear viscoelasticity of ZrP-M600 and ZrP-M1000

Representative examples of the linear viscoelastic response of suspensions containing ZrP nanoplatelets exfoliated with M1000 and M600 oligomers are shown in Figure 3-5 and Figure 3-6, respectively. In the ZrP-TBA and ZrP-M1000 systems, no significant effect of pre-shearing or thermal history was observed following application of large amplitude deformation or steady shear. In the ZrP-M600, the linear viscoelastic and steady shear response was significantly influenced by prior shearing at concentrations of 0.2 vol.% and above, which suggests a change in nature of inter-particle interactions. Potential sources of the distinct response are discussed below. Following brief shearing at ~ 100 1/s, the linear viscoelastic response is reproducible in most cases.

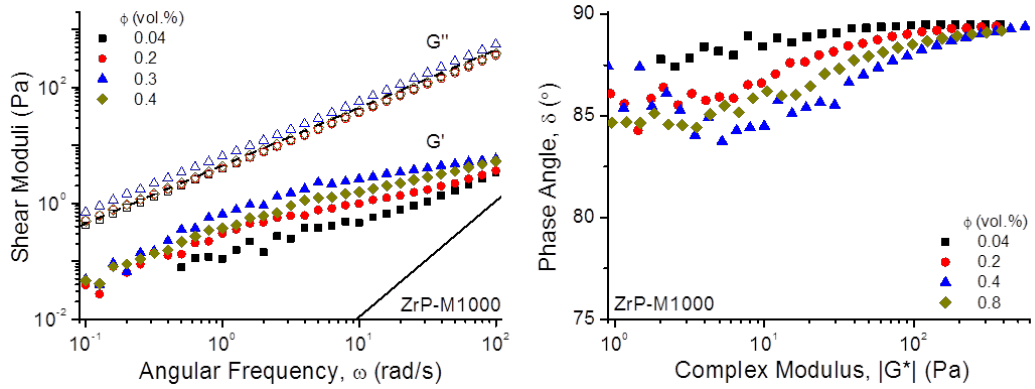

Figure 3-5. Linear viscoelasticity of ZrP-M1000 suspensions at various concentrations. (a) Storage modulus, G' (filled), and loss modulus, G'' (unfilled), as functions of angular frequency, ω. (b) vGP representation of linear viscoelastic response. Storage and loss moduli of unfilled epoxy matrix shown as solid and dashed lines, respectively, in (a). Measurements carried out at T = 25°C.

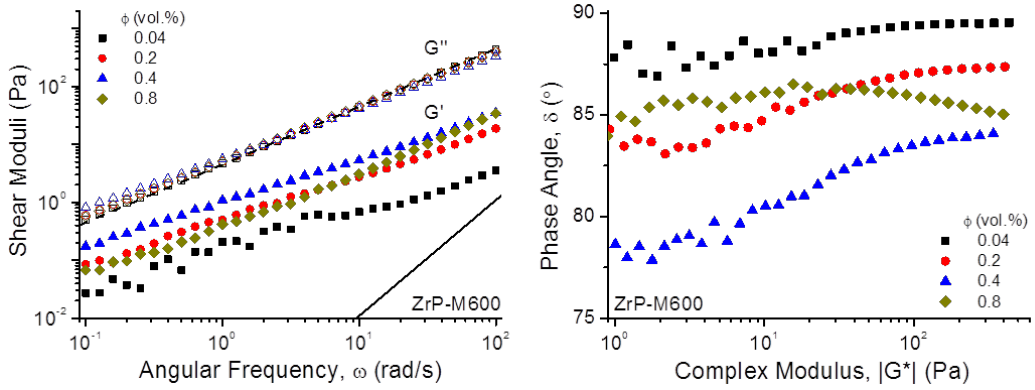

Figure 3-6. Linear viscoelasticity of ZrP-M600 suspensions at various concentrations. (a) Storage modulus, G' (filled), and loss modulus, G'' (unfilled), as functions of angular frequency, ω. (b) vGP representation of linear viscoelastic response. Storage and loss moduli of unfilled epoxy matrix shown as solid and dashed lines, respectively, in (a). Measurements carried out at T = 25°C.

At 0.04 vol.%, the linear viscoelastic response of the suspensions containing ZrP exfoliated with the two types of polyetheramine oligomers is nearly identical. For the ZrP-M1000 system, G' at high frequency is nearly independent of concentration up to 0.4 vol.% (Figure 3-5a). From the vGP representation, the high-frequency phase behavior converges to $\delta \approx 90°$ at each concentration, which indicates that interactions on local length scales are purely hydrodynamic (Figure 3-5b). The results show that for all concentrations investigated, the linear viscoelasticity of the ZrP-M1000 system is dominated by the motion and hydrodynamic interaction of the individual nanoplatelets. The transition to viscous flow behavior is well-defined in each of the ZrP-M1000 systems, and the characteristic frequency decreases with concentration (Table 3-2).

At 0.3 vol.% ZrP-M1000, the magnitude of both G' and G'' are largest, and decrease slightly at 0.4 vol.%. The power-law slope of G' is also decreased at higher concentration. The behavior at 0.4 vol.% was reproducible, even after repeated drying to confirm that no residual solvent was present. At 1.7 vol.%, this system is reported to self-assemble into a smectic liquid crystalline microstructure (Chapter V). During the transition to liquid crystalline mesophase, the hydrodynamic disturbance caused by the particles is minimized [198], and G'' may be expected to decrease over a narrow concentration region. Local alignment will also influence rotational mobility, and depending on the nature of the particle contacts and geometric restrictions, the rotation of the particles may be enhanced or diminished [117, 118]. Various other mechanisms may also be present, particularly related to the interaction of the epoxy molecules with brush structure [199]. At 0.4 vol.% ZrP-M1000, the volume fraction of M1000 is ~ 2.7

vol.%. It is challenging to explicitly determine the role of the M1000 oligomer experimentally because the dynamics and conformation of the chains are strongly influenced by the tethering and molecular-scale confinement of ZrP nanoplatelets, and is beyond the scope of this work.

In the ZrP-M600 system, the response is nearly identical to the ZrP-M1000 system at 0.04 vol.%. The characteristic frequency for the relaxation transition is slightly higher, which indicates a more rapid relaxation process. This is in contrast with a simplistic geometric picture of interactions between nanoplatelets (c.f. Figure 3-1). In the low frequency region, G' and G'' increase weakly with concentration up to 0.4 vol.%. In contrast to the ZrP-TBA and ZrP-M1000 systems, G' increases strongly with concentration at high frequency for the ZrP-M600 system. The vGP representation (Figure 3-6b) shows a progressive decrease in δ at high frequency. The decrease in maxima for δ suggests that the elastic interaction between particles is non-vanishing at high frequency, and therefore non-hydrodynamic in origin. Due to limitations in resolution, it is difficult to clearly evaluate the phase angle at low frequency, but the ZrP-M600 systems at 0.2 and 0.4 vol.% shows a much weaker minima, and may show a plateau, which is characteristic of flocculated structure. At 0.8 vol.%, the relative elastic response diminishes at intermediate frequency, which is not observed in the other systems.

3.3.4 Influence of deformation history

The distinct mechanism of inter-particle interaction in the ZrP-M600 system is also apparent from the significant influence of pre-shearing and heating on rheological behavior. As stated before, the linear and non-linear viscoelasticity, and steady shear response of the ZrP-TBA and ZrP-M1000 suspensions were highly reproducible from consecutive measurements following equilibration. This shows that the elastic and viscous responses are governed by an equilibrium microstructure that is recoverable. For the ZrP-M600 system, history dependent effects are present at concentrations as low as 0.2 vol.% (Figure 3-7a). The linear viscoelastic response was measured before and after steady shear measurements. Following steady shear, the sample was allowed to equilibrate until the linear viscoelastic response stabilized over 10 consecutive measurements. Subsequent measurements show a subtle decrease in G' and G'' at low and intermediate frequencies. Following deformation, the relaxation time of the system is decreased, and the response is less elastic.

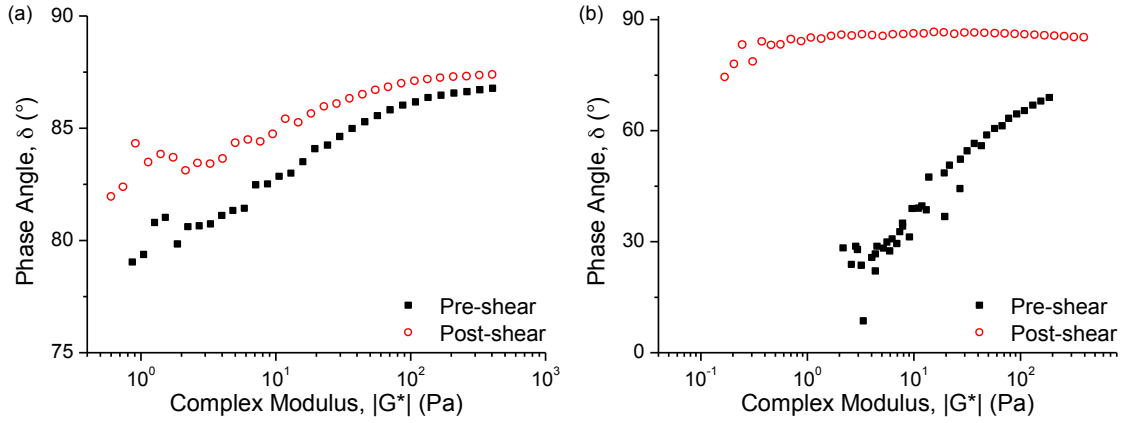

Figure 3-7. Influence of deformation history on rheology of ZrP-M600 systems at volume fraction of (a) 0.2 vol.% and (b) 0.8 vol.%, in epoxy monomer.

At higher concentration, the influence of shearing history is more significant (Figure 3-7b). For suspensions containing 0.8 vol.% ZrP-M600, the initial linear viscoelastic response is solid-like, and shows a distinct gel transition, with $\delta < 45°$. Following steady shear, the solid-like response is diminished. At higher temperature, the solid-like response progressively decreases, and approaches Newtonian behavior. After cooling, the Newtonian response is reproducible for consecutive measurements.

3.3.5 Steady shear behavior

The viscosity from steady shear measurements and dynamic viscosity for linear viscoelastic measurements are shown for representative systems in Figure 3-8. The shear viscosity of the ZrP-TBA systems shows weak initial increase in low shear viscosity, and diverges at high viscosity. The scaling of the zero shear viscosity is consistent with SAOS results. A summary of the measurements of shear viscosity, and

comparison with limiting values of dynamic viscosity from oscillatory shear, is given in Table 3-3.

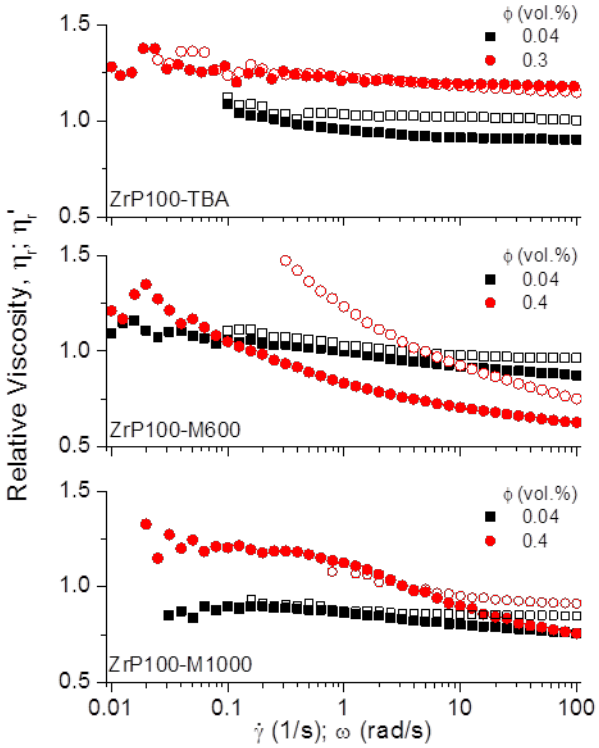

Figure 3-8. Dynamic viscosity, $\eta'(\omega) = G''/\omega$, and shear viscosity, $\eta(\dot{\gamma})$, as functions of angular frequency, ω, and shear rate, $\dot{\gamma}$, respectively, for suspensions containing nanoplatelets exfoliated with different surfactants.

Table 3-3. Summary of limiting values for viscosity from steady shear and oscillatory shear measurements.

System	ϕ vol.%	T °C	η_o/η_m	η_∞/η_m	η'_o/η'_m	η'_∞/η'_m
ZrP-TBA	0.04	25	1.04	0.99	[a,b]	0.99
		30			[a,b]	1.02
	0.3	25	1.26	1.14	1.27	1.18
		30	1.26	1.13	1.26	[b]
	0.5	30	2.20	[b]		
	0.8	25	4.20	2.11	3.01	2.11
		30	3.20	1.89	3.20	1.97
	2.2	30	360.3	[b]		
ZrP-M600	0.04	25	1.10	0.86	1.16	0.96
		30	1.16	0.90	1.37	1.01
	0.2	25	3.38	0.64	[a,b]	0.82
		30	2.25	0.73	[a,b]	0.88
	0.4	25	2.65	0.94	2.21	0.60
		30	2.63	0.72	2.97	0.71
		40			4.32	0.86
		50			6.72	0.66
	0.8	25	6.74[c]	0.54[c]		
		25	1.13[d]	0.89[d]		
		30	1.77[c]	[b]		
		30	1.64[d]	1.18[d]		
ZrP-M1000	0.04	25	0.93	0.74	0.93	0.74
	0.2	25	0.98	0.68	[a,b]	0.77
	0.3	25	1.79	1.08	1.70	1.23
	0.4	25	1.05	0.57	1.47	0.99
		30	1.22	0.72		

Measurements refer to pre-sheared systems unless otherwise noted.
[a] Not well-defined; [b] Only able to measure degree of shear thinning and limiting viscosity at high shear rate; [c] Pre-shear measurement of system with significant history dependence; [d] Measurement after sample sheared and linear viscoelastic measurements reach constant value.

For the ZrP-M1000, the scaling of relative viscosity does not progressively increase with concentration, as expected for high aspect ratio nanoplatelets, and the viscosity at high shear rate is less than the unfilled epoxy. The origin of this behavior is unclear, and may arise from various mechanisms. Due to the large amount of M1000 present in the system and limited understanding of its role in slip between interfaces, or potentially on the contact surfaces during measurement, this effect is not considered further here. The important finding from steady shear behavior is that the dynamic viscosity, measured from oscillatory shear, is in agreement with shear viscosity at low shear rates. This is consistent with the presence of an equilibrium microstructure. At high shear rates, there is an expected divergence between the values because the shear viscosity disrupts the microstructure and aligns the nanoplatelets in the flow direction. Further studies on the normal stress differences, and magnitude of limiting dynamic viscosity, may provide additional details on microstructure and interactions of the system. The steady shear behavior of the ZrP-M600 system shows significant non-equilibrium features and history dependence, and will not be considered in detail here. The notable feature of this system is that in systems with well-defined zero shear and infinite shear viscosity, the relative viscosities increase strongly with temperature (c.f. ZrP-M600 at 0.4 vol.% in Table 3-3). This is a unique observation because with non-interacting particles, the viscosity at a given shear rate is determined by the balance of hydrodynamic stresses and thermal energy, and any temperature-dependent changes are proportional to the change in viscosity of the unfilled matrix. The relative viscosity, given by the ratio of suspension viscosity and matrix viscosity, $\eta_r = \eta/\eta_m$, should therefore be constant with temperature.

3.4 Discussion

The objective of this work is to determine the influence of 3 different surfactants on the rheological behavior of fully exfoliated and well-dispersed ZrP nanoplatelets in epoxy. The nanoplatelets are identical for each suspension. In the ZrP-TBA system, the rheological behavior shows that there is no elastic response associated with non-hydrodynamic interactions between the plates. The behavior is attributed to recoverable, equilibrium microstructure associated with diffusive (Brownian) motion at small rates of deformation. The ZrP-M1000 shows similar behavior to the ZrP-TBA system. Analysis of relaxation behavior indicates that the microstructure consists of hydrodynamically interacting particles. The elastic response of the ZrP-M1000 system is better defined at lower concentration than the ZrP-TBA system, which is attributed to the larger magnitude of hydrodynamic distortion due to the extended brush layer (Figure 3-1). The layer amplifies the influence of ZrP for a given number density of particles. In contrast to the reproducible behavior observed with the ZrP-TBA and ZrP-M1000 systems, the ZrP-M600 shows significant non-equilibrium characteristics that are attributed to non-hydrodynamic interactions and potentially local microstructure.

A few reports have used Jeffamine as a model series of polyethers to investigate the influence of surfactant molecular weight on the intercalation and exfoliation of ZrP in different solvents [183]. The results follow the same qualitative trend observed previously for simpler *n*-alkylamines [200, 201], and no specific distinction between the two was reported. We recently observed that ZrP nanoplatelets exfoliated with M1000 oligomers form smectic liquid crystals above concentration of ~ 1.7 vol.% [187]. The

mechanisms governing the self-assembly of disk-like particles into liquid crystals are generally based purely on geometric consideration of excluded volume. In the case of smectic liquid crystals, few experimental systems are available to provide guidance in potential modifications to theory.

Based on the results from prior studies, the M600 and M1000 form a monolayer on either side of the ZrP plates, and occupy about 50% of the active sites [183]. The active sites of ZrP are arranged in a hexagonal lattice with lattice spacing of 0.53 nm [189]. The mean distance between terminal monoamines on the ZrP surface should be on the order of 1.06 nm for both systems, which gives surface coverage of grafted chains of $\Gamma = 1/s^2 \approx 0.89$ nm^2. From our recent work on identical suspensions of ZrP-M1000 in epoxy, the grafting density is sufficient to force the grafted oligomers into an extended conformation away from the ZrP surface. The extended oligomers behave as a polymer brush layer, and entanglement and inter-penetration of adjacent layers should be prevented by osmotic repulsion between adjacent chains. Relevant studies on the conformation of the surface-attached oligomers with structure of the M600 have not been carried out previously, to our knowledge. The molecular weight of the M600 is smaller than the M1000, and as result, the overlap or entanglement of neighboring chains may be reduced, or absent, at the reported grafting density. In this case, each chain will behave independently, and the resulting conformation and degree of interaction with chains on adjacent nanoplatelets will depend on the solubility of the solvent for the oligomer. This distinction does not directly account for the apparent increase in long-range interaction for the smaller molecular weight oligomer. However, it does provide a

mechanism for enhanced interaction and coupling between neighboring nanoplatelets, which may significantly influence rheological properties in the semi-dilute concentration regime. Further studies on the origin of the observed differences in inter-particle potential will be useful to identify chemical and physical processing approaches to tune phase behavior. ZrP is a model 2-dimensional nanoparticle, and may be used as an archetype to investigate structure-property relationships for other plate-like nanoparticles, which have specific functional properties for advanced applications.

3.5 Conclusions

ZrP nanoplatelets have been used as a model system to investigate the effect of surfactants on inter-particle interaction in epoxy suspensions. These model systems have been shown to be effective in modifying the inter-particle interactions between the high aspect ratio nanoplatelets. For the nanoplatelets exfoliated with TBA, the behavior follows predictions of dilute suspension rheology for the bare ZrP nanoplatelets. The results show that there is no permanent microstructure capable of resisting deformation in the system. The elastic response is attributed to the rotation of the nanoplatelets, and transient non-equilibrium arrangement of nanoplatelets following small amplitude deformation. At intermediate frequencies, the system is unable to recover equilibrium distribution. On longer time scales, the microstructure recovers equilibrium distribution by Brownian motion. For high frequencies, Newtonian response is recovered, which indicates that the presence of the ZrP nanoplatelets results in purely hydrodynamic effects.

The behavior of the ZrP nanoplatelets exfoliated with the M1000 oligomers is similar to the ZrP-TBA system. The hard-plate behavior is attributed to steric repulsion between platelets. The relaxation is more rapid in this case, which may be due either to increased collisions at lower concentration from the volume amplification effect of the extended surface layer, or to a decrease in effective aspect ratio. The well-defined elastic response at low concentration suggests that the increase in inter-particle collisions is more likely. At 0.4 vol.%, there is a decrease in elastic and viscous responses, which may be due to local alignment of the plates prior to the long-range assembly into nematic and smectic liquid crystalline structures. This more complex behavior is consistent with observations of concentrated suspensions presented in Chapter V.

The individual M600 chains have a similar structure to the M1000, but show significantly different behavior when used as surfactants to exfoliate ZrP nanoplatelets. The behavior is attributed to differences in oligomer length, which may influence packing of the monolayer, and differences in chemical structure. The rheological response at semi-dilute concentrations is attributed to non-hydrodynamic interactions between platelets, which may result in a transient microstructure at equilibrium. There may also be a change in interaction, and potentially inter-penetration and entanglement, of the short chain surface-attached oligomers. This study shows that differences in inter-particle interaction may drastically change flow properties and viscoelasticity, even for exfoliated nanoplatelets. The findings have significant practical implications regarding methods to control the viscosity and flow properties of polymer nanocomposites. This system also has fundamental importance as a model plate-like nanoparticles to

investigate structure-property relationships of high aspect ratio 2-D nanoparticles. Further work is anticipated to provide enhanced understanding of the mechanisms governing phase behavior of plate-like nanoparticles, and potentially approaches to tune and characterize the long-range structure.

CHAPTER IV

EFFECT OF ASPECT RATIO ON FLOW PROPERTIES OF SUSPENSIONS CONTAINING MODEL PLATE-LIKE NANOPARTICLES

4.1 Introduction

The linear viscoelastic and steady shear response of model 2-D nanoparticles (nanoplatelets) are investigated over a range of dilute and semi-dilute concentrations. The model particles are α-zirconium phosphate (ZrP) nanoplatelets, which are inorganic metal phosphonates that crystallize in stacks consisting of individual plate-like crystals [189, 202-204]. The nanoplatelets are easily exfoliated into individual sheets with monodisperse thickness using various surface modifiers [201, 205, 206]. Here, tetra-*n*-butyl ammonium hydroxide (TBA^+OH^-) is used as a surface modifier, which introduces net positive charge to surface and provides stability in various media [177-179]. The nanoplatelets are dispersed in an epoxy monomer matrix, which has sufficiently viscous response to measure viscoelasticity over broad ranges of frequency. To study the effect of aspect ratio, the nanoplatelets are synthesized with average diameter ranging from 100 to 1000 nm. For exfoliated nanoplatelets, the thickness is monodisperse, $t \sim 0.69$ nm [207], which provides range of aspect ratios from ~ 150 to 1500.

4.2 Experimental

The materials used here are the same as described in Chapter III. The suspending matrix is DER 332 (DOW Chemical Company), which is a DGEBA epoxy precursor

with narrow monomer molecular weight distribution (172-176 g/mol). The epoxy precursor was dried in a vacuum oven overnight prior to sample preparation to remove entrapped air and moisture.

The synthesis and exfoliation of ZrP with controlled lateral dimensions and uniform thickness has been described in detail previously [39]. Briefly, a sample of 4.0 g $ZrOCl_2 \cdot 8H_2O$ was mixed with 40.0 mL H_3PO_4 with desired molarity and sealed in a Teflon-lined pressure vessel. The vessel was heated to 200°C for between 5 and 48 hr to achieve desired lateral dimensions. After reaction, the products were washed and collected by centrifugation three times. The ZrP was dried at 65°C for 24 hr, and subsequently ground with a mortar and pestle into a fine powder prior to exfoliation.

The ZrP nanoplatelets were exfoliated to individual layers with identical thickness in aqueous solution using TBA^+OH^- as a surface modifier, which was described in Chapter III. The exfoliated ZrP nanoplatelets were subsequently dispersed in acetone after evaporating water. The epoxy precursor was added to the acetone/ZrP suspension at desired loading and sonicated for 30 minutes to ensure good mixing. No curing agent was used to avoid curing reactions during rheological characterization. The solvent was removed with a rotary evaporator to obtain the epoxy/ZrP suspensions. The fluids were dried in a vacuum oven overnight prior to characterization.

The lateral diameter of exfoliated ZrP nanoplatelets was measured using scanning electron microscopy (SEM) and transmission electron microscopy (TEM). The mass fraction of ZrP nanoplatelets in suspension was measured using a Q500 TGA (TA Instruments; New Castle, DE, USA). The TGA measurements were also used to

confirm that all solvent was removed prior to testing. Rheological measurements were carried out using the equipment and measurement techniques described in Chapter III.

4.3 Results and discussion

4.3.1 Microstructure

Meaningful interpretation of the flow behavior of suspensions requires detailed understanding of the particle microstructure in a given suspending medium, for a given set of system state variables [208]. In this work, we report the rheological behavior of suspensions containing ZrP nanoplatelets prepared with a broad range of aspect ratios. The lateral diameter of the ZrP nanoplatelets was verified with TEM and SEM measurements before and after exfoliation. The different systems are designated by the average diameter of the suspended platelets, where ZrP-100, ZrP-400, ZrP-700, and ZrP-1000, refer to suspensions containing ZrP nanoplatelets with average diameter of 100, 400, 700, and 1000 nm, respectively. A summary of several geometric parameters important for flow behavior for the different systems are provided in Table 4-1.

Table 4-1. Geometric parameters of the ZrP nanoplatelets.

System	L nm	r_p	V_p 10^{-3} nm^3	ϕ_D^* vol.%	$D_{r,o}$ 1/s
ZrP-100	100	145	5.4	0.54	2.91
ZrP-400	400	580	87	0.14	6.1×10^{-2}
ZrP-700	700	1014	266	0.08	1.3×10^{-2}
ZrP-1000	1000	1449	542	0.05	4.8×10^{-3}

The average lateral dimension, L, is the maximum length of the ZrP nanoplatelets; $r_p = L/t$ is the aspect ratio; $V_p = \sqrt{3}L^2t/2$ is the volume of an individual ZrP nanoplatelet modeled as hexagonal sheet with largest diameter L; ϕ_D^* is the dilute/semi-dilute transition, defined by $nL^3 = 1$; $D_{r,o}$ is rotary diffusion coefficient for infinitely dilute suspension of oblate spheroid with equivalent hydrodynamic influence, calculated from Brenner [100], using Eqns. (2.17) – (2.21).

The suspensions were prepared with a range of concentrations to probe response in both dilute and semi-dilute regions. The suspensions are transparent, and are macroscopically and microscopically homogeneous at all concentrations reported here. The mass fraction of the suspensions was measured with TGA, and are reported in Table 4-2, along with standard deviation obtained from 3 samples. TGA measurements also confirmed that no residual solvent was present in the suspensions.

Table 4-2. List of conversions used to express volume occupied by nanoplatelet phase.

System	c wt. %		ϕ vol.%	n #/μm^3	nL^3
ZrP-100	0.12	$\pm$ 0.06	0.05	80	0.1
	0.50		0.20	331	0.3
	0.70		0.28	463	0.5
	1.22	$\pm$ 0.14	0.48	810	0.8
	1.87	$\pm$ 0.21	0.74	1246	1.3
	5.20		2.11	3531	3.5
ZrP-400	0.10		0.04	4	0.3
	0.26	$\pm$ 0.10	0.10	11	0.7
	0.79	$\pm$ 0.02	0.31	33	2.1
	1.50	$\pm$ 0.07	0.60	62	4.0
	2.77	$\pm$ 0.09	1.11	116	7.4
ZrP-700	0.10		0.04	1.4	0.5
	0.52	$\pm$ 0.05	0.21	7	2.4
	1.06	$\pm$ 0.20	0.42	14	4.9
	1.91	$\pm$ 0.14	0.76	26	8.9
ZrP-1000	0.50	$\pm$ 0.13	0.20	3.3	3.4
	1.00		0.40	7	6.7
	1.36	$\pm$ 0.05	0.54	9	9.0
	1.93	$\pm$ 0.32	0.77	13	12.9

Mass fraction, c (average and standard deviation determined from 3 samples using TGA); ϕ, volume fraction of ZrP nanoplatelets; n, number density of ZrP per unit volume; nL^3, average number of particle center of masses in random sphere unit cell defined by volume swept by freely rotated, isolated particle.

The rheology of suspensions containing solid particles is a macroscale manifestation of properties and processes that occur on length and time scales governed by the individual suspended particles. The most important parameters that govern flow behavior are the particle volume fraction, ϕ, particle size and shape, inter-particle interactions, spatial arrangement of particles, and the nature of the bulk flow [209]. Additional factors related to colloidal forces are significant in certain systems [73], and

for highly concentrated suspensions, the size and shape distribution of the particles determine the maximum packing behavior and phase transitions [89, 210].

Here, we are interested in the effect of aspect ratio for plate-like nanoparticles suspended in a Newtonian fluid subject to shearing flow. When the suspending fluid is deformed by a shearing field, non-spherical particles undergo periodic rotations [104]. The contribution of the particles to the stress and viscosity of the suspension is time-dependent, and determined by the magnitude of flow disturbance caused by the particles. The magnitude of flow disturbance is strongly dependent on particle size, with order of magnitude L^3, where L is the largest dimension of the particle. This is the characteristic volume for the hydrodynamic distortion caused by the individual particles [142]. The increasing magnitude of distortion with size is balanced by a proportional decrease in the amount of time that the particles spend aligned perpendicular to the flow direction during simple shearing flow. In the semi-dilute region, defined here as $nL^3 > 1$, where $n = \phi/V_p$ is the number density of particles per unit volume and V_p is the particle volume, hydrodynamic interactions between particles are significant and cause more significant increase in viscosity [118, 126, 211]. For fibers, hydrodynamic interactions have also been reported to cause a larger proportion of the particles to shift to orbits that favor orientation across the flow direction [117]. At moderate concentrations, the hydrodynamic interactions may increase the frequency that particles tumble out of the flow direction. This behavior has been experimentally demonstrated in several reports for fiber suspensions by a decrease in the period of rotation at semi-dilute concentrations [117], but analogous behavior for disk-like particles has not been reported.

For the systems of interest here, the range of concentration is limited to dilute and semi-dilute behavior, which should allow effects associated with long-range order and non-hydrodynamic interactions to be neglected. All organization will be limited to local length scales, and is not anticipated to be significant. The transition between dilute and semi-dilute regions may be estimated by a critical number density, $n^* = 1/L^3 = \phi^*/V_p$. The ZrP nanoplatelets used here have regular hexagonal shape, with volume $V_p \approx \sqrt{3}L^2t/2 = \sqrt{3}r_p^2t^3/2$, where $r_p = L/t$, is the aspect ratio of the nanoplatelets. The critical volume fraction for the different systems is given in Table 4-1, and decreases linearly with aspect ratio. This analysis provides the basis for transitions in suspensions of fibers and rigid-rod polymers, but to our knowledge, has not been reported for plate-like particles. We note that the predictions from ϕ^* described here follow identical scaling to numerical calculations provided by Garboczi et al. for particles of arbitrary shape [212], but are ~ 50% lower.

At low concentration, the ZrP nanoplatelets are randomly distributed in the suspending medium as individual particles. The equilibrium microstructure of the suspension depends on the balance between particle mobility and the rate of deformation. For non-spherical particles, the characteristic time scale for motion is given by the rotary diffusion perpendicular to the particle axis of symmetry, D_r [100]. This constant governs the balance between Brownian motion, which acts to randomize the orientation and positions of the suspended particles, and hydrodynamic stresses, which act on the surface of the particles and favor the distortion of orientation distributions toward the shearing direction. The rotary diffusion coefficient can be

estimated for the case of infinite dilution using Eqns. (2.17) – (2.21). The transport properties of any suspension of identical, axially symmetric particles subjected to arbitrary homogeneous shearing field can be determined with this approach by defining an equivalent spheroid with axial ratio $r = a/b$, that has the same period of rotation as the particle of interest. The correspondence between arbitrarily shaped, axially symmetric particles and equivalent spheroids was proven by Bretherton [99], and is well supported by experimental studies (c.f. [106, 111, 213]). For disks with aspect ratio of $r_p = L/t$ (defined here for convenience such that $r_p > 1$ for the plates), a widely used empirical equation to define an equivalent oblate spheroid, where $r < 1$, is given by Eqn. (2.16) [213, 214]. The correlation is based on direct visual evidence of the rotations of fibers and discs of moderate aspect ratio under shearing flow, and provides excellent agreement for disk-like particles [113]. The value of D_r is calculated for the different systems here for T = 30°C and η_m = 2.19 Pa.s, and listed in Table 4-1. For the ZrP-100 system, D_r = 2.9 1/s at T = 30°C, which suggests that Brownian motion will be significant over the observed experimental time scale. As aspect ratio increases, D_r follows power-law scaling of $D_r \propto r_p^{-2.78}$. Increasing aspect ratio results in a significant penalty in mobility that is slightly less than the associated increase in volume of fluid disturbance ($\sim O(r_p^3)$). Based on the calculations listed in Table 4-1, for the ZrP-400 system, Brownian forces will only weakly influence measurements. For the ZrP-700 and ZrP-1000 systems, rotary diffusion may be sufficient to eliminate significant history effects, assuming adequate equilibration time is provided. However, on the experimental time scale, hydrodynamic forces will dominate.

4.3.2 Rheology of unfilled epoxy

The majority of theoretical work is based on the assumption of a Newtonian suspending matrix, which is defined by a rate-independent viscosity, and negligible elastic response. Shear thinning and elasticity in the matrix phase tend to favor dampen particle motion and favor alignment to minimize hydrodynamic disturbance, and must therefore be determined [214]. The linear viscoelastic and steady shear response of the unfilled epoxy used here is reported in Appendix I over a range of temperatures and rates of deformation. Briefly, the unfilled epoxy shows dominant viscous response and weak elasticity characteristic of a Maxwell fluid ($G' \propto \omega^2$ and $G'' \propto \omega$), with mono-exponential relaxation time on the order of 10^{-6} s at 30°C. The elastic response is significant with respect to viscous dissipation only for angular frequencies on the order of $\omega = 2\pi/\tau \approx 6.3\times10^6$, and may therefore be neglected for the conditions presented here. The temperature dependence of linear viscoelasticity and steady shear viscosity are well described by standard models based on free volume. The viscosity is independent of shear rate for all conditions investigated.

4.3.3 Linear viscoelasticity of ZrP suspensions

Several measurements were carried out by increasing the strain amplitude from ~ 0.1 – 500% at fixed frequency to determine the nature of non-linear response and range of linear viscosity. For all concentrations reported in this work, the systems show linear viscoelastic response up to large strain, γ ~ 100% and greater, with strain softening in G'

and G'' in the non-linear region. This behavior is typical for systems of individually dispersed particles with weak interactions with neighboring particles (c.f. Chapter III).

Representative curves summarizing the linear viscoelastic response of the ZrP suspensions are shown in Figure 4-1. The response of the ZrP-100 system is reported in detail in Chapter III, and provides a convenient baseline to describe the ideal behavior of a suspension of ZrP nanoplatelets. The response of the system can be separated into two regions of behavior. At concentration of ~ 0.5 vol.% and below, there is weak increase in G'' with concentration, and the magnitude and scaling of elastic response, G', are not well-defined. For ~ 0.7 vol.% ZrP-100 and above, the concentration dependence of viscous response is increased, and G' is well-defined. At low frequency, G' shows viscous flow behavior characteristic of a fully relaxed viscoelastic fluid, with δ approaching 90°. As frequency increases, there is a transition to a region where G' has less frequency dependence. For the ZrP-100 system, the frequency at the transition region is consistent with the time scale of rotary diffusion.

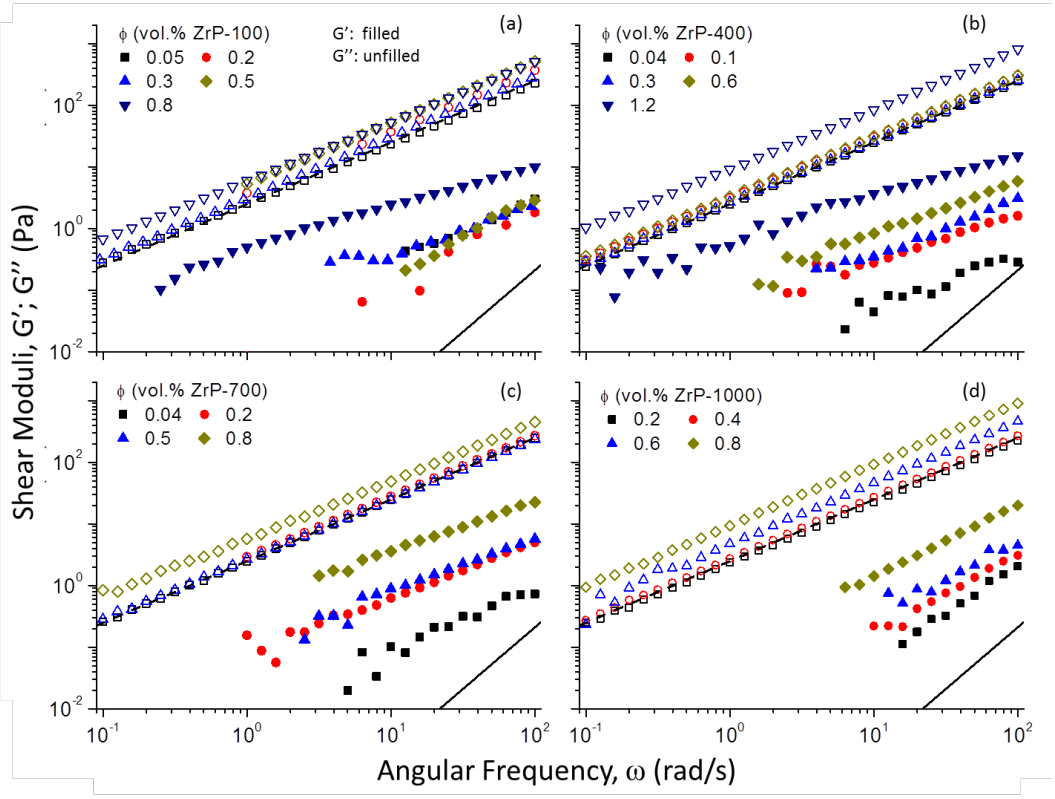

Figure 4-1. Linear viscoelastic response of epoxy monomer containing various concentrations of TBA^+-exfoliated ZrP nanoplatelets with average lateral diameter of (a) 100 nm; (b) 400 nm; (c) 700 nm; and (d) 1000 nm.

The viscoelastic response of the ZrP-100 system is stable, and shows that the ZrP nanoplatelets are rigid, Brownian plates with no permanent mechanism of elastic response. The increase in concentration dependence at 0.7 vol.% is attributed to hydrodynamic interactions between particles at semi-dilute concentrations, which is consistent with the prediction for ϕ^* based on the criterion $n^* = 1/L^3 = 0.6$ vol.% (Table 4-1).

For the ZrP-400 system, the transition is not clearly defined based on the behavior of G' and G'', but may be identified based on the change in phase angle, δ (Figure 4-2). At

0.3 vol.% ZrP-400, δ shows a weak shoulder and decreases with $|G^*|$, which indicates the presence of weak elastic response. The value of nL^3 at this concentration is 2.1, which is consistent with the anticipated concentration dependence. In Figure 4-2, the phase angle, δ, is shown as a function of $|G^*|$, which is often referred to as a van Gurp-Palmen (vGP) representation [190]. This representation has been widely used to identify subtle changes in molecular structure of polymers in the melt state [192-195], and is shown in Chapter III to be useful to describe relaxation behavior in epoxy/ZrP suspensions.

The vGP representation provides a useful method to directly compare between the relaxation behavior of the different systems. The concentration corresponding to the semi-dilute region is decreased for ZrP-400, but the magnitude change in δ is less than in the ZrP-100 system at similar nL^3. For example, at $\phi = 0.74\%$ ZrP-100, $nL^3 = 1.3$, and the relaxation behavior is extremely pronounced. This system shows well-defined maxima in δ at high $|G^*|$, broad decrease in δ corresponding to a region of solid-like response, and finally a minima in δ and subsequent increase at low $|G^*|$, which corresponds to a viscous flow region for $\omega \ll D_r$. For the ZrP-400 system, there is no significant change in δ until $\phi = 1.1$ vol.% ($nL^3 = 7.4$). This suggests that there is a change in the nature of elastic response with aspect ratio.

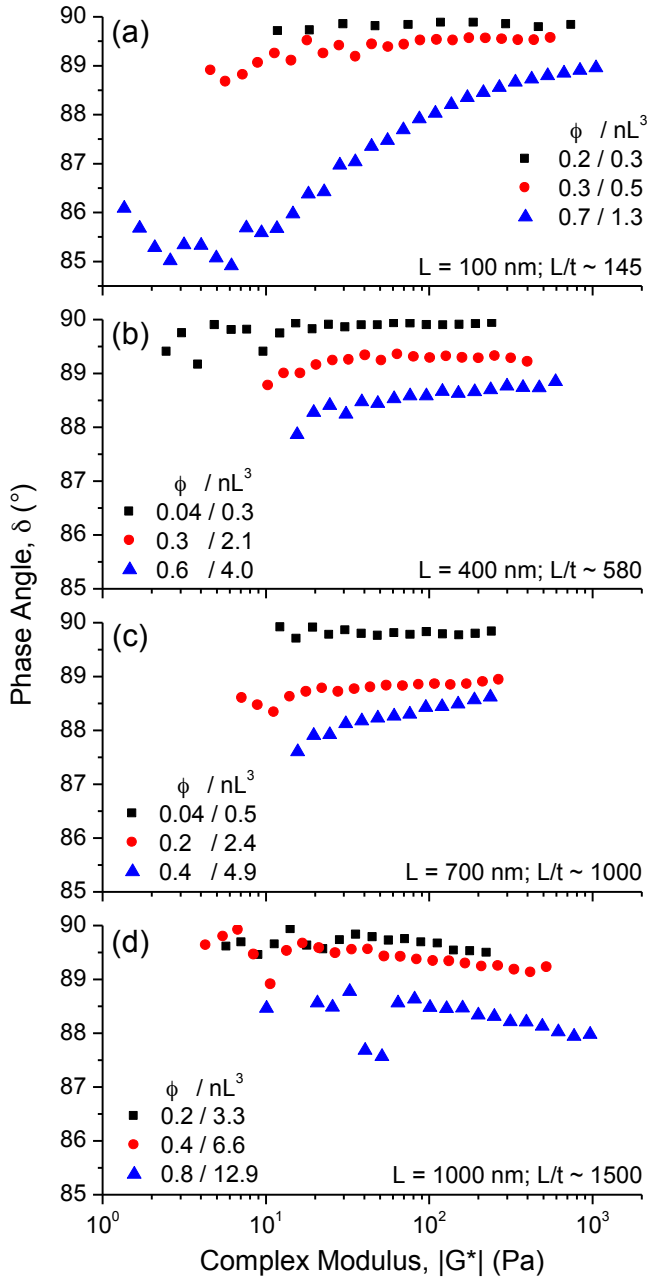

Figure 4-2. Phase angle, δ, shown as function of magnitude of complex modulus, $|G^*|$ (vGP plot) for suspensions containing TBA^+-exfoliated ZrP nanoplatelets with average lateral diameter of (a) 100, (b) 400, (c) 700, and (d) 1000 nm. Measurements carried out at T = 30°C.

For the ZrP-700 system (Figure 4-1c and Figure 4-2c), there is an increase in concentration-dependence of G'' and well-defined G' at high frequency for $\phi = 0.2$ vol.% and higher ($nL^3 \geq 2.4$). However, there is little change in δ until $nL^3 \sim 9$. For the ZrP-1000 system, the scaling of δ is distinct from the other systems. At low $|G^*|$, there is a maxima in δ, and as $|G^*|$ increases, δ decreases weakly. The behavior is subtle, but reproducible and consistent for all ZrP-1000 systems.

The linear viscoelastic results are proposed to originate from a combination of three aspect ratio-dependent effects. As the aspect ratio of the ZrP nanoplatelets increases, there is an observed decrease in ϕ^*, an increase in concentration-dependence of G'', and a progressive suppression of the relative solid-like response. The decrease in ϕ^* is well described by the increase in length scale of hydrodynamic disturbance with size. The increase in viscous response is also consistent with the increase in magnitude of hydrodynamic distortion due to the particle size.

The decrease in relative solid-like response is attributed to the change in time scale for particle motion for the higher aspect ratio systems. For the ZrP-100 system, the time scale for Brownian motion, D_r, is similar to the time scale of the oscillatory measurements. As aspect ratio increases, D_r decreases rapidly ($\propto r_p^{-2.78}$), and the larger nanoplatelets may be essentially regarded as non-Brownian, immobile particles (Table 4-1). In this case, although the microstructure is perturbed by the deformation, the time scale associated with the motion of the suspended particles is extremely slow. The measurements reflect highly localized behavior dominated by hydrodynamic effects.

However, the magnitude of D_r is sufficient that there still should be a relatively randomized microstructure for linear viscoelastic measurements.

4.3.4 Steady shear

Representative curves showing the steady shear response of ZrP suspensions are shown in Figure 4-3. For the ZrP-100 system, there is very weak shear thinning up to 0.8 vol.%, and the low shear rate viscosity increases with concentration. At 0.8 vol.%, the shear thinning behavior is more significant, which is likely dominated by hydrodynamic interactions and associated changes in equilibrium orientation distribution and frequency of tumbling across the flowing direction. The divergence of η' and η at low shear rates indicates that non-hydrodynamic interactions are also present. At 2.2 vol.%, the increase in viscosity is significant, and there is a broad plateau region up to ~ 1 1/s. At higher shear rates, the system gradually shifts to shear thinning behavior, and no high shear rate plateau is observed.

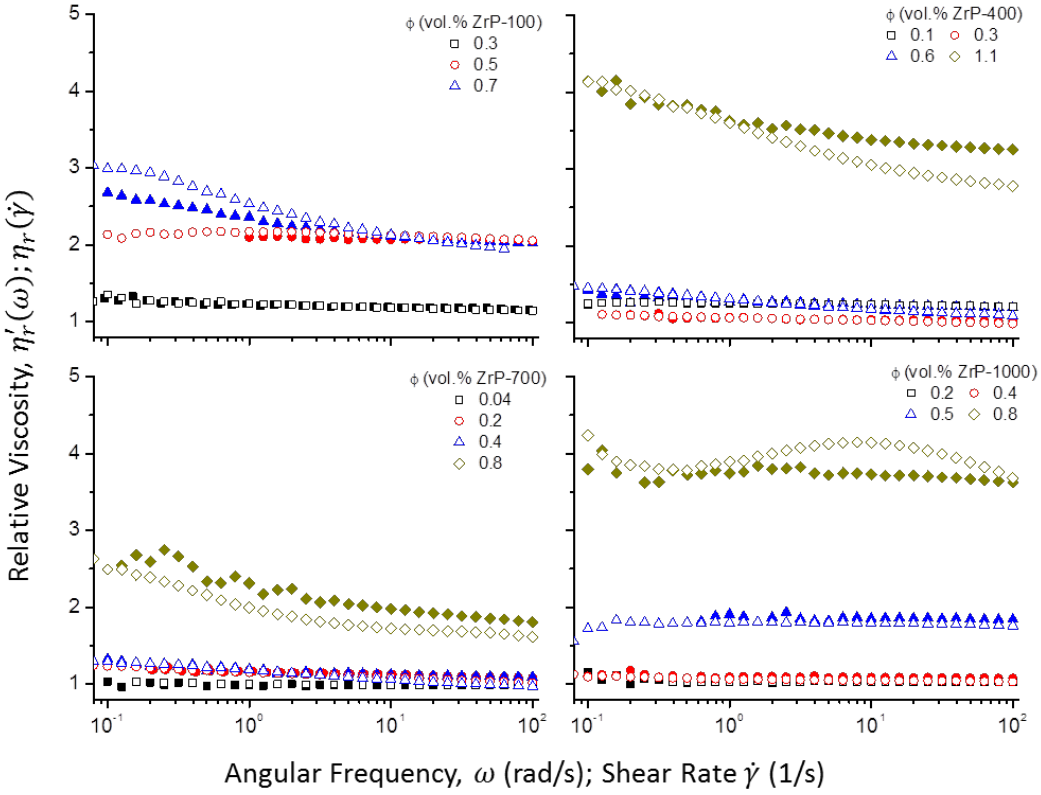

Figure 4-3. Dynamic viscosity, $\eta'(\omega)$ (filled symbols), and steady shear viscosity, $\eta(\dot{\gamma})$ (unfilled symbols), shown as functions of angular frequency, ω, and shear rate, $\dot{\gamma}$, respectively, for (a) ZrP-100, (b) ZrP-400, (c) ZrP-700, and (d) ZrP-1000 systems. Measurements carried out at 30°C.

For the ZrP-400 systems, the viscosity of the suspensions is less than for the ZrP-100 systems at similar concentration, and shows more complex concentration dependence. For the two systems with concentration of $nL^3 < 1$, the response is Newtonian and the viscosity increases with concentration. At 0.3 vol.% ZrP-400 ($nL^3 = 2.1$), there is a significant drop in viscosity and weak increase in shear thinning. As concentration increases in the semi-dilute region, the flow curves are similar. At low shear rate, there is a limiting plateau. There is shear thinning behavior for $\dot{\gamma}\sim$0.3 1/s and higher, and at

high shear rate, there is a limiting viscosity with $\eta' > \eta$. The shear thinning behavior agrees with the predicted $D_r \sim$ 0.06 1/s for this system.

For the ZrP-400 system at 1.2 vol.% (Figure 4-3c), there is a large increase in viscosity, and an apparent low shear rate plateau. The system also shows a secondary shear thinning transition at high shear rate. The rotary diffusion coefficient of this system is $D_r \approx 10^{-2}$ 1/s, which suggests that all measurements should correspond to a region dominated by hydrodynamic stresses. The presence of the high shear rate thinning behavior is unexpected, and is reversible. Additional measurements were carried out over a broader range of temperature to determine the nature of the double shear thinning behavior (Figure 4-4). The double shear thinning behavior is observed between 10 – 30°C. At higher temperatures, the flow curves are consistent, but the double shear thinning is outside of the experimental window. The behavior is reversible in each case, which indicates that it is not an artifact of the measurement, or due to transient microstructure or inhomogeneity. The origin of the double shear thinning is not clear. One potential mechanism for deviations in flow behavior may be related to the increase in particle flexibility with aspect ratio. We have previously reported that in cured epoxy nanocomposites, high aspect ratio nanoplatelets show extremely high curvature, whereas the nanoplatelets with $L = 100$ nm appear to be straight [44, 47, 181]. This claim is difficult to verify because there is no established criterion for the shear-induced buckling of plate-like particles [133].

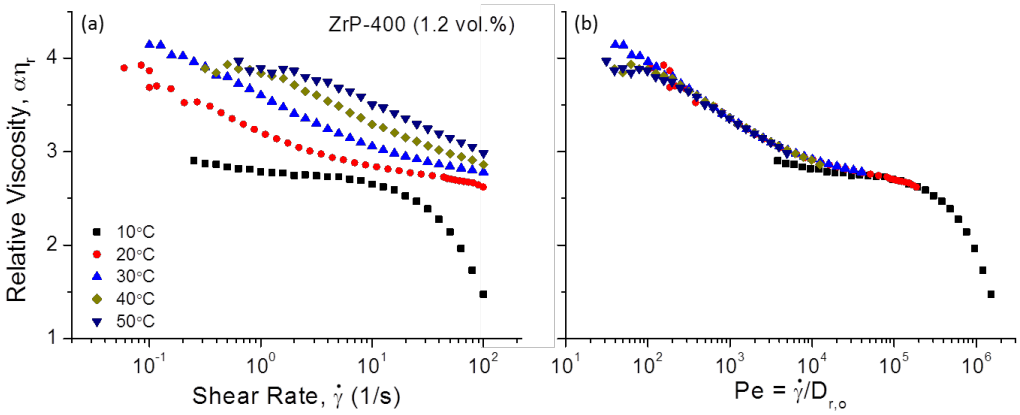

Figure 4-4. Temperature dependence of shear viscosity for suspension of ZrP-400 at 1.2 vol.%: relative shear viscosity, $\eta_r = \eta/\eta_m$, as function of shear rate, and (b) relative shear viscosity as function of Peclet number.

The presence of the well-defined transition provides a convenient point to assess the validity of the approach to calculate rotary diffusion coefficient for the case of the high aspect ratio, disk-like nanoparticles. The shear rate for each measurement was normalized by the associated rotary diffusion coefficient calculated for each temperature, to obtain the dimensionless rotary Peclet number. The obtained scaling of shear rate by the rotary diffusion coefficient provides excellent superposition of the temperature-dependence for the ZrP-400 (1.2 vol.%) system, which shows that the transition is related to the mobility of plates. In Figure 4-4, a small vertical shift factor is used to match the height of the viscosities at the different temperatures. The shift factor was small and did not show any consistent temperature dependence, and is attributed to experimental uncertainties in the value of the matrix viscosity, which is very small at higher temperatures. There may be additional effects related to size scale, but this is

unclear from the data. From the master curve, it appears that for Pe approaching 1, the system is approaching a low shear rate plateau. However, this is not clear from the data.

For the ZrP-1000 systems, there is negligible increase in viscosity or shear thinning behavior up to 0.4 vol.%. At 0.6 vol.%, there is an increase in viscosity, but no change in shear thinning behavior. The increase in viscosity without change in shear thinning behavior is consistent with the expected behavior of well-dispersed, Brownian particles for $nL^3 \gg 1$. At 0.8 vol.%, there is a well-defined shear thickening behavior region observed at intermediate shear rate (Figure 4-5). It is interesting to note that there is excellent agreement between η and η' for each of the ZrP-1000 systems, including the 0.8 vol.% system at high and low rates of deformation.

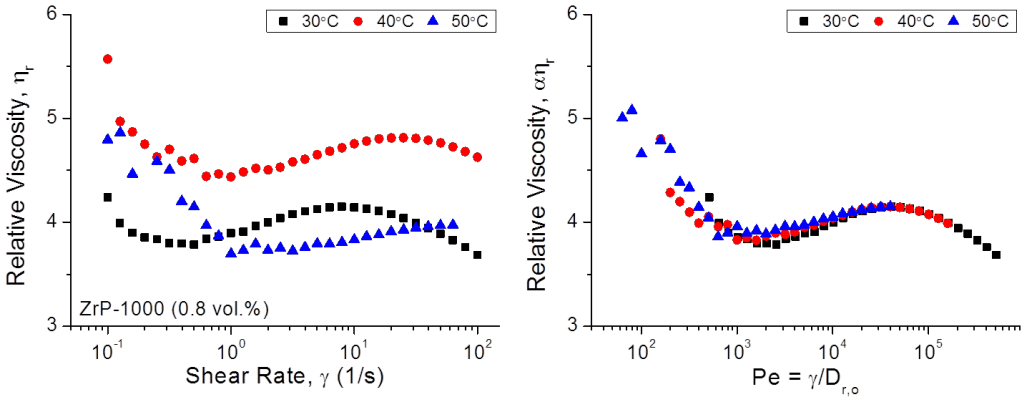

Figure 4-5. Temperature dependence of shear viscosity for suspension of ZrP-1000 at 0.8 vol.%. (a) Relative shear viscosity, $\eta_r = \eta/\eta_m$, as function of shear rate, and (b) relative shear viscosity as function of Peclet number.

To provide insight into the origin of the flow behavior for ZrP-1000 system at 0.8 vol.%, measurements were carried out at higher temperatures. At each temperature, the shear thickening behavior was observed. The temperature dependence of the shear rate at the shear thickening maxima is in excellent agreement with the calculated values of rotary diffusion coefficient for dilute spheroids. Similar to the ZrP-700 system, there is some variation in the magnitude of the maxima that is not accounted for by scaling with the viscosity of the matrix. The main finding here is that the relative temperature-dependent scaling of viscosity follows predictions for rotary diffusivity. This shows that the unique transition in flow behavior is associated with the mobility of the individual particles. Further work is needed to more clearly determine the origin of these behaviors.

4.4 Conclusions

The effect of particle size on the rheology of suspensions containing model inorganic nanoplatelets has been investigated. The α-zirconium phosphate (ZrP) nanoplatelets were synthesized with average diameters ranging from 100 nm to 1 μm, and were uniformly dispersed in an epoxy matrix as individual, sheets with monodisperse thickness. The linear viscoelastic and steady shear properties were investigated, and revealed distinct changes in elastic and viscous behaviors with aspect ratio. The magnitude and concentration-dependence of viscous response are increased for the larger nanoplatelets, but the relative elastic behavior is suppressed. The behaviors are attributed to a competition between excluded volume, which increases linearly with L, and mobility, which decreases with L^3. As the nanoplatelet size increases, the mobility of the particles decreases significantly, and the measurements reflect localized properties of the individual nanoparticles in the absence of hydrodynamic interactions with neighboring particles. The steady shear response of the smaller nanoplatelets shows weak shear thinning at low concentration, which is characteristic of the change in orientation distribution due to shearing forces. At high concentration, the degree of shear thinning is increased, which is attributed to hydrodynamic and non-hydrodynamic interactions. As aspect ratio increases, the steady shear response for semi-dilute suspensions shows complex behaviors that are attributed to a complex relationship between hydrodynamic interactions and shift in particle orients and average orientations. For the systems with larger aspect ratio at high concentration, additional non-Newtonian behaviors are observed. The temperature dependence of non-linear response follows

theoretical calculations of rotary diffusion coefficient. The origin of the behavior is unclear at this time, and may arise from a number of mechanisms that have been observed for fiber suspensions. However, the influence of these mechanisms on the behavior of high aspect ratio plate-like particles is not known and may deviate significantly due to the differences in shape. The model system used here provides an extremely broad range of length and size scales to be meaningfully connected to the motion and interactions of the individual particles. Further theoretical and numerical studies are needed to better understand the effects of concentration on mobility, interactions, and phase transitions for high aspect ratio, disk-like particles. These studies will provide insights into the origins of complex non-equilibrium response observed here.

CHAPTER V

RHEOLOGY OF EXFOLIATED INORGANIC NANOPLATELET SUSPENSIONS WITH SMECTIC ORDER

5.1 Introduction

There is significant interest in using nanoparticles to drastically modify, and potentially tune, a range of bulk properties of fluid and polymer systems. At relatively small volume fractions, well-dispersed nanoparticles are able to directly interact with a large fraction of polymer chains in the matrix [215], and may profoundly influence a diverse range of transport properties and relaxation behaviors of the polymer [216-218]. Depending on the size, shape, and interaction potentials, nanoparticles may self-assemble into ordered structures that show unique properties originating on longer length scales [27, 219-222]. However, the molecular-scale dimensions and large surface area pose severe thermodynamic challenges to achieving controlled and stable spatial dispersion (local structure) and organization (mesoscale structure) of the nanoparticle phase. As a result, the factors governing the spatial organization of nanoparticles and the relationships among particle-level parameters, mesoscale order, and bulk response of polymer nanocomposites remain poorly understood [7, 223]. The similar dimensions of the nanoparticles and polymer chains also limit the application of continuum-based modeling approaches to describe bulk properties. Model systems of nanoparticles with well-defined size, shape, and composition, and small polydispersity are needed to

investigate robust methods in controlling dispersion and organization of nanoparticles, and relate the resulting structure to a desired set of macroscale properties.

Recent success in guiding the self-assembly of spherical and low aspect ratio nanoparticles has been largely driven by the development of novel methods to synthesize these nanoparticles with low polydispersity and their well-defined physical and chemical structure [224]. In concert with numerical simulation, these experimental developments have fueled theoretical investigations aiming to understand structure-property relationships and the origins of phase behavior [215]. Much less progress has been made regarding colloidal dispersions of high aspect ratio nanoparticles because of a lack of available materials with suitable size and shape selectivity for fundamental study.

High aspect ratio nanoparticles show a number of unique properties desired for engineering applications, which are associated with their anisotropic geometry [174]. The large difference in characteristic dimensions results in a large excluded volume if the particles are randomly packed, which increases the significance of inter-particle interactions at low volume fraction [212]. In some cases, interactions between nanoparticles may favor the formation of mesoscale structure suitable for certain properties. For example, carbon nanotubes (CNTs) are 1-dimensional cylindrical nanoparticles that tend to cluster into aggregates of primary nanoparticles. If the aggregates are initially broken down and allowed to flocculate into a percolated network, significant changes in material properties may be observed at extremely low concentrations, particularly electrical conductivity, viscoelasticity, rheology, and the distribution of internal stresses [225-229]. In this case, the macroscale response of the

polymer nanocomposites is originated from the complex interplay between non-local inter-particle interactions and mesoscale organization of particle clusters, which limits development of unambiguous structure-property relationships.

Here, we investigate the relationship between rheology and spatial organization of a suspension of model plate-like nanoparticles, or nanoplatelets, with well-defined long-range order. Nanoplatelets have strong, covalent bonding along a primary plane and interact with neighboring particles through weak out-of-plane van der Waals (vdW) or hydrogen bond interactions [174]. The weak interactions favor the formation of layered structures, and the inter-layer spacing is governed by forces balancing the charges between layers. In many layered materials, the inter-layer forces are determined by counter-ions, and may be modified using ion-exchange reactions [230, 231]. If the distance between layers is increased sufficiently to overcome the weak interactions between layers, the stacked nanoplatelets will exfoliate into individual sheets [183, 205].

The rheological behavior of suspensions provides insight into the structure, organization, and interactions between particles, and between the nanoparticles and its suspending medium. In polymer melts containing exfoliated nanoplatelets that are not strongly attached to the polymer chains, there is generally a monotonic increase in viscosity and shear modulus with nanoplatelet concentration, and shows no shift in relaxation behavior [232]. If the polymer chains are tethered at one end to the nanoplatelet surface, the magnitude increase of viscosity and shear modulus is more significant, and the relaxation behavior changes drastically [197]. In particular, the resistance to deformation becomes solid-like, even over long experimental times, which

indicates that a permanent elastic network is formed by the interactions between phases. For concentrated suspensions of nanoplatelets in low molecular weight suspending fluid, similar changes in solid-like response over long times are often related to severe restrictions in particle mobility approaching a gelation transition [233]. Depending on the nature of inter-particle and particle/matrix interactions, several mechanisms have been proposed to account for the origin of the non-terminal viscoelastic response [196, 234-237]. Unique rheological features in the non-linear viscoelastic region, and during steady shear, have also been reported, such as strain-hardening in the case of surface-attached polymer brush layers [197].

In this work, we investigate the rheology of a suspension containing high aspect ratio, sterically stabilized α-zirconium phosphate (ZrP) nanoplatelets that self-assemble in a smectic liquid crystalline mesophase over a range of concentrations [185, 187]. ZrP is an acidic, inorganic metal phosphonate that crystallizes in a α-form layered structure [202, 204]. The size, shape, and polydispersity of the individual ZrP crystals can be controlled over a broad range by varying reaction conditions [39], which makes ZrP an ideal material for structure-property investigations relevant to 2-dimensional nanomaterials [44, 45, 47, 49, 181]. Here, the ZrP nanoplatelets are exfoliated into individual sheets and sterically stabilized in suspension by densely grafting polyetheramine oligomers to the nanoparticle surfaces. Similar approaches have been used to control dispersion and prevent agglomeration in polymer nanocomposites [238-240]. In a few cases, liquid crystalline ordering of sterically-stabilized rod-like [241, 242] and plate-like [243-246] colloids has been reported in aqueous solution. This work

is the first detailed rheological investigation of a suspension of colloidal plate-like nanoparticles that exhibit smectic liquid crystalline order.

5.2 Experimental

5.2.1 Materials

Zirconyl chloride ($ZrOCl_2 \cdot 8H_2O$, 98%, Aldrich) and phosphoric acid (H_3PO_4, 85%, EM Science) were used as received. Jeffamine M1000 (M1000), a commercial polyoxyalkyleneamine with reported average molecular weight of ~ 1000 g/mol, was donated by Huntsman Chemical. EPON 862, a diglycidyl ether of bisphenol F (DGEBF) liquid epoxy monomer, was obtained from Hexion Specialty Chemicals (Columbus, OH).

5.2.2 Preparation of exfoliated ZrP nanoplatelets and dispersion in epoxy

The ZrP nanoplatelets were prepared using a hydrothermal method, which has been described in detail previously [39], and summarized in Chapter III. The ZrP nanoplatelets were exfoliated using M1000 using the procedure recently reported in detail by Wong et al. [185, 187].

After removing the excess polyoxyalkyleneamine, the exfoliated ZrP nanoplatelets were dispersed in acetone. The epoxy monomer was dissolved in acetone and added dropwise to the acetone/ZrP suspension under stirring to achieve desired concentration. No curing agent was used in this work. The dispersion was allowed to stir for 4 hr. The solvent was removed with a rotary evaporator to obtain the epoxy/ZrP suspensions.

5.2.3 Characterization

The mass fraction of ZrP nanoplatelets in the suspension was measured with a Q500 TGA (TA Instruments). The TGA measurements also confirmed that all solvent was removed. Rheology measurements were carried out using the same equipment described in Chapter III. The rheological behavior was measured with cone and plate (50 mm diameter, 0.02 rad cone angle, 0.051 mm truncation spacing) and parallel plate geometries (25 mm and 40 mm diameter, with gap of 1.5 – 3 mm). For suspensions with $\phi = 0.3 – 4.0$ vol.% ZrP, both fixtures were used and found to provide consistent results. At higher concentration, parallel plates were used due to the high viscosity at low shear rate and long recovery time.

To determine the role of loading history, measurements were carried out before and after the application of steady shear. Unless otherwise noted, linear and non-linear viscoelastic measurements were reproducible following steady shear, and the reported measurements are from representative pre-sheared suspensions. Sample recovery was verified by measuring the real and imaginary components of the complex shear modulus, $G^*(\omega)$, with small strain amplitude, $\gamma = 1\%$, at angular frequency of $\omega = 1$ rad/s, immediately following steady shear or large amplitude deformation. For the unfilled epoxy monomer and suspensions at low concentration, no equilibration time was detected following steady shear. The recovery time increased with concentration, and ranged from a few minutes at low concentration, up to several hours at high concentration. Individual measurements were carried out following the procedures described in Chapter III.

5.3 Results

5.3.1 Microstructure of ZrP colloidal liquid crystals

To meaningfully interpret the rheological response of the colloidal smectic liquid crystals, it is necessary to first consider the hierarchical structure of the suspensions (Figure 5-1). The individual ZrP layers consist of a plane of Zr atoms sandwiched between tetrahedrally coordinated phosphate groups (Figure 5-1a) [204]. Each phosphate contributes three oxygen atoms to link three different Zr atoms. The remaining P-OH groups are oriented perpendicular to the plane of Zr atoms, and organized in a dense hexagonal lattice. The negatively charged inter-layer oxygen atoms provide active sites for intercalation reactions [247].

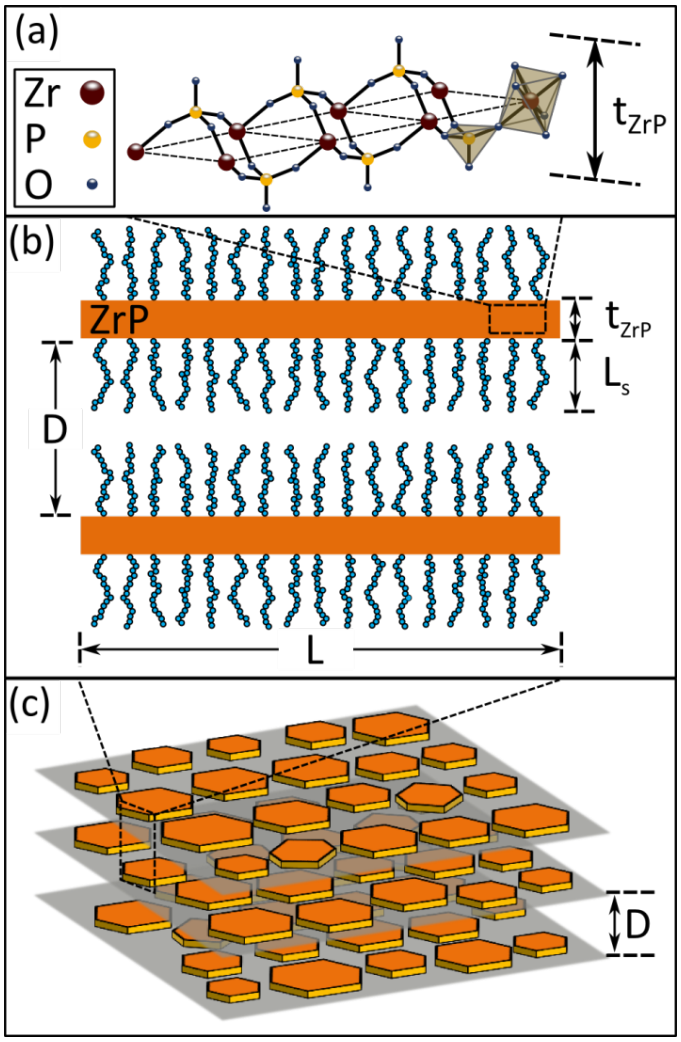

Figure 5-1. Idealized schematic of the microstructure of suspensions containing ZrP nanoplatelets with smectic liquid crystalline order. (a) Detail of crystal unit cell of individual ZrP nanoplatelet, adapted from Alberti and Costantino [247]. (b) Individual ZrP nanoplatelet with polyoxyalkyleneamine oligomer brush attached at surface. (c) Self-assembly of ZrP nanoplatelets into independent layers to form smectic liquid crystal mesophase.

ZrP crystallizes into hexagonal 2-dimensional crystals. The size, shape, and polydispersity of the crystals are determined by reaction conditions, particularly the concentration of phosphoric acid and reaction time [39]. During synthesis, the

hexagonal crystals self-assemble into stacked aggregates, or tactoids, due to inter-layer vdW forces [189]. Guest molecules containing proton-accepting functional groups readily diffuse between layers and increase the inter-layer spacing [183, 231, 247-252]. Linear *n*-alkyl-monoamines form a non-interpenetrating bilayer between adjacent layers [200, 201]. For the M1000 polyoxyalkyleneamine oligomers used here, the increase in spacing is sufficient to overcome the attraction between layers in aqueous solution, and results in spontaneous delamination of ZrP tactoids into individual sheets [183]. The average lateral diameter of the exfoliated nanoplatelets, measured with transmission electron microscopy (TEM), is 100 nm, with standard deviation of ~ 30 – 50 nm [39, 176, 185, 187]. The exfoliated ZrP nanoplatelets have monodisperse thickness, which has been previously estimated in the range of $t_{ZrP} \approx 6.7 – 6.9$ Å (Figure 5-1a) [182, 207].

In this work, the ZrP tactoids are exfoliated to individual sheets using M1000 oligomer. Polyetheramines are linear block copolymers consisting of a primary amino group attached to the end of a flexible polyether backbone based on propylene oxide (PO) and ethylene oxide (EO) blocks. The M1000 oligomers are densely grafted at the surface of the ZrP nanoplatelets, and form an extended brush layer (Figure 5-1b) [185, 187]. Using molecular dynamics (MD) simulation [253] (Appendix II), the equilibrium length of the extended M1000 chains was estimated to be $L_s \approx 7.9 – 8.0$ nm, which is consistent with recent atomic force microscopy (AFM) measurements [187].

The exfoliated ZrP nanoplatelets were dispersed in an epoxy monomer with volume fraction ranging from $\phi = 0.04$ to 8.6 vol.% ZrP. At all concentrations, the suspensions

were homogeneous under optical microscopy, and no phase separation was observed over several months. Visual observation of birefringence between crossed polars and synchrotron-source small-angle X-ray scattering (SAXS) measurements have revealed that the suspensions show long-range smectic liquid crystalline order at concentrations of $\phi = 1.7$ vol.% ZrP and higher [187]. The individual ZrP nanoplatelets self-assemble into discrete layers with regular, well-defined inter-layer spacing, D, and random (liquid-like) order within each layer (Figure 5-1c). The distance between smectic layers, calculated from the primary SAXS diffraction peaks, decreases from 47 nm at 1.7 vol.%, to 6 nm at 5.3 vol.% . Several higher order scattering peaks were detected, which are not typically observed for smectic liquid crystals formed from organic molecules. The higher order scattering peaks indicate that the domain size of the smectic mesophase is large relative to the lateral dimensions of the nanoplatelets [176].

The liquid crystalline suspensions show mild turbidity, which is typically associated with random fluctuations in the average orientation of the mesophase domains, and of molecules within the mesophase [254]. In smectic liquid crystals formed from ordered block copolymers, small molecules, and liquid crystalline polymers (LCPs), significant light scattering is often related to high concentrations of immobile defects, which strongly influence rheology and processability [255, 256]. Here, the domain size of the mesophase is large, and turbidity was not affected by the application of shearing forces, which suggests that the role of defects in the colloidal smectic liquid crystals should be minor, if any.

5.3.2 Rheology of unfilled epoxy monomer

The rheological response of the unfilled epoxy monomer was extensively characterized with SAOS and steady shear measurements. A sample containing a high concentration of free M1000 oligomer (21.9 wt.% ≈ 24.6 vol.%) was also prepared as a control. At all temperatures and frequencies investigated, both systems behave as simple viscoelastic fluids and show Newtonian response over the experimental conditions investigated here. The linear viscoelastic response of the unfilled epoxy shows weak elastic response at high ω and low temperature. The behavior is well described by the Maxwell model for a simple viscoelastic fluid with mono-exponential relaxation time of $\tau = 24.3$ μs and zero-frequency viscosity of $\eta_o = 3.76$ Pa.s at 25°C (Appendix I). Any development of elastic response or non-Newtonian viscosity may therefore be assigned to the behavior of the behavior of the individual ZrP nanoplatelets or relaxation of longer-range microstructure containing the nanoplatelet phase. At high concentration, changes in the relaxation behavior of the epoxy monomer matrix or surface-attached brush layer may also contribute to viscoelasticity.

5.3.3 Rheology of isotropic suspensions of ZrP nanoplatelets

Representative linear viscoelastic measurements of the epoxy monomer containing ZrP nanoplatelets with concentration ranging from 0.04 – 8.6 vol.% are shown in Figure 5-2. The influence of surface modifier and aspect ratio of ZrP nanoplatelets uniformly dispersed in a Newtonian suspending matrix at low concentration is reported in detail in Chapter III and Chapter IV. The prior results will be briefly summarized here. At ϕ =

0.04 – 0.4 vol.% ZrP, suspensions containing ZrP nanoplatelets exfoliated with M1000 oligomers do not show long-range order and are regarded as isotropic dispersions. At equilibrium, the distribution of suspended particles is determined by Brownian motion, which acts to randomize the position and orientation of the individual particles. In this case, the suspensions have liquid-like order and behave as weakly viscoelastic fluids, with dominant dissipative response and shear moduli that follow scaling given by $G' \propto \omega^2$ and $G'' \propto \omega$, where $G'' \gg G'$. The change in magnitude and scaling of G'' is very weak in this concentration range. The frequency dependence of G' is attributed to random motion of the individual ZrP nanoplatelets, and localized interactions and collisions between nanoplatelets at higher concentration. At high frequency, the suspending matrix may also provide weak contributions to G' (Figure 5-2a).

At low and intermediate frequency, the elastic response may be characterized by a single relaxation time, τ_c. For the isotropic suspensions, the relaxation time is attributed to the time scale for free rotation of the nanoplatelets, and defined by the characteristic frequency separating the two regions of response, $\tau_c = 2\pi/\omega_c'$ (Table 5-1). For $\omega < \omega_c$, the suspended nanoplatelets are able to freely rotate, and the suspension shows predominantly dissipative response, with power-law scaling approaching $G' \propto \omega^2$ and $G'' \propto \omega$ at low concentration and frequency. As concentration increases, the relaxation time increases, and the viscoelastic response at low frequency remains characteristic of a terminal flow region.

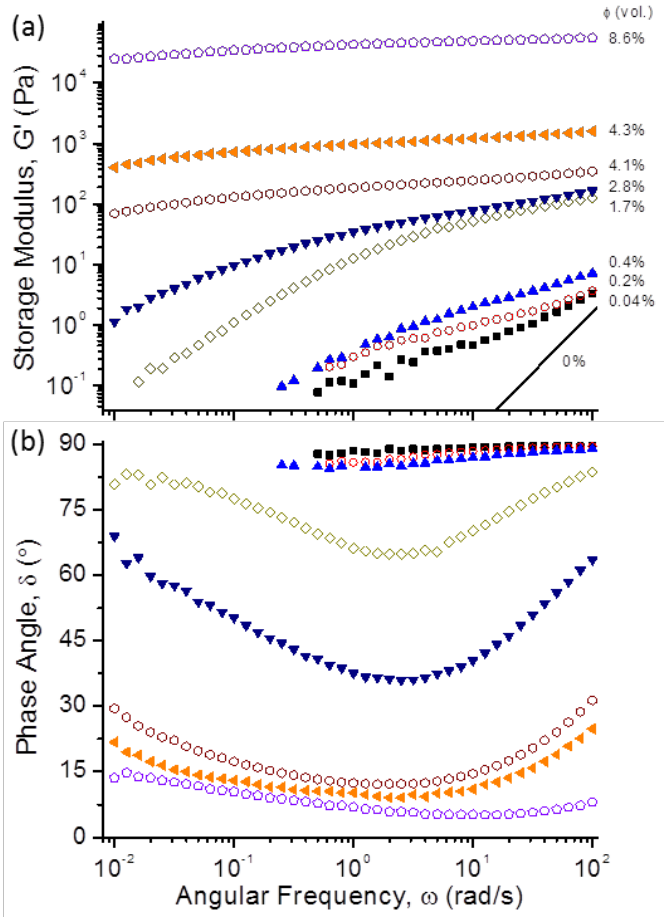

Figure 5-2. Linear viscoelastic response of representative ZrP suspensions in epoxy precursor matrix over range of concentrations: (a) storage modulus, G', and (b) phase angle, δ, as functions of angular frequency, ω. Measurements made at 25°C. The response of the unfilled epoxy precursor matrix is shown as a solid line for clarity. Suspensions with $\phi = 0.04 - 0.4$ vol.% ZrP do not show any long-range organization. Suspensions at 1.7 vol.% ZrP and higher show smectic liquid crystalline order.

In the intermediate frequency range, $\omega > \omega_c'$, the frequency-dependence of G' decreases, which indicates that the system is unable to recover equilibrium structure on the experimental time scale, $2\pi/\omega$. Various mechanisms that may contribute to G' in this system are discussed in detail in Chapter III and IV of this dissertation. The scaling of G' for the isotropic suspensions here is attributed primarily to the limitation in rotational

freedom for $\omega > \omega_c'$. As frequency increases, the phase angle reaches a minimum, δ_n, which corresponds to the maximum solid-like response of the suspension. The magnitude of δ_n decreases weakly with concentration for the isotropic suspensions, and shows stronger scaling for the liquid crystalline suspensions reported here.

At high frequency, there is no time for the individual particles or microstructure to relax, and the linear viscoelastic response is determined purely by hydrodynamics [155]. In this case, there is a vanishing contribution associated with rotary and translational Brownian motion, and the out-of-phase viscosity, $\eta''(\omega) = G'/\omega$, tends to zero. The vanishing $\eta''(\omega)$ is consistent with the anticipated behavior of individually dispersed, infinitely rigid particles that interact only through short-range excluded volume interactions, and confirms the model nature of the ZrP suspensions.

5.3.4 Linear viscoelasticity of ZrP suspensions with smectic order

The linear viscoelastic response of the ZrP suspensions with smectic liquid crystalline order may be differentiated into two concentration regimes (Figure 5-3). For concentrations of $\phi = 1.7 – 2.8$ vol.% ZrP, the suspensions are viscoelastic fluids. At low frequency, the suspensions show viscous flow behavior characteristic of terminal relaxation of homopolymers, with $G' \propto \omega^2$ and $G'' \propto \omega$. At high frequency, there is a broad region of G' with decreased frequency dependence. The characteristic frequency separating the regions, ω_c', decreases with concentration (Table 5-1), which indicates an increase in relaxation time due to local restrictions in rotational and translational motion by neighboring particles. As concentration approaches 4 vol.%, the relaxation time

rapidly diverges, and appears to approach a constant value at higher concentration. The constant relaxation time indicates a change in relaxation mechanism associated with G', which is attributed to the increasing role of collective motion within the smectic mesophase rather than motion of individual nanoparticles, as ϕ approaches 4 vol.%.

Table 5-1. Summary of linear viscoelastic parameters for ZrP suspensions.

ϕ vol.% ZrP	ω_c' rad/s	ω_{c1}'' rad/s	ω_{c2}'' rad/s	δ_n °
0.04	4.46	0.62	1.3	87.9
0.2	2.75	0.54	2.6	85.5
0.3	2.35	0.23	1.6	84.3
0.4	2.32		3.6	84.2
1.7	1.45	0.17	5.9	64.9
2.5	0.81	0.10	7.9	48.3
2.8	0.35	0.04	12.0	35.9
3.9	0.02	~ 0.01	~ 15[b]	7.6
4.1	0.02	~ 0.01	~ 20[b]	12.1
4.3	0.03	~ 0.01	~ 35[b]	9.6
5.3	0.02		~ 40[b]	6.4
8.6	0.02		~ 40[b]	5.1

Characteristic angular frequency defining transition between viscous flow and plateau regions of G' is ω_c'; long-time and short-time relaxation modes associated with G'' are ω_{c1}'' and ω_{c2}'', respectively; minimum phase angle during SAOS measurement is δ_n. [a] Measurement without pre-shearing due to long relaxation time; [b] Value of ω_{c2}'' poorly defined and estimated by extrapolating high frequency power-law slope of G'' and intermediate frequency transition region.

The high frequency power-law slope of G' is independent of concentration, and follows scaling of $G' \sim \omega^a$, where $a = 0.35 \pm 0.04$. In this concentration regime, the magnitude of G' at high frequency is nearly independent of concentration, which is in

contrast with the typical behavior of colloidal suspensions. The power-law slope of G'' is not significantly change at high frequency, and the magnitude of G'' consistently decreases in this regime. The constant value of G' and decrease in G'' suggest that the magnitude of hydrodynamic disturbance associated with the nanoparticles decreases over a narrow range of concentration. In analogy to previous reports on liquid crystalline transitions of rod-like polymers [165], this may be tentatively attributed to an increase in regularity and organization within the smectic layers as concentration increases.

At $\phi \approx 4$ vol.% ZrP and higher, the suspensions are viscoelastic solids with dominant elastic response. At intermediate frequency, G' is weakly dependent on frequency, with power-law scaling of $a = 0.09 \pm 0.03$, independent of concentration. In the limit of low frequency, the phase angle increases, which suggests that the concentrated suspensions show fluid-like relaxation behavior on sufficiently long time scales.

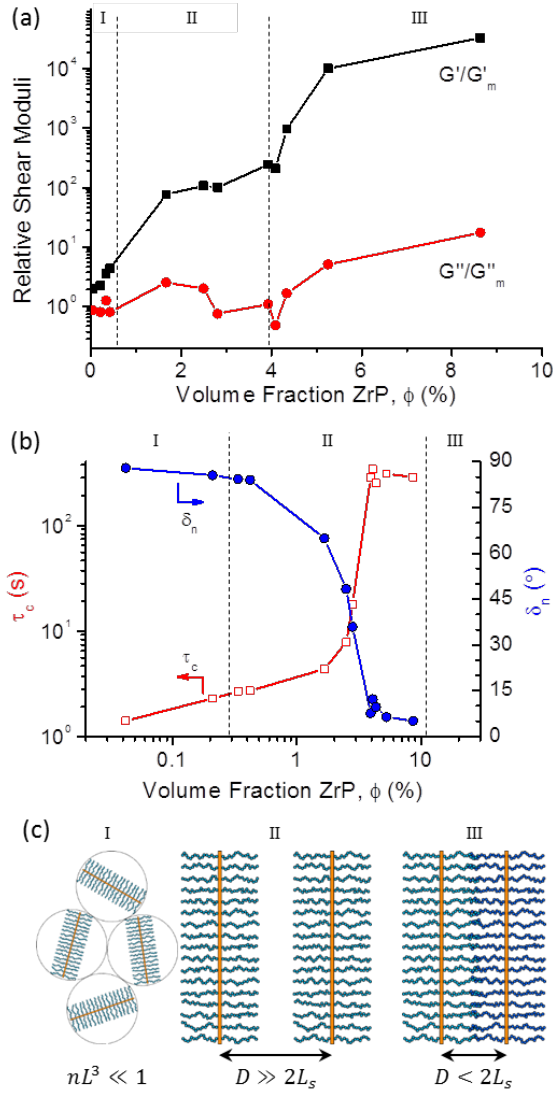

Figure 5-3. Concentration dependence of linear viscoelastic response for ZrP suspensions: (a) normalized storage modulus, G'/G'_m, and loss modulus, G''/G''_m, as function of volume fraction at $\omega = 100$ rad/s, where G'_m and G''_m are the storage and loss moduli of the unfilled epoxy matrix at 100 rad/s; (b) relaxation time, τ_c, and minimum phase angle, δ_n, of ZrP suspensions as function of volume fraction; and (c) schematic showing the proposed microstructure associated with the three regions of linear viscoelastic response. The regions correspond to (I) isotropic suspensions; (II) suspensions with smectic order and dominant fluid-like response; and (III) suspensions with smectic order and dominant solid-like response at intermediate frequency.

Compared to G', the magnitude and scaling of G'' shows much greater sensitivity to the presence of the ZrP nanoplatelets at intermediate concentrations (Figure 5-4). At $\phi = 2.8$ vol.% ZrP, the low-frequency response is similar to homopolymer-like terminal relaxation ($G'' \propto \omega$). There is a weak plateau region in G'' at intermediate frequency, and at high frequency, the power-law slope of G'' increases and approaches $G'' \propto \omega$. The high frequency scaling of G'' is primarily attributed to viscous dissipation of the epoxy monomer matrix, but may also be associated with time scales where diffusion of the individual particles within the layer structure is sufficiently localized to prevent any relaxation of perturbed microstructure.

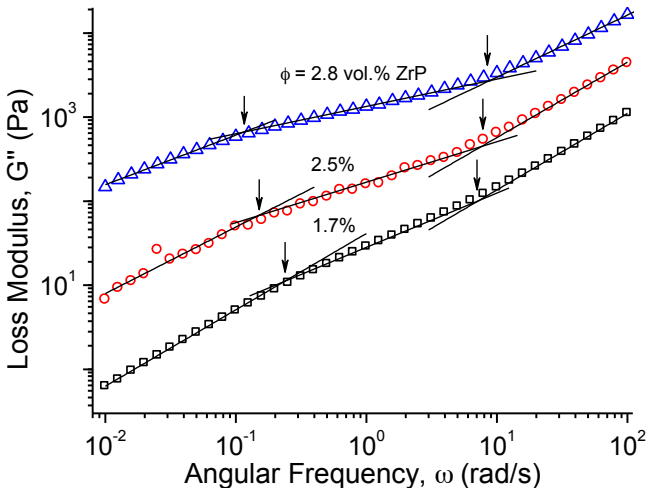

Figure 5-4. Divergence of relaxation times in G'' at intermediate concentrations, $\phi = 1.7$ – 2.8 vol.%. Curves displaced vertically for clarity.

As concentration decreases, the width of the intermediate frequency plateau region in G'' decreases. The plateau region is defined using two characteristic frequencies, ω''_{c1}

and ω''_{c2}, which represent distinct dissipative relaxation modes associated with the low-frequency and high-frequency transitions in G'', respectively. For the suspensions with $\phi = 0.3 – 2.8$ vol.% ZrP, three distinct regions of behavior are easily discerned and the transitions are determined by extrapolating a constant power-law slope in each region to a crossover frequency in the transition zone. At $\phi = 4.0$ vol.% ZrP and higher, the transition to viscous flow is not well defined in the experimental window. In this concentration regime, there is a minima in G'' for each of the suspensions, and at $\phi =$ 4.3 and 5.3 vol.% ZrP, a weak maxima is also observed. In the concentrated suspensions, the high frequency transition in G'', ω''_{c2} was estimated from the deviation in the limiting power-law region at high frequency.

At the lowest frequencies investigated in this work, the response of the suspension containing ϕ = 4.0 vol.% ZrP appears to approach a maxima in G''. Based on similar observations from suspensions that show soft glassy rheology, this suggests that the suspension is metastable [257, 258]. No aging or other characteristics of metastable structure were observed, even at much higher concentration of 8.6 vol.% over long experimental time frames. The results strongly indicate that there is a significant transition in microstructure at $\phi \approx 4$ vol.%.

The low relaxation frequency mode, ω''_{c1}, decreases approximately linearly with concentration, which indicates a progressive increase in relaxation time. The more rapid, shorter-range relaxation process observed at higher frequency, ω''_{c2}, is well described by the exponential relationship, $\omega''_{c2} \approx \exp[0.78\phi]$, and shows a strong decrease in relaxation time with concentration. The results show that increasing

concentration results in a rapid divergence in relaxation times associated with two distinct dissipative modes (Figure 5-4). The divergence of relaxation modes is also apparent in the frequency-dependence of phase angle, which shows a progressively broader minima as concentration increases (Figure 5-2b).

5.3.5 Non-linear viscoelasticity

Linear viscoelastic measurements are sensitive probes of quiescent structure, but are limited to small amplitude deformation. At amplitudes larger than the critical strain amplitude, γ_c, which defines the limit of the LVR, G' and G'' are no longer independent of strain amplitude and lose direct physical significance. The amplitude-dependence of the shear moduli is very sensitive to changes in the microstructure and interactions of the fluid. Prior to all SAOS measurements, a strain amplitude sweep was carried out to determine the LVR for each suspension. The magnitude of γ_c was determined for each suspension based on the initial decrease of G' from its value in the LVR, which generally preceded any change in G'' (Table 5-2). Several alternative definitions of γ_c were considered and yielded qualitatively similar results.

Table 5-2. Summary of non-linear viscoelastic response of ZrP suspensions.

ϕ vol.% ZrP	γ_c %	G''_{max}/G''_o
0.3	22.0	
1.7	11.8	
2.5	17.5	
2.8	8.5	
3.9[a]	6.3	
3.9	5.0	1.1
4.1	5.9	1.3
4.3	4.7	1.5
5.3[a]	4.8	1.8
8.6[a]	3.9	2.1

For suspensions with concentration of 0.3 – 4.0 vol.% ZrP, measurements made after shearing and recovery using cone-and-plate fixture. For suspensions containing 4.3 vol.% ZrP and higher, measurements made with 25 mm diameter parallel plates.
[a] Measurement without pre-shearing.

At concentration of 0.04 – 2.8 vol.% ZrP, γ_c decreases weakly with concentration, and follows power-law scaling of $\gamma_c \propto \phi^{-0.26}$. For suspensions with 3.9 – 7.2 vol.%, the decrease in γ_c with concentration is significantly increased, $\gamma_c \propto \phi^{-1.76}$, but still relatively small compared to concentrated suspensions with disordered or jammed microstructures. The measured value of γ_c was highly reproducible provided that adequate time for equilibration was allowed between measurements. In nearly all systems, the total variation of γ_c between measurements was less than the step size of the strain amplitude test. The reproducibility of γ_c indicates that the equilibrium structure associated with linear viscoelastic response is recovered following large amplitude deformation.

To compare between the ZrP suspensions, the non-linear storage and loss moduli were normalized by their respective values in the LVR, and the shear strain amplitude was normalized by $\gamma_c(\phi)$ (Figure 5-5). For all suspensions, G' gradually decreases above γ_c. For $\gamma \gg \gamma_c$, the strain amplitude dependence of G′ follows scaling of $G' \sim \gamma^{-c}$, where $c \sim 0.75$ for $\phi \leq 2.5$ vol.% ZrP. At $\phi = 2.8$ vol.% ZrP and higher, the power-law slope increases with concentration, which indicates an increase in relative strain sensitivity for the concentrated suspensions.

At $\phi = 0.04 - 2.8$ vol.% ZrP, G'' gradually decreases at slightly higher strain amplitude than γ_c. In this concentration range, there is a weak minima in G'' for $\gamma \gg \gamma_c$. The onset and depth of the minima increase with ϕ. At $\phi = 4.0$ vol.% ZrP and higher, there is a sharp change in the LAOS behavior of G''. At $\gamma/\gamma_c \approx 10$, G'' shows strain hardening and increases to a distinct peak, G''_{max}. The magnitude of G''_{max} and relative intensity, G''_{max}/G''_o, increase with concentration (Table 5-2).

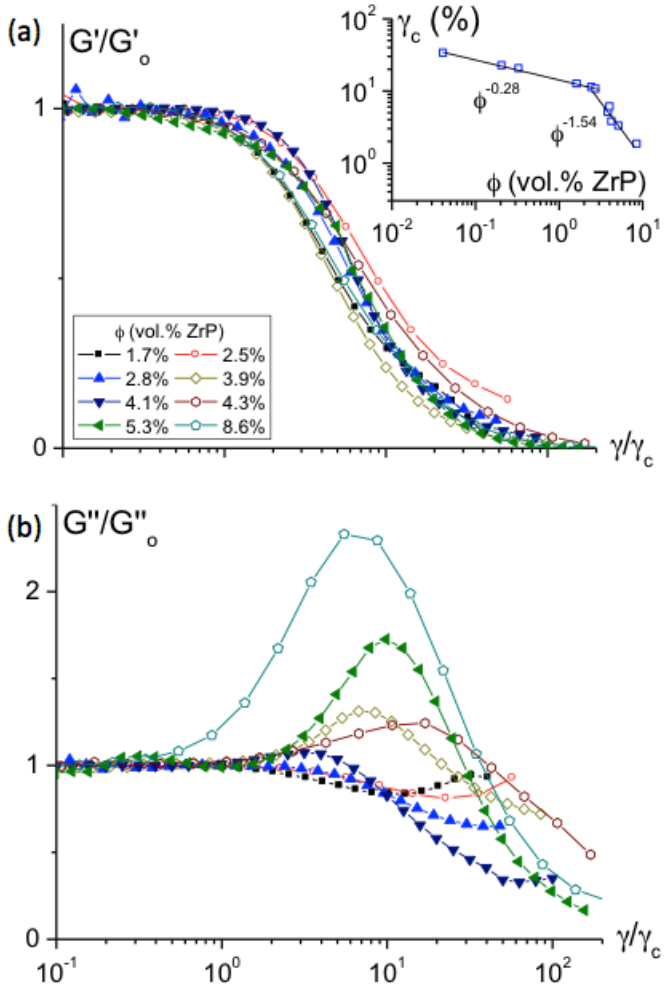

Figure 5-5. Large-amplitude oscillatory shear response of the ZrP suspensions with smectic mesophase in epoxy precursor: (a) reduced storage modulus, $G'(\gamma,\omega)/G'_o(\omega)$, and (b) reduced loss modulus, $G''(\gamma,\omega)/G''_o(\omega)$, as functions of reduced shear strain amplitude, γ/γ_c. Volume fraction of suspensions ranges from 1.7 – 7.2 vol.% ZrP. Measurements carried out at angular frequency, ω = 10 rad/s, and temperature of 25°C.

Despite the striking change in LAOS behavior observed near 4 vol.% ZrP, each of the smectic liquid crystalline suspension shows a similar, gradual transition from elastic to dissipative response in the non-linear region. The scaling for all of the smectic liquid

crystalline suspensions follows $\tan\delta = G''/G' \sim \gamma^{0.73\pm0.04}$, in the power-law region observed at $\gamma \gg \gamma_c$.

With the exception of the suspension containing 4.0 vol.% ZrP, the LAOS response is insensitive to shearing history. At $\phi = 4.0$ vol.% ZrP, the suspension exhibits strain softening in both G' and G'' prior to shearing, which is similar to the suspensions at lower concentration. After shearing, the magnitude of G' and G'' are much larger, and there is a weak strain overshoot in G''. At higher concentration, the dissipative strain overshoot becomes more pronounced. The LAOS results suggest that 4.0 vol.% ZrP is near a critical concentration that corresponds to a decoupling between elastic and dissipative components of response in non-linear viscoelasticity.

5.3.6 Steady shear

The response of the suspensions to steady shear was measured with two subsequent tests to minimize the influence of loading histories, which were found to be insignificant at intermediate shear rate in suspensions containing up to 4.0 vol.% ZrP. Up to 5 minutes of equilibration was allowed for each measurement at a fixed shear rate. As an additional control, a separate set of experiments was carried out for each suspension at a constant shear rate to determine any change of viscosity over time. The reported values are representative steady-state measurements. Transient measurements are not considered in this work. The unfilled epoxy precursor exhibits Newtonian flow properties under the experimental conditions probed in this work.

The relative viscosity, $\eta_r = \eta/\eta_m$, where η is the suspension viscosity and η_m is the viscosity of the unfilled matrix, of a representative set of ZrP suspensions are shown in Figure 5-6. The curves were fitted to the Cross equation (Eq.(2.11)), which is a useful empirical equation to describe rate-dependent flow behavior [68]. Here, η_∞ and η_o are the limiting, rate-independent viscosities at high and low shear rates, respectively, λ is a characteristic time associated with the mid-point of the shear-thinning region, $\dot{\gamma}$ is the shear rate, and n is a power-law exponent describing the magnitude of shear thinning.

In suspensions with $\phi = 0.04 – 2.5$ vol.%, the increase in viscosity at low shear rate is attributed to a yield stress, σ_y, which is clearly observed by plotting viscosity as a function of shear stress, σ (Appendix II). The magnitude of σ_y is small, < 1 Pa, for each of the suspensions, and increases weakly with concentration (Table 5-3). The onset of the yield stress region decreases with ϕ, and at $\phi = 2.8$ vol.% and higher, is not clearly observed.

The magnitudes of σ_y are consistent with visual flow observations, which indicate that yield stresses are negligibly small for suspensions with $\phi = 2.8$ vol.% and smaller. The flow of epoxy suspensions containing 4.0 and 4.3 vol.% ZrP can only be detected over a period of hours and days, respectively. At $\phi = 5.3$ vol.% ZrP, the suspension does not flow in the absence of shear over several weeks, which suggests that the quiescent structure is a gel with finite yield stress.

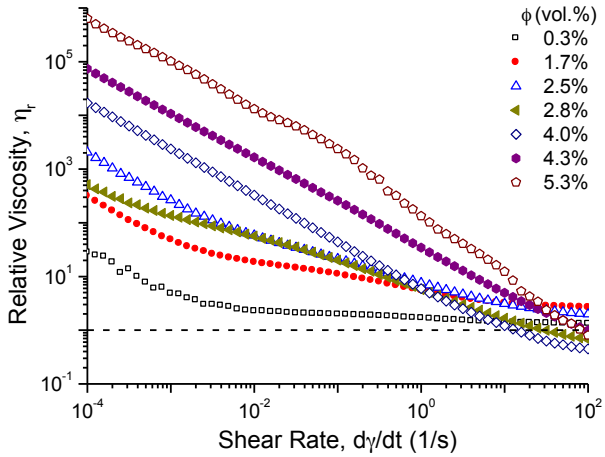

Figure 5-6. Relative viscosity of ZrP as function of shear rate, with concentration ranging from 0.04 – 7.2 vol.% ZrP. Measurements carried out at 25°C, with shear rate logarithmically decreased from 100 to 10^{-4} 1/s following pre-shearing. Up to 5 minutes equilibration time given for each measurement. Viscosity of the unfilled epoxy precursor shown by dotted line at $\eta_r = 1$.

Table 5-3. Summary of steady shear response.

ϕ vol.% ZrP	σ_y Pa	η_o Pa.s	η_∞ Pa.s	λ s	n	$\dot{\gamma}_c$ 1/s
0.3	0.01	8.1	4.9	1.3	0.07	0.10
1.7	0.11	94.6	8.5	24.1	0.57	0.03
2.5	0.21	464.6	5.6	134.3	0.57	0.01
2.8	0.05	515.8	2.5	176.3	0.65	0.002
4.1		$> 1.7 \cdot 10^4$	1.6	134.3	0.90	$< 10^{-4}$
4.3	4.7	$> 7.3 \cdot 10^4$	1.9	$5.0 \cdot 10^4$	0.86	$< 10^{-4}$
5.3[a]	4.8	$> 6.2 \cdot 10^5$		$1.3 \cdot 10^4$	0.97	$< 10^{-4}$
8.6[a]	3.9					

For suspensions with concentration of 0.3 – 4.0 vol.% ZrP, measurements made after shearing and recovery using cone-and-plate fixture. For suspensions containing 4.3 vol.% ZrP and higher, measurements made with 25 mm diameter parallel plates.
[a] Measurement without pre-shearing.

At stresses above σ_y, and shear rate below $\dot{\gamma}_c$, the suspensions containing up to 2.8 vol.% ZrP show a low shear rate plateau region, with rate-independent viscosity of η_o. Although the plateau region is narrow and poorly defined in some suspensions, the magnitude of η_o is consistent between measurements, and in good agreement with SAOS measurements of zero-frequency dynamic viscosity, η_o', which support the assignment. At $\phi = 4.0$ vol.% ZrP and higher, the shear thinning region extends to the lowest shear rates probed, which obscures clear identification of any low shear rate plateau region. The results suggest that the magnitude of η_o increases rapidly with concentration. However, the significant decrease in $\dot{\gamma}_c$ in the concentrated suspensions limits meaningful quantitative description of the concentration-dependence of η_o.

In the isotropic suspension, there is an observable transition to shear thinning, $\dot{\gamma}_c$, at shear rate of ~ 0.1 1/s, but $n \approx 0$, which indicates nearly Newtonian flow properties. In the smectic suspensions with $\phi = 1.7 – 2.8$ vol.%, the transition to shear thinning decreases with concentration, and the degree of shear-thinning is much larger than in the isotropic suspension ($n \approx 0.6 – 0.7$). At $\phi = 4.0$ vol.% ZrP and higher, the transition to shear thinning is outside of the experimental range, $\dot{\gamma}_c < 10^{-4}$ 1/s, and the degree of shear thinning is significantly increased, with $n \approx 0.9 – 0.95$.

In the high shear rate region, the limiting viscosity increases with concentration up to $\phi = 1.7$ vol.% ZrP, and decreases with further increase in concentration. At $\phi = 2.8$ vol.% and higher, the high shear rate viscosity is less than that of the unfilled epoxy matrix. The trend is surprising, given the large magnitude of η_o and the considerable size and concentration of the nanoparticles. The decrease in high shear rate viscosity

was observed with both parallel plate and cone and plate geometries, and after varying the gap diameter of the parallel plate fixtures. There was no change in gap distance or temperature during the measurement, and the behavior does not appear to be an artifact or due to any measurement instability. As an additional control experiment, the epoxy was filled with a concentration of M1000 equivalent to the grafted content at 4.0 vol.% ZrP. The epoxy/M1000 suspension behaves as a Newtonian fluid, and the viscosity is slightly larger than the unfilled epoxy matrix, with $\eta_r = 1.35$. However, this observation is not necessarily representative of the rheological behavior of the oligomers here, which is densely grafted to the nanoplatelet surfaces. Based on the change in G'' at high frequency with concentration (Figure 5-3a), it is clear that there is a complex relationship between the purely hydrodynamic perturbation caused by the ZrP nanoplatelets and concentration.

5.4 Discussion

Controlling mesoscale organization of nanoparticles into higher-order structures offers substantial opportunities to substantially modify a diverse combination of material properties across distinct length scales. However, the parameters governing spatial dispersion and organization, and how the nanoscale and mesoscale features relate to a desired set of macroscale properties, are not well understood, especially for high aspect ratio nanoparticles. Model systems with well-defined particle-level properties and longer-range microstructure are needed to generalize experimental findings and elucidate clear structure-property relationships relevant to nanoparticle-filled materials.

In this work, we provide the first detailed rheological investigation of a smectic liquid crystal formed from the self-assembly of model high aspect ratio plate-like nanoparticles in epoxy monomer. The most striking feature is the rapid transition in rheological behavior near $\phi = 4$ vol.% ZrP. At lower concentrations, the smectic liquid crystals in epoxy are viscoelastic liquids, and show well-defined terminal relaxation at low frequency. In the non-linear region, the suspensions show gradual strain softening in both G' and G''. Both steady shear, the suspensions display a negligible yield stress and moderate shear thinning. The high frequency elastic response is nearly independent of concentration, and G'' decreases weakly. At high frequency, the measurements reflect localized length scales and the interactions between particles are minimal [173]. The limited change in high-frequency viscoelastic response indicates that for the smectic liquid crystals containing $\phi = 1.7 – 2.8$ vol.% ZrP, incorporating additional nanoplatelets does not increase the magnitude of hydrodynamic distortion in the fluid phase. This unique behavior is attributed to the uniform integration of the nanoplatelets within the layer structure of the smectic mesophase. More detailed description of the decrease in hydrodynamic perturbation in this region requires investigation of local ZrP surface brush features under equilibrium and non-equilibrium conditions, and is being pursued.

Above the critical concentration near 4 vol.% ZrP, the suspensions show dominant solid-like response at intermediate frequency. In the limit of low frequency, the suspensions show liquid-like behavior (Figure 5-3b), which indicates that the network responsible for elastic response at intermediate frequencies is transient and able to relax

over the experimental time scale. In the non-linear viscoelastic region, the concentrated suspensions show a weak strain overshoot in G''. Weak strain overshoot in G'' with gradual softening in G' has been observed for a diverse variety of soft materials, but no transition in response is generally reported. The transition in LAOS behavior here suggests the presence of a mechanism associated with enhanced dissipative response that increases with concentration. During steady shear, the concentrated smectic suspensions show an extremely large degree of shear thinning and at high shear rate show a viscosity similar to, or less than, the unfilled epoxy monomer matrix.

The unique rheological behaviors observed here are not typical of concentrated suspensions of plate-like nanoparticles with short-range geometric order. The unique flow behavior observed here is attributed to interactions between layers of the smectic microstructure (Figure 5-1c). The exfoliated ZrP nanoplatelets are ordered in discrete smectic layers with regular inter-layer spacing, D, and random order within the layers [187]. At low concentration, the distance between layers is much greater than the length of the brush layers extended from the surface of adjacent nanoplatelets, $D \gg 2L_s$. In this case, the layers of the smectic mesophase behave independently and fluid flow occurs predominantly in the suspending fluid layer confined between surface-attached brushes [259]. As concentration increases, lubrication interactions between the oligomer chains in the brush layers become more significant and modify the distribution of normal and shear forces in the system during deformation. At $D \sim 2L_s$, the surface-attached brushes begin to overlap and the suspending fluid is forced to flow through the brush network,

which results in additional forces associated with the viscous drag of the suspending liquid through the brush network [259].

Assuming that the rheological behavior is primarily due to brush-mediated interactions, the critical concentration associated with the transition in rheological response, ϕ^*, will occur when the distance between the approaching brush layers is zero, i.e. at $D = 2L_s$. The critical concentration may be estimated from a simple model of an ideal lamellar mesophase, with geometric parameters shown in Figure 5-1. We assume that the length of the extended oligomer brush layer is $L_s = 8$ nm, and that the osmotic pressure between adjacent grafted oligomers is sufficient to prevent significant coiling or collapse of the chains as the nanoplatelet surfaces approach. The latter assumption may be relaxed with more detailed investigation of interactions within the mesophase structure. The repeat unit of the layer structure consists of two square half-platelets, with length and width of L, and thickness of $t_{ZrP}/2$. The platelets are aligned and separated by a distance of D. Neglecting the edge-to-edge distance between nanoplatelets within each layer, the volume of the unit cell is $V_c = L^2(t_{ZrP} + D)$, and the volume occupied by the 2 individual half-platelets is $V_p = L^2 t_{ZrP}$. The volume fraction of the platelets is $\phi = V_p/V_c = t_{ZrP}/[t_{ZrP} + D]$. At the overlap concentration, $D = 2L_s$, the volume fraction is

$$\phi^* = \left(1 + \frac{2L_s}{t_{ZrP}}\right)^{-1} \tag{5.1}$$

For L_s = 8 nm and t_{ZrP} = 0.69 nm, the critical concentration is ϕ^* = 4.1 vol.% ZrP, which agrees well with the observed transition in rheological response.

The simple lamellar model may be used to predict the concentration-dependent change in inter-layer spacing of the smectic mesophase by rearranging Eqn. (5.1):

(5.2) $$D = t_{ZrP}\left(\frac{1-\phi}{\phi}\right)$$

The prior SAXS investigations provide measurements of the center-to-center distance between smectic layers [187], denoted D_{SAXS}, and may be related to the inter-layer distance defined in Figure 5-1b by $D = D_{SAXS} - t_{ZrP}$. The lamellar model again provides excellent agreement with the SAXS measurements for suspensions with concentration up to 4 vol.% ZrP (Table 5-4). The disagreement between the model and SAXS measurements occurs at concentrations above the overlap transition, i.e., for $D < 2L_s$, where additional factors related to the conformation of chains and packing between layers cannot be neglected.

Table 5-4. Concentration-dependent change in inter-layer separation for smectic mesophase.

ϕ vol.% ZrP	D_{SAXS}[a] nm	D (Model)[b] nm	$D/2L_s$[b]
0.3		229.3	14.33
1.7	31.5	39.9	2.49
2.5	21.9	26.9	1.68
2.8	17.8	24.0	1.50
4.0	16.4	16.6	1.04
4.3	4.7	15.4	0.96
7.2	5.3	12.3	0.77

Calculations made assuming platelet thickness of $t_{ZrP} = 0.69$ nm and M1000 brush layer length of $L_s = 8$ nm. [a] Distance between platelet surfaces, D, calculated from prior synchrotron-source SAXS measurements using relation $D = D_{SAXS} - t_{ZrP}$. [b] Calculated from (5.2).

The agreement between SAXS measurements and the simple lamellar model suggests that for $\phi = 1.7 – 2.8$ vol.% ZrP, the organization of nanoplatelets in the layer structure is regular and independent of concentration, which is consistent with the proposed interpretation of the high-frequency measurements of G' and G'' (Figure 5-3a). In this concentration regime, the low-frequency increase in G' and G'' is attributed to fluctuations in mesophase structure and flow-dependent interactions at the interface between the non-overlapping oligomer brushes. If the lateral diameter of the nanoplatelets, L, is significantly larger than the separation between layers, i.e. $L \gg D \gg 2L_s$, normal lubrication forces will oppose any decrease in inter-layer separation during deformation [259]. The magnitude of lubrication forces is proportional to the relative velocity of the approaching surfaces. Increasing frequency is therefore anticipated to proportionally increase the repulsive hydrodynamic forces separating the mesophase layers, and may be responsible for the scaling of elastic response of the suspensions with non-overlapping brush layers.

The transition in rheological response at $\phi = 4.0$ vol.% ZrP and higher is attributed to the interaction and overlap of the brush layers. In the overlapping region, flow of the viscous matrix is confined within the brush layers, which introduces additional dissipative forces during deformation. In polymer brushes, excluded volume effects at the interface between the ends of the surface-attached polymers chains prevent strong interpenetration of the chains, and results in a fluid interface with extremely low friction coefficient [260]. The low shear rate at the onset of shear thinning and extreme degree of shear thinning observed here are attributed to the weak interpenetration of the brush

layer. In this concentration range, the divergence of relaxation times indicates that on the time scale of the experiments, the system may be significantly out of equilibrium. The conformation and length of the oligomer chains may change due to the substantial normal forces between layers as $D/2L_s$ approaches unity. These factors may contribute to the discrepancies between expected and measured values of D in Table 5-4. Any non-uniform distribution of smectic layers within the fluid will further invalidate the assumptions of the simple model.

Several additional mechanisms may also be present and merit further investigation. The local dynamics and relaxation behavior of the epoxy precursor and grafted brush layers will be modified due to crowding and confinement for small separations between layers. Previous experimental and numerical investigations have shown that a transition to solid-like behavior occurs in simple fluids confined to length scales of ~ 6 molecular units or less [259]. The equilibrium radius of gyration of the epoxy monomer molecules utilized here is estimated to be ~ 1.4 nm using molecular dynamics simulation. Based on the simple lamellar model derived in Eq. (5.3), epoxy molecules restricted to the region between brush layers, given by $D - 2L_s$, will begin to exhibit confined behavior at concentrations of ~ 2.8 vol.% ZrP. This estimate neglects any penetration of the matrix phase into the brush layer, but suggests that the deviations in steady shear behavior observed at low shear rate for the suspensions containing $\phi = 2.8$ vol.% ZrP may originate, in part, from molecular-scale confinement of the epoxy monomer and M1000 oligomer phases. In the more concentrated suspensions, the confined matrix molecules may form an ordered interface, which provides a mechanism for the observed decrease

in viscosity below that of the unfilled matrix at moderate shear rate. Further work is needed to elucidate the nature and significance of the complicated mechanisms of interaction at the interfacial region between layers.

In most layer-forming small molecules and LCPs, the linear viscoelastic response is predominantly solid-like, and no transition to viscous flow is observed at extremely low frequency. The non-terminal response is due to the significant concentration of immobile defects throughout the layered structure [255, 261]. In this work, the mesogens are colloidal particles with length and width substantially larger than the length scale of localized defects. The mesogens are not physically connected and therefore retain individual translational freedom on small length scales, and possibly also limited rotational freedom. The length scale and relative freedom of motion are likely responsible for the decrease in significance of detectable defects observed in this work.

In many systems, gelation or jamming limits introduction of high concentration of non-spherical nanoparticles in a media of interest [233]. The rheological behavior of the colloidal smectic liquid crystals reported here shows that if long-range order prevails, the concentration of nanoparticles may be significantly increased without negatively influencing processability at moderate levels of shear. The use of model 2-dimensional nanoparticles is anticipated to motivate further theoretical and experimental works to better understand the origins of phase behavior for colloidal liquid crystals, and guide progress regarding the thermodynamically driven organization of nanoparticles.

5.5 Conclusions

We have investigated the rheological response of model suspensions containing high aspect ratio, sterically stabilized nanoplatelets that exhibit smectic liquid crystalline order over a range of concentrations in epoxy monomer. At low concentration, the smectic liquid crystals behave as viscoelastic fluids. At low frequency, the suspensions show viscous flow response, and the shear moduli increase weakly with concentration. At high frequency, the storage modulus is independent of concentration, and loss modulus decreases. At concentration of 4.0 vol.% ZrP and higher, there is a sharp transition in response to a viscoelastic solid, although a transition to fluid-like response is retained at low frequency. Large-amplitude oscillatory shear and steady shear measurements both indicate a significant change in response at this concentration. It is proposed that the primary mechanism responsible for the change in behavior is the overlapping of the brush layer and associated changes in the dynamics and ordering of the matrix and brushes caused by molecular-scale confinement. The suspensions with $\phi = 4.0$ vol.% ZrP and higher are processable and show viscosity similar to the unfilled matrix at moderate shear rates. The use of a model nanoparticle system provides an opportunity to study fundamental relationships involving phase transitions of 2-dimensional materials. The findings are anticipated to aid in elucidating mechanisms responsible for transitions in other smectic systems because of the diminished role of molecular-scale defects on flow response.

CHAPTER VI

RHEOLOGY OF STABLE SUSPENSIONS CONTAINING DISENTANGLED MULTI-WALLED CARBON NANOTUBES IN EPOXY PRECURSOR

6.1 Introduction

Multi-walled carbon nanotubes (MWCNTs) are high aspect ratio, fiber-like nanoparticles, that show an exceptional combination of mechanical [262, 263], electrical [264-266], and thermal properties [267-271]. However, individual MWCNTs tend to aggregate into mechanically cohesive flocs that are challenging to disperse without damaging the nanoparticle structure or modifying its ability to interact with the matrix. As a result, it is challenging to clearly attribute macroscale properties of a polymer nanocomposite to particle-level attributes. Recently, Bauhofer et al. [272] showed that even if MWCNT clusters are adequately dispersed in the polymer matrix through mechanical processing, the properties of the nanocomposite tend to be recover with time and approach a limiting value independent of the initial dispersion state. This finding, and others that reported similar convergence of properties after treatment [273-275], suggest that most approaches to integrate MWCNTs in polymeric or fluid media result in a thermodynamically unstable dispersion state.

One major consequence of the lack of processing methods suitable to achieve a stable dispersion is that the majority of experimental results reflect properties of the nanoparticle clusters rather than the individual nanoparticles. It is not likely that individual dispersion will be necessary for most applications, and in some situations,

controlled degree of aggregation has been reported to provide a desirable combination of properties [52, 56, 227, 228]. If the aggregate structure is relatively well defined and reproducible, this type of self-assembling system may provide a useful route to tailor properties across length scales [16]. However, unambiguous relationships between particle-level properties and desired macroscale response cannot be reasonably developed in these cases. Fundamental structure-property relationships are needed to identify mechanisms responsible for change in bulk response, and to guide approaches to most effectively utilize this unique class of nanoparticles.

In this work, as-received MWCNTs are disentangled to individual nanoparticles by reacting nanotubes with 4-nitroaniline in acetonitrile solution. The recovered functionalized MWCNTs (F-MWCNTs) are decorated with nitrobenzene, and are uniformly dispersed in organic solvent as individual nanoparticles. The F-MWCNTs remain disentangled after dispersion in epoxy, and are shown to be uniformly dispersed in solid epoxy nanocomposites at 1 wt.% concentration. The rheological behavior is compared with the response of suspensions containing clustered MWCNTs to show the role of individual nanoparticles in the fluid response. Ongoing work is focused on relating these properties to processing conditions and behavior in solid-state nanocomposites. An epoxy monomer matrix was used because of its good stability and limited reactivity with the MWCNTs at elevated temperature, which enables application of time-temperature superposition to identify changes in relaxation behavior. The monomer has sufficient viscosity to introduce significant hydrodynamic stresses during shearing. Any change in dynamics or organization of the matrix at the interface should

be negligible at concentrations investigated in this work, and the size difference between the MWCNTs and the epoxy monomers should be sufficient to neglect any finite size effects. The flow properties of nanoparticle-filled epoxies are of practical importance because of their widespread use in resin transfer molding (RTM) and coating applications [228, 276-278]. Partial curing studies may potentially be carried out to dynamically modify the length-scale and configurational freedom of the epoxy molecules, and provide more direct connection between liquid and solid state properties.

6.2 Experimental

6.2.1 Materials

MWCNTs (Sigma-Aldrich) with 5-15 graphene wall average, >90% carbon basis, 2-6 nm inner diameter, 10-15 nm outer diameter, and length 0.1-10 μm were suspended inside of a diglycidyl ether of bisphenol F (DGEBF) epoxy monomer, EPIKOTE™ 862 (Hexion Specialty Chemicals, Inc.). Sigma-Aldrich reported the MWCNT density to be 2.1 g/cm^3.

6.2.2 Treatment and dispersion of clustered MWCNTs

Suspensions of clustered MWCNTs were prepared following the procedure described in our previous work [227]. The as-received MWCNTs were dispersed in acetone by ultrasonication for one hour. The epoxy monomer was added to the mixture and dissolved at room temperature. The mixture was sonicated for 15 minutes and dried

by rotary evaporation at 80°C. Samples were collected and dried in a vacuum oven overnight to remove any remaining solvent.

6.2.3 Functionalization and dispersion of exfoliated MWCNTs

As-received MWCNTs were pre-treated in a mixture of concentrated sulfuric and nitric acids (3:1 ratio by volume) in a sonication bath (Branson 2510) for 1.5 hr at room temperature. DI water was then added to dilute the acid solution, and the mixture was sonicated for an additional 2 hr. Oxidized MWCNTs (O-MWCNTs) were isolated using a polyvinylidene difluoride (PVDF) filter membrane (Millipore, 0.45 μm pore size) under vacuum, and were washed several times with DI water until the pH was nearly neutral. Seventy mg O-MWCNT was mixed in 140 mL SDBS aqueous solution (1 wt.%) and sonicated for 4 hr at room temperature. After sonication, the SDBS/O-MWCNT solution was added to a homogeneous solution of 140 mL acetonitrile containing 3 g nitroaniline. Under nitrogen atmosphere, 3 mL isoamyl nitrite was slowly added dropwise to the solution. The mixture was heated to 70°C and mechanically stirred for 12 hrs. The mixture was filtered and washed with DI water and acetone several times. The resulting MWCNTs, referred to here as functionalized MWCNT (F-MWCNTs), were re-dispersed in acetone at concentration of 0.5 mg/mL. The epoxy monomer was added to the acetone/F-MWCNT solution at room temperature to achieve desired concentration. The mixture was sonicated for 15 minutes and dried by rotary evaporation at 80°C. Samples were collected and dried in a vacuum oven overnight to remove any remaining solvent.

6.2.4 Characterization

Thermogravimetric analysis (TGA) of samples was carried out in nitrogen atmosphere using a Q500-TGA from TA instruments. The ramp rate was 10°C/min. Fourier transform infrared spectroscopy in attenuated total reflectance mode (FTIR-ATR) was performed using a Nicolet Avatar 360. The absorbance was measured between 1000 and 4000 cm^{-1}, with resolution of 4 cm^{-1}.

The morphology of the modified MWCNTs in acetone solution was investigated using an Olympus BX60 optical microscope (OM). Solid epoxy nanocomposites were prepared to using the same curing procedure as previously reported [227]. The dispersion and degree of disentanglement of the F-MWCNTs was investigated using a Technai T20 computerized transmission electron microscope (TEM) operating at an accelerating voltage of 200 kV. The cured epoxy nanocomposite contained 1.1 wt.% F-MWCNTs. TEM thin sections, with thickness of about 100 nm, were prepared using a Reichert-Jung Ultracut E microtome with diamond knife.

Rheology measurements were carried out using the same equipment and testing conditions described in Chapter III.

6.3 Results

6.3.1 Functionalization of MWCNTs and dispersion in epoxy

Chemical oxidation with strong acids is a common method used to purify and disperse MWCNTs. However, to achieve suitable degree of dispersion, extensive treatment at elevated temperatures is usually required, which may compromise the

structure and physical properties of the nanotubes. Here, the oxidative treatment was carried out under moderate conditions, which we previously reported preserves the structural integrity and electrical properties of the MWCNTs [51-54]. The oxidized MWCNTs were functionalized by reacting with isoamyl nitrite in acetonitrile solvent (Figure 6-1).

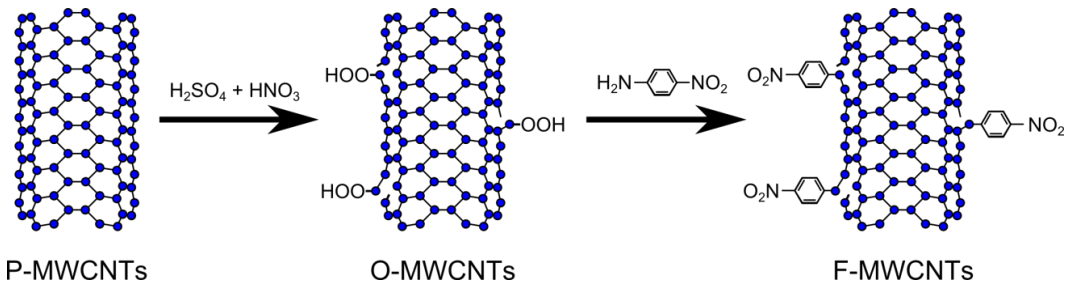

Figure 6-1. Schematic illustrating functionalization route for MWCNTs used in this work. The untreated MWCNTs are initially oxidized to introduce reactive sites. The O-MWCNTs are reacted with 4-nitroaniline. The recovered F-MWCNTs contain nitrobenzene functional groups along sidewall, and are easily dispersed in acetone and other organic media as individual nanoparticles.

The dispersion and stability of the MWCNTs in organic solvent is significantly improved after functionalization. From visual and optical microscopy inspect, the F-MWCNTs appear to be homogeneously dispersed in acetone, and there is no observable precipitation after 2 days (Figure 6-2a). For the untreated MWCNTs, significant phase separation is observed minutes after sonication (Figure 6-2b). The detail morphology and dispersion state of the F-MWCNTs were analyzed with TEM (Figure 6-2c). The samples were prepared by drop-drying from acetone solution, and show that the F-

MWCNTs are dispersed to the individual level without observable damage or decrease in length.

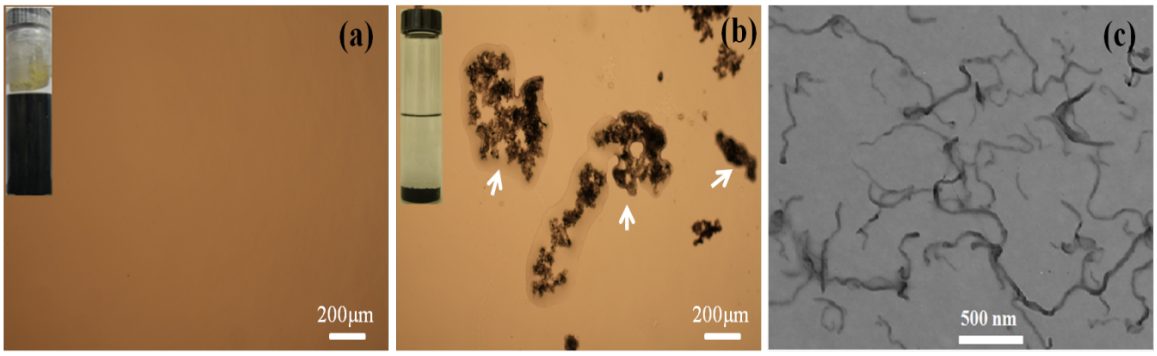

Figure 6-2. OM images of (a) functionalized and (b) untreated MWCNTs in acetone. Inset are photographs of MWCNT dispersions after sitting for 2 days. White arrows highlight aggregated MWCNTs. (c) TEM of functionalized MWCNTs obtained by drop-drying from acetone solution.

FTIR-ATR was used to identify the presence of functional groups on the MWCNT surface following the reaction (Figure 6-3a). The functionalities were identified by comparing the absorption spectra of the F-MWCNTs with untreated MWCNTs. The absorption spectra of O-MWCNTs prepared with the same oxidative treatment has been previously reported [56], and detailed discussion regarding the absorbance of oxidized MWCNTs is provided by Shaffer et al. [279]. The spectrum of the F-MWCNTs prepared here shows distinct absorbance peaks at ~ 1512 and 1342 cm^{-1}, which are consistent with the dominant IR peaks for nitrobenzene [280-282]. The sharp peak at 1512 cm^{-1} is assigned to the asymmetric stretching of NO2, and ring stretching of the benzene. The second pronounced peak at 1342 cm^{-1} is assigned to symmetric stretching

of NO_2 groups. The absorbance peaks of the F-MWCNTs indicate that there is an amidation reaction between the carboxylic acid functionalities on the MWCNTs and the isoamyl nitrite, and the nitrobenzene functionality is covalently grafted to the nanotube sidewalls. The concentration of functionalities was estimated using TGA (Figure 6-3b). The untreated MWCNTs show no significant weight loss upon heating up to 800°C in N_2 atmosphere. For the O-MWCNTs, a mass loss of ~ 7 wt.% is observed, and attributed to the decomposition of oxidized species. The F-MWCNTs show much larger mass loss, ~ 23 wt.%, which confirms that a large concentration of functional groups are present. The concentration of functional groups is estimated from the mass loss to be roughly 1 nitrobenzene functionality per 52 carbon atoms.

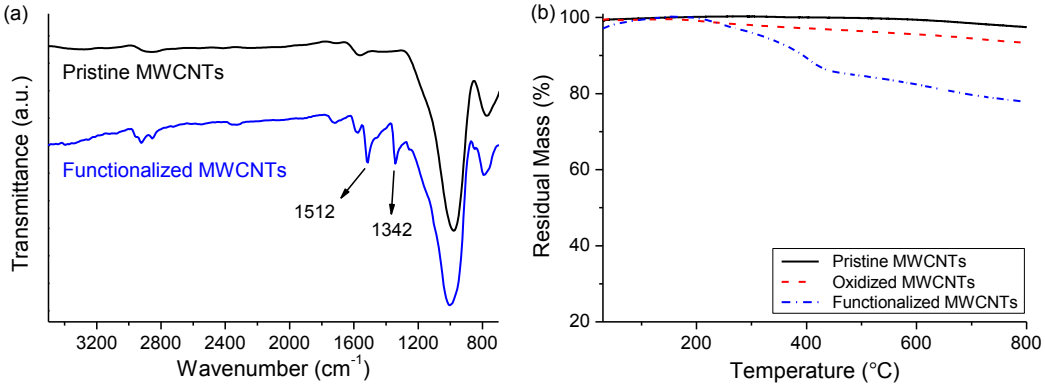

Figure 6-3. (a) FTIR-ATR spectra of pristine MWCNTs and F-MWCNTs. (b) Thermogravimetric degradation curves of pristine, oxidized, and F-MWCNTs.

The F-MWCNTs were transferred to an epoxy matrix without any visible aggregation or change in dispersion state. Solid epoxy nanocomposites were prepared at

relatively high concentration, 1.1 wt.%, and analyzed with TEM (Figure 6-4). Previous studies found that untreated and oxidized MWCNTs are highly entangled and poorly dispersed on the individual level at similar concentrations [56, 227]. The micrographs show that the F-MWCNTs are fully disentangled in the epoxy. Individually dispersed, high aspect ratio MWCNTs are observed to be well distributed throughout the system, and there is no evidence of heterogeneities, entanglements, or reduction in nanotube length. The micrograph in Figure 6-4is representative of the observed dispersion state throughout the system.

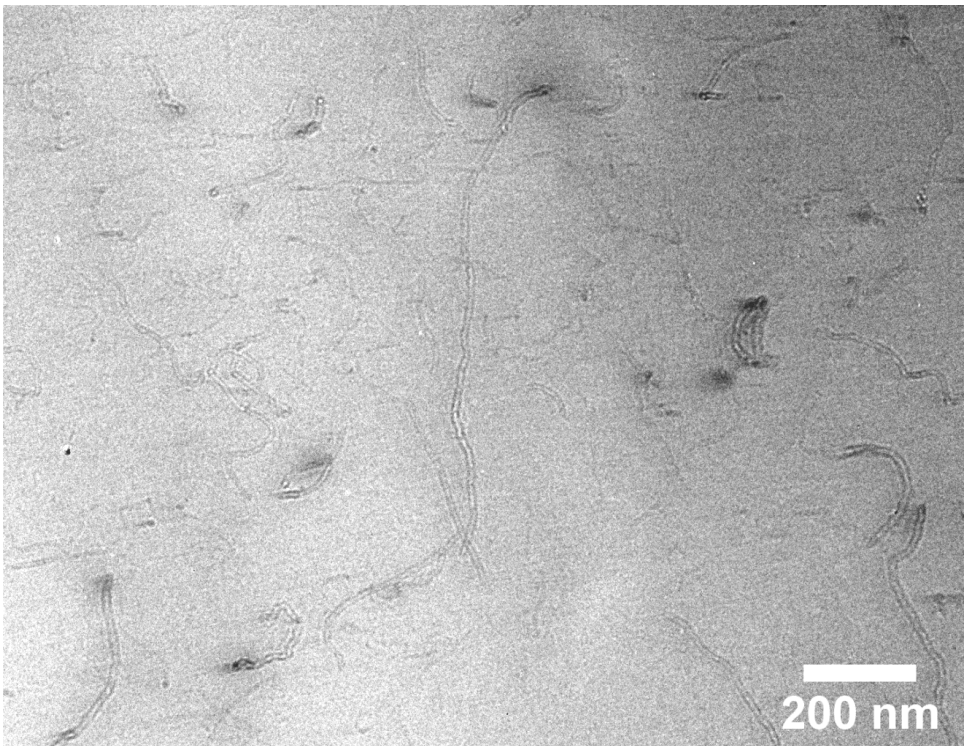

Figure 6-4. TEM of solid epoxy/F-MWCNT (1.1 wt.%) nanocomposite.

The F-MWCNTs prepared here show excellent dispersion and stability, even after long curing time in a low viscosity fluid (~ 4 hr cure). The results suggest that the covalently reacted nitrobenzene functionalities provide sufficient repulsion sufficient to prevent the formation of flocculated MWCNT aggregates. The stability is likely related to the steric repulsion of the bulky functional groups. It is challenging to directly evaluate the nature of inter-particle interaction using most characterization methods. Here, we use rheology as a probe to investigate the microstructure and interactions of the dispersed MWCNTs.

6.3.2 Linear viscoelasticity

An initial series of investigations were carried out on the rheological response of untreated MWCNTs. Pristine MWCNTs (P-MWCNTs) were dispersed in acetone by brief sonication at room temperature. The epoxy monomer was dissolved in the acetone/MWCNT mixture, and the mixture was slowly dried with a rotary evaporator. This dispersion approach follows our previous work, which showed that the sonicated P-MWCNTs assemble into space-filling, conductive network at ~ 0.1 wt.%, consisting large, clustered aggregates [227, 228]. The clustered network appears to represent the equilibrium structure for most MWCNT systems [272-275, 283, 284], and therefore provides a useful reference for discussion of the behavior of exfoliated MWCNTs.

Suspensions of P-MWCNTs were prepared with mass fraction, c varied out 4 decades, from 0.001 – 10 wt.%. At low concentration, $c \approx 0.001 – 0.09$ wt.%, the systems are visually homogeneous and settle over a period of a few hours. Although

OM studies show that the MWCNTs are clustered on the micron scale (not shown), there is no discernible change in fluid properties up to mass fraction, c, of 0.09 wt.%. At c ~ 0.1 wt.%, there is a drastic change in behavior. Large clusters are observed in the solution and adhere to walls of the vial. As concentration increases, there is no longer clear visible heterogeneity due to the density and light absorption of the systems. At ~ 2 wt.%, the systems no longer flow and behave as gels. For these systems, viscoelastic measurements were carried out by removing the samples with a razor blade and manually loading the fixtures. At 5 and 10 wt.%, the gels were not able to be compressed by vertical displacement of the transducer at room temperature (maximum normal force of 2000 g). These suspensions are strong gels with an apparent bulk modulus, and were only able to be loaded by increasing temperature to 120°C and applying a constant compressive axial force, combined with steady shearing deformation at low shear rate. The qualitative trend of behavior is similar to earlier reports [279], and shows that that the nature of response observed here is an appropriate baseline for discussion of clustered structure.

The linear viscoelastic response of several representative P-MWCNT suspensions is shown in Figure 6-5. The storage modulus, G', is a measure of the ability of a material to store strain energy and recover original shape during oscillatory deformation, and corresponds to solid-like response. For relatively dilute systems, G' increases weakly with concentration, and is most significant at low frequency. At ~ 0.2 wt.%, there is an inflection in G' at intermediate frequency, and in the limit of low frequency, a limiting plateau modulus, G_o, is present. As concentration increases, the power-law slope of G'

progressively decreases, and the plateau region extends to higher frequency. The magnitude of G_o increases weakly with concentration up to ~ 1 wt.%. At higher concentration, G' is relatively independent of frequency over the experimental range, and G_o rapidly diverges with concentration. The divergence in elastic response is characteristic of a sol-gel transition [285, 286].

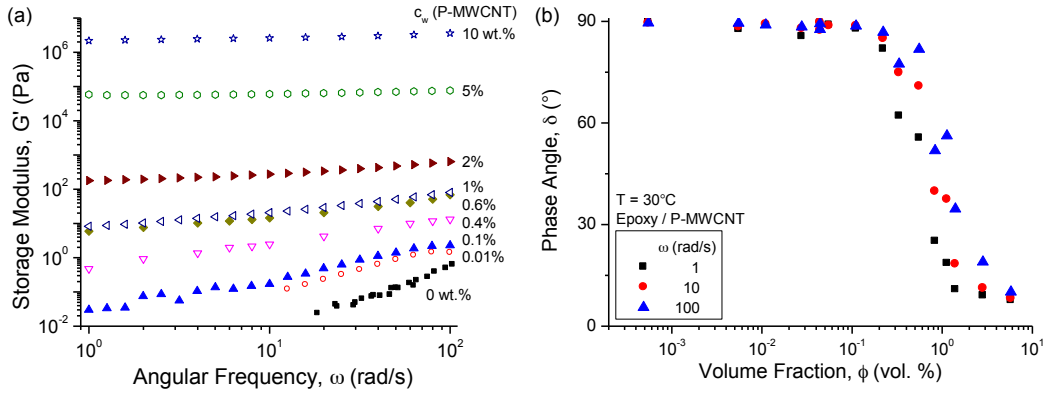

Figure 6-5. Linear viscoelasticity of clustered MWCNT suspensions in epoxy. (a) Storage modulus, G', as function of angular frequency, ω, for MWCNT suspensions with mass fraction, c, ranging from 0.01 – 10 wt.%. (b) Phase angle, δ, as function of volume fraction, ϕ, for measurements at angular frequencies of 1, 50, and 100 rad/s. Measurements at 30°C.

The transition behavior can be clearly observed from the change in phase angle, δ, with volume fraction, ϕ (Figure 6-5b). The volume fraction was calculated assuming the density of the MWCNTs is equal to bulk graphite, $\rho \approx 2.1$ g/cm^3. The phase angle is a characteristic measure of relative liquid-like or solid-like response, and ranges from 90° for an ideal Newtonian liquid, to 0° for an ideal Hookean solid. There is a clear change in behavior from predominantly Newtonian response at $\phi \approx 0.1$ vol.% (≈ 0.2

wt.%). Above this limit, δ decreases with concentration, and is most significant at low frequency. At the highest concentration, $\phi = 0.055$ vol.%, $\delta \approx 10°$, independent of frequency, and the system behaves as a solid material.

The linear viscoelasticity of MWCNT suspensions has been reported for a range of systems considering different treatment methods, and for Newtonian and non-Newtonian media [273, 287-294]. The prior reports are consistent with the trends reported in Figure 6-5. The most distinctive feature of the linear viscoelastic response is the low-frequency plateau in G', which is observed here for P-MWCNT loadings of ~ 0.2 wt.% and higher. This behavior indicates that the suspension is unable to relax and recover liquid-like response on the experimental time scale.

Suspensions containing the disentangled F-MWCNTs were prepared at concentrations of 0.1, 0.5, and 1.0 wt.%. The linear viscoelastic response of the F-MWCNT suspensions is shown in Figure 6-6. Each of the systems shows similar response, which indicates that there is no transition in microstructure with concentration. The magnitude of G' and G'' increase with concentration, and there appear to be three regions of frequency in G'. In the limit of high and low frequency, the scaling of G' is approximately linear with frequency. At intermediate concentration, there is a narrow region with lower frequency dependence. It is difficult to differentiate between the regions due to the noise in G' for the lower concentration systems, but it is clear that the transition between the low frequency and intermediate frequency regions, designated ω_c, increases with concentration.

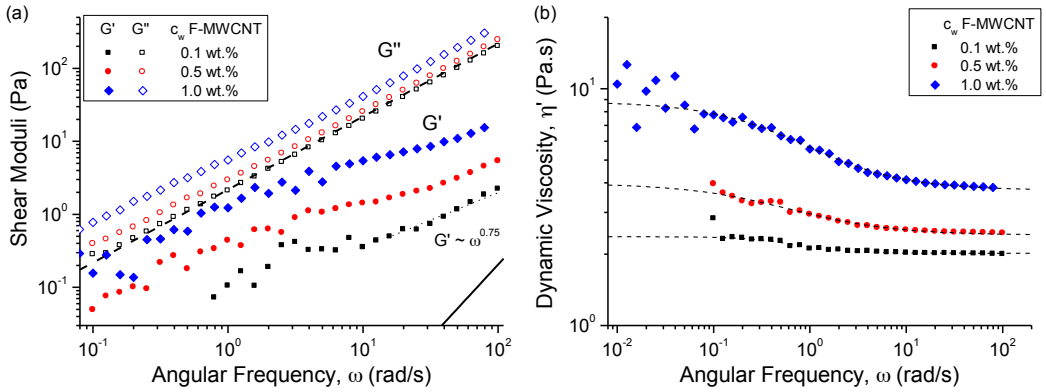

Figure 6-6. Linear viscoelasticity of disentangled MWCNT suspensions. (a) Storage modulus, G' (filled) and loss modulus, G'' (unfilled) as functions of angular frequency, ω, for 0.1, 0.5, and 1.0 wt.% F-MWCNT. (b) Dynamic viscosity, $\eta' = G''/\omega$, as function of complex modulus. Lines in (a) show response of unfilled epoxy matrix. Dotted lines in (b) fitted to Cross equation, Eqn. (2.11). Measurements at T = 30°C.

Closer inspection also reveals three regions of frequency behavior in G''. At high and low frequency, $G''\sim\omega$, which indicates that the dynamic viscosity, given by $\eta'(\omega) = G''/\omega$, is constant. The zero frequency and infinite frequency dynamic viscosities are defined by $\eta'_o = \lim_{\omega\to 0}\eta'$ and $\eta'_\infty = \lim_{\omega\to\infty}\eta'$, and shown in Figure 6-6b. The dynamic viscosity provides useful information about the relative contributions of Brownian motion and hydrodynamic interactions for the equilibrium structure. In the limit of zero frequency, both Brownian motion and hydrodynamic interactions are present and make distinct contributions to viscous dissipation that are linear with frequency. In the limit of high frequency, the time scale of oscillation is too rapid for significant Brownian motion to occur, and η'_∞ reflects only hydrodynamic contributions [63]. Each of the F-MWCNT systems show a clear transition to a high frequency plateau region with constant dynamic viscosity η'_∞. There appears to be a

low-frequency region for each concentration as well. However, as a result of small variations in measurement of G'', the noise in $\eta' = G''/\omega$ is significant at low frequency and it is difficult to clearly tell if there is a limiting plateau. The magnitudes of limiting dynamic viscosity may be fit using the Cross equation [68], which is given in Eq. (2.11). The parameters for the F-MWCNT systems are given in Table 6-1.

Table 6-1. Summary of parameters for dynamic viscosities from linear viscoelastic measurements.

c	η'_o	η'_∞	λ	n
wt.%	Pa.s	Pa.s		
0.1	2.37	2.02	1.45	1.66
0.5	3.98	2.41	2.19	0.79
1.0	8.80	3.73	1.80	0.85

c is mass fraction; η'_o and η'_∞ and zero-frequency and infinite-frequency dynamic viscosities; λ and n are the time constant and degree of shear thinning obtained from the Cross equation fit. Measurements at T = 30°C on pre-sheared samples.

The shear moduli, G' and G'', are useful measurements of the magnitude and scaling behavior of suspensions. However, both parameters are derived from the magnitude of complex modulus, $|G^*|$, and phase angle, and are therefore inter-related. As a result, it is challenging to clearly determine subtle changes in relaxation behavior based on these quantities alone. Van Gurp and Palmen [190] showed that plotting $\delta = f(|G^*|)$ provides a temperature-independent representation to compare between sets of data. The original approach was proposed for validation of the application of time-temperature superposition [191]. In this dissertation, we have shown that it also a very sensitive to the concentration and relaxation processes of the dispersed nanoparticles.

The vGP representation of linear viscoelasticity of the F-MWCNT systems is shown in Figure 6-7. High values of $|G^*|$ correspond to high frequency and low temperature measurements, and reflect localized, short-range processes dominated by hydrodynamic interactions. As $|G^*|$ decreases, the relaxation behavior reflects slower, longer-range processes. For the F-MWCNT suspensions, the curves are similar at all concentrations. There is an approach to a plateau region of $\delta \approx 90°$ at high $|G^*|$, and a progressive decrease in δ on longer time scales. There is a shift in the curve to higher $|G^*|$ and lower δ with concentration. At 1 wt.%, there is a minima at $\delta_n \approx 75°$. The minima in phase angle approaches 90° for decreasing concentration, which agrees with behavior of ZrP nanoplatelets suspensions in Chapters III-V. There is some noise in this value due to the low magnitude of oscillation stress at the corresponding low frequency.

Additional measurements at higher temperature were carried out and showed similar δ_n (Figure 6-7b), which indicate the existence of a minima rather than a plateau. The relaxation behavior clearly shows a transition to viscous flow behavior at low frequency, and confirms that there is no longer-range microstructure associated with the MWCNT phase. In contrast, the P-MWCNT systems above the transition concentration show a sharp shift in vGP behavior to higher $|G^*|$ and lower δ, and show no change in slope at lower $|G^*|$. This corresponds to a progressive increase in solid-like response on longer time scales, and shows the dominant role of elastic stresses within the clustered network. This observation fits with the proposed mechanism for elastic instabilities suggested by Lin-Gibson et al. [287]. The robustness of this claim is considered in detail below.

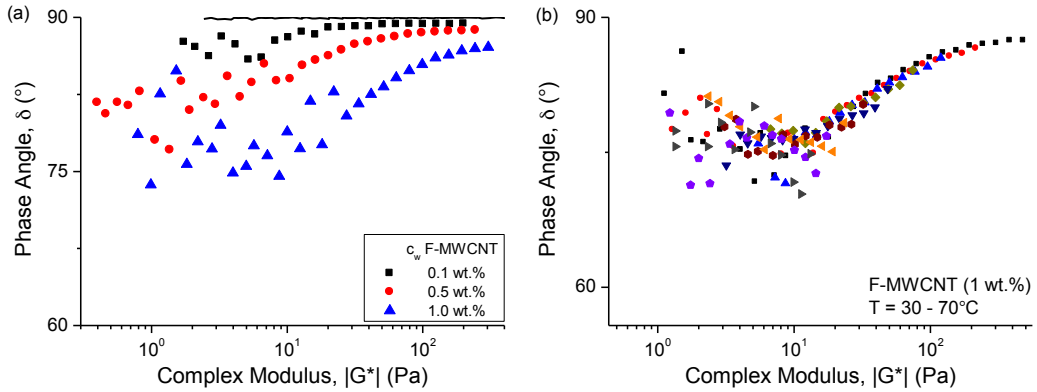

Figure 6-7. Relaxation behavior of disentangled MWCNT suspensions. (a) Phase angle, δ, plotted as function of complex modulus, $|G^*|$ (vGP plot), for 0.1, 0.5, and 1.0 wt.% F-MWCNT. Lines show response of unfilled epoxy matrix. Values correspond to measurements in Figure 6-6. (b) vGP plot for 1.0 wt.% F-MWCNT showing measurements at range of temperatures. No shift factor used to account for temperature effects.

The concentration dependence of storage modulus and loss modulus at high-frequency for are shown in Figure 6-8 for the untreated and functionalized MWCNTs. Both shear moduli are normalized by measurements at 0.005 wt.% P-MWCNT for clarity. The scaling behavior is not affected by the normalization. In the suspensions containing P-MWCNTs at low concentration, there is a weak increase in storage modulus and negligible change in loss modulus with concentration. At $\phi \approx 0.2$ vol.%, there is a divergence in G', which scales with ϕ^4. At slightly higher concentration, $\phi \approx$ 0.6 vol.% (1 wt.%), G'' diverges with smaller power-law exponent, ϕ^3. The significance of the power-law exponents and related percolation-type behavior has been discussed at length in prior works and will not be considered here. The F-MWCNT systems do not show the same divergence, and appear to increase at a lower rate. More detailed range of concentrations is necessary to determine if the behavior reflects an

increase in threshold for sol-gel transition, or if there is a change in the network formation behavior in the system. Given the results discussed so far, it is more likely that the latter is true.

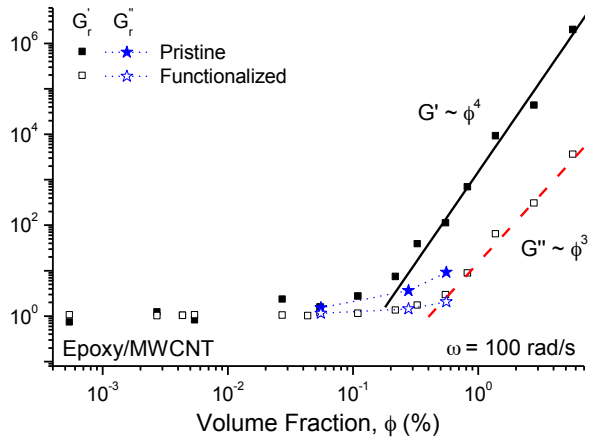

Figure 6-8. High-frequency normalized shear moduli as functions of volume fraction, ϕ, for pristine and functionalized MWCNT suspensions in epoxy. Measurements at T = 30°C. Moduli normalized by G' and G'' for epoxy/P-MWCNT (0.005 wt.%). Lines are power-law fits to scaling of storage modulus (solid) and loss modulus (dashed) in concentrated P-MWCNT systems. Dotted lines are meant to guide eye for F-MWCNT suspensions, which do not show same divergence.

At low concentration, the F-MWCNT systems shows nearly identical G' and G'' as the P-MWCNT at all frequencies. At 1 wt.%, significant differences are present that relate to the transition in microstructure for the untreated MWCNTs. However, the magnitude of differences show considerable frequency dependence and in the limit of high frequency, G'' is nearly independent of dispersion state.

The differences in linear viscoelastic response in this concentration range were investigated by carrying out measurements over a range of temperatures. Time-

temperature superposition was carried out by independently determining time and stress shift factors, a_T and b_T, based on the discussion provided by Dealy [191]. The significance of the shift factors is discussed below. The linear viscoelastic master curve for the P-MWCNT and F-MWCNT suspensions at 1 wt.% is shown Figure 6-9.

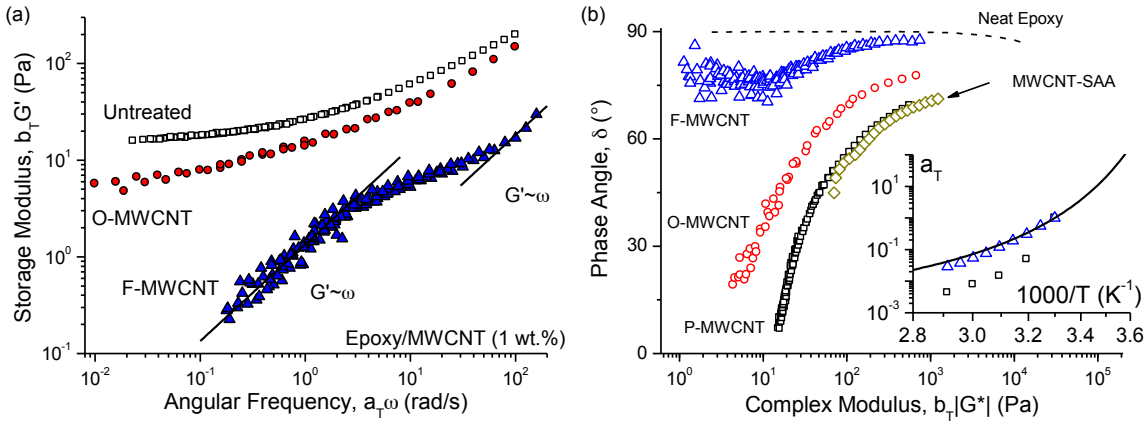

Figure 6-9. (a) Linear viscoelastic master curves for suspensions containing 1 wt.% MWCNTs in different dispersion states. Solid line shows limiting scaling of disentangled F-MWCNT system at high and low frequency, $G' \sim \omega$. (b) Corresponding vGP plots for same systems. Dotted line shows response of unfilled epoxy. Inset is horizontal shift factor for time-temperature superposition, a_T. Solid line is WLF fit to unfilled epoxy. Symbols in inset same as (b).

The storage modulus of the suspension containing untreated MWCNTs is largest, with clearly defined low-frequency plateau and high-frequency scaling of $\omega^{0.75}$, which has been previously observed and related to elasticity in an entanglement-like network [290, 292]. The oxidized MWCNTs show much better dispersion, but only slightly reduced G'. The difference is largest at low frequency, which may indicate that the long-range network is more significantly disrupted than the short-range microstructure.

For the F-MWCNT system, the measurements obtained over a range of temperatures are consistent with the room temperature measurements, and are consistent with the presence of transient elasticity due to the motion and interaction of individual nanotubes. The high-frequency scaling behavior of the three systems is similar, and may relate the internal modes of flexibility for the F-MWCNTs. Nanotubes have high modulus, but flexibility decreases strongly with aspect ratio ($\propto r_p^{-4}$). This indicates that the high frequency measurements correspond to behavior on length scales corresponding to the individual nanotubes, and is consistent with the similar magnitudes of G'' observed, which show that the magnitude of hydrodynamic disturbance between the systems are similar.

The vGP plots shown in Figure 6-9b are consistent with the discussion above. The relaxation behavior of the F-MWCNTs here is distinct from the effect of chemical oxidation alone. An additional system is included where the MWCNTs are oxidized and functionalized with sulfanilamide, MWCNT-SAA. The functionalization route is identical to that described by [277], and results in significantly improved dispersion state. However, there is apparently no significant change in the nature of inter-particle interaction for this system.

For the unfilled epoxy and F-MWCNT systems, no stress shift factor, b_T was used to obtain time-temperature superposition. It is possible that the fit could be improved somewhat at lower frequency with the additional shift factor to account for the change in matrix density, but the fit was acceptable with $b_T = 1$ for temperatures between 30 and 70°C. For the untreated and oxidized MWCNTs, a stress shift factor was required,

which indicates the presence of an additional temperature-dependent mechanism associated with the nanoparticle network. The magnitude of the time shift factor is also larger for the untreated MWCNTs. For the F-MWCNTs, a_T is nearly identical to the unfilled matrix (Figure 6-9b).

6.3.3 Steady shear response of MWCNT suspensions

The steady shear response of the F-MWCNT suspensions is shown in Figure 6-10. The shear viscosity, $\eta(\dot{\gamma})$, and dynamic viscosity, $\eta'(\omega)$, are in excellent agreement for the suspensions at 0.1 and 0.5 wt.% at all shear rates. The agreement between viscosity measurements obtained under small amplitude oscillatory deformation and steady shearing is commonly referred to as the empirical Cox-Merz law, and does not have specific physical implications. The correlation indicates that the relationship between structure and rate are the same for the weakly and strongly perturbed microstructure, which suggests that there is no significant breakdown or change in microstructure. Here, the superposition is regarded as evidence of a recoverable microstructure with Brownian-dominated processes at low rates of deformation, and hydrodynamically-dominated behavior at high rates.

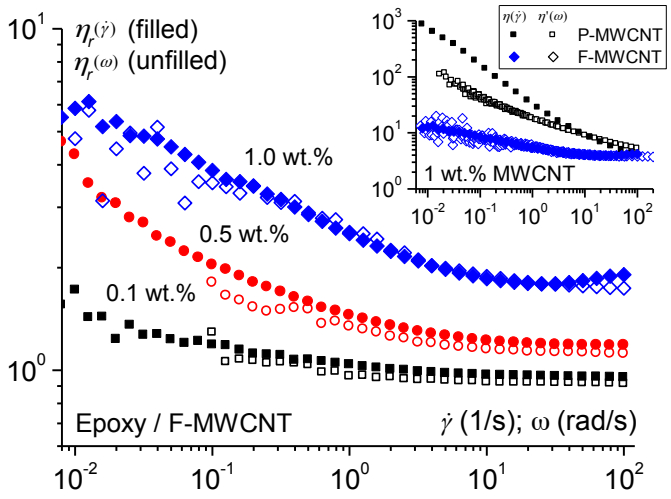

Figure 6-10. Cox-Merz plot for F-MWCNT suspensions. Steady shear viscosity, $\dot{\gamma}$, and dynamic viscosity, $\eta' = G''/\omega$, of the F-MWCNT suspensions in epoxy plotted as functions of shear rate, $\dot{\gamma}$, and angular frequency, ω, respectively. Inset shows Cox-Merz plot P-MWCNT and F-MWCNT suspensions at 1 wt.%, with dynamic viscosity obtained using linear viscoelastic master curves.

For the 1 wt.% system, there is good agreement with the Cox-Merz rule for all measurements except at high shear rate. During steady shear, the system shows shear thickening behavior over consecutive measurements independent of the direction of shear rate sweeps, with equilibration time of 30s, or for shear rate ramps. The significance of the shear thickening behavior is considered in the discussion.

The steady shear response of the P-MWCNT and F-MWCNT systems at concentration of 1 wt.% are shown in the inset of Figure 6-10. The dynamic viscosity from the linear viscoelastic master curves are also shown. The P-MWCNT shows nearly identical viscosity to the disentangled system at high shear rates. As shear rate decreases, there is a significant increase in viscosity. The size of the flocculated structure results from a dynamic equilibrium of attractive forces and hydrodynamic

stresses, which is consistent with the behavior observed here, and indicates that the MWCNTs are broken down to the individual level at high shear rates.

6.4 Discussion

The objective of this work has been to identify the influence of individual MWCNTs on the rheological behavior of a system. We have shown evidence that the MWCNTs are disentangled and do not flocculate over time. The lack of a low-frequency plateau in G' and divergence at high concentration are consistent with the expected behavior of initial, high aspect ratio fillers at semi-dilute concentrations. Some additional features are also observed that merit further consideration.

In the absence of significant colloidal interaction, the rate-dependent properties of a suspension of solid, rigid particles are predominantly governed by the balance between Brownian motion and hydrodynamic stresses. For non-spherical particles, Brownian motion has two effects. First, it randomizes the position and orientation of the particles, which provides measurements that are independent of initial conditions. The second is that there are additional viscous and elastic stresses due to Brownian torques. The significance of Brownian motion is determined by the rotary Peclet number, $Pe = \dot{\gamma}/D_r$, where D_r is the rotary diffusion coefficient of the suspended phase. For rods, the rotary diffusion in an infinitely dilute suspension may be approximated by

$$D_{r,o} = 3k_BT\frac{\ln(r_p)-0.8}{\pi\eta_m L^3} \tag{6.1}$$

where k_BT is the thermal energy in the system. For a suspension containing MWCNTs with $L \approx 1$ μm and $r_p = 100$, at 30°C, $D_{r,o} \sim 7\times10^{-3}$ 1/s, which indicates that

Brownian motion will not be significant for the frequency range reported here at 30°C. For the 0.5 and 1.0 wt.% system, predictions based on infinite dilution are not appropriate. Corrections to account for semi-dilute concentration reflect the increase in confinement due to neighboring particles, which should decrease rotary diffusion even further.

One potential explanation is that the MWCNTs do not have aspect ratio of 100, as expected. The TEM evidence shows direct evidence of MWCNTs with length ~ 1 μm, but it is challenging to clearly identify the original size distribution due to the aggregation. Assuming that the aspect ratio is 50, and average length is $L = 500$ nm, $D_{r,o} \approx 4.5\times10^{-2}$ 1/s. There is an order of magnitude increase, but this is significantly smaller than the observed transition at $\omega_c \sim 7$ rad/s.

An alternative explanation is that the relaxation behavior is due to the rotational motion of the individual nanoparticles. In the case of Brownian motion acting to randomize the orientation and positional distribution of the non-spherical particles, the relevant time scale for elastic response should be for $\omega_c > D_r$. For low frequencies, the microstructure is able to fully relax during the time scale of oscillatory deformation and there is no change in free energy. In contrast, if the MWCNTs are assumed to be rigid rods that are subjected to Brownian torques, then the elasticity should increase linearly with frequency up to $\omega \sim \tau_{rot}$, which is the relaxation time for end-over-end rotation. This mechanism is strictly relevant for infinitely dilute suspensions, but the low-frequency range of behavior is not sensitive to inter-particle interactions and should be

reasonable for higher concentrations [164]. Based on Yamakawa's model for cylinders [163], assuming high aspect ratio, the rotation time is

$$\tau_o = \frac{\pi \eta_m L^3}{18 k_B T \ln(r_p)} \tag{6.2}$$

Returning to the original assumption of $L \approx 1$ μm and $r_p \approx 100$, the rotation time at 30°C is $\tau_o \approx 20$ s. For $\omega \tau_{rot} \approx 1$, G' increases up to a maximum, and there is an inflection in G''. This suggests that there should be an inflection in response at $\omega \approx 0.05$ rad/s, with no increase in G' due to rotation at higher frequency, and $G' \propto \omega$ below. For $r_p = 50$, the plateau is expected at $\omega \approx 0.3$ rad/s. This is consistent with the behavior of the 0.1 wt.% system. At concentration increases, an increase in the frequency at the intermediate plateau region was observed. This suggests a decrease in relaxation time, which is not consistent with cage models or other approaches to account for suppressed rotational diffusivity. From the perspective of the individual rod rotating, there are a number of reports that have found the hydrodynamic interaction in the semi-dilute concentration range increases the rate of fiber flipping and tumbling during shearing deformation. It should be reasonable to assume that these hydrodynamic contributions may enhance the time-scale for end-over-end rotation, and account for the observed concentration behavior.

This argument also accounts for the Cox-Merz rule providing excellent agreement. From $D_{r,o}$, it is clear that the response of the system is in the hydrodynamically dominated region and the effects of Brownian motion will be minor. However, the shear thinning may reflect the shift in orientation distribution into the flow direction. In this

case, there will be a high shear rate plateau associated with the time scale where rotational motion of the particles is no longer significant. This explanation should loosely account for the phenomenological agreement, and should be promising to more directly investigation with additional experiments and numerical approaches.

The final feature of the system that merits discussion is the observed shear thickening in the 1.0 wt.% F-MWCNT system at high shear rate. To probe the time scale associated with the transition, additional measurements were carried out at higher temperature (Figure 6-11). The shear thickening behavior was consistently observed up to 50°C, where it was no longer within the experimental range due to the increase in shear rate at the transition with temperature. The measurements were reduced using the rotary Peclet number, with rotary diffusion coefficient given by Eq. (6.1). Scaling by D_r provided excellent superposition of the in individual measurements.

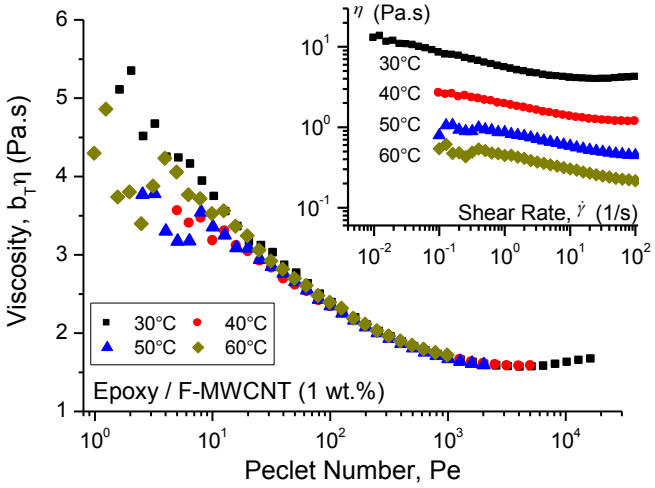

Figure 6-11. Shear thickening of disentangled MWCNTs in epoxy monomer at 1.0 wt.% concentration. (a) Raw measurements, with critical stress for onset of shear thickening shown. (b) Shifted shear viscosity as function of Peclet number.

Shear thickening is generally associated with a system-wide instability, such as the disruption of a layered structure, or the hydrodynamic compression of deformable spheres [76, 77]. In this system, the MWCNTs are individually dispersed and disentangled, which indicates that there is no mesoscale structure or organization, and the shear thickening should be related to the individual MWCNTs. One possible explanation is that there is a change in shape of the MWCNTs due to shear-induced stresses. The relevant shear rate for deformation of an individual MWCNT during simple shearing may be estimated from the dimensionless bending stiffness proposed by Forgacs and Mason [110, 133]. Assuming that the suspended MWCNTs are extended fibers, the dimensionless bending stiffness is given by

(6.3) $$BS = E_Y \pi / \eta_m \dot{\gamma} r_p^4$$

The dimensionless bending stiffness decreases with shear rate, and for $BS \ll 1$, the rigidity of the fibers is less than the magnitude of viscous shear stresses, and the fibers will tend to buckle due to compressional stresses experienced during steady shear. Here, the Young's modulus of the MWCNTs is on the order of 50 GPa, and the aspect ratio assumed to be $r_p \approx 100$. At shear rate of $\dot{\gamma}$ = 100 1/s, the dimensionless bending stiffness is 0.09 at T = 30°C. This indicates that viscous stresses are dominant and the fibers aligned in the shearing plane will tend to deform during shearing. The shear rate where $BS \approx 1$ is at $\dot{\gamma}^*$ = 8.96 1/s, which is in excellent agreement with the observed transition to shear thickening behavior for the epoxy/F-MWCNT (1 wt.%) suspension. From Eqn. (6.3), it is also apparent that the bending stiffness will increase with temperature, due to the decrease in viscosity, which is consistent with the observations. The deformation of the MWCNTs above a critical shear rate will alter the period of rotation for the individual particles, and change its orbit distribution. As a result, the microstructure in the vicinity of the particle is disoriented. The system should be able to recover from this distortion rapidly, which accounts for the weak nature of the thickening behavior. To our knowledge, this behavior has not been previously reported for suspensions of fiber-like particles, which suggests that there may be some degree of local organization in the system.

The rheological results presented here show that the functionalization approach used to obtain disentangled MWCNTs results in a stable structure that prevents flocculation. The similarity in high frequency measurements is indirect evidence that suggests there is no significant damage or reduction in length. In many applications, unique properties

have been reported due to the formation of an controlled MWCNT aggregate structure [225, 227, 228, 295]. In these cases, an individual, stable dispersion may be not desired. However, in many systems, the MWCNTs modify the properties of the surrounding matrix, and individually dispersed structure are preferable for maximum effect at low concentration [52, 56, 57]. For fundamental studies, the individual structure also allows distinction between clustered and individual MWCNTs to be determined.

6.5 Conclusions

This work has investigated the evolution of rheological and viscoelastic response of clustered and disentangled MWCNTs dispersed in a stable, non-reaction Newtonian matrix. The rheological behavior of the clustered MWCNTs showed strong rate-dependent behavior. The development of linear viscoelastic and steady shear response in the suspension containing individually dispersed, functionalized MWCNTs was significantly suppressed, and characteristic Brownian relaxation behavior was observed at low frequency. Characteristic features of the disentangled MWCNTs were a lack of low-frequency plateau in storage modulus and shear thickening at high shear rate. The behavior of the disentangled MWCNTs is in agreement with continuum-level predictions based on the motion of individual, semi-flexible fibers under shearing flows.

CHAPTER VII

RHEOLOGICAL INVESTIGATION OF UNUSUAL REINFORCEMENT ROLE OF ELECTROSTATICALLY TETHERED NANOPLATELETS AND CARBON NANOTUBE HYBRIDS IN GLASSY EPOXY

7.1 Introduction

Micron-sized fillers modify the mechanical properties of a polymer through either direct reinforcement due to load transfer, or through indirect changes in the behavior of the surrounding matrix. In composites reinforced with micrometer-diameter fibers, load transfer across a continuous interface between phases is the principal mechanism for mechanical reinforcement. The change in properties is due to the replacement of the matrix material with an equivalent volume of a reinforcing phase that has some desired set of properties. Simple rule-of-mixtures approaches, with various refinements, are often sufficient to describe the composite properties [169].

The formation of an interphase region with modified properties is a well-known phenomenon observed with micron-scale fibers [296-299]. For example, the reinforcing fiber surface may be able to induce a high density of crystal nuclei, which results in the formation of an oriented transcrystalline domain extending normal to the fiber surface [299]. The interphase region has different mechanical properties than the bulk resin due to the distinct transcrystalline morphology, and in some cases, has been reported to improve mechanical properties of the composite [296, 297, 300]. Coatings are often used to improve interfacial adhesion or environmental stability of fibers. The thin coating

layer has more compliant properties than the fiber and may be regarded as an interphase. In general, the size of the interphase is typically much smaller than the diameter of the micron-scale fibers, and only influences local properties, such as interfacial adhesion. The interphase effects of isolated micrometer-scale fibers may be sufficiently accounted for with a three-phase continuum model, or by defining boundary conditions with a compliant interface [301].

For nanometer-scale particles, the mechanisms responsible for changes in properties are very poorly understood [7]. There are significant experimental challenges related to controlling dispersion and interactions of nanoparticles that undermine unambiguous investigation of structure-property relationships. In many cases, the change in bulk properties is interpreted using continuum-level approaches, without strong regard for the relevant physics associated with behavior. For example, based on predictions from continuum-level micro-mechanical models, the incorporation of high aspect ratio nanoparticles with excellent mechanical properties, such as carbon nanotubes (CNTs), should provide remarkable improvement in modulus and strength at extremely low loadings. Using continuum-level predictions of the Mori-Tanaka model, Liu and Brinson showed that the addition of only 2.5 vol.% SWCNT, aspect ratio of 1,000, with random in-plane orientation will increase Young's modulus by 5 times [302]. If the SWCNTs are aligned in the tensile direction, more than 15 times improvement is predicted. The reported behavior of nanoparticle-filled polymers often falls well below predictions from these models.

In some cases, the change in properties deviates dramatically from expectations developed for micron-scale particles. For epoxy containing clustered MWCNTs, we found that strength and ductility are enhanced relative to the unfilled matrix, but the modulus is not affected [227]. The change in mechanical properties is in sharp contrast to direct load-transfer mechanisms, and was attributed to the formation of a coherent microstructure containing individual MWCNTs [227, 228]. The size scale of the aggregate structure is sufficiently small to avoid acting as a stress concentration site, but was proposed to be able to modify the distribution of stresses in the glassy epoxy matrix. Several other reports have found surprising changes in composite behavior that cannot reasonably be attributed to the behavior of the individual particles alone [56, 57, 303-305]. Significant change in behavior at extremely low concentration is often due to long-range changes in morphology or dynamics of the bulk matrix due to the presence of the nanoparticle phase.

The indirect contribution of nanoparticles may be substantial at low concentration, because the volume of the interphase is comparable or even larger than the particle volume in some cases. The size scale of interest depends on the features of the polymer matrix and the property of interest. For electrical conductivity, effective charge transport between conductive particles separated by an insulating matrix may occur through hopping or tunneling processes on the order of a few nanometers [306]. High aspect ratio, rigid nanoparticles may perturb modify conformation of polymer coils, which influences behavior on the length scale of the polymer radius of gyration. In the case of nanoparticle-induced crystallization, significant changes in morphology may be

introduced several microns away from the isolated particle. From these examples, it is clear that there is significant potential to modify the behavior of polymers across a range of length scales, which results in a substantial amplification effect of the particle influence. Depending on the details of the particular system, it may be possible to introduce a global change in properties due to the surface area and interphase effects with very low concentrations of nanoparticles [57].

A number of potential reinforcement mechanisms have been proposed to describe the influence of nanoparticles on the surrounding matrix. Many of the effects have been reviewed by Jancar et al. [7]. In amorphous thermoplastic polymers, the principal reinforcing mechanism appears to be segmental immobilization of adsorbed polymer chains at the surface of the nanoparticles [307]. In this case, the influence of the nanoparticle on polymer chain dynamics may extend several times the radius of gyration of the host polymers. Several reports have shown changes in the density and glass transition temperature of the polymer near the interphase region [7]. A single high molecular weight chains may adsorb onto several isolated nanoparticles. In this case, the nanoparticles will exhibit cooperative motion at extremely low loadings, which has been proposed to be responsible for a jamming-like transition in viscoelastic response. Nanoparticles may also be able to act as temporary or permanent entanglements in high molecular weight systems, which results in a transient network [215]. These reinforcement mechanisms are based on non-local effects of the nanoparticle phase due to processes mediated by the matrix phase. In polymers where the characteristic length

scale for motion or relaxation is extremely small, such as amorphous polymers in the glassy state, these mechanisms should not be effective.

A number of reports have found that nanoscale particles show much better reinforcing efficiency than an equal concentration of micron-scale particles in rubbery systems. However, below the glass transition temperature, the superior reinforcing efficiency is no longer present, and the composite modulus is independent of particle size. For example, several early computational and experimental studies showed excellent interaction between epoxy molecules and CNTs [308, 309], and found substantial property improvements of epoxies in rubbery state [310-312]. However, the performance of CNT-filled epoxies in the glassy state shows moderate or negligible improvements in general. Liu and Wagner [313] investigated the mechanical properties of covalently functionalized MWCNTs in an epoxy cured using two different curing agents, to provide a direct comparison between rubbery and glassy systems. In the rubbery epoxy nanocomposites, the mechanical properties were drastically improved relative to the neat epoxy, and showed better performance than the system containing untreated MWCNTs. At 1 wt.% loading, the modulus, tensile strength, and elongation at break were improved by ~ 30%, 100%, and 60%, respectively. However, in the glassy epoxy, there was negligible change (<5%) in in mechanical properties, and no significant difference between treated and untreated nanotubes. Ci et al. [314] investigated effect of the matrix modulus on the reinforcing efficiency of MWCNTs by preparing nanocomposites with non-stoichiometric ratios of curing agent and incomplete curing schedules. At a fixed volume fraction of MWCNTs, the composite Young's modulus

and tensile strength decrease monotonically as the matrix modulus increased. These recent findings are consistent with much earlier studies on rubber toughening [315, 316], and show that as crosslink density increases, the ability to reinforce and improve toughness decreases. The diminished reinforcement efficiency is associated with the extremely localized mechanical behavior of the highly crosslinked, glassy epoxies [307]. This suggests that the ability of the matrix to provide non-local interaction between nanoparticles is suppressed. Due to these limitations, there are no clear approaches to effectively address strengthening of glassy epoxies without compromising ductility.

Our recent work on glassy epoxies containing two different types of nanoparticles indicates that the interaction between nanoparticles provides a route to greatly improve mechanical properties at low concentration. We found an anomalous strengthening effect in a highly crosslinked epoxy containing a binary dispersion of MWCNTs (0.2 vol.%) and α-zirconium phosphate (ZrP) nanoplatelets (0.8 vol.%). In this system, the modulus, strength, and elongation at break were simultaneously improved by 40%, 54%, and 15% relative to the unfilled epoxy. The profound improvement in tensile strength without decrease in ductility is highly unusual, and suggests that a novel mechanism may be present, and is likely related to the interaction between nanoparticle phases.

The mechanical behavior of individually exfoliated ZrP nanoplatelets has been systematically studied in prior work [40-42, 44, 45], and provides a useful basis to determine the role of the individual phases. At similar concentration of 0.7 vol.%, using ZrP nanoparticles with identical surface treatment, size, and dispersion methods, we previously found only ~ 5% increase in modulus, and a significant decrease in strength

and ductility [44]. The modulus of the nanocomposite increases with volume fraction, but comparable improvement in modulus to the hybrid nanocomposite was not observed until 2 vol.% ZrP [45]. The strength and ductility of the nanocomposites are primarily related to the surface group used to exfoliate the nanoplatelets, and generally decrease [40-42, 44, 45].

In the nanocomposite containing the binary dispersion, the surface was modified with TBA^+ to introduce a positive charge to interact with the MWCNTs, which were weakly oxidized and had a negative surface charge. Prior testing of epoxy containing only TBA^+ at equivalent loading to the epoxy/ZrP (0.7 vol.%) system showed a substantial decrease in strength and ductility, ~ 50%, and no change in modulus [44].

It is challenging to clearly determine the reinforcing role of the MWCNTs because of the lack of prior systematic experiments able to introduce individually dispersed MWCNTs into an epoxy with well-defined particle-level parameters. In addition, the magnitude of modulus and strength improvement depend strongly on the modulus of the neat matrix [313, 314], so care must be taken when comparing between different works. Based on our prior studies and other reports, it is safe to assume that at concentration 0.2 vol.% (~ 0.4 wt.%), the MWCNTs will have very limited reinforcing role in glassy epoxy, and should not significantly influence modulus or strength [227, 317].

There is no change in the dispersion state of the ZrP due to the binary processing approach. The exfoliation of the MWCNTs is improved by the process, and individual nanotubes were reported to be uniformly dispersed in the epoxy [55]. In the absence of a change in the interaction with the matrix, improved dispersion is not anticipated to

significantly affect modulus. This is supported by studies on the influence of dispersion state on mechanical properties of untreated MWCNTs by Song et al. [318]. They found a slight improvement in strength and ductility of the epoxy containing better dispersed MWCNTs, but this is likely due to a decrease in size of aggregates, which behave as stress concentration sites [227, 319].

Based on these comparisons, it appears that the reinforcing mechanism cannot be attributed to the role of either individual phase. We previously proposed that the change in behavior was related to the electrostatic interactions between nanoparticles, but did not provide any description of mechanism or support for the conjecture [55]. Here, we characterize linear viscoelastic and steady shear properties of the epoxy/ZrP/MWCNT systems in the uncured state. Rheology is a powerful tool to probe molecular-scale interactions in systems. The findings are related to the fracture behavior of the solid state. We propose that the unique strengthening behavior observed in epoxy/MWCNT/ZrP hybrid is due to the role of MWCNTs in delocalizing a local strain-shielding mechanism associated with the continuum-level behavior of the ZrP nanoplatelets. The reinforcing role of the MWCNTs was proposed in our previous work on a similar epoxy system containing untreated MWCNTs [227, 228]. The strengthening role of the ZrP nanoplatelets is based on the strain distribution around a high aspect ratio plate, where regions parallel to the inclusion are subject to smaller strain than the far field, and the ends of the inclusion are subject to larger strains. Analysis of the failed surface shows that failure does not occur at any localized point, which indicates the nanoparticles, and any related stress concentration, are much smaller

than the largest flaws in the system. The results provide insight into potential mechanisms to improve the strength of highly crosslinking epoxies.

7.2 Experimental

ZrP micro-crystals were synthesized with average lateral diameter of 100 nm using the hydrothermal method described in detail by Sun et al. [39]. The microcrystals were exfoliated in aqueous solution by adding tetra-*n*-butylammonium hydroxide (TBA^+OH^-, Aldrich) at molar ratio of 0.8 TBA^+/ZrP in water. MWCNTs were obtained with Sigma-Aldrich, with inner and outer diameter of 2-6 and 10-15 nm, respectively, and length of ~ 1-10 μm. The MWCNTs were pre-treated and mixed with the ZrP nanoplatelets following the procedure described by Sun et al. [51, 55]. Mild oxidative pre-treatment was carried out by sonicating the MWCNTs in a concentrated H_2SO_4:HNO_3 mixture (3:1 ratio by volume) for 3 hours at room temperature. This processing approach was developed to introduce sufficient negative surface charge for the MWCNTs to favor electrostatic interaction with the TBA^+-exfoliated nanoplatelets. We previously reported that this processing route does not result in detectable change in electronic properties or decrease in length of the CNTs [51-54, 56].

Aqueous solutions of oxidized MWCNTs and TBA^+-exfoliated ZrP nanoplatelets were directly mixed at a ratio of ZrP:MWCNT = 5:1 by weight (~ 2:1 by volume), and sonicated for 30 minutes. During this step, as-received MWCNT clusters are disentangled down to individual nanotubes. The disentangled MWCNTs are

electrostatically tethered to the ZrP nanoplatelets to form ZrP/MWCNT hybrid nanostructures [51, 53, 55].

Aqueous dispersions of exfoliated ZrP/MWCNT hybrid nanostructures were transferred to acetone and subsequently dispersed in epoxy monomer based on the previous procedure [55]. A diglycidyl ether of bisphenol A (DGEBA) epoxy monomer (DER 332, The Dow Chemical Company) was used. For rheological testing, no curing agent added. Suspensions were prepared at similar concentrations as the previous work on mechanical properties [55]. One high concentration was prepared containing 2 wt.% O-MWCNT and 5.2 wt.% ZrP, but could not be easily processed as a solid system due to high viscosity. This range of ZrP concentration was selected for comparison with other works on epoxy/ZrP nanocomposites [40-42, 44, 45].

For discussion of rheological properties, it is more meaningful to use units of volume rather than mass fraction. We calculated volume fraction, ϕ, by weighting the measured masses of the individual phases with the reported densities. The volume fraction refers to the total space physically occupied by the nanoparticles. The number density, n, is also important for differentiating between regions of concentration. An isolated, freely rotating particle is only able to interact with other particles within a volume swept by its largest dimension, $\sim O(L^3)$. For $nL^3 \gg 1$, inter-particle interactions will begin to influence rheological behavior, and at $nL^3 \sim 60$, significant aggregation is common for fiber-like fillers. The concentration region is generally defined based by $nL^2 d > 1$, which refers to suspensions where the average distance between particles is on the order of the smallest dimension of the particle ($d = t$ for the ZrP nanoplatelets). The number

density was calculated for the individual phases as $n = \phi/V_p$, where $V_p = \pi d^2 L$ for the MWCNTs and $\sqrt{3}L^2 t/2$ for the ZrP nanoplatelets. For the nanoplatelets, the thickness of an individual layer was assumed to be t = 0.69 nm. For convenience, the mass fraction, c_w, and volume fraction, ϕ, for the suspensions investigated this work as summarized in Table 7-1. The quantities nL^3 and $nL^2 d$ are also reported for the single-phase systems.

Table 7-1. Summary of different measures of concentrations for suspensions reported here.

	ZrP		**MWCNT**			
System	c_w **wt.%**	ϕ **vol.%**	c_w **wt.%**	ϕ **vol.%**	nL^3	$nL^2 d$
O-MWCNT			0.2	0.11	14	0.14
			0.4	0.22	28	0.28
			1.0	0.55	70	0.70
ZrP-TBA	1.0	0.42			0.7	0.005
	1.9	0.81			1.4	0.01
	5.2	2.24			3.8	0.03
Hybrid-1	1.0	0.42	0.2	0.11		
Hybrid-2	2.0	0.85	0.4	0.22		
Hybrid-3	5.2	2.26	1.0	0.57		

c_w is mass fraction; ϕ is volume fraction; n is number density, which is calculated from $n = \phi/V_p$, for MWCNTs, $V_p = \pi d^2 L/4$, where d = 10 nm and L = 1 μm; for ZrP, $V_p = \sqrt{3}L^2 t/2$, where L = 100 nm and t = 0.69 nm.

For analysis of fracture surfaces, a solid epoxy nanocomposite was prepared with 2.0 wt.% ZrP and 0.4 wt.% MWCNT, which is the concentration previously reported to provide the most substantial improvement in mechanical properties [55]. The curing agent, 4,4'-diaminodiphenylsulfone (DDS), was added and stoichiometric ratio, and

panels were prepared using standard curing procedure [55]. The solvent was removed with a rotary evaporator.

7.2.1 Characterization

Thermogravimetric analysis (TGA) was carried out using a Q500 TGA (TA Instruments; New Castle, DE, USA) to determine the mass fraction of ZrP nanoplatelets in the suspension, and to confirm that all solvent was removed. Rheological measurements were carried out using the same equipment and approaches described in earlier chapters.

Solid epoxy/ZrP (2.0 wt.%)/MWCNT (0.4 wt.%) nanocomposites were prepared and fractured using the double-notch four-point bending (DN-4PB) test at room temperature [320]. The damage zone at the arrested crack tip of the epoxy nanocomposite was isolated, trimmed, and thin sectioned for TEM observation.

7.3 Results

7.3.1 Fracture surface

To investigate the role of interacting nanoparticles on the mechanical behavior of the epoxy in the solid state, solid nanocomposites were fractured with the DN-4PB test at room temperatures [320]. The solid epoxy nanocomposite was prepared with ZrP/MWCNT concentration at 0.85 and 0.22 vol.%, respectively, using same procedure for previous mechanical property study [55]. The DN-4PB method was originally developed for toughened plastics to clearly show the role of filler particles during the

crack growth process. Two nearly identical cracks are cut into a rectangular beam, which is then loaded in a four-point bending geometry. As load increases, plastic zones form in front of the crack tips, and due to random differences, one crack propagates unstably. The surviving crack has a sub-critically developed process zone at the tip. In most reports, the failure behavior of nanocomposites is analyzed using SEM of completely failed specimens prepared in various ways, or by etching the surface to expose the distribution of reinforcing particles. Events that take place in the crack tip process zone are lost during unstable propagation of the crack, and there is no way to identify mechanisms responsible for formation and failure of the process zone [315, 320, 321].

Detailed investigations of the sub-fracture surface zone revealed the presence of ruptured MWCNTs at the crack tip (Figure 7-1). Several reports have shown telescopic fracture of MWCNTs in epoxy and other polymer media, but in most cases, analysis was limited to SEM images of completely failed specimens [322-324]. In this case, it is difficult to distinguish between modes of failure, and there is no indication that the observed morphological features are active during the fracture process.

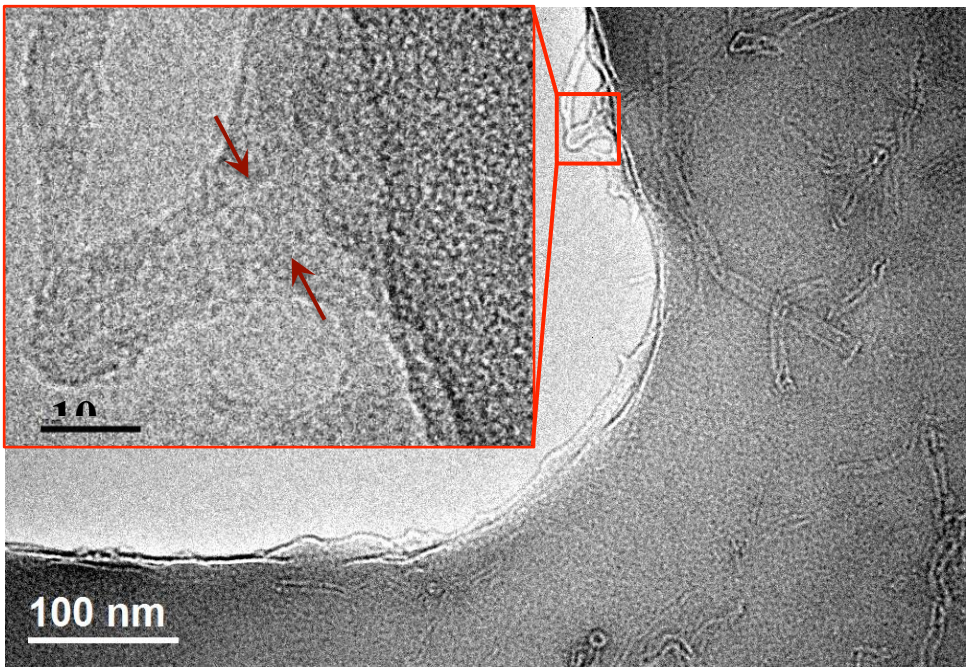

Figure 7-1. TEM micrograph taken at the DN-4PB crack tip of fully cured epoxy/ZrP/MWCNT (0.85 / 0.22 vol.%) nanocomposite. Inset shows greater detail of MWCNT ruptured at the crick tip in the sub-critically propagated process zone.

This is the first observation of the in-situ fracture of MWCNTs in a sub-critically developed process zone. No deflection, crack pinning, or other fracture mechanisms are observed, and the crack extends in a purely straight fashion prior to arrest. This suggests that there is no direct interaction between the crack tip and the MWCNT phase. The cross-sectional area of the MWCNTs is substantially smaller than any length scale associated with the fracture or crack growth in the epoxy, so it is reasonable that individual MWCNTs should not be able to influence the fracture process. We previously provided detailed images of the tensile fracture surface of the epoxy/ZrP/MWCNT nanocomposites [55], which substantial deformation distributed uniformly across the surface of the failed specimen. Typically, glassy epoxies fail in

brittle fashion, and the crack originates from a single point. No points of stress concentration or critical flaws were observed.

The nature of fracture behavior is consistent with our prior investigations of epoxy/ZrP and epoxy/MWCNT systems. Boo et al. [45] investigated the effect of nanoplatelet dispersion on fracture behavior, and found that for poorly dispersed nanoplatelets, there is significant crack bifurcation and distortion at the crack tip. When the nanoplatelets are fully exfoliated and well-dispersed, no interaction with the crack tip was observed. The lack of interaction between the crack tip and the nanoparticle phase was proposed to originate from a size effect. If the nanoparticles are sufficiently small and uniformly dispersed, the dispersion becomes homogeneous from the perspective of the crack, which operates on longer length scales that are associated with the natural crack tip radius. During the fracture process, the crack cannot "see" the nanoparticle phase, and stresses build up uniformly throughout the system up to failure. In a separate study, it was found that epoxy/ZrP nanocomposites containing fully exfoliated and well-dispersed nanoplatelets with lateral diameter ~ 1 μm show active fracture mechanisms [44]. The surface modifier was identical in both systems, which strongly supports the proposed size effect. Similar behavior has been reported for epoxy/MWCNT systems. Small improvements in fracture toughness were reported for systems containing clustered MWCNTs, but analysis of the fracture surface showed deformation features were limited to the large aggregates [227]. Similar behavior has been reported elsewhere [319], and suggests that if the MWCNTs are uniformly dispersed, there will not be any interaction with the fracture process.

For the epoxy/ZrP/MWCNT nanocomposite investigated here, the rupture of the high modulus, high strength MWCNT in the process zone is strong evidence that the continuum-level description of load transfer is not a dominant mechanism for reinforcement. The uniform fracture surface also shows that despite the relative bulkiness that may be anticipated from the tethering between two nanoparticles with large individual excluded volumes, the hybrid structures are part of a homogeneous single-phase system from the perspective of the crack.

The fracture results provide strong evidence that the ZrP/MWCNT hybrids are well integrated in the epoxy matrix, and result in a system-wide change in behavior on length scales smaller than the natural crack tip. The findings give some idea of the effect of the dispersed phase, but do not provide any indication regarding the mechanism responsible for the behavior. We anticipate that the behavior is a consequence of the interaction between phases. The nature of inter-particle interaction may be due to number of different mechanisms and are challenging to clearly identify. Here, we use rheology as a molecular scale probe to investigate the relationship between dispersed phases across different length scales. The ZrP/MWCNT hybrids were dispersed in the epoxy monomer matrix without addition of curing agent.. Suspensions were prepared with ZrP concentration ranging from 0.4 – 2.2 vol.%, and fixed ratio between nanoparticles of 5:1 ZrP:MWCNT by weight (~ 4:1 by volume).

7.3.2 Rheology of oxidized MWCNT suspensions

For the ZrP nanoplatelets, the rheological behavior may be interpreted based on the motion and orientation of the individual particles under shearing flow (Chapter III and Chapter IV). In sharp contrast, the rheological behavior of suspensions containing MWCNTs is dominated by a supramolecular structure of mechanically cohesive aggregates (Chapter VI). The rheology of SWCNT and MWCNT suspensions has been investigated in a number of previous works, and comparison with electrical conductivity provides useful insights into system-level features of behavior [229]. For the system investigated here, we are interested in the influence of oxidation on the flow behavior, and how this relates to changes in interaction and supramolecular organization of the MWCNTs. A few earlier studies reported the influence of oxidation and functionalization on rheology, but provided little insight into the relevant physics involved.

Oxidation is a common method to improve degree of dispersion and diminish aggregation, but the effect on flow behavior and the potential change in inter-particle interaction is not clear. We reported detailed investigation of the linear viscoelasticity of suspensions containing fully disentangled MWCNTs at semi-dilute concentrations in Chapter V. The observed behavior shows Brownian relaxation at low frequencies, which may be regarded as characteristic of the behavior of individual nanotubes in the absence of flocculated structure. Here, we prepared several suspensions containing oxidized MWCNTs (O-MWCNTs). The linear viscoelasticity of the O-MWCNT

suspensions is shown in Figure 7-2. The results are compared with the relaxation behavior of other MWCNT systems with different degrees of flocculation in Figure 7-3.

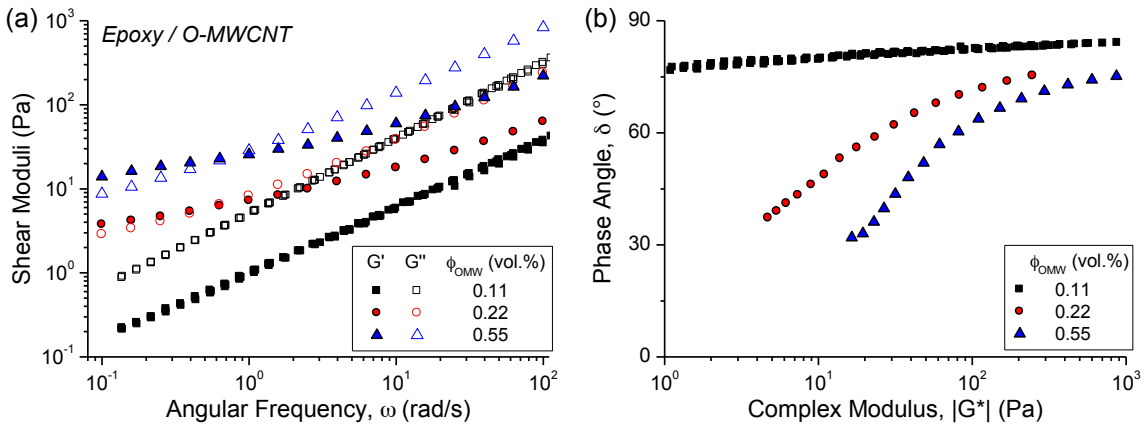

Figure 7-2. Linear viscosity and relaxation behavior of suspensions containing oxidized MWCNTs: (a) storage modulus, G', and loss modulus, G'', as functions of angular frequency, ω; and (b) phase angle, δ, shown as function of magnitude of complex modulus, $|G^*|$ (vGP plot). Measurements carried out at T = 30° C. For 0.1 vol.% system, additional measurements carried out at higher temperatures to extend range of measurable elastic response at lower frequencies.

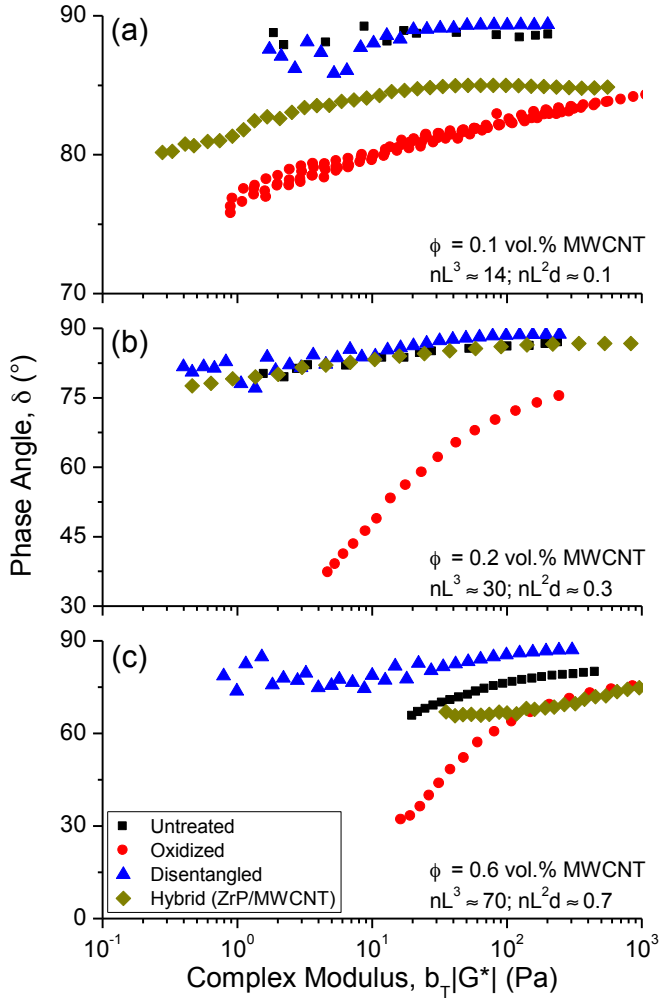

Figure 7-3. Comparison of relaxation behavior for several suspensions containing MWCNTs with different degrees of dispersion at similar concentration: $\phi \approx$ (a) 0.1 vol.%, (b) 0.2 vol.%; and (c) 0.6 vol.% MWCNT.

The dispersion of the MWCNTs is significantly improved by the chemical oxidation approach, which is generally attributed to a decrease in flocculation. However, the relaxation behavior shows an increase in solid-like response for the O-MWCNTs, which suggests that the mild oxidation does not prevent flocculation to any significant extent, and appears to enhance the elastic cohesion of the flocs. This surprising behavior

attributed to initial breakdown of as-received aggregates and removal of impurities during oxidation; mechanism provides little ability to prevent re-flocculation, which is more uniform in the oxidized systems and found to result in significant solid-like response at lower concentration. The presence of the oxidized sites apparently do not provide sufficient magnitude of repulsion to limit mechanical contacts between fibers, or to prevent vdW interactions from stabilizing the contact. The dominant role of the flocculated structure is characteristic of nearly all suspensions containing semi-dilute concentration of MWCNTs, with the exception of the disentangled MWCNTs.

There are some interesting features of relaxation behavior that should be mentioned and have not been previously discussed to our knowledge. In the limit of high frequency, each of the suspensions shows δ approaching a maxima. For low concentration, the maxima is near 90°, but increases strongly with concentration in the semi-dilute suspensions, which suggests that there is a permanent microstructure that gives limiting value of elastic response. For the disentangled MWCNTs, the maxima approaches 90° even at semi-dilute concentrations. This indicates that the observed maxima for the clustered systems is due to the localized elastic interactions within the flocculated structure. As $|G^*|$ decreases, δ decreases rapidly, and no inflection or minima in the curve is observed. The range of relaxation behavior was expanded using measurements obtained at range of temperatures. Even for extremely broad range of measurements, which showed excellent superposition, no limiting value in δ is observed. The results suggest that as time and length scale increase, there is a progressive increase in the relative elastic response. For flocculated structures, the magnitude of elasticity

may be related to the number of elastically active junctions in network, which increases with contact points between particles [325, 326]. As the time scale of the measurement increases, the length scale of suspension microstructure probed will also increase. For the clustered MWCNT suspensions, the monotonic decrease in δ is evidence of a spanning elastic network of inter-connected aggregates. The increase in elasticity with temperature also shows that the solid-like response is not dependent on energy scale of system, as expected for colloidal interactions. The origin of solid-like response is likely due to the presence of a mechanically interlocked network, which is consistent with our recent results.

7.3.3 Linear viscoelasticity of hybrid suspensions

Representative curves for linear viscoelasticity of suspensions containing ZrP and MWCNTs at three different concentrations shown in Figure 7-4. The systems are referred to in order of increasing nanoparticle content as Hybrid-1, Hybrid-2, and Hybrid-3, respectively (Table 7-1). The volume fraction of each phase is equal to the concentrations of the single-phase systems discussed above, and the ratio between ZrP and MWCNTs is fixed at 5:1 ZrP:MWCNT by weight. In our previous work, we found that this ratio results in full disentanglement of MWCNTs for ZrP nanoplatelets with diameter of 100 nm [51-54]. This indicates that every MWCNT is able to interact with at least 1 ZrP nanoplatelet, which provides a mechanism to inhibit extensive flocculation.

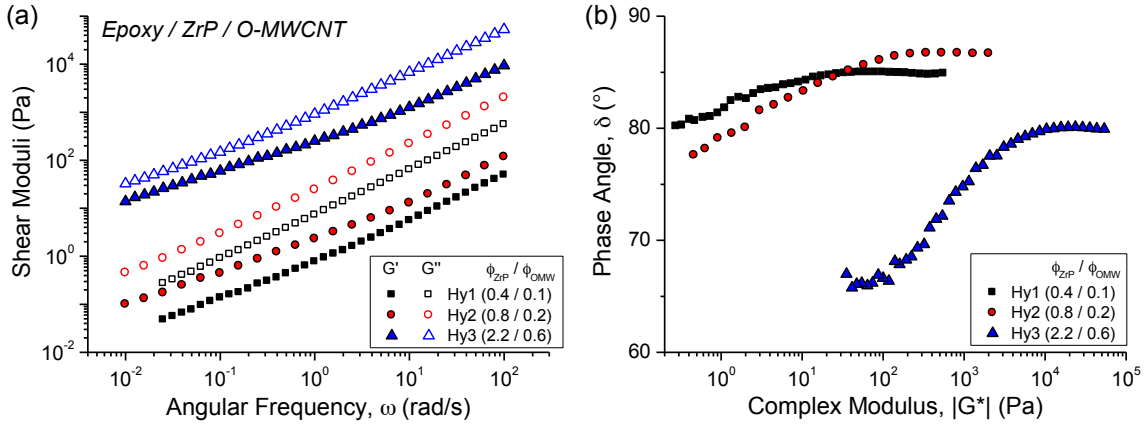

Figure 7-4. Linear viscosity and relaxation behavior of ZrP/MWCNT suspensions: (a) storage modulus, G', and loss modulus, G'', as functions of angular frequency, ω; and (b) phase angle, δ, shown as function of magnitude of complex modulus, $|G^*|$ (vGP plot). Measurements carried out at T = 30° C.

In the Hybrid-1 and Hybrid-2 suspensions, there is a high-frequency region with increased frequency dependence, and the power-law slope of G' decreases as frequency is reduced. The difference in G' between the Hybrid-1 and Hybrid-2 suspensions increases at lower frequencies. The apparent low-frequency plateau region suggests that there is a persistent elastic network in the suspensions. For the Hybrid-3 suspension, there is an intermediate plateau region in G', but the frequency-dependence increases at low frequency. This suggests that the network has a finite relaxation time.

The vGP curves of the Hybrid-1 and Hybrid-2 systems are similar to the behavior of the single-phase O-MWCNT suspensions. Both systems shows an asymptote in δ at high $|G^*|$, and progressive decrease in δ as $|G^*|$ decreases. The maxima increases slightly between the Hybrid-1 and Hybrid-2 systems, which is surprising because the concentration of nanoparticles is twice as large. Generally, δ is relatively insensitive to

external effects and strongly related to concentration. This has been demonstrated in previous chapters of this dissertation for suspensions containing ZrP nanoplatelets exfoliated with different surface groups (Chapter II), high aspect ratio nanoplatelets Chapter III), concentrated suspensions with liquid crystal order (Chapter IV), and disentangled MWCNTs (Chapter V). The difference is small, but well within experimental error. At lower $|G^*|$, δ decreases more sharply for the Hybrid-2 suspension, which is consist with the expected concentration-dependence of the single-phase MWCNT suspensions. The specific mechanism for the increase in the maxima of δ for the Hybrid-2 suspension is not clear, but shows that the behavior of the suspension is no longer dominated by the elastic cohesion within flocculated MWCNTs. In the Hybrid-3 system, the low-frequency transition in G' is present as a plateau in δ at low $|G^*|$. It is not clear from these measurements if there is any subsequent increase corresponding to viscous flow behavior.

It is helpful to directly compare the different hybrid suspensions with their corresponding single-phase fluids (Figure 7-5). For the Hybrid-1 system, at low frequency, the storage modulus of the ZrP/MWCNT is nearly the same as the O-MWCNT suspension. At high frequency, G' increases more rapidly for the hybrid system, but there is no pronounced change in phase angle. For the Hybrid-2 suspension, the order of the different systems with respect to G' follows the same trends as the Hybrid-1. The hybrid suspension shows increasing frequency-dependence of G' at high frequency, and weak inflection to a region with lower frequency dependence of G' below ~ 10 rad/s. It is interesting that at high frequency, δ is nearly identical for the ZrP

and ZrP/MWCNT suspensions. At lower frequency, the scaling of δ follows O-MWCNT phase and shows no hint of transition to viscous flow behavior. This suggests that the response of the individual phases is preserved in the hybrid system, although on distinct length scales.

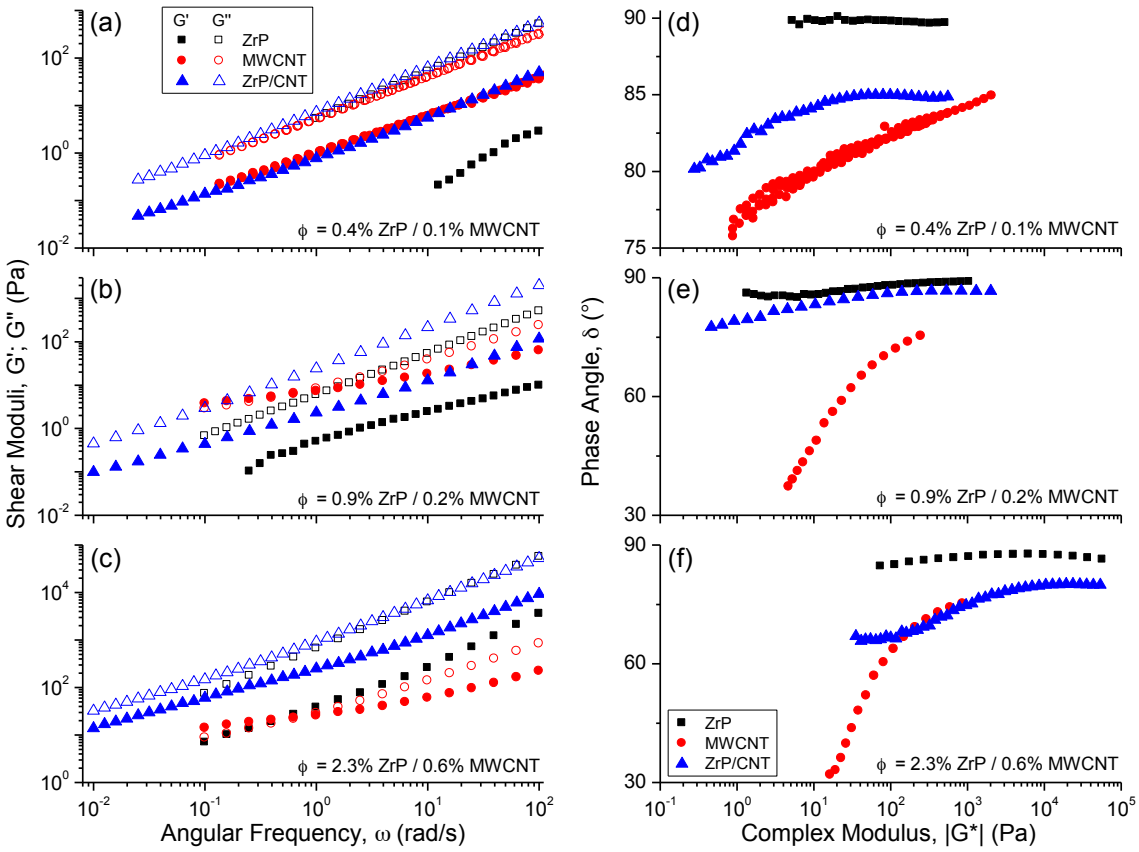

Figure 7-5. Linear viscoelastic response of suspensions containing electrostatically tethered ZrP nanoplatelets and MWCNTs, compared with behavior of corresponding single-phase fluids. (a,b,c) Storage modulus, G' (filled symbols) and loss modulus (unfilled symbols) as functions of angular frequency; (d,e,f) phase angle, δ, as function of magnitude of complex modulus, $|G^*|$ (vGP plot). Volume fractions for each phase are designated in the figure.

For the Hybrid-3 system, the linear viscoelastic response appears to correspond to a transition between behavior of the single-phase systems. At high frequency, G' of the ZrP and ZrP/MWCNT systems are nearly identical. In both systems, there appears to be a maxima in δ, and a weak decrease on longer length scales. As frequency decreases, the difference between the two systems progressively increases, which suggests that the role of the O-MWCNTs increases. However, the phase angle of the ZrP/MWCNT systems shows a plateau at low frequency. It is not clear if there is any transition to viscous flow due to the limited data set, but the plateau clearly shows a distinct response from the limiting behavior of the O-MWCNT system at low frequency.

7.3.4 Steady shear

The steady shear response of the hybrid suspensions is shown in Figure 7-6. For each of the systems, the magnitude of viscosity at high shear rate is similar to the single-phase ZrP nanoplatelet phase. At low shear rate, the viscosity increases significantly, and suggests that interaction between the MWCNTs is still significant. The limiting behavior at low shear rate is nearly identical to the dynamic viscosity from linear viscoelastic measurements, which suggests that the measurements reflect the equilibrium structure of the resting fluids.

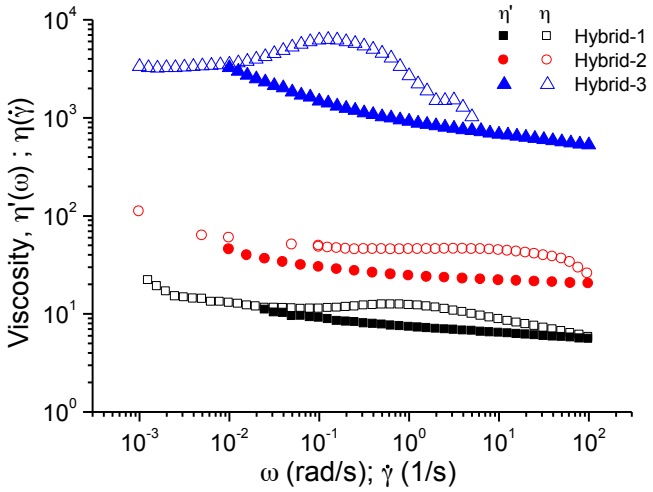

Figure 7-6. Dynamic viscosity, $\eta'(\omega)$ and steady shear viscosity, $\dot{\gamma}$, plotted as functions of angular frequency and shear rate, respectively for (a) epoxy/ZrP/MWCNT suspensions, and (b) 2-phase suspension containing 2 vol.% ZrP and 0.5 vol.% MWCNT, along with corresponding single-phase suspensions for comparison.

The major distinction between the hybrid suspensions and the corresponding single-phase systems is the pronounced shear-thickening behavior at intermediate shear rates (Figure 7-6). The behavior is observed in each of the hybrid suspensions. No associated behavior was observed in SAOS, which suggests a highly non-equilibrium behavior. The change in non-linear response shows that the behavior of the nanoparticle phases is coupled, which is attributed to the electrostatic tethering between the ZrP nanoplatelets and oxidized MWCNTs.

Based on the rheological results, we propose that the ZrP nanoplatelets behave as immobile boundaries that may prevent non-affine displacement or slip of the MWCNTs during deformation. On long length scales, the intermediate level of elastic response (decrease in δ) suggests that the system-wide supramolecular structure is disrupted by

the interaction between the phases. However, the magnitude of δ is still decreased significantly compared to the case of fully disentangled MWCNTs, which shows that long-range interaction between the MWCNTs is still present. The coupled response provides a mechanism for reinforcement across a broad range of length scales, and may be responsible for the observed combination of enhanced modulus (short-range) and strength (long-range) at very low particle loading. The use of similar approaches of hybrid nanoparticles with strong interactions may provide a route to introduce and tune functional degrees of response not possible with individual nanoparticle phases.

7.4 Discussion

The ability of material to interact with their environment depends on the length scale of their constituent units. For brittle epoxies, strength and fracture are generally caused by stress concentration at randomly distributed flaws and voids that are introduced during processing. During deformation, stresses build at these flaws, causing them to grow to a critical size and subsequently propagate as unstable cracks. A wide range of fillers are effective at improving modulus of glassy epoxies, which is local, small-strain behavior, and requires the formation of a continuous interface between the matrix and a filler with higher modulus. Strengthening is more difficult because the filler particles are generally larger than the inherent flaws, and act as larger stress concentration sites.

For non-spherical reinforcing materials, there is a distribution of strain at the filler/matrix interface due to the transfer of load from the matrix to the fiber. Near the center of the mid-point of the filler axis, the strains in the interface are much lower than

the average strain in the matrix. Any inherent flaws or cracks in this region are effectively shielded from growth during deformation. However, there is a region at the edge of the fibers that is subject to larger stresses than the far-field average. Any flaws in this region will be subject to larger strains and result in premature failure.

One potential method to strengthen brittle epoxies may be to take advantage of the inherent length-scale dependence of a crack. Assuming all flaws in the matrix are randomly distributed, non-overlapping, and identical shape, failure will occur at the largest flaw. From the perspective of strength and ductility, any features in the system smaller than this feature size are homogeneous and do not influence behavior. If non-spherical particles are dispersed in the epoxy on a length scale significantly smaller than the largest flaws, stress concentration at the edges may not be sufficient to initiate fracture. As a result, the matrix behaves in a flaw insensitive manner and shows homogeneous deformation. In this case, the nanoparticles will not interact with the crack and are essentially part of the background.

We previously observed this mode of failure in epoxy nanocomposites containing ZrP nanoplatelets [40-42, 44, 45]. However, the strengthening effect was minor, which was attributed to the highly localized nature of the shielding effect in the highly crosslinked epoxy, and potential disruption of the network due to the surface modifiers used to exfoliate the ZrP. In the initial studies on fracture behavior of ZrP, long-chain polyetheramines were used to exfoliate the nanoplatelets. Monoamines show a strong thermodynamic drive to interact with the densely packed proton donor sites in the inter-layer region of ZrP, and self-assemble as monolayers aligned at an angle from the

surface. The hydrocarbon backbone provides steric repulsion that increases spacing between layers, and if amount of molecules can be intercalated, the micro-crystalline stacks will exfoliate into individual sheets.

In epoxy, the polyetheramines were found to disrupt network formation and plasticize the epoxy. The amines may also undergo uncatalyzed reactions with the epoxides during curing and form aminoalcohols, which further disrupt mechanical properties. This effect may be clearly observed by comparing the effect of different surface groups used to exfoliate ZrP in previous studies [37, 40, 41, 44, 45, 327]. At fixed concentration of 2 vol.% ZrP, the modulus decreases with increasing molecular weight of functional group. Exfoliating the ZrP nanoplatelets with an excess of intercalating molecules has been found to decrease ductility in some systems [40, 41]. In epoxies containing only the various surface groups, the glass transition temperature, T_g, decreases with increasing molecular weight and concentration. In later studies, TBA^+ was used to avoid the plasticization effect associated with the polyether chains. TBA is a quaternary ammonium, and nanocomposites prepared using TBA^+-exfoliated ZrP nanoplatelets showed the best balance of properties.

If the behavior of epoxy/ZrP (1 vol.%) nanocomposite, exfoliated with M600, is compared to the epoxy containing an equivalent concentration of M600, the modulus improvement remains moderate at 23%, but the increase in strength and ductility become very significant (1.5x and 2x). At 2 vol.% ZrP, the modulus improvement is 70%, the strength increase is 186%, and the elongation at break increased 217%. Based on these results, we propose that the ZrP nanoplatelets are able to participate into the described

stress-shielding mechanism, but that the effect is limited due to the localization of deformation in the brittle epoxy, and diminished interfacial characteristics due to the effect of the surface groups.

The role of MWCNTs in strengthening of epoxies is not clear, because it is very difficult to control the dispersion state of high aspect ratio nanoparticles, and characterization is also challenging due to the differences in length scale. We previously investigated the dispersion of pristine MWCNTs in a glassy epoxy and observed that at 1 wt.% MWCNT concentration, the elastic modulus and dynamic mechanical behavior were nearly identical to the unfilled epoxy, which indicates negligible interaction between phases [227]. However, the MWCNTs were able to form an electrically conductive network, and the composite strength, ductility, and fracture toughness were moderately improved. This combination of properties is in strong contrast with continuum-level expectations. We found that strong oxidation and functionalization significantly improved dispersion of the MWCNTs, enhanced modulus moderately, but the improvements in strength, ductility, and toughness were no longer observed. These results are consistent with the reported behavior of most epoxy/MWCNT systems in literature. Based on these findings, we proposed that the MWCNTs do not interact strongly with the epoxy matrix, but do interact with other MWCNTs over long ranges [227, 228]. The interactions between MWCNTs provide a mechanism to delocalize stresses in the system.

This network mechanism was supported by later work on interlayered composites, where the individual MWCNTs were not found to directly contribute to any fracture

behavior, but were able to involve a greater number of toughening particles in the process away from the crack tip [227, 228]. The rheology results in this work are consistent with the proposed long-range interaction of MWCNTs, and show that this interaction is preserved in the hybrid system.

The main finding from the rheology results presented here was that the behavior of the individual phases was preserved on distinct time scales. We propose that in the solid epoxy/ZrP/MWCNT hybrid suspensions, the MWCNTs interact over long distances and act to increase the length-scale influenced by the ZrP nanoplatelets, which show only local interactions. As a result, the proposed stress shielding mechanism is independent of the precise orientation between the crack and the nanoplatelet. This supports proposed strengthening mechanism, which is that the ZrP nanoplatelets prevent the development of defects near their interface due to conventional load transfer, but the MWCNTs interconnect the nanoplatelets and homogenize the network.

7.5 Conclusions

The linear viscoelastic and steady shear properties of epoxy/ZrP/MWCNT suspensions has been investigated in the uncured state, and related to the solid state mechanical and fracture behavior. The relaxation behavior of the ZrP/MWCNT hybrid suspensions retains the characteristics of the individual phases on different length scales. The high frequency behavior is qualitatively identical in magnitude and scaling to the ZrP suspensions, which indicates that the nanoplatelets determine the short-range behavior of the systems. The low-frequency behavior (long range) is consistent with the

magnitude of the MWCNTs, but shows diminished solid-like response. This suggests that the system-wide flocculated system is no longer present, but significant long-range interactions between MWCNTs are still present. The steady shear viscosity of the systems similarly shows features associated with the individual phases on distinct length scales, and shear-thickening behavior is observed at intermediate shear rates. The unique shear-thickening behavior is not observed in either single-phase system and is attributed to the coupled response of the nanoparticle phases. Based on these findings, we proposed a mechanism to account for the strengthening behavior observed in epoxy/MWCNT/ZrP hybrid. Based on our description, the MWCNTs able to delocalize the local strain-shielding mechanism associated with the continuum-level behavior of the ZrP nanoplatelets. The strengthening role of the ZrP nanoplatelets is based on the strain distribution around a high aspect ratio plate, where regions parallel to the inclusion are subjected to smaller strains than the far field, and the ends of the inclusion are subject to larger strains Analysis of the failed surface shows that failure does not occur at any localized point, which indicates the nanoparticles, and any related stress concentration, are much smaller than the largest flaws in the system. The results provide insight into potential mechanisms to improve the strength of highly crosslinking epoxies.

CHAPTER VIII

CONCLUSIONS AND FUTURE WORK

8.1 Summary

The dissertation research has probed the origin of rheological properties for suspensions containing high aspect ratio nanoparticles. The use of model systems allowed the response to be discussed based on the nature of inter-particle forces and nanoscale features of the individual particles. Specific mechanisms associated with the solid-state behavior of nanocomposite systems were proposed based on the observed behavior. A summary of the results for the individual systems is given below.

8.1.1 Rheology of ZrP nanoplatelet suspensions

Surfactant effect

The influence of inter-particle interaction on the rheology of suspensions containing rigid model 2-dimensional α-zirconium phosphate (ZrP) nanoplatelets with average aspect ratio of 150 was investigated. The ZrP nanoplatelets were exfoliated in epoxy monomer with three different surfactants to probe how the sizes of a surfactant affect inter-particle interaction at different length scales. Suspensions containing nanoplatelets exfoliated with tetra-n-butyl ammonium hydroxide (TBA), a quaternary ammonium base with diameter similar to the thickness of the nanoplatelets, show short-range repulsive particle interactions with weak elastic response at low concentration. At semi-dilute concentration, the suspensions are solid-like at high frequency, and transition to viscous

flow on longer time scales. The relaxation time is in quantitative agreement with the rotary diffusion coefficient over a wide range of temperatures, and increases exponentially with concentration. The suspensions show dominant viscous response up to the highest concentration investigated. Suspensions containing nanoplatelets exfoliated with a large hydrophilic polyetheramine oligomer show similar behavior to the ZrP-TBA system, but at lower concentration. The rheological behavior is attributed to steric stabilization of the nanoplatelets by an extended oligomer brush with short-range repulsive interactions. For nanoplatelets exfoliated with a shorter chain, hydrophobic polyetheramine, the linear viscoelastic and steady shear response at moderate concentrations show significant non-equilibrium characteristics that are attributed to the presence of local microstructure. The present findings provide insight into the role of surfactants on inter-particle interactions on the rheological behavior of stable suspensions containing exfoliated high aspect ratio nanoplatelets at low concentration. Potential rheological signatures associated with equilibrium dispersions of nanoparticles with repulsive interactions and with non-equilibrium microstructure were discussed. The relationship between surface modifier and resulting flow properties and phase behavior of concentrated suspensions were also considered.

Aspect ratio effect

The effect of particle size on the rheology of suspensions containing model inorganic nanoplatelets was investigated by synthesizing the ZrP nanoplatelets with average lateral diameter, L, ranging from 100 nm to 1 μm. The nanoplatelets were uniformly dispersed

in a viscous epoxy monomer fluid as individual, sheets with monodisperse thickness ~ 0.7 nm. The linear viscoelastic and steady shear properties were investigated, and revealed distinct changes in elastic and viscous behaviors with aspect ratio. The magnitude and concentration-dependence of viscous response are increased for the larger nanoplatelets, but the relative elastic behavior is suppressed. The behaviors are attributed to a competition between excluded volume, which increases linearly with L, and mobility, which decreases with L^3. As the nanoplatelet size increases, the particles become increasingly immobile, and measurements reflect localized properties in the absence of collisions or hydrodynamic interactions with neighboring particles. The steady shear response of the smaller nanoplatelets are consistent with the behavior of Brownian plates at low concentration. At high concentration, inter-particle interaction and tumbling increase the magnitude of shear thinning. As aspect ratio increases, the steady shear response shifts to a region dominated by hydrodynamic effects. For the systems with average diameter of 700 and 1000 nm, several unique and reversible features are present, including double shear thinning and shear thickening. The temperature dependence of non-linear response follows theoretical calculations of rotary diffusion coefficient. The behaviors are proposed to originate from the combined effects of excluded volume interactions on particle tumbling, and the change in mobility and microstructure due to particle flexibility and shear-induced deformation. The model system used here provide a broad range of behavior to be probed and meaningfully connected to the behavior of the individual particles using physics-based descriptions. Further theoretical and numerical studies on similar systems may contribute to better

fundamental understanding of the effects of concentration on mobility, interactions, and phase transitions for high aspect ratio, disk-like particles. These studies will provide insights into the origins of macroscopic response for more complex systems.

Colloidal liquid crystal behavior

The rheological behavior of smectic liquid crystals formed from a dispersion of high aspect ratio, sterically stabilized nanoplatelets in epoxy monomer was investigated. The α-zirconium phosphate (ZrP) nanoplatelets were synthesized with average diameter of 100 nm with moderate polydispersity, and exfoliated to individual sheets with monodisperse thickness using a monoamine-terminated oligomer, which was densely grafted to the nanoplatelet surfaces. The exfoliated nanoplatelets are well dispersed in an epoxy monomer and self-assemble into a smectic mesophase at concentrations of 1.7 vol.% and higher. At low ZrP concentration, the suspensions are viscoelastic fluids with storage modulus independent of concentration, with negligible yield stress and moderate shear thinning characteristics. At concentrated suspensions, i.e., > 4.0 vol.% ZrP, there exists a strongly solid-like behavior at intermediate frequency, but retains a transition to liquid-like response in the limit of low and high frequencies. The non-linear viscoelasticity and steady shear response similarly show significant transitions at the same concentration regimes. The transition in rheological response is attributed to the interaction and interpenetration of the surface-attached monoamine brush layers above a critical concentration. The possible influence of topology and defect structure on rheology appears to be insignificant in the colloidal liquid crystals, which should be

useful to elucidate phase transitions and flow phenomena for layer-forming fluid systems. The results show that controlling the long-range organization of high aspect ratio nanoparticles is a useful method to increase the volume fraction of solid particles in organic media without compromising processability.

8.1.2 Rheology of MWCNT suspensions

We report a method to introduce high density of functional groups along the sidewalls of multi-walled carbon nanotubes (MWCNTs) without significant reduction of length or damage to structure. The modified MWCNTs are individually dispersed in an epoxy matrix, and show no flocculation or entanglement at concentration of 1 wt.% in liquid and solid states. The focus of this work is on the rheology and linear viscoelasticity of the individually dispersed MWCNTs, which is compared with other MWCNT systems prepared with conventional mechanical and chemical oxidation routes. The development of linear viscoelasticity and viscosity in the suspensions containing disentangled MWCNTs is significantly suppressed relative to the untreated and oxidized MWCNTs on long time scales. On shorter time scales, which correspond to localized motion and interaction, the linear viscoelastic response of suspensions containing clustered and disentangled MWCNTs are nearly identical at a given volume fraction. Suspensions containing the disentangled MWCNTs show a transition to viscous response at low frequency, and well-defined shear thickening at high shear rate, which is in sharp contrast to the behavior of clustered MWCNTs in suspension. The results suggest that the inter-particle interactions between disentangled MWCNTs are

dominated by short-range, repulsive interactions at the surface. The functionalization route described here provides a method to prepare stable dispersions of disentangled MWCNTs, which may be used to unambiguously identify contribution of individual MWCNTs in the bulk response of composite materials. Implications of dispersion state on the processability and performance of polymer nanocomposites are discussed.

8.1.3 Rheology of interacting nanoparticle suspensions

The linear viscoelasticity and rheology of a viscous Newtonian fluid containing electrostatically tethered nanoplatelets and carbon nanotubes was investigated. The study was motivated by previous findings that glassy epoxy containing the interacting nanoparticle phase shows unique improvement in modulus, strength, and ductility at low particle concentration. The nature of improvement could not be attributed to either individual phase, which indicates that the behavior must be due to either enhancement or change of reinforcement mechanism due to the interactions between phases. Rheology is used to characterize nature inter-particle interactions in the system, and determine the role of the individual phases across length scales. Behavior compared to recent studies on model suspensions containing the individual phases in fully dispersed state. The findings are related to fracture behavior and strengthening of system in solid state. We propose that unique strengthening behavior observed in solid state is due to combination of continuum-level phase transfer due to the ZrP nanoplatelets, and an additional role of MWCNTs to increase the length scale of the ZrP phase. The results provide insight into novel mechanisms to modify mechanical properties of highly crosslinked epoxies.

8.2 Concluding remarks and future work

The level of fundamental detail achieved in this work is significant compared to other works on high aspect ratio systems, because the structure of the particles is well characterized and tunable. However, the description of molecular-scale features was largely qualitative, particularly for the semi-dilute suspensions of the plate-like particles. This largely reflects the lack of robust theoretical and numerical tools available for these systems. Development in these fields is limited due to the extremely complex microstructure of the systems. However, one significant barrier has been the lack of experimental systems with model, high aspect ratio particles. The findings in this work establish a strong connection between particle-level parameters and bulk response, and are anticipated to motivate development in theoretical and numerical tools. This level of detail is necessary to provide quantitative determination of inter-particle forces for conditions relevant to industrial applications, which has only recently been successfully demonstrated in systems containing well-defined spherical particles [168].

The most significant limitation of this work is that all measurements were carried out using conventional dynamic mechanical measurements. This approach was used because it is convenient for measurement of a large number of samples, and benefits from a well-established theoretical framework. However, the measurements are inherently volume-averaged. The interpretation of the macroscale response is based on assumptions that the local microstructure and heterogeneities in the system are much smaller than the particle size, which may not be appropriate for some nanoparticle-filled systems [7].

In nanoparticle-filled systems, interfacial and geometric interactions may drastically change the thermodynamic and kinetic properties of the matrix molecules [199]. Colloidal interactions and fluid-mediated hydrodynamic interactions between nanoparticles may also significantly influence properties. Mechanisms associated with local structure cannot be realistically resolved using conventional rheological tools. Local structure and interactions will play a critical role in phase behavior and transitions in response for systems containing nanoparticles with long-range order, and must be explicitly considered to meaningfully interpret changes in macroscale response.

A number of techniques are available to measure local features of microstructure. These approaches have been widely used for micron-scale spherical particles, but extension to non-spherical, nanometer-scale particles is challenging. These experimental measurements of inter-particle forces may be integrated into theoretical models to predict rheological behavior and develop predictive structure-property relationships for concentrated systems. Further investigations that combine the local and global features of the suspensions reported here will expand our ability to directly identify relationships across length scales. There are a number of useful measurement techniques to directly probe inter-particle interactions, such as total internal reflectance microscopy (TIMS), surface force measurements, colloidal force microscopy, and optical tweezers. These techniques are able to resolve forces on the scale of 10^{-9} to 10^{-12} N, over distances of 1 nm and smaller [168]. For the optical tweezers, tracer particles are manipulated in solution by established an optical gradient using focused laser light. The micrometer-diameter tracer particle displaces from the trap center under a certain gradient, which

provides measurements of the force. In a flowing field, the displacement of the micron-scale particle may be used to generate force-displacement curves, and thereby serve as a micro-rheometer for probing the length-scale dependent behavior of complex fluids [328-330]. This is one example of an active micro-rheological approach. Passive micro-rheology may also be used, where tracer particles are dispersed in the fluid and their mean square displacement due to Brownian stochastic forces provides a measure of the local character of fluid response. This approach has recently been used to investigate the rheology of SWCNT suspensions, and provided unique insights into the microstructure of the system across hierarchical length scales [331].

Further investigation of suspensions of ZrP nanoplatelets are of interest to show the mechanisms driving self-assembly of plate-like nanoparticles into ordered domains. Very few systems have been reported with smectic organization, and the mechanisms governing the transition are not well understood [20]. The thermodynamic driving force for self-assembly is the large excluded volume of the particles, and it is likely that the tendency to assemble into columnar or smectic crystals is determined by the relationship between particle shape and size, and the polydispersity in diameter and thickness. Few systems are available that can be synthesized with well-defined shape, tunable diameter, and mono-disperse thickness, which indicates that the ZrP nanoplatelet system may provide important insights into parameters driving mesoscale organization (Figure 8-1). Insights into methods to control the long-range structure through particle shape, anisotropy, and external fields will guide future development of nanostructure materials with tailorable structure and response. The use of model nanoparticles with controllable

dimensions will also allow the findings to be generalized for systems containing nanoparticles of similar shape, which include graphene and smectite clays.

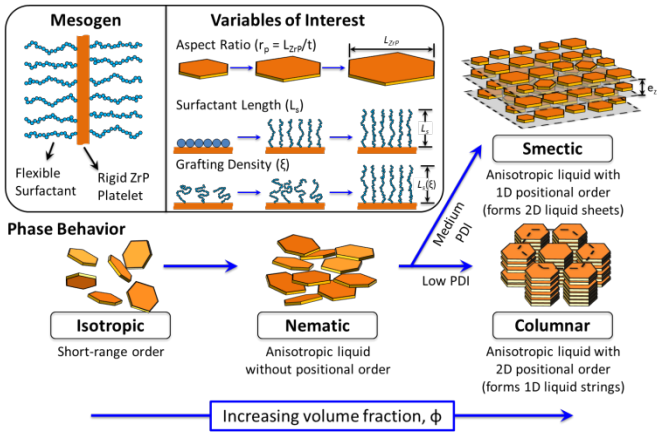

Figure 8-1. Schematic showing potential phase behavior of suspensions containing high aspect ratio, plate-like nanoparticles. At low concentration, the suspensions are isotropic and any correlation between particles is due to transient interactions on short length scales. As concentration increases, the large excluded volume of the particle drives local correlations in organization. If the inter-particle interactions are sufficiently controlled to avoid a gelation transition, the particles may assemble into a nematic mesophase. The nematic liquid crystals are composed of particles with orientational order, but no positional order. At higher concentration, there may be additional transitions to columnar or smectic organization. The specific conditions that favor the presence of the different crystal phases are not well established for plate-like nanoparticles due to the lack of experimental systems with well-defined, tunable structure.

REFERENCES

[1] Murray C, Kagan C, Bawendi M. Self-Organization of CdSe Nanocrystallites into Three-Dimensional Quantum Dot Superlattices. Science. 1995;270(5240):1335-8.

[2] Alivisatos AP. Semiconductor Clusters, Nanocrystals, and Quantum Dots. Science. 1996;273:993-37.

[3] Kagan C, Murray C, Nirmal M, Bawendi M. Electronic Energy Transfer in CdSe Quantum Dot Solids. Physical Review Letters. 1996;76(9):1517-20.

[4] Kagan C, Murray C, Bawendi M. Long-Range Resonance Transfer of Electronic Excitations in Close-Packed CdSe Quantum-Dot Solids. Phys Rev B. 1996;54(12):8633.

[5] Artemyev M, Bibik A, Gurinovich L, Gaponenko S, Woggon U. Evolution from Individual to Collective Electron States in a Dense Quantum Dot Ensemble. Phys Rev B. 1999;60(3):1504-6.

[6] Damasceno PF, Engel M, Glotzer SC. Predictive Self-Assembly of Polyhedra into Complex Structures. Science. 2012;337(6093):453-7.

[7] Jancar J, Douglas JF, Starr FW, Kumar SK, Cassagnau P, Lesser AJ, et al. Current Issues in Research on Structure-Property Relationships in Polymer Nanocomposites. Polymer. 2010;51(15):3321-43.

[8] Lauffer MA. The Size and Shape of Tobacco Mosaic Virus Particles. J Amer Chem Soc. 1944;66(7):1188-94.

[9] Schachman H, Lauffer MA. The Hydration, Size and Shape of Tobacco Mosaic Virus. J Amer Chem Soc. 1949;71(2):536-41.

[10] Vand V. Viscosity of Solutions and Suspensions. I. Theory. J Phys Chem. 1948;52(2):277-99.

[11] Eirich F, Simha R. A Contribution to the Theory of Viscous Flow Reactions for Chain-Like Molecular Substances. J Chem Phys. 1939;7:116.

[12] McKenna GB. Deformation and Flow of Matter: Interrogating the Physics of Materials Using Rheological Methods. J Rheol. 2011;56(1):113-58.

[13] Doi M, Edwards SF. The Theory of Polymer Dynamics. New York, NY: Oxford University Press; 1988.

[14] Sastry S, Debenedetti PG, Stillinger FH. Signatures of Distinct Dynamical Regimes in the Energy Landscape of a Glass-Forming Liquid. Nature. 1998;393(6685):554-7.

[15] Roland C, Hensel-Bielowka S, Paluch M, Casalini R. Supercooled Dynamics of Glass-Forming Liquids and Polymers under Hydrostatic Pressure. Rep Prog Phys. 2005;68(6):1405-78.

[16] Vaia RA, Maguire JF. Polymer Nanocomposites with Prescribed Morphology: Going Beyond Nanoparticle-Filled Polymers. Chem Mater. 2007;19(11):2736-51.

[17] Torquato S, Hyun S, Donev A. Multifunctional Composites: Optimizing Microstructures for Simultaneous Transport of Heat and Electricity. Phys Rev Lett. 2002;89(26):266601.

[18] Torquato S, Hyun S, Donev A. Optimal Design of Manufacturable Three-Dimensional Composites with Multifunctional Characteristics. J Appl Phys. 2003;94(9):5748-55.

[19] Davidson P, Gabriel J-CP. Mineral Liquid Crystals. Curr Opin Colloid Interf Sci. 2005;9(6):377-83.

[20] Lekkerkerker H, Vroege G. Liquid Crystal Phase Transitions in Suspensions of Mineral Colloids: New Life from Old Roots. Philos T R Soc A. 2013;371(1988):1-20.

[21] Langmuir I. The Role of Attractive and Repulsive Forces in the Formation of Tactoids, Thixotropic Gels, Protein Crystals and Coacervates. J Chem Phys. 1938;6:873.

[22] Zhu J, Li M, Rogers R, Meyer W, Ottewill R, Russel W, et al. Crystallization of Hard-Sphere Colloids in Microgravity. Nature. 1997;387(6636):883-5.

[23] Penn RL, Banfield JF. Imperfect Oriented Attachment: Dislocation Generation in Defect-Free Nanocrystals. Science. 1998;281(5379):969-71.

[24] Song W, Kinloch IA, Windle AH. Nematic Liquid Crystallinity of Multiwall Carbon Nanotubes. Science. 2003;302(5649):1363-.

[25] van der Beek D, Lekkerkerker HN. Liquid Crystal Phases of Charged Colloidal Platelets. Langmuir. 2004;20(20):8582-6.

[26] Novoselov K, Jiang D, Schedin F, Booth T, Khotkevich V, Morozov S, et al. Two-Dimensional Atomic Crystals. P Natl Acad Sci USA. 2005;102(30):10451-3.

[27] Joannopoulos JD, Villeneuve PR, Fan S. Photonic Crystals: Putting a New Twist on Light. Nature. 1997;386(6621):143-9.

[28] Bailey RT, North AM, Pethrick RA. Molecular Motion in High Polymers. Oxford, UK: Clarendon Press; 1981.

[29] Yang RD, Tripathy S, Li Y, Sue H-J. Photoluminescence and Micro-Raman Scattering in ZnO Nanoparticles: The Influence of Acetate Adsorption. Chem Phys Lett. 2005;411(1):150-4.

[30] Sun D, Wong M, Sun L, Li Y, Miyatake N, Sue H-J. Purification and Stabilization of Colloidal ZnO Nanoparticles in Methanol. J Sol-Gel Sci Techn. 2007;43(2):237-43.

[31] Zhang X, Sun D, Sue HJ, Nishimura R. Colloidal Crystallization of Surfactant-Free ZnO Quantum Dots. ChemPhysChem. 2011;12(18):3533-8.

[32] Sun D, Miyatake N, Sue H-J. Transparent PMMA/ZnO Nanocomposite Films Based on Colloidal ZnO Quantum Dots. Nanotechnology. 2007;18(21):215606.

[33] Sun D, Sue H-J. Tunable Ultraviolet Emission of ZnO Quantum Dots in Transparent Poly (Methyl Methacrylate). Applied Physics Letters. 2009;94(25):253106--3.

[34] Sun D, Sue H-J, Miyatake N. Optical Properties of ZnO Quantum Dots in Epoxy with Controlled Dispersion. The Journal of Physical Chemistry C. 2008;112(41):16002-10.

[35] Sun D, Everett WN, Wong M, Sue H-J, Miyatake N. Tuning of the Dispersion of Ligand-Free ZnO Quantum Dots in Polymer Matrices with Exfoliated Nanoplatelets. Macromolecules. 2009;42(5):1665-71.

[36] Sun L, Boo WJ, Browning RL, Sue H-J, Clearfield A. Effect of Crystallinity on the Intercalation of Monoamine in α-Zirconium Phosphate Layer Structure. Chem Mater. 2005;17(23):5606-9.

[37] Liu J, Boo WJ, Clearfield A, Sue H-J. Intercalation and Exfoliation: A Review on Morphology of Polymer Nanocomposites Reinforced by Inorganic Layer Structures. Mater Manuf Process. 2006;21(2):143-51.

[38] Xu S, Whitin JC, Yu TTS, Zhou H, Sun D, Sue H-J, et al. Capture of Phosphopeptides Using α-Zirconium Phosphate Nanoplatelets. Anal Chem. 2008;80(14):5542-9.

[39] Sun L, Boo WJ, Sue H-J, Clearfield A. Preparation of α-Zirconium Phosphate Nanoplatelets with Wide Variations in Aspect Ratios. New J Chem. 2007;31(1):39-43.

[40] Sue H-J, Gam KT, Bestaoui N, Spurr N, Clearfield A. Epoxy Nanocomposites Based on the Synthetic α-Zirconium Phosphate Layer Structure. Chem Mater. 2004;16(2):242-9.

[41] Sue H-J, Gam KT, Bestaoui N, Clearfield A, Miyamoto M, Miyatake N. Fracture Behavior of α-Zirconium Phosphate-Based Epoxy Nanocomposites. Acta Mater. 2004;52(8):2239-50.

[42] Boo W, Sun L, Liu J, Clearfield A, Sue H-J, Mullins M, et al. Morphology and Mechanical Behavior of Exfoliated Epoxy/α-Zirconium Phosphate Nanocomposites. Compos Sci Techn. 2007;67(2):262-9.

[43] Sun L, Boo WJ, Liu J, Tien CW, Sue H-J, Marks MJ, et al. Preparation of Intercalating Agent-Free Epoxy/Clay Nanocomposites. Polym Eng Sci. 2007;47(10):1708-14.

[44] Boo WJ, Sun L, Warren G, Moghbelli E, Pham H, Clearfield A, et al. Effect of Nanoplatelet Aspect Ratio on Mechanical Properties of Epoxy Nanocomposites. Polymer. 2007;48(4):1075-82.

[45] Boo WJ, Sun L, Liu J, Moghbelli E, Clearfield A, Sue H-J, et al. Effect of Nanoplatelet Dispersion on Mechanical Behavior of Polymer Nanocomposites. J Polym Sci Pol Phys. 2007;45(12):1459-69.

[46] Boo WJ, Sun L, Liu J, Clearfield A, Sue H-J. Effective Intercalation and Exfoliation of Nanoplatelets in Epoxy Via Creation of Porous Pathways. J Phys Chem C. 2007;111(28):10377-81.

[47] Sun L, Boo WJ, Clearfield A, Sue H-J, Pham H. Barrier Properties of Model Epoxy Nanocomposites. J Membrane Sci. 2008;318(1):129-36.

[48] Moghbelli E, Sun L, Jiang H, Boo WJ, Sue H-J. Scratch Behavior of Epoxy Nanocomposites Containing α-Zirconium Phosphate and Core-Shell Rubber Particles. Polym Eng Sci. 2009;49(3):483-90.

[49] Sun L, Boo WJ, Liu J, Clearfield A, Sue H-J, Verghese NE, et al. Effect of Nanoplatelets on the Rheological Behavior of Epoxy Monomers. Macromol Mater Eng. 2009;294(2):103-13.

[50] Sun L, Liu J, Kirumakki SR, Schwerdtfeger ED, Howell RJ, Al-Bahily K, et al. Polypropylene Nanocomposites Based on Designed Synthetic Nanoplatelets. Chemistry of Materials. 2009;21(6):1154-61.

[51] Sun D, Everett WN, Chu CC, Sue H-J. Single-Walled Carbon Nanotube Dispersion with Electrostatically Tethered Nanoplatelets. Small. 2009;5(23):2692-7.

[52] White KL, Shuai M, Zhang X, Sue H-J, Nishimura R. Electrical Conductivity of Well-Exfoliated Single-Walled Carbon Nanotubes. Carbon. 2011;49(15):5124-31.

[53] Zhang X, Sue HJ, Nishimura R. Electrostatically Controlled Isolation of Debundled Single-Walled Carbon Nanotubes from Nanoplatelet Dispersant. J Mater Chem. 2012;22(13):6156-64.

[54] Zhang X, Sue H-J, Nishimura R. Acid-Mediated Isolation of Individually Dispersed SWCNTs from Electrostatically Tethered Nanoplatelet Dispersants. Carbon. 2013;56:374-82.

[55] Sun D, Chu CC, Sue H-J. Simple Approach for Preparation of Epoxy Hybrid Nanocomposites Based on Carbon Nanotubes and a Model Clay. Chem Mater. 2010;22(12):3773-8.

[56] Chu CC, White KL, Liu P, Zhang X, Sue H-J. Electrical Conductivity and Thermal Stability of Polypropylene Containing Well-Dispersed Multi-Walled Carbon Nanotubes Disentangled with Exfoliated Nanoplatelets. Carbon. 2012;50(12):4711-21.

[57] Liu P, White KL, Sugiyama H, Xi J, Higuchi T, Hoshino T, et al. Influence of Trace Amount of Well-Dispersed Carbon Nanotubes on Structural Development and Tensile Properties of Polypropylene. Macromolecules. 2012;46(2):463-73.

[58] Cussler EL. Diffusion: Mass Transfer in Fluid Systems. 2nd ed. New York, NY: Cambridge University Press; 1997.

[59] Stachel JJ. Einstein's Miraculous Year: Five Papers That Changed the Face of Physics. Princeton, NJ: Princeton University Press; 1998.

[60] Isaacson W. Einstein: His Life and Universe. New York, NY: Simon and Schuster; 2007.

[61] Einstein A. Eine Neue Bestimmung Der Moleküldimensionen (a New Determination of Molecular Dimensions). Ann Phys-Berlin. 1906;19:289-306.

[62] Rigden JS. Einstein 1905: The Standard of Greatness. Cambridge, MA: Harvard University Press; 2009.

[63] Mewis J, Wagner NJ. Colloidal Suspension Rheology. Cambridge, UK: Cambridge University Press; 2012.

[64] Macosko CW. Rheology: Principles, Measurements, and Applications. 1 ed. New York, NY: Wiley; 1994.

[65] Batchelor G. The Stress System in a Suspension of Force-Free Particles. J Fluid Mech. 1970;41(3):545-70.

[66] Batchelor G, Green J. The Determination of the Bulk Stress in a Suspension of Spherical Particles to Order C^2. J Fluid Mech. 1972;56(3):401-27.

[67] Batchelor GK. The Effect of Brownian Motion on the Bulk Stress in a Suspension of Spherical Particles. J Fluid Mech. 1977;83(01):97-117.

[68] Cross MM. Rheology of Non-Newtonian Fluids: A New Flow Equation for Pseudoplastic Systems. J Coll Sci. 1965;20(5):417-37.

[69] Cross M. Analysis of Flow Data on Molten Polymers. Euro Polym J. 1966;2(3):299-307.

[70] Cross MM. Polymer Rheology: Influence of Molecular Weight and Polydispersity. J Appl Polym Sci. 1969;13(4):765-74.

[71] Cross MM. Kinetic Interpretation of Non-Newtonian Flow. J Coll Interf Sci. 1970;33(1):30-5.

[72] Zarraga IE, Hill DA, Leighton Jr DT. The Characterization of the Total Stress of Concentrated Suspensions of Noncolloidal Spheres in Newtonian Fluids. J Rheol. 2000;44:185.

[73] Russel W. Review of the Role of Colloidal Forces in the Rheology of Suspensions. J Rheol. 1980;24:287.

[74] Chaffey C. Mechanisms and Equations for Shear Thinning and Thickening in Dispersions. Coll Polym Sci. 1977;255(7):691-8.

[75] Vrahopoulou E, McHugh A. Shear-Thickening and Structure Formation in Polymer Solutions. J Non-Newt Fluid Mech. 1987;25(2):157-75.

[76] Barnes H. Shear-Thickening ("Dilatancy") in Suspensions of Nonaggregating Solid Particles Dispersed in Newtonian Liquids. J Rheol. 1989;33:329.

[77] Hoffman RL. Explanations for the Cause of Shear Thickening in Concentrated Colloidal Suspensions. J Rheol. 1998;42:111-23.

[78] Hu Y, Boltenhagen P, Pine D. Shear Thickening in Low-Concentration Solutions of Wormlike Micelles. I. Direct Visualization of Transient Behavior and Phase Transitions. J Rheol. 1998;42:1185.

[79] Takeda M, Matsunaga T, Nishida T, Endo H, Takahashi T, Shibayama M. Rheo-SANS Studies on Shear Thickening in Clay− Poly (Ethylene Oxide) Mixed Solutions. Macromolecules. 2010;43(18):7793-9.

[80] Jones DAR, Leary B, Boger DV. The Rheology of a Concentrated Colloidal Suspension of Hard Spheres. J Coll Interf Sci. 1991;147(2):479-95.

[81] Brady JF. The Rheological Behavior of Concentrated Colloidal Dispersions. J Chem Phys. 1993;99(1):567-81.

[82] Shikata T, Pearson DS. Viscoelastic Behavior of Concentrated Spherical Suspensions. J Rheol. 1994;38:601.

[83] Sierou A, Brady J. Rheology and Microstructure in Concentrated Noncolloidal Suspensions. J Rheol. 2002;46:1031.

[84] Morris JF. A Review of Microstructure in Concentrated Suspensions and Its Implications for Rheology and Bulk Flow. Rheol Acta. 2009;48(8):909-23.

[85] Klein J, Kumacheva E. Confinement-Induced Phase Transitions in Simple Liquids. Science. 1995;269(5225):816-9.

[86] Anastasiadis S, Karatasos K, Vlachos G, Manias E, Giannelis E. Nanoscopic-Confinement Effects on Local Dynamics. Phys Rev Lett. 2000;84(5):915-8.

[87] Krieger IM, Dougherty TJ. A Mechanism for Non-Newtonian Flow in Suspensions of Rigid Spheres. J Rheol. 1959;3:137.

[88] Ball RC, Richmond P. Dynamics of Colloidal Dispersions. Phys Chem Liq. 1980;9(2):99-116.

[89] Bicerano J, Douglas JF, Douglas AB. Model for the Viscosity of Particle Dispersions. J Macromol Sci A. 1999;39(4):561-642.

[90] de Kruif Cd, Van Iersel E, Vrij A, Russel W. Hard Sphere Colloidal Dispersions: Viscosity as a Function of Shear Rate and Volume Fraction. J Chem Phys. 1985;83:4717.

[91] Quemada D. Rheology of Concentrated Disperse Systems and Minimum Energy Dissipation Principle. Rheol Acta. 1977;16(1):82-94.

[92] Bihannic I, Baravian C, Duval JF, Paineau E, Meneau F, Levitz P, et al. Orientational Order of Colloidal Disk-Shaped Particles under Shear-Flow Conditions: A Rheological− Small-Angle X-Ray Scattering Study. J Phys Chem B. 2010;114(49):16347-55.

[93] Paineau E, Bihannic I, Baravian C, Philippe A-M, Davidson P, Levitz P, et al. Aqueous Suspensions of Natural Swelling Clay Minerals. 1. Structure and Electrostatic Interactions. Langmuir. 2011;27(9):5562-73.

[94] Michot LJ, Baravian C, Bihannic I, Maddi S, Moyne C, Duval JF, et al. Sol− Gel and Isotropic/Nematic Transitions in Aqueous Suspensions of Natural Nontronite Clay. Influence of Particle Anisotropy. 2. Gel Structure and Mechanical Properties. Langmuir. 2008;25(1):127-39.

[95] Philippe A, Baravian C, Bezuglyy V, Angilella J, Meneau F, Bihannic I, et al. Rheological Study of Two-Dimensional Very Anisometric Colloidal Particle Suspensions: From Shear-Induced Orientation to Viscous Dissipation. Langmuir. 2013;29(17):5315-24.

[96] Baravian C, Michot L, Paineau E, Bihannic I, Davidson P, Impéror-Clerc M, et al. An Effective Geometrical Approach to the Structure of Colloidal Suspensions of Very Anisometric Particles. Europhys Lett. 2010;90(3):36005.

[97] Philippe A, Baravian C, Imperor-Clerc M, De Silva J, Paineau E, Bihannic I, et al. Rheo-SAXS Investigation of Shear-Thinning Behaviour of Very Anisometric Repulsive Disc-Like Clay Suspensions. J Phys - Condens Mat. 2011;23(19):194112.

[98] Batchelor G. The Stress Generated in a Non-Dilute Suspension of Elongated Particles by Pure Straining Motion. J Fluid Mech. 1971;46(4):813-29.

[99] Bretherton FP. The Motion of Rigid Particles in a Shear Flow at Low Reynolds Number. J Fluid Mech. 1962;14(2):284-304.

[100] Brenner H. Rheology of a Dilute Suspension of Axisymmetric Brownian Particles. Int J Multiphase Flow. 1974;1(2):195-341.

[101] Petrie CJ. The Rheology of Fibre Suspensions. J Non-Newt Fluid Mech. 1999;87(2):369-402.

[102] Derakhshandeh B, Kerekes R, Hatzikiriakos S, Bennington C. Rheology of Pulp Fibre Suspensions: A Critical Review. Chem Engin Sci. 2011;66(15):3460-70.

[103] Ganani E, Powell R. Suspensions of Rodlike Particles: Literature Review and Data Correlations. J Compos Mater. 1985;19(3):194-215.

[104] Jeffery GB. The Motion of Ellipsoidal Particles Immersed in a Viscous Fluid. P R Soc Lond A Mat. 1922;102(715):161-79.

[105] Mason S. The Motion of Fibres in Flowing Liquids. Pulp Paper Mag Can. 1950;5:1.

[106] Trevelyan B, Mason S. Particle Motions in Sheared Suspensions. I. Rotations. J Coll Sci. 1951;6(4):354-67.

[107] Mason S, Manley RSJ. Particle Motions in Sheared Suspensions: Orientations and Interactions of Rigid Rods. P Roy Soc A - Mat Phy. 1956;238(1212):117-31.

[108] Bartok W, Mason S. Particle Motions in Sheared Suspensions: V. Rigid Rods and Collision Doublets of Spheres. J Coll Sci. 1957;12(3):243-62.

[109] Nawab M, Mason S. Viscosity of Dilute Suspensions of Thread-Like Particles. J Phys Chem. 1958;62(10):1248-53.

[110] Forgacs O, Mason S. Particle Motions in Sheared Suspensions: X. Orbits of Flexible Threadlike Particles. J Coll Sci. 1959;14(5):473-91.

[111] Goldsmith H, Mason S. Particle Motions in Sheared Suspensions. J Fluid Mech. 1962;12(1):88-96.

[112] Anczurowski E, Mason S. The Kinetics of Flowing Dispersions: III. Equilibrium Orientations of Rods and Discs (Experimental). J Coll Interf Sci. 1967;23(4):533-46.

[113] Okagawa A, Mason S. The Kinetics of Flowing Dispersions. VII. Oscillatory Behavior of Rods and Discs in Shear Flow. J Coll Interf Sci. 1973;45(2):330-58.

[114] Zuzovsky M, Priel Z, Mason S. Memory Impairment in Flowing Suspensions. III. Brownian Rotation of Spheroids. J Coll Interf Sci. 1980;75(1):230-9.

[115] Anczurowski E, Cox R, Mason S. The Kinetics of Flowing Dispersions: IV. Transient Orientations of Cylinders. J Coll Interf Sci. 1967;23(4):547-62.

[116] Okagawa A, Cox R, Mason S. The Kinetics of Flowing Dispersions. VI. Transient Orientation and Rheological Phenomena of Rods and Discs in Shear Flow. J Coll Interf Sci. 1973;45(2):303-29.

[117] Stover CA, Koch DL, Cohen C. Observations of Fibre Orientation in Simple Shear Flow of Semi-Dilute Suspensions. J Fluid Mech. 1992;238:277-96.

[118] Petrich MP, Koch DL, Cohen C. An Experimental Determination of the Stress–Microstructure Relationship in Semi-Concentrated Fiber Suspensions. J Non-Newton Fluid Mech. 2000;95(2):101-33.

[119] Hinch E, Leal L. The Effect of Brownian Motion on the Rheological Properties of a Suspension of Non-Spherical Particles. J Fluid Mech. 1972;52(4):683-712.

[120] Koch DL, Shaqfeh ES. The Average Rotation Rate of a Fiber in the Linear Flow of a Semidilute Suspension. Phys Fluids A - Fluid Dyn. 1990;2:2093.

[121] Rahnama M, Koch DL, Iso Y, Cohen C. Hydrodynamic, Translational Diffusion in Fiber Suspensions Subject to Simple Shear Flow. Phys Fluids A - Fluid Dyn. 1993;5:849.

[122] Koch DL. A Model for Orientational Diffusion in Fiber Suspensions. Phys Fluids. 1995;7:2086.

[123] Rahnama M, Koch DL, Cohen C. Observations of Fiber Orientation in Suspensions Subjected to Planar Extensional Flows. Phys Fluids. 1995;7:1811.

[124] Rahnama M, Koch DL, Shaqfeh ESG. The Effect of Hydrodynamic Interactions on the Orientation Distribution in a Fiber Suspension Subject to Simple Shear Flow. Phys Fluids. 1995;7(3):487-506.

[125] Sundararajakumar R, Koch DL. Structure and Properties of Sheared Fiber Suspensions with Mechanical Contacts. J Non-Newt Fluid Mech. 1997;73(3):205-39.

[126] Petrich MP, Koch DL. Interactions between Contacting Fibers. Phys Fluids. 1998;10:2111.

[127] Petrich MP, Chaouche M, Koch DL, Cohen C. Oscillatory Shear Alignment of a Non-Brownian Fiber in a Weakly Elastic Fluid. J Non-Newt Fluid Mech. 2000;91(1):1-14.

[128] Chaouche M, Koch DL. Rheology of Non-Brownian Rigid Fiber Suspensions with Adhesive Contacts. J Rheol. 2001;45:369.

[129] Cox R. The Motion of Long Slender Bodies in a Viscous Fluid. Part 1. General Theory. J Fluid Mech. 1970;44(4):791-810.

[130] Cox R. The Motion of Long Slender Bodies in a Viscous Fluid. Part 2. Shear Flow. J Fluid Mech. 1971;45(4):625-57.

[131] Karnis A, Goldsmith H, Mason S. The Kinetics of Flowing Dispersions: I. Concentrated Suspensions of Rigid Particles. J Coll Interf Sci. 1966;22(6):531-53.

[132] Anczurowski E, Mason S. The Kinetics of Flowing Dispersions: II. Equilibrium Orientations of Rods and Discs (Theoretical). J Coll Interf Sci. 1967;23(4):522-32.

[133] Forgacs O, Mason S. Particle Motions in Sheared Suspensions: IX. Spin and Deformation of Threadlike Particles. J Coll Sci. 1959;14(5):457-72.

[134] Sherwood J. Brownian Dynamics Simulations of a 2-D Suspension of Charged Colloidal Plates under Shear. J Non-Newt Fluid Mech. 1992;43(2):195-228.

[135] Yamamoto S, Matsuoka T. Dynamic Simulation of a Platelike Particle Dispersed System. J Chem Phys. 1997;107:3300.

[136] Yamamoto S, Matsuoka T. Dynamic Simulation of Rod-Like and Plate-Like Particle Dispersed Systems. Comp Mater Sci. 1999;14(1):169-76.

[137] Meng Q, Higdon JJ. Large Scale Dynamic Simulation of Plate-Like Particle Suspensions. Part I: Non-Brownian Simulation. J Rheol. 2008;52:1.

[138] Meng Q, Higdon JJ. Large Scale Dynamic Simulation of Plate-Like Particle Suspensions. Part II: Brownian Simulation. J Rheol. 2008;52:37.

[139] Leal L, Hinch E. The Effect of Weak Brownian Rotations on Particles in Shear Flow. J Fluid Mech. 1971;46(4):685-703.

[140] Simha R. The Influence of Brownian Movement on the Viscosity of Solutions. J Phys Chem. 1940;44(1):25-34.

[141] Kuhn W, Kuhn H. Die Abhängigkeit Der Viskosität Vom Strömungsgefälle Bei Hochverdünnten Suspensionen Und Lösungen (Dependence of Viscosity on Flow Gradient in Highly Diluted Suspensions and Solutions). Helv Chim Acta. 1945;28(97).

[142] Batchelor G. Slender-Body Theory for Particles of Arbitrary Cross-Section in Stokes Flow. J Fluid Mech. 1970;44(3):419-40.

[143] Berry DH, Russel WB. Rheology of Dilute Suspensions of Slender Rods in Weak Flows. J Fluid Mech. 1987;180:475-94.

[144] Doi M, Edwards S. Dynamics of Concentrated Polymer Systems. Part 1.—Brownian Motion in the Equilibrium State. J Rheol. 1978;74:1789-801.

[145] Doi M, Edwards S. Dynamics of Concentrated Polymer Systems. Part 2.—Molecular Motion under Flow. J Chem Soc, Faraday Trans 2. 1978;74:1802-17.

[146] Doi M, Edwards S. Dynamics of Concentrated Polymer Systems. Part 4.—Rheological Properties. J Chem Soc, Faraday Trans 2. 1979;75:38-54.

[147] Edwards S, Vilgis TA. The Tube Model Theory of Rubber Elasticity. Rep Prog Phys. 1988;51(2):243.

[148] de Gennes P-G. Reptation of a Polymer Chain in the Presence of Fixed Obstacles. J Chem Phys. 1971;55:572.

[149] Boek E, Coveney P, Lekkerkerker H, van der Schoot P. Simulating the Rheology of Dense Colloidal Suspensions Using Dissipative Particle Dynamics. Phys Rev E. 1997;55(3):3124.

[150] Lagaly G. Principles of Flow of Kaolin and Bentonite Dispersions. Appl Clay Sci. 1989;4(2):105-23.

[151] Litchfield DW, Baird DG. The Rheology of High Aspect Ratio Nano-Particle Filled Liquids. Rheol Rev. 2006:1-60.

[152] Lagaly G. Colloid Clay Science. In: Bergaya F, Theng BKG, Lagaly G, eds. Handbook of Clay Science. Oxford, UK: Elsevier 2006.

[153] Marechal M, Cuetos A, Martínez-Haya B, Dijkstra M. Phase Behavior of Hard Colloidal Platelets Using Free Energy Calculations. J Chem Phys. 2011;134:094501.

[154] Morales-Anda L, Wensink HH, Galindo A, Gil-Villegas A. Anomalous Columnar Order of Charged Colloidal Platelets. J Chem Phys. 2012;136:034901.

[155] Van der Werff J, De Kruif C, Blom C, Mellema J. Linear Viscoelastic Behavior of Dense Hard-Sphere Dispersions. Phys Rev A. 1989;39(2):795.

[156] Zimm BH. Dynamics of Polymer Molecules in Dilute Solution: Viscoelasticity, Flow Birefringence and Dielectric Loss. J Chem Phys. 1956;24:269.

[157] Osaki K. Viscoelastic Properties of Dilute Polymer Solutions. Fortschritte Der Hochpolymeren-Forschung. Berlin, Germany: Springer 1973, p. 1-64.

[158] Zimm BH, Kilb RW. Dynamics of Branched Polymer Molecules in Dilute Solution. J Polym Sci. 1959;37(131):19-42.

[159] Osaki K, Schrag JL. Numerical Calculations of the Viscoelastic Properties of Solutions of Branched Polymers Based on the Zimm-Kilb Theory. J Polym Sci Pol Phys. 1973;11(3):549-58.

[160] Osaki K, Mitsuda Y, Schrag JL, Ferry JD. Numerical Calculations of the Viscoelastic Properties of Dilute Solutions of Comb-Shaped Branched Polymers. J Rheol. 1974;18:395.

[161] Kirkwood JG, Auer PL. The Visco-Elastic Properties of Solutions of Rod-Like Macromolecules. J Chem Phys. 1951;19(3):281-3.

[162] Kirkwood JG, Riseman J. The Intrinsic Viscosities and Diffusion Constants of Flexible Macromolecules in Solution. J Chem Phys. 1948;16:565.

[163] Yamakawa H. Viscoelastic Properties of Straight Cylindrical Macromolecules in Dilute Solution. Macromolecules. 1975;8(3):339-42.

[164] Nemoto N, Schrag JL, Ferry JD, Fulton RW. Infinite-Dilution Viscoelastic Properties of Tobacco Mosaic Virus. Biopolymers. 1975;14(2):409-17.

[165] Hermans J. The Viscosity of Concentrated Solutions of Rigid Rodlike Molecules (Poly-γ-Benzyl-l-Glutamate in *m*-Cresol). J Coll Sci. 1962;17(7):638-48.

[166] Warren TC, Schrag JL, Ferry JD. Infinite-Dilution Viscoelastic Properties of Poly-γ-Benzyl-L-Glutamate in Helicogenic Solvents. Biopolymers. 1973;12(8):1905-15.

[167] Mackay ME, Dao TT, Tuteja A, Ho DL, Van Horn B, Kim H-C, et al. Nanoscale Effects Leading to Non-Einstein-Like Decrease in Viscosity. Nat Mater. 2003;2(11):762-6.

[168] Wagner NJ, Bender JW. The Role of Nanoscale Forces in Colloid Dispersion Rheology. MRS Bull. 2004;29(2):100-6.

[169] Batchelor G. Transport Properties of Two-Phase Materials with Random Structure. Annu Rev Fluid Mech. 1974;6(1):227-55.

[170] Van der Werff J, De Kruif C. Hard-Sphere Colloidal Dispersions: The Scaling of Rheological Properties with Particle Size, Volume Fraction, and Shear Rate. J Rheol. 1989;33:421.

[171] Mellema J, van der Werff J, Blom C, de Kruif C. Interpretation of the Complex Viscosity of Dense Hard-Sphere Dispersions. Phys Rev A. 1989;39(7):3696.

[172] Russel WB, Sperry PR. Effect of Microstructure on the Viscosity of Hard Sphere Dispersions and Modulus of Composites. Prog Org Coat. 1994;23(4):305-24.

[173] Brady JF. Model Hard-Sphere Dispersions: Statistical Mechanical Theory, Simulations, and Experiments. Curr Opin Colloid Interf Sci. 1996;1(4):472-80.

[174] Butler SZ, Hollen SM, Cao L, Cui Y, Gupta JA, Gutierrez HR, et al. Progress, Challenges, and Opportunities in Two-Dimensional Materials Beyond Graphene. ACS Nano. 2013;7(4):2898-926.

[175] van der Kooij FM, Boek ES, Philipse AP. Rheology of Dilute Suspensions of Hard Platelike Colloids. J Coll Interf Sci. 2001;235(2):344-9.

[176] Sun D, Sue H-J, Cheng Z, Martínez-Ratón Y, Velasco E. Stable Smectic Phase in Suspensions of Polydisperse Colloidal Platelets with Identical Thickness. Phys Rev E. 2009;80(4):041704.

[177] Keller SW, Kim H-N, Mallouk TE. Layer-by-Layer Assembly of Intercalation Compounds and Heterostructures on Surfaces: Toward Molecular "Beaker" Epitaxy. J Amer Chem Soc. 1994;116(19):8817-8.

[178] Garcia ME, Naffin JL, Deng N, Mallouk TE. Preparative-Scale Separation of Enantiomers Using Intercalated α-Zirconium Phosphate. Chem Mater. 1995;7(10):1968-73.

[179] Kaschak DM, Johnson SA, Hooks DE, Kim HN, Ward MD, Mallouk TE. Chemistry on the Edge: A Microscopic Analysis of the Intercalation, Exfoliation, Edge Functionalization, and Monolayer Surface Tiling Reactions of α-Zirconium Phosphate. J Amer Chem Soc. 1998;120(42):10887-94.

[180] Takei T, Kobayashi Y, Hata H, Yonesaki Y, Kumada N, Kinomura N, et al. Anodic Electrodeposition of Highly Oriented Zirconium Phosphate and Polyaniline-Intercalated Zirconium Phosphate Films. J Amer Chem Soc. 2006;128(51):16634-40.

[181] Sun L, Boo WJ, Sun D, Clearfield A, Sue H-J. Preparation of Exfoliated Epoxy/α-Zirconium Phosphate Nanocomposites Containing High Aspect Ratio Nanoplatelets. Chem Mater. 2007;19(7):1749-54.

[182] Kim H-N, Keller SW, Mallouk TE, Schmitt J, Decher G. Characterization of Zirconium Phosphate/Polycation Thin Films Grown by Sequential Adsorption Reactions. Chem Mater. 1997;9(6):1414-21.

[183] Bestaoui N, Spurr NA, Clearfield A. Intercalation of Polyether Amines into α-Zirconium Phosphate. J Mater Chem. 2006;16(8):759-64.

[184] Gérard J, Espuche E. Modification of α-ZrP Nanofillers by Amines of Different Chain Length: Consequences on the Morphology and Mechanical Properties of Styrene Butadiene Rubber Based Nanocomposites. Euro Polym J. 2012;48(1):217-27.

[185] Wong M, Ishige R, Hoshino T, Hawkins SA, Li P, Takahara A, et al. Solution Processable Iridescent α-ZrP Nanoplatelets with Finely Tunable Inter-Layer Distances Using Charge- and Sterically-Stabilizing Oligomeric Surfactants. Submitted to Chem Mater.

[186] White KL, Wong M, Li P, Sue H-J. Rheology of Smectic Liquid Crystals Formed from Exfoliated Nanoplatelets Dispersed in Epoxy Precursor. Submitted to Langmuir.

[187] Wong M, Ishige R, White KL, Li P, Higuchi T, Jinnai H, et al. Large-Scale Self-Assembled Nanoplatelet/Polymer Layers with Tunable Gas Permeability Via Spray-Coating of Nanoplatelet Filled Solutions. Submitted to Nat Comm.

[188] Li P, White KL, Nishimura R, Kim D, Krishnamoorti R, Sue H-J. Bioinspired Design and Self-Assembly of Ultrastrong Epoxy Nanocomposites Containing Nanoplatelets with Smectic Mesophase. To be submitted.

[189] Troup J, Clearfield A. Mechanism of Ion Exchange in Zirconium Phosphates. 20. Refinement of the Crystal Structure of α-Zirconium Phosphate. Inorg Chem. 1977;16(12):3311-4.

[190] van Gurp M, Palmen J. Time-Temperature Superposition for Polymeric Blends. Rheol Bull. 1998;67(1):5-8.

[191] Dealy J, Plazek D. Time-Temperature Superposition—a Users Guide. Rheol Bull. 2009;78(2):16-31.

[192] Trinkle S, Friedrich C. Van Gurp-Palmen-Plot: A Way to Characterize Polydispersity of Linear Polymers. Rheol Acta. 2001;40(4):322-8.

[193] Trinkle S, Walter P, Friedrich C. Van Gurp-Palmen Plot II–Classification of Long Chain Branched Polymers by Their Topology. Rheol Acta. 2002;41(1-2):103-13.

[194] White KL, Jin L, Ferrer N, Wong M, Bremner T, Sue H-J. Differentiating Structure and Stability in High-Performance Thermoplastics. Plast Res Online. 2013; dx.doi.org/10.2417/spepro.004517.

[195] White KL, Jin L, Ferrer N, Wong M, Bremner T, Sue H-J. Rheological and Thermal Behaviors of Commercial Poly(Aryletherketone)S. Polym Eng Sci. 2013;53(3):651-61.

[196] Giannelis EP, Krishnamoorti R, Manias E. Polymer-Silicate Nanocomposites: Model Systems for Confined Polymers and Polymer Brushes. Adv Polym Sci. 1999;118:108-47.

[197] Krishnamoorti R, Giannelis EP. Rheology of End-Tethered Polymer Layered Silicate Nanocomposites. Macromolecules. 1997;30(14):4097-102.

[198] Mueller S, Llewellin E, Mader H. The Rheology of Suspensions of Solid Particles. P Roy Soc A - Math Phy. 2010;466(2116):1201-28.

[199] Israelachvili J. Intermolecular and Surface Forces. 3rd ed. Burlington, MA: Academic Press; 2011.

[200] Clearfield A, Tindwa RM. On the Mechanism of Ion Exchange in Zirconium Phosphates—XXI Intercalation of Amines by α-Zirconium Phosphate. J Inorg Nucl Chem. 1979;41(6):871-8.

[201] Tindwa RM, Ellis DK, Peng G-Z, Clearfield A. Intercalation of *N*-Alkylamines by α-Zirconium Phosphate. J Chem Soc, Faraday Trans 1. 1985;81(2):545-52.

[202] Clearfield A, Stynes JA. The Preparation of Crystalline Zirconium Phosphate and Some Observations on Its Ion Exchange Behaviour. J Inorg Nucl Chem. 1964;26(1):117-29.

[203] Clearfield A, Smith SD. The Crystal Structure of Zirconium Phosphate and the Mechanism of Its Ion Exchange Behavior. J Coll Interf Sci. 1968;28(2):325-30.

[204] Clearfield A, Smith GD. Crystallography and Structure of α-Zirconium Bis (Monohydrogen Orthophosphate) Monohydrate. Inorg Chem. 1969;8(3):431-6.

[205] Alberti G, Casciola M, Costantino U. Inorganic Ion-Exchange Pellicles Obtained by Delamination of α-Zirconium Phosphate Crystals. J Coll Interf Sci. 1985;107(1):256-63.

[206] Clearfield A, Costantino U, Alberti G, Bein T. Layered Metal Phosphates and Their Intercalation Chemistry. In: Alberti G, Bein T, eds. Comprehensive Supramolecular Chemistry: Pergamon Press, New York 1996, p. 107-49.

[207] Hoppe R, Alberti G, Costantino U, Dionigi C, Schulz-Ekloff Gn, Vivani R. Intercalation of Dyes in Layered Zirconium Phosphates. 1. Preparation and Spectroscopic Characterization of α-Zirconium Phosphate Crystal Violet Compounds. Langmuir. 1997;13(26):7252-7.

[208] Jomha A, Merrington A, Woodcock L, Barnes H, Lips A. Recent Developments in Dense Suspension Rheology. Powder Technol. 1991;65(1):343-70.

[209] Mewis J, Spaull A. Rheology of Concentrated Dispersions. Adv Coll Interf Sci. 1976;6(3):173-200.

[210] Jeffrey D, Acrivos A. The Rheological Properties of Suspensions of Rigid Particles. AIChE J. 1976;22(3):417-32.

[211] Folgar F, Tucker CL. Orientation Behavior of Fibers in Concentrated Suspensions. J Reinf Plast Comp. 1984;3(2):98-119.

[212] Garboczi EJ, Snyder KA, Douglas JF, Thorpe MF. Geometrical Percolation Threshold of Overlapping Ellipsoids. Phys Rev E. 1995;52(1):819.

[213] Anczurowski E, Mason S. Particle Motions in Sheared Suspensions. XXIV. Rotation of Rigid Spheroids and Cylinders. J Rheol. 1968;12:209.

[214] Gauthier F, Goldsmith H, Mason S. Particle Motions in Non-Newtonian Media. Rheol Acta. 1971;10(3):344-64.

[215] Allegra G, Raos G, Vacatello M. Theories and Simulations of Polymer-Based Nanocomposites: From Chain Statistics to Reinforcement. Prog Polym Sci. 2008;33(7):683-731.

[216] Fragiadakis D, Pissis P, Bokobza L. Glass Transition and Molecular Dynamics in Poly (Dimethylsiloxane)/Silica Nanocomposites. Polymer. 2005;46(16):6001-8.

[217] Fragiadakis D, Bokobza L, Pissis P. Dynamics near the Filler Surface in Natural Rubber-Silica Nanocomposites. Polymer. 2011;52(14):3175-82.

[218] Betancourt BAP, Douglas JF, Starr FW. Fragility and Cooperative Motion in a Glass-Forming Polymer–Nanoparticle Composite. Soft Matter. 2013;9(1):241-54.

[219] Yang P, Deng T, Zhao D, Feng P, Pine D, Chmelka BF, et al. Hierarchically Ordered Oxides. Science. 1998;282(5397):2244-6.

[220] Ruokolainen J, Saariaho M, Ikkala O, Ten Brinke G, Thomas E, Torkkeli M, et al. Supramolecular Routes to Hierarchical Structures: Comb-Coil Diblock Copolymers Organized with Two Length Scales. Macromolecules. 1999;32(4):1152-8.

[221] Fratzl P, Weinkamer R. Nature's Hierarchical Materials. Prog Mater Sci. 2007;52(8):1263-334.

[222] Boal AK, Ilhan F, DeRouchey JE, Thurn-Albrecht T, Russell TP, Rotello VM. Self-Assembly of Nanoparticles into Structured Spherical and Network Aggregates. Nature. 2000;404(6779):746-8.

[223] Kumar SK, Krishnamoorti R. Nanocomposites: Structure, Phase Behavior, and Properties. Annu Rev Chem Biomol Engin. 2010;1:37-58.

[224] Glotzer SC, Solomon MJ. Anisotropy of Building Blocks and Their Assembly into Complex Structures. Nat Mater. 2007;6(8):557-62.

[225] Sandler JKW, Kirk JE, Kinloch IA, Shaffer MSP, Windle AH. Ultra-Low Electrical Percolation Threshold in Carbon-Nanotube-Epoxy Composites. Polymer. 2003;44(19):5893-9.

[226] Bauhofer W, Kovacs JZ. A Review and Analysis of Electrical Percolation in Carbon Nanotube Polymer Composites. Compos Sci Techn. 2009;69(10):1486-98.

[227] White KL, Sue H-J. Electrical Conductivity and Fracture Behavior of Epoxy/Polyamide-12/Multiwalled Carbon Nanotube Composites. Polym Eng Sci. 2011;51(11):2245-53.

[228] White KL, Sue H-J. Delamination Toughness of Fiber Reinforced Composites Containing a Carbon Nanotube/Polyamide-12 Epoxy Thin Film Interlayer. Polymer. 2011;53(1):37-42.

[229] Kharchenko SB, Douglas JF, Obrzut J, Grulke EA, Migler KB. Flow-Induced Properties of Nanotube-Filled Polymer Materials. Nat Mater. 2004;3(8):564-8.

[230] Clearfield A. Inorganic Ion Exchangers with Layered Structures. Annu Rev Mater Sci. 1984;14(1):205-29.

[231] Clearfield A. Role of Ion Exchange in Solid-State Chemistry. Chem Rev. 1988;88(1):125-48.

[232] Krishnamoorti R, Vaia RA, Giannelis EP. Structure and Dynamics of Polymer-Layered Silicate Nanocomposites. Chem Mater. 1996;8(8):1728-34.

[233] Mourchid A, Delville A, Lambard J, Lecolier E, Levitz P. Phase Diagram of Colloidal Dispersions of Anisotropic Charged Particles: Equilibrium Properties, Structure, and Rheology of Laponite Suspensions. Langmuir. 1995;11(6):1942-50.

[234] Sternstein S, Zhu A-J. Reinforcement Mechanism of Nanofilled Polymer Melts as Elucidated by Nonlinear Viscoelastic Behavior. Macromolecules. 2002;35(19):7262-73.

[235] Zhu A-J, Sternstein S. Nonlinear Viscoelasticity of Nanofilled Polymers: Interfaces, Chain Statistics and Properties Recovery Kinetics. Compos Sci Techn. 2003;63(8):1113-26.

[236] Hooper JB, Schweizer KS. Theory of Phase Separation in Polymer Nanocomposites. Macromolecules. 2006;39(15):5133-42.

[237] Sen S, Xie Y, Kumar SK, Yang H, Bansal A, Ho DL, et al. Chain Conformations and Bound-Layer Correlations in Polymer Nanocomposites. Phys Rev Lett. 2007;98(12):128302.

[238] Mackay ME, Tuteja A, Duxbury PM, Hawker CJ, Van Horn B, Guan Z, et al. General Strategies for Nanoparticle Dispersion. Science. 2006;311(5768):1740-3.

[239] Green DL, Mewis J. Connecting the Wetting and Rheological Behaviors of Poly (Dimethylsiloxane)-Grafted Silica Spheres in Poly (Dimethylsiloxane) Melts. Langmuir. 2006;22(23):9546-53.

[240] Bansal A, Yang H, Li C, Benicewicz BC, Kumar SK, Schadler LS. Controlling the Thermomechanical Properties of Polymer Nanocomposites by Tailoring the Polymer/Particle Interface. J Polym Sci Pol Phys. 2006;44(20):2944-50.

[241] Buining P, Lekkerkerker H. Isotropic-Nematic Phase Separation of a Dispersion of Organophilic Boehmite Rods. J Phys Chem. 1993;97(44):11510-6.

[242] van Bruggen MP, van der Kooij FM, Lekkerkerker HN. Liquid Crystal Phase Transitions in Dispersions of Rod-Like Colloidal Particles. J Phys-Condens Mat. 1996;8(47):9451.

[243] van der Kooij FM, Lekkerkerker HN. Formation of Nematic Liquid Crystals in Suspensions of Hard Colloidal Platelets. J Phys Chem B. 1998;102(40):7829-32.

[244] van der Kooij FM, Vogel M, Lekkerkerker HNW. Phase Behavior of a Mixture of Platelike Colloids and Nonadsorbing Polymer. Phys Rev E. 2000;62(4):5397-402.

[245] van der Kooij FM, Kassapidou K, Lekkerkerker HN. Liquid Crystal Phase Transitions in Suspensions of Polydisperse Plate-Like Particles. Nature. 2000;406(6798):868-71.

[246] van der Kooij F, van der Beek D, Lekkerkerker H. Isotropic-Nematic Phase Separation in Suspensions of Polydisperse Colloidal Platelets. J Phys Chem B. 2001;105(9):1696-700.

[247] Alberti G, Costantino U. Recent Progress in the Intercalation Chemistry of Layered α-Zirconium Phosphate and Its Derivatives, and Future Perspectives for Their Use in Catalysis. J Mol Catal. 1984;27(1):235-50.

[248] Behrendt D, Beneke K, Lagaly G. Intercalation Compounds of Zirconium Phosphate. Angew Chem Int Edit. 1976;15(9):544-5.

[249] Yamanaka S, Koizumi M. Structural Consideration of Zirconium Phosphate and Its Organic Complexes. Clay Clay Miner. 1975;23(6):477-8.

[250] Costantino U. Intercalation of Alkanols and Glycols into Zirconium (IV) Hydrogen Phosphate Monohydrate. J Chem Soc Dalton. 1979(2):402-5.

[251] Costantino U, Vivani R, Zima V, Beneš Lk, Melánová K. Microwave-Assisted Intercalation of 1-Alkanols and 1, ω-Alkanediols into α-Zirconium Phosphate. Evidence of Conformational Phase Transitions in the Bimolecular Film of Alkyl Chains. Langmuir. 2002;18(4):1211-7.

[252] Alberti G, Casciola M, Costantino U, Vivani R. Layered and Pillared Metal (IV) Phosphates and Phosphonates. Adv Mater. 1996;8(4):291-303.

[253] Hanwell MD, Curtis DE, Lonie DC, Vandermeersch T, Zurek E, Hutchison GR. Avogadro: An Advanced Semantic Chemical Editor, Visualization, and Analysis Platform. J Cheminformatics. 2012;4(1):1-17.

[254] Wissbrun KF. Rheology of Rod-Like Polymers in the Liquid Crystalline State. J Rheol. 1981;25(6):619-62.

[255] Rubin SF, Kannan RM, Kornfield JA, Boeffel C. Effect of Mesophase Order and Molecular Weight on the Dynamics of Nematic and Smectic Side-Group Liquid-Crystalline Polymers. Macromolecules. 1995;28(10):3521-30.

[256] Mezzenga R, Meyer C, Servais C, Romoscanu AI, Sagalowicz L, Hayward RC. Shear Rheology of Lyotropic Liquid Crystals: A Case Study. Langmuir. 2005;21(8):3322-33.

[257] Bandyopadhyay R, Liang D, Harden JL, Leheny RL. Slow Dynamics, Aging, and Glassy Rheology in Soft and Living Matter. Solid State Commun. 2006;139(11):589-98.

[258] Sollich P. Soft Glassy Rheology. In: Weiss RG, Terech P, eds. Molecular Gels. Netherlands: Springer 2006, p. 161-92.

[259] Klein J. Shear, Friction, and Lubrication Forces between Polymer-Bearing Surfaces. Annu Rev Mater Sci. 1996;26(1):581-612.

[260] Klein J, Kumacheva E, Mahalu D, Perahia D, Fetters LJ. Reduction of Frictional Forces between Solid Surfaces Bearing Polymer Brushes. Nature. 1994;370(6491):634-6.

[261] Colby RH, Ober CK, Gillmor JR, Connelly RW, Duong T, Galli G, et al. Smectic Rheology. Rheol Acta. 1997;36(5):498-504.

[262] Salvetat J-P, Bonard J-M, Thomson N, Kulik A, Forro L, Benoit W, et al. Mechanical Properties of Carbon Nanotubes. Appl Phys A. 1999;69(3):255-60.

[263] Yu M-F, Lourie O, Dyer MJ, Moloni K, Kelly TF, Ruoff RS. Strength and Breaking Mechanism of Multiwalled Carbon Nanotubes under Tensile Load. Science. 2000;287(5453):637-40.

[264] Ebbesen T, Lezec H, Hiura H, Bennett J, Ghaemi H, Thio T. Electrical Conductivity of Individual Carbon Nanotubes. Nature. 1996;382:54-6.

[265] Yao Z, Kane CL, Dekker C. High-Field Electrical Transport in Single-Wall Carbon Nanotubes. Phys Rev Lett. 2000;84(13):2941.

[266] Yao Z, Dekker C, Avouris P. Electrical Transport Measurements on Single-Walled Carbon Nanotube. Top Appl Phys. 2001;80:147-71.

[267] Che J, Cagin T, Goddard III WA. Thermal Conductivity of Carbon Nanotubes. Nanotechnology. 2000;11(2):65-9.

[268] Sevik C, Sevinçli H, Cuniberti G, Cagın T. Phonon Engineering in Carbon Nanotubes by Controlling Defect Concentration. Nano Lett. 2011;11(11):4971-7.

[269] Berber S, Kwon Y-K, Tomanek D. Unusually High Thermal Conductivity of Carbon Nanotubes. Phys Rev Lett. 2000;84(20):4613.

[270] Yang D, Wang S, Zhang Q, Sellin P, Chen G. Thermal and Electrical Transport in Multi-Walled Carbon Nanotubes. Phys Lett A. 2004;329(3):207-13.

[271] Yu C, Shi L, Yao Z, Li D, Majumdar A. Thermal Conductance and Thermopower of an Individual Single-Wall Carbon Nanotube. Nano Lett. 2005;5(9):1842-6.

[272] Bauhofer W, Schulz S, Eken A, Skipa T, Lellinger D, Alig I, et al. Shear-Controlled Electrical Conductivity of Carbon Nanotubes Networks Suspended in Low and High Molecular Weight Liquids. Polymer. 2010;51(22):5024-7.

[273] Alig I, Skipa T, Lellinger D, Pötschke P. Destruction and Formation of a Carbon Nanotube Network in Polymer Melts: Rheology and Conductivity Spectroscopy. Polymer. 2008;49(16):3524-32.

[274] Skipa T, Lellinger D, Saphiannikova M, Alig I. Shear-Stimulated Formation of Multi-Wall Carbon Nanotube Networks in Polymer Melts. Phys Status Solidi B. 2009;246(11-12):2453-6.

[275] Skipa T, Lellinger D, Böhm W, Saphiannikova M, Alig I. Influence of Shear Deformation on Carbon Nanotube Networks in Polycarbonate Melts: Interplay between Build-up and Destruction of Agglomerates. Polymer. 2010;51(1):201-10.

[276] Ganguli S, Roy AK, Anderson DP. Improved Thermal Conductivity for Chemically Functionalized Exfoliated Graphite/Epoxy Composites. Carbon. 2008;46(5):806-17.

[277] Warren GL, Sun L, Hadjiev VG, Davis D, Lagoudas D, Sue HJ. B-Staged Epoxy/Single-Walled Carbon Nanotube Nanocomposite Thin Films for Composite Reinforcement. J Appl Polym Sci. 2009;112(1):290-8.

[278] Sun L, Warren GL, Sue H-J. Partially Cured Epoxy/SWCNT Thin Films for the Reinforcement of Vacuum-Assisted Resin-Transfer-Molded Composites. Carbon. 2010;48(8):2364-7.

[279] Shaffer MS, Fan X, Windle A. Dispersion and Packing of Carbon Nanotubes. Carbon. 1998;36(11):1603-12.

[280] Laposa J. Vibrational Spectra of Nitrobenzene-d_5. Spectrochim Acta A. 1979;35(1):65-71.

[281] Clarkson J, Ewen Smith W. A DFT Analysis of the Vibrational Spectra of Nitrobenzene. J Mol Struct. 2003;655(3):413-22.

[282] Kuwae A, Machida K. Vibrational Spectra of Nitrobenzene-d_0, -*p*-*d* and -d_5 and Normal Vibrations of Nitrobenzene. Spectrochim Acta A. 1979;35(1):27-33.

[283] Schulz SC, Bauhofer W. Shear Influenced Network Dynamics and Electrical Conductivity Recovery in Carbon Nanotube/Epoxy Suspensions. Polymer. 2010;51(23):5500-5.

[284] Alig I, Lellinger D, Engel M, Skipa T, Pötschke P. Destruction and Formation of a Conductive Carbon Nanotube Network in Polymer Melts: In-Line Experiments. Polymer. 2008;49(7):1902-9.

[285] Winter HH, Chambon F. Analysis of Linear Viscoelasticity of a Crosslinking Polymer at the Gel Point. J Rheol. 1986;30(2):367-82.

[286] Winter HH, Mours M. Rheology of Polymers near Liquid-Solid Transitions. Adv Polym Sci. 1997;134:165-234.

[287] Lin-Gibson S, Pathak J, Grulke E, Wang H, Hobbie E. Elastic Flow Instability in Nanotube Suspensions. Phys Rev Lett. 2004;92(4):048302-1-4.

[288] Fry D, Langhorst B, Kim H, Grulke E, Wang H, Hobbie EK. Anisotropy of Sheared Carbon-Nanotube Suspensions. Phys Rev Lett. 2005;95(3):038304.

[289] Wang H, Christopherson G, Xu Z, Porcar L, Ho D, Fry D, et al. Shear-SANS Study of Single-Walled Carbon Nanotube Suspensions. Chem Phys Lett. 2005;416(1):182-6.

[290] Hobbie E, Fry D. Nonequilibrium Phase Diagram of Sticky Nanotube Suspensions. Phys Rev Lett. 2006;97(3):036101.

[291] Fry D, Langhorst B, Wang H, Becker M, Bauer B, Grulke E, et al. Rheo-Optical Studies of Carbon Nanotube Suspensions. J Chem Phys. 2006;124:054703.

[292] Hobbie E, Fry D. Rheology of Concentrated Carbon Nanotube Suspensions. J Chem Phys. 2007;126:124907.

[293] Rahatekar SS, Koziol KK, Kline SR, Hobbie EK, Gilman JW, Windle AH. Length-Dependent Mechanics of Carbon-Nanotube Networks. Adv Mater. 2009;21(8):874-8.

[294] Hobbie EK. Shear Rheology of Carbon Nanotube Suspensions. Rheol Acta. 2010;49(4):323-34.

[295] Gryshchuk O, Karger-Kocsis J, Thomann R, Konya Z, Kiricsi I. Multiwall Carbon Nanotube Modified Vinylester and Vinylester–Based Hybrid Resins. Compos Part A. 2006;37(9):1252-9.

[296] Kwei T, Schonhorn H, Frisch H. Dynamic Mechanical Properties of the Transcrystalline Regions in Two Polyolefins. J Appl Phys. 1967;38(6):2512-6.

[297] Matsuoka S, Daane J, Bair H, Kwei T. A Further Study of the Properties of Transcrystalline Regions in Polyethylene. J Polym Sci B Pol Lett. 1968;6(1):87-91.

[298] Frisch H, Schonhorn H, Kwei T. Transcrystalline Phenomena and Adhesion. J Elastom Plast. 1971;3(4):214-21.

[299] Chen EJ, Hsiao BS. The Effects of Transcrystalline Interphase in Advanced Polymer Composites. Polym Eng Sci. 1992;32(4):280-6.

[300] Lee Y, Porter RS. Crystallization of Poly(Etheretherketone) (PEEK) in Carbon Fiber Composites. Polym Eng Sci. 1986;26(9):633-9.

[301] Hashin Z. Thermoelastic Properties of Fiber Composites with Imperfect Interface. Mech Mater. 1990;8(4):333-48.

[302] Liu H, Brinson LC. Reinforcing Efficiency of Nanoparticles: A Simple Comparison for Polymer Nanocomposites. Compos Sci Techn. 2008;68(6):1502-12.

[303] Cadek M, Coleman J, Ryan K, Nicolosi V, Bister G, Fonseca A, et al. Reinforcement of Polymers with Carbon Nanotubes: The Role of Nanotube Surface Area. Nano Lett. 2004;4(2):353-6.

[304] Coleman JN, Cadek M, Blake R, Nicolosi V, Ryan KP, Belton C, et al. High Performance Nanotube-Reinforced Plastics: Understanding the Mechanism of Strength Increase. Adv Funct Mater. 2004;14(8):791-8.

[305] Coleman JN, Cadek M, Ryan KP, Fonseca A, Nagy JB, Blau WJ, et al. Reinforcement of Polymers with Carbon Nanotubes. The Role of an Ordered Polymer Interfacial Region. Experiment and Modeling. Polymer. 2006;47(26):8556-61.

[306] Simmons JG. Generalized Formula for the Electric Tunnel Effect between Similar Electrodes Separated by a Thin Insulating Film. J Appl Phys. 1963;34:1793.

[307] Kalfus J, Jancar J. Reinforcing Mechanisms in Amorphous Polymer Nano-Composites. Compos Sci Techn. 2008;68(15):3444-7.

[308] Barber AH, Cohen SR, Eitan A, Schadler LS, Wagner HD. Fracture Transitions at a Carbon-Nanotube/Polymer Interface. Adv Mater. 2006;18(1):83-7.

[309] Gou J, Minaie B, Wang B, Liang Z, Zhang C. Computational and Experimental Study of Interfacial Bonding of Single-Walled Nanotube Reinforced Composites. Comp Mater Sci. 2004;31(3):225-36.

[310] Allaoui A, Bai S, Cheng H-M, Bai J. Mechanical and Electrical Properties of a MWNT/Epoxy Composite. Compos Sci Techn. 2002;62(15):1993-8.

[311] Richard P, Prasse T, Cavaille J-Y, Chazeau L, Gauthier C, Duchet J. Reinforcement of Rubbery Epoxy by Carbon Nanofibres. Mater Sci Engin A. 2003;352(1):344-8.

[312] Bai J. Evidence of the Reinforcement Role of Chemical Vapour Deposition Multi-Walled Carbon Nanotubes in a Polymer Matrix. Carbon. 2003;41(6):1325-8.

[313] Liu L, Wagner HD. Rubbery and Glassy Epoxy Resins Reinforced with Carbon Nanotubes. Compos Sci Techn. 2005;65(11):1861-8.

[314] Ci L, Bai J. The Reinforcement Role of Carbon Nanotubes in Epoxy Composites with Different Matrix Stiffness. Compos Sci Techn. 2006;66(3):599-603.

[315] Yee AF, Pearson RA. Toughening Mechanisms in Elastomer-Modified Epoxies. J Mater Sci. 1986;21(7):2462-74.

[316] Pearson R, Yee A. Toughening Mechanisms in Elastomer-Modified Epoxies. J Mater Sci. 1989;24(7):2571-80.

[317] Coleman JN, Khan U, Blau WJ, Gun'ko YK. Small but Strong: A Review of the Mechanical Properties of Carbon Nanotube–Polymer Composites. Carbon. 2006;44(9):1624-52.

[318] Song YS, Youn JR. Influence of Dispersion States of Carbon Nanotubes on Physical Properties of Epoxy Nanocomposites. Carbon. 2005;43(7):1378-85.

[319] Thostenson ET, Chou T-W. Processing-Structure-Multi-Functional Property Relationship in Carbon Nanotube/Epoxy Composites. Carbon. 2006;44(14):3022-9.

[320] Sue H-J, Yee AF. Study of Fracture Mechanisms of Multiphase Polymers Using the Double-Notch Four-Point-Bending Method. J Mater Sci. 1993;28(11):2975-80.

[321] Sue H-J, Yee AF. Toughening Mechanisms in a Multi-Phase Alloy of Nylon 6, 6/Polyphenylene Oxide. J Mater Sci. 1989;24(4):1447-57.

[322] Cooper CA, Cohen SR, Barber AH, Wagner HD. Detachment of Nanotubes from a Polymer Matrix. Appl Phys Lett. 2002;81(20):3873-5.

[323] Barber AH, Cohen SR, Kenig S, Wagner HD. Interfacial Fracture Energy Measurements for Multi-Walled Carbon Nanotubes Pulled from a Polymer Matrix. Compos Sci Techn. 2004;64(15):2283-9.

[324] Barber AH, Cohen SR, Wagner HD. Static and Dynamic Wetting Measurements of Single Carbon Nanotubes. Phys Rev Lett. 2004;92(18):186103-.

[325] Schmid CF, Switzer LH, Klingenberg DJ. Simulations of Fiber Flocculation: Effects of Fiber Properties and Interfiber Friction. J Rheol. 2000;44:781.

[326] Schmid C, Klingenberg D. Mechanical Flocculation in Flowing Fiber Suspensions. Phys Rev Lett. 2000;84:290-3.

[327] Boo WJ, Liu J, Sue H-J. Fracture Behaviour of Nanoplatelet Reinforced Polymer Nanocomposites. Mater Sci Tech. 2006;22(7):829-34.

[328] Mason TG, Weitz D. Optical Measurements of Frequency-Dependent Linear Viscoelastic Moduli of Complex Fluids. Phys Rev Lett. 1995;74(7):1250.

[329] Starrs L, Bartlett P. One-and Two-Point Micro-Rheology of Viscoelastic Media. J Phys - Condens Mat. 2003;15(1):S251.

[330] Meyer A, Marshall A, Bush BG, Furst EM. Laser Tweezer Microrheology of a Colloidal Suspension. J Rheol. 2006;50:77.

[331] Chen D, Chen K, Hough L, Islam M, Yodh A. Rheology of Carbon Nanotube Networks During Gelation. Macromolecules. 2010;43(4):2048-53.

[332] Williams ML, Landel RF, Ferry JD. The Temperature Dependence of Relaxation Mechanisms in Amorphous Polymers and Other Glass-Forming Liquids. J Amer Chem Soc. 1955;77(14):3701-7.

[333] Richert R, Angell C. Dynamics of Glass-Forming Liquids. V. On the Link between Molecular Dynamics and Configurational Entropy. J Chem Phys. 1998;108:9016.

APPENDIX I

RHEOLOGY OF UNFILLED EPOXY PRECURSOR

The model nanoparticle systems investigated in this dissertation were prepared using two different suspending matrices: DER332, a DGEBA monomer, and EPON862, a DGEBF monomer. The rheological response of the unfilled epoxy monomers were extensively characterized with SAOS and steady shear measurements, and found to show similar behavior. The master curve of linear viscoelastic response of the unfilled DGEBF epoxy monomer is shown in Figure A-I.1. At a reference temperature of 30°C, the epoxy monomer behaves as a simple viscous fluid, with dominant loss modulus and negligible storage modulus. The frequency range was extended using isothermal measurements obtained over a temperature range from 10 - 70°C. At higher temperature, the measured stress is not sufficient to obtain reliable measurements of the in-phase component of periodic stress. The measurements were superimposed using the time-temperature superposition (TTS) principle, which is based on the assumption that the dominant relaxation times governing viscoelastic response follow the same temperature dependence [28, 191]. The linear viscoelasticity of the epoxy monomer follows simple scaling of a viscous fluid with single relaxation time, τ. The validity of TTS was confirmed by plotting δ as a function of $|G^*|$ (Figure A-I.1b), which is commonly referred to as a van Gurp-Palmen (vgP) plot [190]. The vGP representation is an extremely sensitive measure of the distribution of dominant relaxation times in the system.

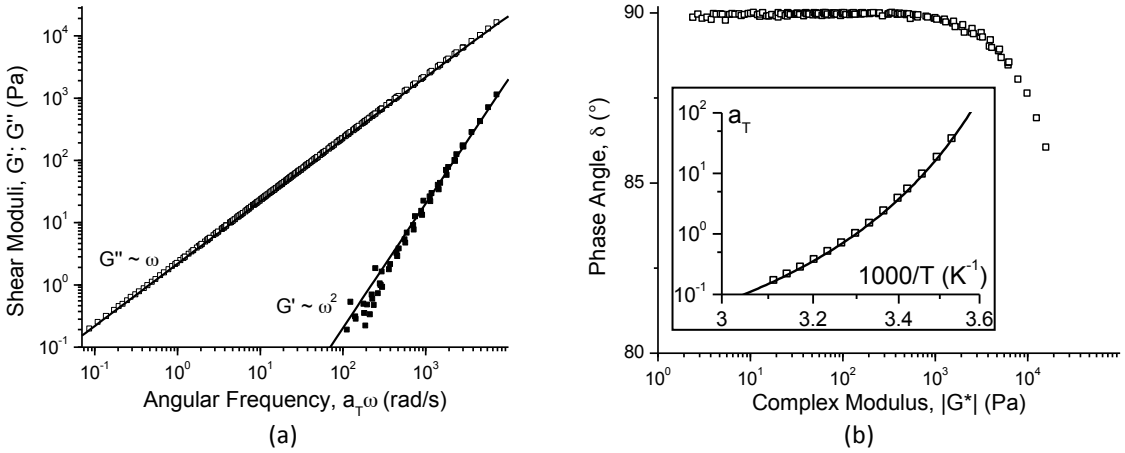

Figure A-I.1. (a) Master curves of linear viscoelastic response of unfilled DGEBF epoxy precursor EPON 862. Storage modulus, G', loss modulus, G'', and phase angle, δ, as functions of angular frequency. Measurements collected over temperature range of 10 - 70°C. Solid lines are fit to equations for Maxwell material. (b) vGP plot and (inset) shift factors used to obtain linear viscoelastic master curve.

Two shift factors are generally used to independently account for temperature-dependence of stress and time. The stress shift factor, b_T, accounts for the change in density, but was not significant for the unfilled epoxy monomer over this temperature range and is fixed at 1. The time shift factor a_T physically represents the magnitude of frequency shift needed to match response at the measurement temperature, *T*, with the behavior at a reference temperature, T_{ref}. The value of a_T was determined by plotting the magnitude of complex viscosity, $|\eta^*|\ b_T/a_T = b_T|G^*|/a_T\omega$, as a function of $b_T|G^*|$. This approach provides a consistent methodology to independently determine the shift factors in a meaningful way [191]. The range of a_T for the unfilled epoxy monomer is well-described by the empirical Williams-Landel-Flory (WLF) equation [332]:

(A-I.1) $$\log(a_T) = -\frac{C_1(T-T_{ref})}{C_2+(T-T_{ref})}$$

where C_1 = 3.67, and C_2 = 66.68 K, for T_{ref} = 303.15 K.

For measurements well above the resolution of the transducer, there is excellent superposition between data collected over the range of temperatures and frequencies. At low frequency and high temperature, the phase angle is nearly 90°, with a very narrow scatter of values within ~ 0.5°. The behavior of the unfilled matrix follows Maxwell's model for a viscous dashpot and elastic spring connected in series, which is the simplest mathematical expression of a viscoelastic fluid. The viscoelastic parameters are given by the expressions

(A-I.2) $$G'(\omega) = G_o \frac{(\omega\tau)^2}{1+(\omega\tau)^2}$$

(A-I.3) $$G''(\omega) = G_o \frac{\omega\tau}{1+(\omega\tau)^2}$$

where G_o is the magnitude of $|G^*| = \sqrt{G'^2 + G''^2}$ as $\omega \to \infty$, and τ is the characteristic relaxation time. The model provides an excellent fit, shown as solid lines in Figure A-I.1, for relaxation time of τ = 24.3 μs, and infinite frequency modulus of G_o = 9000 Pa. The zero-shear viscosity at T_{ref} = 30°C is $\eta_o = G_o\tau$ = 2.19 Pa.s.

The steady shear behavior of the epoxy precursor shows simple response characteristic of a Newtonian material (). The shear viscosity is independent of shear rate over the temperature range of 10 – 90°C, and is 2.19 Pa.s at the reference temperature of 30°C, in agreement with linear viscoelastic measurements. The temperature dependence is well described by the empirical Volger-Fulcher-Tammann (VFT) equation:

(A-I.4) $$\eta(T) = \eta_o^{VFT} \exp\left[\frac{B}{T-T_o}\right]$$

where η_o^{VFT} is the limiting viscosity as $(T - T_o) \to \infty$, B is a constant related to the fragility near the glass transition, and T_o is the temperature where the configurational entropy vanishes [333].

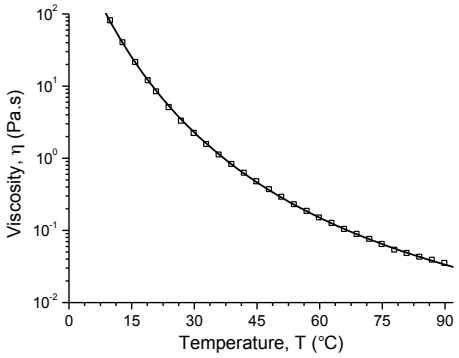

Figure A-I.2. Steady shear viscosity of unfilled EPON 862 fluid as function of temperature over range of 10 – 90°C. Solid curve is fit to VFT equation (Eqn. (A-I.4)).

APPENDIX II

SUPPLEMENTAL INFORMATION FOR RHEOLOGY OF ZRP NANOPLATELETS

WITH LIQUID CRYSTALLINE ORGANIZATION

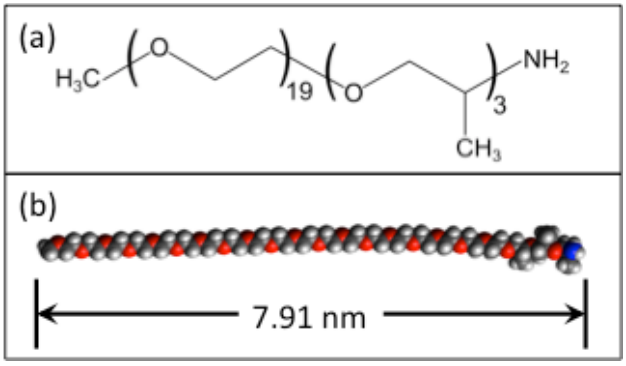

Figure A-II.1. Jeffamine M1000, a commercial polyoxyalkyleneamine, was used to exfoliate the zirconium phosphate nanoplatelets in the work. (a) Chemical structure of M1000. (b) Equilibrium structure of extended M1000 molecule constructed with Avogadro software and optimized using the MMFF94 force field. The length of an extended M1000 chain is ~ 7.9 nm.

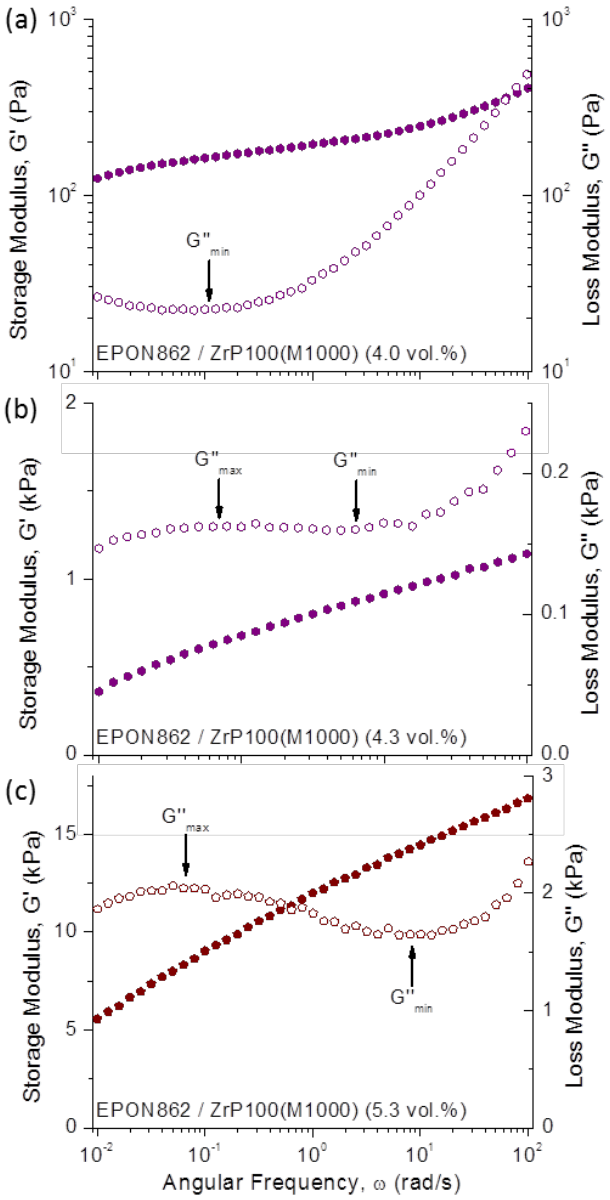

Figure A-II.2. Detail on linear viscoelastic response of concentrated ZrP suspensions in epoxy monomer matrix: storage modulus, G′, and loss modulus, G″, as functions of angular frequency, ω, for suspensions containing (a) 4.0 vol.% ZrP, (b) 4.3 vol.% ZrP, and (c) 5.3 vol.% ZrP. The minima and maxima in G″ are designated on the graphs. In (a), *y*-axes are shown in log scale for clarity. In (b,c), the *y*-axes are shown on a linear scale.

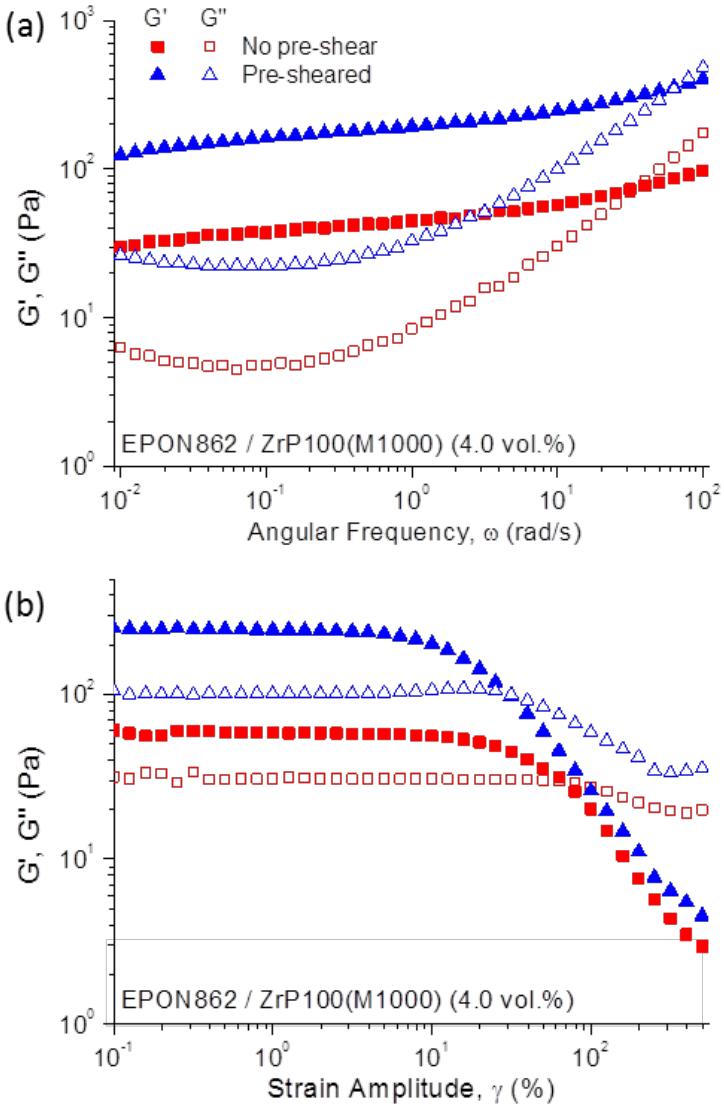

Figure A-II.3. Shear history dependence of epoxy monomer matrix filled with 4.0 vol.% ZrP.

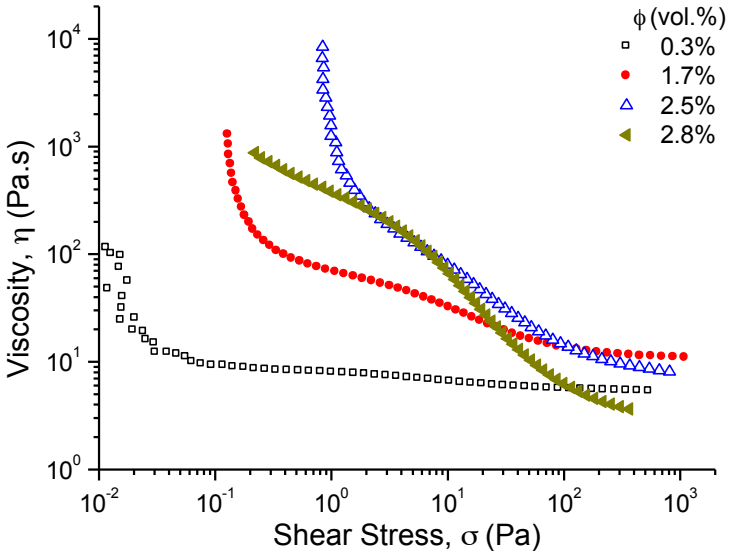

Figure A-II.4. Steady shear rheology of suspensions containing 0.3 – 2.8 vol.% ZrP in epoxy monomer matrix. Shear viscosity shown as a function of shear stress.

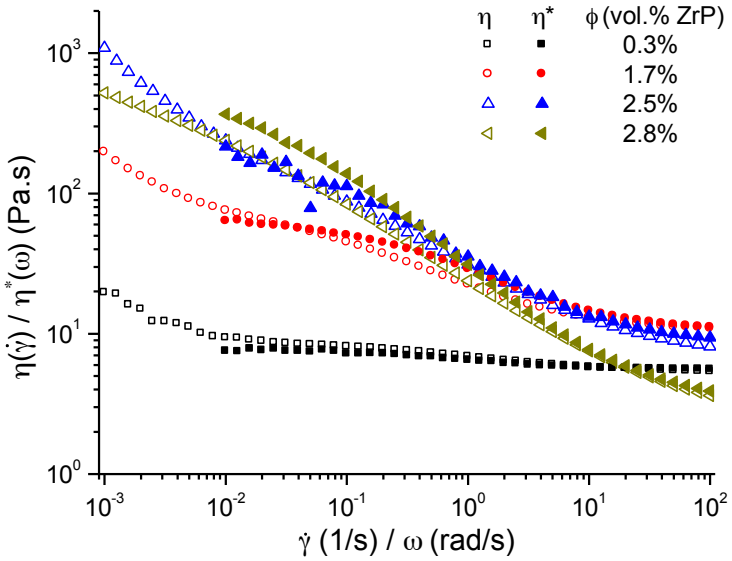

Figure A-II.5. Complex viscosity, η*, and shear viscosity, η, as functions of angular frequency, ω, and shear rate, $\dot{\boldsymbol{\gamma}}$, respectively, of suspensions containing 0.3 – 2.8 vol.% ZrP in epoxy monomer matrix.

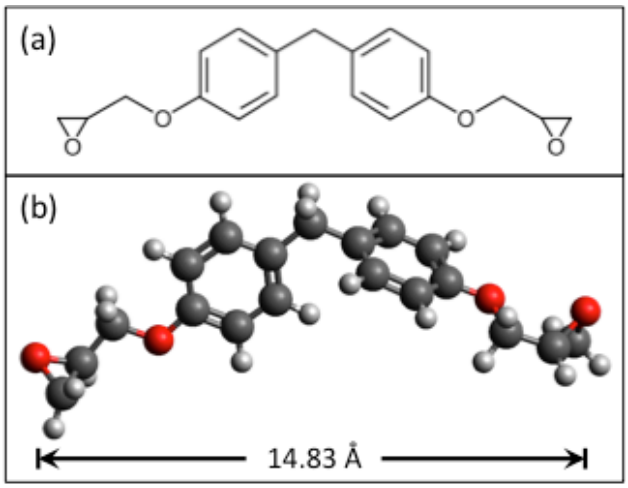

Figure A-II.6. (a) Chemical structure of DGEBF monomer. (b) Equilibrium structure of isolated DGEBF molecule determined from Avogadro software. The molecular structure was optimized using the MMFF94 force field. The minimum diameter of a sphere enclosing the DGEBF molecule is ~ 1.5 nm.